学位論文

The Formation of Massive Starbursts and Super Massive Black Holes in a Proto-cluster at a Redshift of 3

（赤方偏移 3 の原始銀河団における大質量爆発的星形成銀河及び超大質量ブラックホールの形成）

平成 26 年 12 月博士（理学）申請

東京大学大学院理学系研究科

天文学専攻

梅畑豪紀

The Formation of Massive Starbursts and Super Massive Black Holes in a Proto-cluster at a Redshift of 3

Hideki Umehata

Department of Astronomy, School of Science

The University of Tokyo

A Thesis for the degree of

Doctor of Philosophy

December 2014

Abstract

In this thesis we present a study on ecology of submillimeter galaxies (SMGs). SMGs are the most massive and active dusty starbursts in the early universe and some of them harbor massive supermassive black holes (SMBHs). Therefore SMGs are the key population in understanding the formation and evolution of the massive galaxies and evolutionary link between galaxies and SMBHs. Our objective is to illustrate how such extremely active population is formed within the cosmic large-scale structure. In the regime of hierarchical structure formation model, such massive galaxies are predicted to reside in the massive dark matter haloes and hence SMGs can preferentially formed in the dense environment within the large-scale structure. However the observational evidence is still sparse due to a number of obstacles. The known density structure in the early universe is rare and to determine redshift of SMGs has been also accompanied with difficulties such as faintness in optical to near-infrared bands and the crude angular resolution of single-dish wide surveys at submillimeter wavelengths.

To overcome such trouble and clarify the environmental dependence of SMG and SMBH formation, we focus on the $z = 3.1$ proto-cluster, SSA22. This proto-cluster has been known to be the most remarkable over density in the era and has a filamentary large-scale structure traced by Lyman-α emitters (LAEs). First we performed wide and deep 1.1 mm survey with AzTEC bolometer camera onboard the ASTE 10 m submillimeter telescope. We swept more than a 900 arcmin^2 sky area toward the denset region of the proto-cluster to discover 125 SMGs with signal to noise ratio (S/N) $\geq$3.5. As a next step, we selected 45 SMGs which possibly lie at $z = 3.1$ based on counterpart identification using radio and near- to mid-infrared data and photometric redshift estimates to conduct a 1.1 mm follow-up campaign utilizing ALMA for the 45 SMGs . Our 1.1 mm continuum imaging achieved angular resolution of 0.6$''$, which is 50 times better than that of AzTEC/ASTE (30$''$). Hence we succeeded to be released from the nightmare in counterpart identification almost completely. In this ALMA survey we totally find 64 individual SMGs.

To inspect the environmental effect, we adopt the ALESS survey as a comparison criterion. The survey is one of the largest SMG survey until today and their field, ECDF-S, is known to be a general field. At the beginning, we derived number counts and photometric

redshift distributions and compared them with the result in the ECDF-S. As a result, both analysis indicate that relatively large number of SMGs can lie in the SSA22 proto-cluster. There is a possible excess in number counts at 1.1 mm flux density of 2–3 mJy. The median redshift of SSA22 SMG is 3.0 while that of ECDF-S is estimated to be 2.5.

Then we step forward to more detailed comparison. We address the density environment at the position of SMGs using the number surface density of $z = 3.1$ LAEs for both fields and inspect the influence of environment on the nature of SMGs. Consequently three remarkable trends are discovered. First, the number of SMGs per unit area increases as the environment becomes dense. Second, there is no recognizable environmental dependence on individual properties such as star formation rate, stellar mass, specific star formation rate. Third, the AGN fraction of SMGs steeply increases at the densest regions.

In addition, it is suggested that the majority of SMGs in SSA22 are mergers. The object size in ALMA images are generally compact (less than $0''.6$) and some have the high-resolution near-infrared counterparts which comprise two components.

Considering the observational evidences above, we suggest to address how SMGs are formed in biased and general fields as follows. The violent starburst seen in SMGs are preferentially caused by mergers, which results in high frequency of SMGs in the dense environment where the interaction rate is expected to be high. Though SMGs are relatively rare in a general field due to the low interaction rate, the individual nature of star-formation is predominated by local factors such as starburst ages and gas fraction and not affected by the large-scale density environment once the merger events occur. In the area around the density peak the high interaction rate, high interaction efficiency, and large amount of destabilized gas can cause rapid growth of central SMBHs.

Our results strongly suggest that environment predominates the formation of SMGs and SMBHs within them.

Declaration

The work in this thesis is based on research carried out at the Department of Astronomy, the University of Tokyo, Japan. No part of this thesis has been submitted elsewhere for any other degree or qualification.

Hideki Umehata
December 2014

Acknowledgements

First of all, I am deeply grateful to Kotaro Kohno, my supervisor. He guided me to the exciting world of submillimeter astronomy and I received generous support from him in my life as a graduate student. His curiosity and great knowledge about wide-ranging topics were really good example for me. I would like to express the deepest appreciation to Yoichi Tamura for sharing a large amount of time to discuss various matter related to this thesis. He is a pioneer in studying massive dusty starbursts from the view point of their dependence on the large-scale structure. I learned severe attitude to statistical analysis from him. I would like to thank the members of the Kohno laboratory who gave me a lot of stimulation and motivation: Hirofumi Inoue, Kenta Suzuki, Soh Ikarashi, Takuma Izumi, Akio Taniguchi, Yuki Yamaguchi, Ryo Ando, Ryu Makiya, Shun Ishii, Takashi Tsukagoshi, Seiji Fujimoto, and Takeshi Sakai.

I would like to thank the ALMA staff for their great effort. I would particularly like to express my gratitude to Akiko Kawamura, contact scientist for my ALMA project, for many help and support for the observations. I owe a very important debt to Aretxaga Itzier, David Hughes, Jason Austermann, Ryan Cybulski, Thushara Perera, Kimberly Scott, Grant Wilson, Min Yun, Bunyo Hatsukade, Iono Daisuke, Ryohei Kawabe, Hajime Ezawa, Hiroshi Matsuo, Tai Ohshima, and all AzTEC team members for providing me a great opportunity to study submillimeter galaxies using the map taken with AzTEC/ASTE. I would like to offer my special thanks to the researchers of the SSA22 field: Toru Yamada, Yuichi Matsuda, Kouichiro Nakanishi, Tomoki Hayashino, Tadafumi Takata, Mariko Kubo, Yuta Kato, Ikuru Iwata, and Akio Inoue for sharing their data and/or giving me a fruitful comment. Rob Ivison gave me insightful comments and suggestions from the view point of an expert of radio astronomy.

I want to thank my classmates. I especially spent a lot of time with the Institute of Astronomy (IoA) members: Mizuho Uchiyama, Ken Tateuchi, Satoshi Hamano, and Hirokazu Fujii.

I owe my deepest gratitude to the members of my first curling team, HAYABUSA: Kota Onodera, Koki Tonuma, Toyoyuki Miyazaki, and Tsubasa Yamamoto. I will never forget that we won the all Tokyo curling championship.

I really appreciate the referees of this thesis: Kazuhiro Shimasaku, Hideyuki Kobayashi, Masami Ouchi, Tadayuki Kodama, Masayuki Akiyama. Advice and comments given by them have been a great help in improving this work.

Finally my deepest appreciation goes to my family who have supported me all the times.

Table of contents

Table of contents ix

List of figures xiii

List of tables xvii

Nomenclature xviii

1 Introduction 1

1.1 Submillimeter Galaxies 1

1.1.1 The Most Active Dusty Starbursts in the Universe 1

1.1.2 The Identification Issue 5

1.1.3 The Dawn of the ALMA Era 6

1.2 Submillimeter Galaxies and Environment 6

1.2.1 Environmental Dependence on Galaxy Formation 6

1.2.2 Environmental Dependence on SMG Formation 6

1.3 The Large-scale Structure at $z = 3.1$ 8

1.3.1 The History of the Discovery 8

1.3.2 Previous Submm/mm Explorations toward the Proto-cluster 9

1.4 Scope of This Thesis 10

2 Observations and Data Analysis: Submillimeter/Millimeter 11

2.1 The 1.1 mm Mapping with AzTEC/ASTE 11

2.1.1 Observations 11

2.1.2 Data Reduction 12

2.1.3 Map and Catalog 13

2.2 The 1.1 mm Mapping with ALMA Band 6 21

2.2.1 Observations 21

2.2.2 Data Reduction 23

2.2.3 Cataloging the SMGs in the ALMA maps 32
2.3 The 870 μm Mapping with ALMA Band 7 43
2.3.1 Observations 43
2.3.2 Data Reduction 43
2.3.3 Catalog 43

3 The Nature of SMGs: Submillimeter/Millimeter 47
3.1 Number Counts 47
3.1.1 The ALMA 1.1 mm Number Counts 48
3.1.2 Discussion 50
3.2 Radio/IR Identification 54
3.2.1 Counterpart Identification Methods 54
3.2.2 ALMA's Answer 55

4 The Nature of SMGs: Optical to Near-IR 69
4.1 Photometric Redshift 69
4.1.1 Data Preparation 70
4.1.2 SED Fitting 81
4.1.3 Results 81
4.1.4 Redshift Distribution 84
4.2 Stellar Mass 90
4.2.1 Importance 90
4.2.2 Method 90
4.2.3 Results 91
4.2.4 Comparison with other surveys 91

5 AGNs and SMBHs in SMGs 95
5.1 Chandra X-ray Observations 95
5.1.1 X-ray Source Catalog 95
5.1.2 Catalog Matching 95
5.2 SMGs as AGN-host galaxies 98
5.2.1 X-ray Properties 98
5.2.2 AGN Diagnostics 103
5.3 AGN Fraction 107
5.3.1 Methodology 107
5.3.2 The AGN fractions 107

6 Dusty Starburst Formation and SMBH Growth in the z=3.1 Proto-cluster 111
6.1 Dusty Starburst Formation at a z=3 Biased Environment 111
6.1.1 Excess of SMGs in the SSA22 field 112
6.1.2 Where are SMGs Located within a Large-scale Structure? 118
6.1.3 Individual Properties of SMGs for General and Biased fields 128
6.1.4 Mergers as the Most Plausible Trigger 134
6.1.5 The Role of Environment in SMG Formation 139
6.1.6 Extended Star-formation Activity–Density Relation 140
6.2 The SMBH Growth within the $z = 3.1$ Large-scale Structure 141
6.2.1 AGNs within SMGs in SSA22 141
6.2.2 The Nature of AGN-host SMGs 144
6.2.3 The Role of Large-scale Density Environment in the SMBH Growth 146

7 Summary 149

Appendix A Muti-wavelength Data Set of ALMA SMGs 153
A.1 Photometries and SEDs 153
A.2 Postage Stamps 153

Appendix B Spectra of ALMA SMGs 167
B.1 Optical Spectroscopy with VLT/VIMOS 167
B.2 CO Spectra Obtained with NRO45m 170

Appendix C Additional Remarks 171
C.1 Source Size Measurement in u-v Plane 171
C.2 K-S test 175
C.3 Picture of the Kohno Laboratory Members 176

References 177

List of figures

1.1 The SCUBA 850 μm Image of The First SMGs 1
1.2 ASTE and AzTEC 2
1.3 The Spectral Energy Distribution 3
1.4 The Illustration of Negative-k Correction 4
1.5 The Evolutionary Track Including SMGs 5
1.6 The HST Image of The Proto-cluster around AzTEC3 7
1.7 The Large-scale Structure in SSA22 8
1.8 SMG/LAE Cross-correlation Function in SSA22 9

2.1 AzTEC/ASTE 1.1 mm map 14
2.2 AzTEC False Detection Rate 19
2.3 AzTEC Completeness 20
2.4 AzTEC Positional Uncertainty 21
2.5 ALMA Images (AzTEC1-12) 25
2.6 ALMA Images (AzTEC13-28) 26
2.7 ALMA Images (AzTEC30-49) 27
2.8 ALMA Images (AzTEC50-75) 28
2.9 ALMA Images (AzTEC77-116) 29
2.10 False Detection Rate 33
2.11 Completeness 34
2.12 Flux of AzTEC and ALMA 35
2.13 ALMA Astrometry 36
2.14 ALMA 870 μm Images 44

3.1 Differential Number Counts 51
3.2 Cumulative Number Counts 52
3.3 Histogram of ALMA flux densities 57
3.4 VLA Images (AzTEC1-12) 59

3.5 VLA Images (AzTEC13-28) 60
3.6 VLA Images (AzTEC30-49) 61
3.7 VLA Images (AzTEC50-75) 62
3.8 VLA Images (AzTEC77-116) 63
3.9 IRAC Images (AzTEC1-12) 64
3.10 IRAC Images (AzTEC13-28) 65
3.11 IRAC Images (AzTEC30-49) 66
3.12 IRAC Images (AzTEC50-75) 67
3.13 IRAC Images (AzTEC77-116) 68

4.1 Apparent magnitude distribution 74
4.2 $z_{\rm spec}$ vs $z_{\rm phot}$ 85
4.3 Redshift Distribution in the SSA22 86
4.4 Photometric redshift vs 1.1 mm Flux 87
4.5 Photo-z Distribution of Various Surveys 89
4.6 Stellar mass against photometric redshift 93

5.1 Full-band X-ray Sensitivity 96
5.2 The enlarged view of AGN007.1 97
5.3 Chandra Stamp (1.1 mm selected SMGs) 98
5.4 Chandra Stamp (870 μm selected SMGs) 99
5.5 The column density against the band ratio 100
5.6 Effective Photon Index vs X-ray Luminosity 105
5.7 Luminosity Ratio between radio and X-ray 106
5.8 The AGN Fraction 108

6.1 2D distribution of AzTEC SMGs and z=3.1 LAEs 114
6.2 2D distribution of LABOCA SMGs and z=3.1 LAEs 115
6.3 LAE Surface Density Map in SSA22 120
6.4 LAE Surface Density Map in ECDFS 121
6.5 1.1mm Flux density against Density in SSA22 123
6.6 Source counts against Environment in SSA22 124
6.7 870 μm Flux density against Density in ECDFS 125
6.8 Source counts against Environment in ECDFS 126
6.9 Source counts against Environment in SSA22 and ECDFS 127
6.10 SFR vs LAE Density 131
6.11 Stellar mass vs LAE Density 132
6.12 sSFR vs LAE Density 133

6.13 High resolution NIR images of High S/N z=3.1 sources 136
6.14 The High resolution 1.1 mm image of ASA 1.1 138
6.15 ADF22 and LSS 143
6.16 X-ray Luminosity vs FIR Luminosity 145
6.17 X-ray Luminosity vs Growth Ratio 147

A.1 SEDs (1/6) 154
A.2 SEDs (2/6) 155
A.3 SEDs (3/6) 156
A.4 SEDs (4/6) 157
A.5 SEDs (5/6) 158
A.6 SEDs (6/6) 159
A.7 Postage Stamp (1/7) 160
A.8 Postage Stamp (2/7) 161
A.9 Postage Stamp (3/7) 162
A.10 Postage Stamp (4/7) 163
A.11 Postage Stamp (5/7) 164
A.12 Postage Stamp (6/7) 165
A.13 Postage Stamp (7/7) 166

B.1 Rest-frame UV Spectra of ASA 20.1 168
B.2 Rest-frame UV Spectra of ASA 34.1 169
B.3 Possible CO(3-2) Spectra of ASA 1.1 170

C.1 u, v plot of ASA 1.1 172
C.2 The results of u, v model fit 173
C.3 The results of u, v model fit 174
C.4 Picture of the Kohno Laboratory members 176

List of tables

2.1 Map properties in the 50% and the 30-50% coverage regions. N(source) and N(False) show number of sources and false detections ($\leq 3.5\sigma$ for both). . 13
2.2 AzTEC/ASTE source catalog(1/4) 15
2.3 AzTEC/ASTE source catalog (2/4) 16
2.4 AzTEC/ASTE source catalog (3/4) 17
2.5 AzTEC/ASTE source catalog (4/4) 18
2.6 Summary of ALMA Observations 23
2.7 ALMA Observations of SSA22 Field (1/2) 30
2.8 ALMA Observations of SSA22 Field (2/2) 31
2.9 ALMA Main Source Catalog (1/3) 38
2.10 ALMA Source Catalog (2/3) 39
2.11 ALMA Main Source Catalog (3/3) 40
2.12 ALMA Supplementary Source Catalog (1/2) 41
2.13 ALMA Supplementary Source Catalog (2/2) 42
2.14 ALMA Observations of #2011.0.00725.S 44
2.15 ALMA 870 μm Source Catalog ($\geq 5\sigma$) 45

3.1 ALMA Number Counts (> 1.1 mJy) 50

4.1 Optical and NIR Photometry 71
4.2 Photometry ($U - z'$) (1/3) 75
4.3 Photometry ($U - z'$) (2/3) 76
4.4 Photometry ($U - z'$) (3/3) 77
4.5 Photometry ($J - 8.0$ μm) (1/3) 78
4.6 Photometry ($J - 8.0$ μm) (2/3) 79
4.7 Photometry ($J - 8.0$ μm) (3/3) 80
4.8 Photometric properties (1/2) 82
4.9 Photometric properties (2/2) 83

5.1 X-ray SMG Catalog 101
5.2 X-ray Properties of SMGs 102
5.3 X-ray SMG Catalog 109

6.1 Properties of LAE surveys in SSA22 and ECDF-S 116
6.2 Properties of SMG surveys in SSA22 and ECDF-S 117
6.3 Merger Classification of SSA22 ALMA SMGs 137
6.4 FIR Luminosity of AGN-SMGs 144

C.1 KS-test: Photo-z Distribution 175

Chapter 1

Introduction

1.1 Submillimeter Galaxies

1.1.1 The Most Active Dusty Starbursts in the Universe

Discovery of SMGs

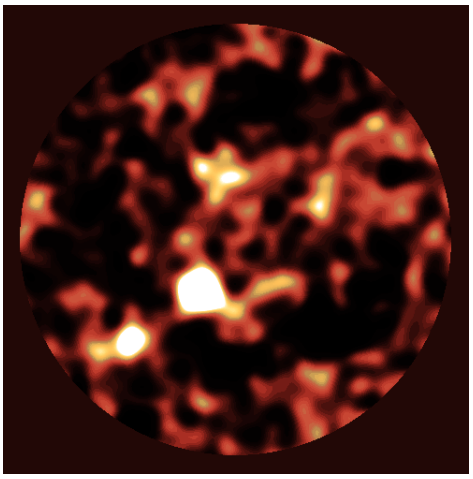

Fig. 1.1 The 850 μm image of HDF 850.1 taken with SCUBA. The image area is a circle with a radius of 100″ (Hughes et al. 1998).

At the end of the twentieth century, the first deep extragalactic survey was taken at 850 μm with the Submillimeter Common-User Bolometer Array (SCUBA, Holland et al. 1999) on the James Clerk Maxwell Telescope (JCMT) to unveil a new population of galaxies, which lies in the distant redshift universe and is extremely bright at submillimeter/millimeter (submm/mm) wavelengths (Smail et al. 1997, Hughes et al. 1998, Barger et al. 1998). These galaxies has been called as SMGs (submillimeter galaxies or submillimeter-bright galaxies).

The first age survey was followed by several wide surveys at submm/mm wavelengths, which have been conducted to discover more and more such galaxies (e.g., Greve et al. 2004, Scott et al. 2008, Coppin et al. 2009, Hatsukade et al. 2011).

The astronomical thermal emission camera (AzTEC)/Atacama Submillimeter Telescope Experiment (ASTE) survey is one of such single dish surveys. The AzTEC camera operating at 1.1 mm was developed by members at the University of Massachusetts, Amherst (Wilson et al. 2008, Figure 1.2). It was mounted on the ASTE 10-m submillimetre telescope (Ezawa et al. 2004, Ezawa et al. 2008) located on Pampa la Bola, near Cerro Chajnantor in northern Chile to perform deep and wide field surveys. The AzTEC camera has a large number of bolometer pixels (144-element) and the AzTEC/ASTE survey had nice ability in survey speed compared to other previous or same generation surveys such as SCUBA/JCMT and MAMBO/IRAM. The AzTEC/ASTE system provides an angular resolution of $30''$ in full width at half maximum (FWHM).

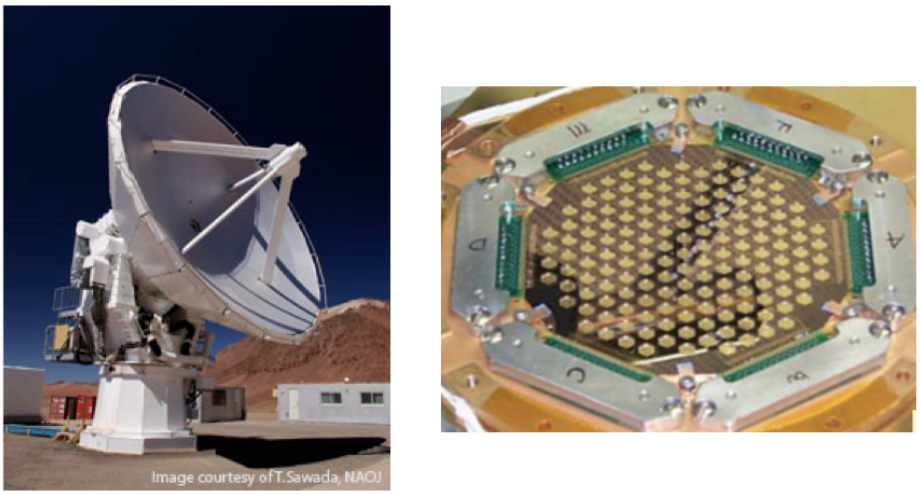

Fig. 1.2 The ASTE telescope and the AzTEC camera. (Image courtesy of T.Sawada, NAOJ in the left figure).

Characteristics of SMGs

The SMGs have huge rest-frame infrared (IR) luminosities ($L_{\rm IR} \gtrsim 10^{12} - 10^{13} L_{\odot}$), which should be caused mainly by highly dust-enshrouded massive star formation and are indicative of a star-formation rate (SFR) of $\sim$ a few 100–1000 $M_{\odot}$/yr. The majority of SMGs are at $z > 1$ (e.g., Chapman et al. 2005). SMGs typically have the spectral energy distribution (SEDs) like Figure 1.3. It is remarkable that the rest-frame far-infrared (FIR) parts are dominated by the re-radiation from warmed dust.

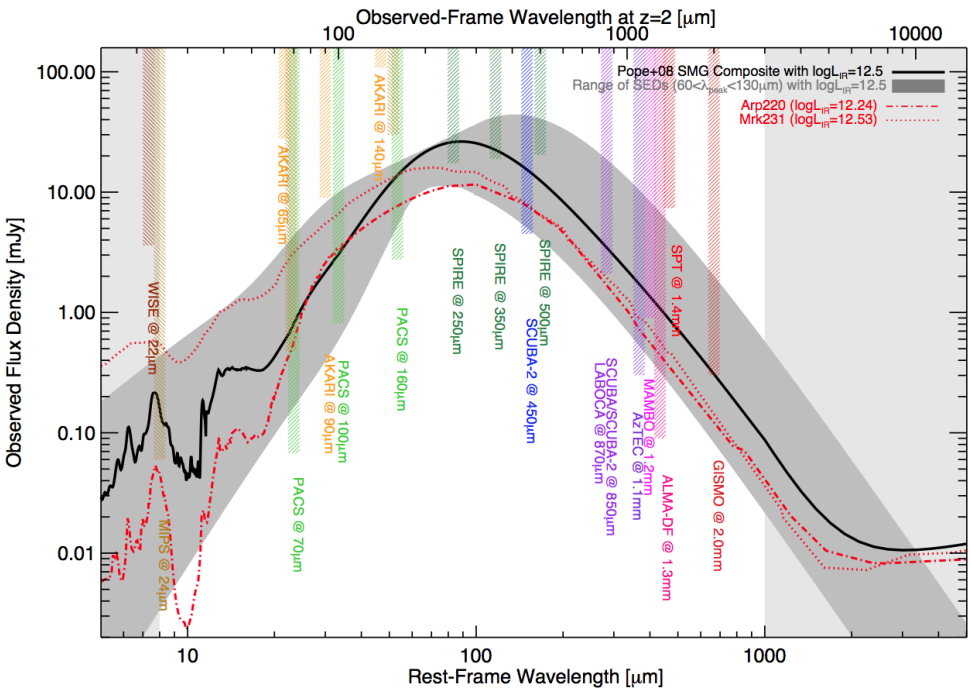

Fig. 1.3 Representative spectral energy distributions (SEDs) of SMGs (Casey et al. 2014 and reference therein).

This characteristics seen in the SED profile generates a 'magic', which is really favorable for astronomers. Their flux at submm/mm wavelengths is almost constant for galaxies with a given FIR luminosity at $z \sim 1$–10 due to the negative k-correction. It is hence of great benefit to discover high redshift objects (Figure 1.4). As shown in the figure, 1.1 mm surveys are more effective to explore higher redshift universe compared to 850 and 870 μm.

In addition to their high activity of star formation, spectroscopic observations of the submm/mm transitions of molecular carbon monoxide (CO) have unveiled that SMGs have large dynamical and gas masses (e.g., Greve et al. 2005). These observational evidences shows that SMGs are the most active, massive star forming galaxies in the early universe. Therefore the clarification of the nature of SMGs and their formation process thoroughly is seriously important to understand the galaxy formation and evolution.

Evolutionally Sequence

It has been argued that SMGs are progenitors of massive elliptical galaxies seen in the cores of present-day clusters (e.g., Eales et al. 1999) and moreover the evolutionary link between quasi–stellar objects (QSOs) has been suggested by several works (e.g., Sanders et al. 1988, Hopkins et al. 2008) as shown in Figure 1.5.

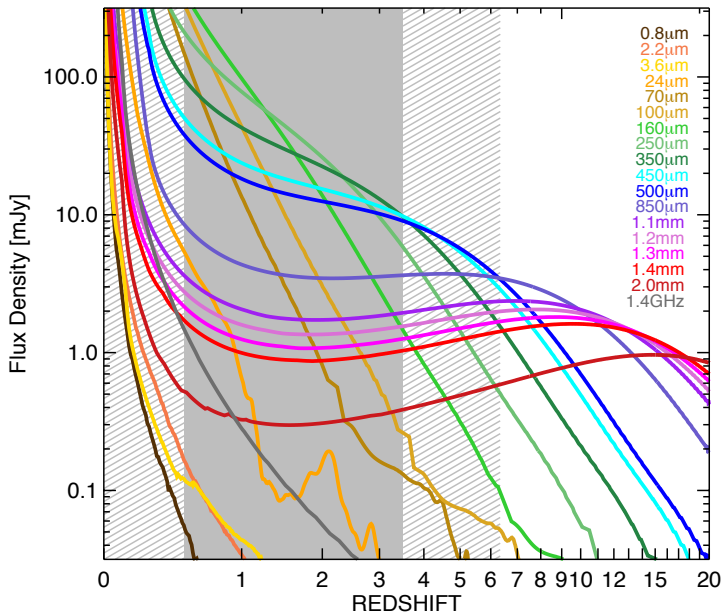

Fig. 1.4 The predicted observed flux densities as a function of redshift (Casey et al. 2014 and reference therein). Here a typical SMGs of which infrared luminosity is $10^{12.5}$ $L_{\odot}$.

Recently a convincing scenario including these insights has been suggested (e.g., Toft et al. 2014). It has been discovered that half of the most massive galaxies ($M_* > 10^{11}$ $M_{\odot}$) at $z \sim 2$ are old compact quiescent systems (e.g., Toft et al. 2007, van Dokkum et al. 2008) and their evolved, dense stellar populations suggest formation within intense, compact starbursts 1–2 Gyr earlier (at $3 \leq z \leq 6$). Toft et al. (2014) shows z = 3–6 SMGs are consistent with being the progenitors of $z = 2$ quiescent galaxies, matching their redshifts, sizes, stellar masses, and internal velocities.

SMGs as a Growth Phase of SMBHs

As illustrated in Figure 1.5, some SMGs are considered to evolve into QSOs. Thus SMGs also present an unique opportunity for studying the co-evolution of galaxies and their central supermassive black holes (SMBHs). It is argued that major gas-rich mergers at high redshift should provide the gas to the center, which ignite a massive nuclear starburst followed by an active galactic nucleus (AGN)/QSO phase that quenches the star-formation (e.g., Sanders et al. 1988, Hopkins et al. 2006). Thus to examine the AGNs within SMGs is crucial to understand both of the origin of the co-evolution and the mechanism of quenching. Wang et al. (2013b) reported that at least 20% of SMGs identified by ALMA should harbor AGNs mainly based on *Chandra* X-ray data.

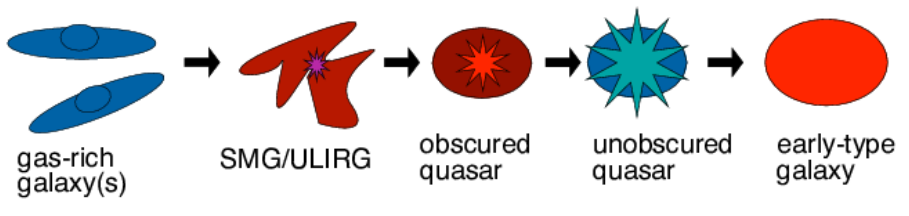

Fig. 1.5 Schematic illustration of the evolutionary track for massive galaxies originally suggested by Sanders et al. (1988) (Alexander & Hickox 2012).

1.1.2 The Identification Issue

Whilst the single-dish surveys have discovered numerous submm/mm sources, astronomers have been faced a serious issue in source identification. The typical beam size of the single-dish telescopes used for such wide field SMG surveys is insufficient to determine position accurately. In the case of the AzTEC/ASTE survey, we can achieve $\sim 30''$ FWHM, which is also not enough. Accurate positions of SMGs could ideally be obtained with a submillimeter interferometer such as SMA, PdBI, and CARMA, but these observations are so time-consuming that it is really difficult to obtain the high resolution images for a large number of targets without the Atacama Large Millimeter/submillimeter Array (ALMA).

Some previous works have shown that multi-wavelength identification utilizing radio, MIPS (Rieke et al. 2004), and IRAC (Fazio et al. 2004) imaging data is somewhat useful (e.g., Ivison et al. 2007, Biggs et al. 2011; Wardlow et al. 2011; Yun et al. 2012). However eventually the large uncertainties in this problem have prevent us from improving the understanding of SMGs.

1.1.3 The Dawn of the ALMA Era

After ALMA started the science observations, the study of SMGs has progressed revolutionary. For instance, 122 out of 126 sources detected by LABOCA, which is one of the submm survey instruments equipped with APEX, a single dish telescope, were observed by ALMA to provide sophisticated number counts, source positions, and fluxes allow us to derive photometric redshifts, AGN fraction, morphologies of stellar components, and so on (Karim et al. 2013, Hodge et al. 2013, Simpson et al. 2014b, Wang et al. 2013b, Chen et al. 2014). Vieira et al. (2013) and Weiß et al. (2013) detected molecular lines from 23 strong lensing sources and derived redshift distribution of SMGs. ALMA should also play a main role in SMG study in future.

1.2 Submillimeter Galaxies and Environment

1.2.1 Environmental Dependence on Galaxy Formation

The environment where galaxies inhabit is expected to play a critical role in shaping their evolution. In the local universe the morphology-density relation has been well-known. Observations have revealed a higher fraction of early-type galaxies in denser environments (Dressler, 1980). This trend has been confirmed for up to $z \sim 1$ universe (e.g., Postman et al. 2005). Although this is one of the most established environmental effects on galaxy evolution, it is difficult to examine the relation directly at higher redshifts. Instead, the color-density or color-magnitude relations were examined as proxies. For instance, Kodama et al. (2007) examined the color-magnitude relation in proto-clusters and found that the red sequence of galaxies, which is well-established in clusters at least out to $z \sim 1$, first appeared at $z = 2-3$. This suggests that massive galaxies were assembled in proto-clusters in this era.

1.2.2 Environmental Dependence on SMG Formation

Most of these studies are based on optical to near-infrared observations. However, recent studies unveiled that the dust-obscured, that is, 'hidden' part of star-formation largely contributes to the total star formation history in the Universe (e.g., Madau & Dickinson 2014 and reference therein). Hence understanding such dusty star-forming galaxies is essential to unveil the ecology in the early universe and SMGs, which are a population of the most violent starburst galaxies, play undoubtedly the key role.

Theoretical Picture

Cosmological simulations using the current cold dark matter model also predict that SMGs should be formed within a proto-cluster – an overdensity of galaxies at high redshift – where the mass densities are high and correspondingly merger rates are also high (e.g., Springel et al. 2005).

Case Studies

While the connection between SMGs and massive dark matter haloes has been statistically indicated by clustering analysis (e.g., Blain et al. 2004; Hickox et al. 2012), the connection in individual cluster/proto-cluster is still unclear, although previous papers have reported some cases. Capak et al. (2011) and Daddi et al. (2009) reported the discovery of SMGs in overdense region at $z = 5.3$ (Figure 1.6) and $z = 4.05$, respectively. These results indicate that the overdense regions might be sites of SMG formation. On the other hand, Chapman et al. (2009) shows that SMGs are formed in less overdence regions at $z = 1.99$. Thus the environmental dependence on SMG formation has not established yet. We introduce another unique laboratory field in the following section.

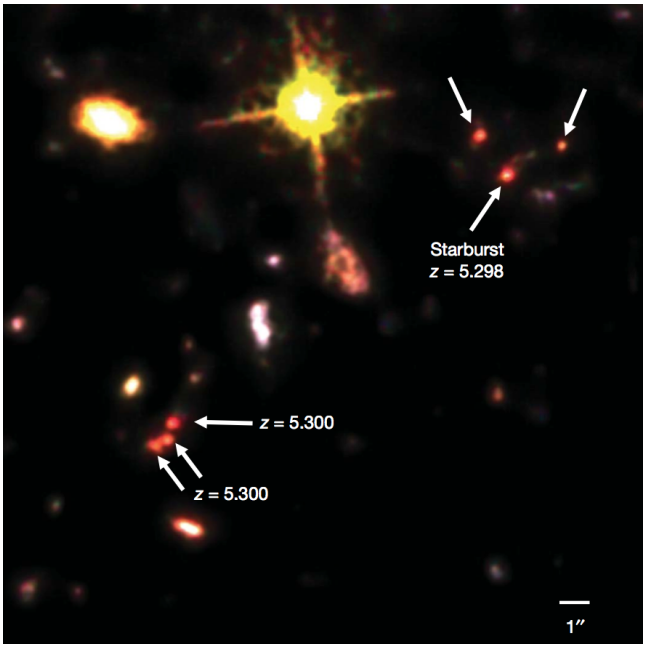

Fig. 1.6 The HST near-infrared image of COSMOS-AzTEC3 and surrounding area (Capak et al. 2011)

1.3 The Large-scale Structure at $z = 3.1$

1.3.1 The History of the Discovery

Steidel et al. (1998) firstly discovered a proto-cluster as a concentration of Lyman break galaxies (LBGs) at z = 3.09 in the SSA22 field. Subsequently a lot of Lyα emitters (LAEs) have been found at the same redshift by Steidel et al. (2000). Hayashino et al. (2004) extended the LAE survey using Subaru/Suprime-Cam equipped with a narrowband filter (NB497) area 10 times larger than Steidel's one and revealed the large-scale structure at the redshift. Furthermore an extremely wide field survey with Suprime-Cam/NB497 has revealed a structure which was traced by LAEs and spread over 1 deg^2(Yamada et al. 2012). This SSA22 proto-cluster is the most spectacular one amongst the known overdensities at redshift beyond 2 and a comparison with the blank fields shows that only one such overdensity would be expected in the whole sky (Yamada et al. 2012). Hence the SSA22 field can provide us with unique insights regarding galaxy formation in an overdense environment. The excess of other populations such as Lymanα blobs (LABs, e.g., Steidel et al. 2000) and distant red galaxies (DRGs, e.g., Uchimoto et al. 2012, Kubo et al. 2013) has been also found in the field.

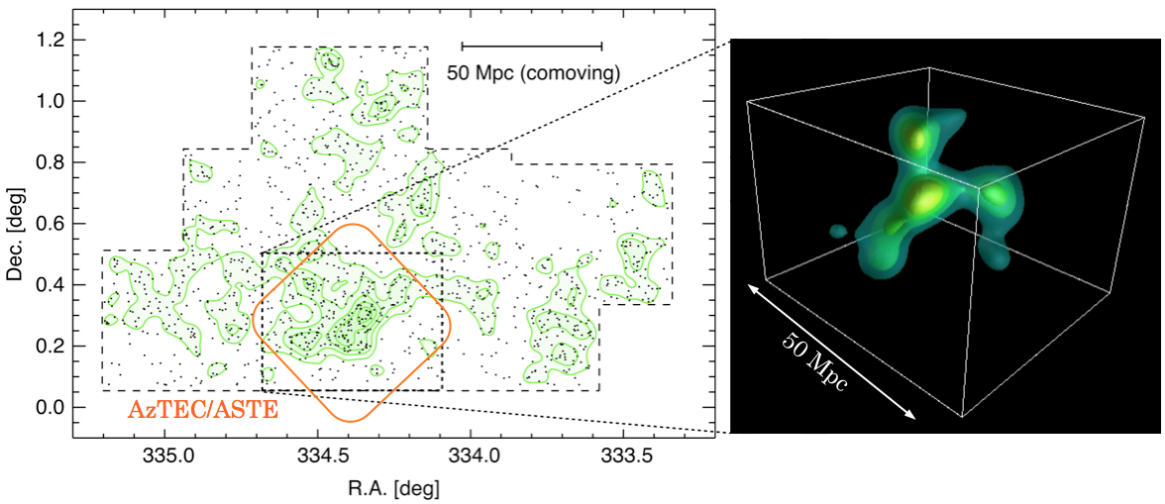

Fig. 1.7 (left) The large-scale structure traced out by z = 3.1 LAEs across the sky covering 1.38 deg^2 (Yamada et al. 2012). The area of the AzTEC/ASTE 1.1mm survey also shown (orange, Umehata et al. 2014). (right) The close up view of three-dimensional distribution of LAEs (Matsuda et al. 2005).

1.3.2 Previous Submm/mm Explorations toward the Proto-cluster

Several previous works on SMGs discovered by SCUBA and AzTEC/ASTE surveys in this field have been reported.

SCUBA Survey in SSA22

The first deep SMG survey was conducted by SCUBA team (Scott et al. 2006). They observed 26 arcmin^2 area around the LBG peak to find 10 sources with $> 3.0\ \sigma$. The source identification utilizing a VLA 1.4 GHz map and optical spectroscopy taken with Keck/Low Resolution Imaging Spectrograph (LRIS) revealed that three sources have $z_{\rm spec} = 3.1$ (Blain et al. 2004, Chapman et al. 2005). These works were the first discovery of the proto-cluster member SMGs.

AzTEC Survey in SSA22

The first AzTEC survey was covered 390 arcmin^2 area to discover 30 SMGs with $> 3.5\sigma$ (Tamura et al. 2009). They expanded the observed area ($\times 15$) compared to the previous SCUBA survey. Tamura et al. (2009) calculated the two-point angular cross-correlation function between the 15 brightest AzTEC SMGs and NB497-selected (i.e., $z = 3.1$ LAE candidates) and found significant correlation (Figure 1.8). Though they didn't consider redshift information absolutely, it was firstly indicated that a number of SMGs would reside in the large-scale structure. For the second AzTEC survey, which covers much larger area, the details are written in this thesis.

In this way, while we had been far away from an exhaustive view, some previous works suggested that SMGs would be associated with the $z = 3.1$ large-scale structure.

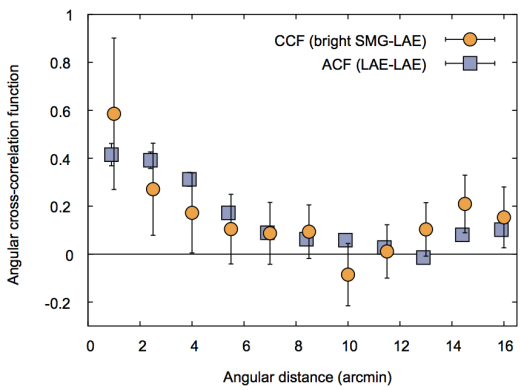

Fig. 1.8 The cross-correlation function between NB497-selected LAEs and bright SMGs in SSA22 (Tamura et al. 2009)

1.4 Scope of This Thesis

Throughout this thesis, the primary objective is to understand the environmental dependence on the formation and evolution of SMGs.

The organization of this paper is as follows. After the Introduction described in this Section, in Section 2 we address the details of key SMG observations, which comprise of AzTEC/ASTE, ALMA Band6, and ALMA Band7. Next we investigate the properties of ALMA-detected SMGs focusing on the exact ALMA data in Section 3. In Section 4, we derive photometric and spectroscopic redshifts and evaluate stellar mass. Then we derive the AGN-fraction of ALMA-detected SMGs utilizing deep *Chandra* X-ray data and examine their characteristics in Section 5. Subsequently we discuss the environmental dependence on SMG formation and the SMBH growth within SMGs in Section 6. Finally in Section 7 we summarize this work.

We assume a cosmology with $\Omega_m = 0.3, \Omega_\lambda = 0.7$, H_0=70 km s^{-1} Mpc^{-1} and all magnitudes are given according to the AB system throughout the paper.

Chapter 2

Observations and Data Analysis: Submillimeter/Millimeter

2.1 The 1.1 mm Mapping with AzTEC/ASTE

We observed the SSA22 field as a part of the AzTEC/ASTE 1.1 mm survey. The details are as follows.

2.1.1 Observations

All of the AzTEC/ASTE observations of SSA22 were carried out at night in August–September 2007 and August–September 2008(Tamura et al. 2009 and Tamura et al. 2013) The dry weather at the high site (4860 m in elevation) provided an excellent data set that was taken under 220 GHz zenith opacities of $\tau_{220\,\mathrm{GHz}} = 0.01$–$0.10$. We mapped a 50-arcmin diameter region centered at R.A. (J2000) = 22h 17.6m, Decl. (J2000) = +0° 15.0′. Observations were made using the on-the-fly (OTF) mode by continuously scanning the telescope boresight in azimuth and elevation in a modified Lissajous scan pattern, which is described as a function of time t by,

$$\delta Az = A \sin at + B \sin(at/f) \tag{2.1}$$

$$\delta El = C \sin bt + D \sin(bt/f), \tag{2.2}$$

In 2007, we use a scan pattern with $(A,B,C,D,a,b,f) = (7'40'',7'40'',3'40'',3'40'',5.0,4.0,45.0)$. The actual values of a and b are normalized to limit the peak telescope slew velocity to 330 arcsec s^{-1}. In order to go deeper and wider, we used another scan pattern for the 2008 observations with $(A,B,C,D,a,b,f) = (22',22',2',2',6.0,5.0,23)$. The coverage was cen-

tered at the same position as those in 2007, but swept a doughnut-like region surrounding the 2007 coverage. The total integrated time on source through 2007–2008 was 74 hr. The area of the co-added map where the noise levels are below 1 mJy was estimated to reach 900 arcmin^2. The wind speeds during the runs were 1–10 m/s and typically 5 m/s, providing a random telescope pointing offset of $< 1''$. The astrometry was checked using a bright quasar 3C446, 5.6 deg away from SSA22, every 1-1.5 hr during the observations. The correction to the telescope pointing model was small (typically $< 2''$) and applied to all scans toward SSA22, resulting in an absolute pointing accuracy better than $4''$ (Tamura et al. 2013). For flux calibration, beam shape measurements and array flat-fielding, beammaps of Uranus and Neptune were taken at least once, typically twice, a night. The beammaps were made so that each bolometer pixel raster-scans and images the planets. The flux calibration accuracy was estimated to be 10% or better.

2.1.2 Data Reduction

The data were reduced in the standard manner described in Scott et al. (2008) and Downes et al. (2012). Therefore we mention only the outline here. We employed an atmospheric noise removal technique based on principal component analysis (PCA cleaning) to isolate the low-frequency atmospheric noise from the astronomical signals involved in time-stream data. The cleaned time-stream data of each scan were projected into a map by binning them into $3'' \times 3''$ pixels and the individual scans were coadded into a single map by weighted-averaging.

We also generated 100 noise realizations by jackknifing the time-stream data (i.e., by multiplying each 15-s time-stream interval by ± 1 randomly and then reducing in the standard manner), which were free of astronomical emission and hence represented the underlying photon noises from the atmosphere and instruments. These random maps were used to estimate a "noise map" by computing pixel-to-pixel standard deviations, which represents the local noise level. We also create a weight map by computing an inverse-square of the noise map. Since the PCA cleaning was AC-coupled to the time-stream and hence worked as a high-pass filter (i.e., the resulting map is zero-mean), it attenuated the peak flux and caused negative sidelobes around a source. To correct these effects, we simulated the profile of the point-source response function (a point source kernel) following the method presented in Downes et al. (2012).

Coverage	Area [arcmin^2]	Noise level [mJy beam^{-1}]	N(Source)	N(False)
50%	749	0.72–1.00	107	6.2±2.4
30-50%	205	1.00–1.32	18	2.4±0.8

Table 2.1 Map properties in the 50% and the 30-50% coverage regions. N(source) and N(False) show number of sources and false detections ($\leq 3.5\sigma$ for both).

2.1.3 Map and Catalog

Map

The resulting 1.1-mm map is shown in Figure 2.1. In this paper we consider the area where the weight (i.e., inverse-square of the noise level) is equal to or greater than 30% of the maximum weight as the survey area in this paper. The surface area that AzTEC covered was 0.27 deg^2, in which the 1σ noise level ranges from 0.7 to 1.3 mJy beam^{-1} (50% of the region has < 0.8 mJy beam^{-1}). The map area corresponds to approximately 60×60 Mpc^2 in a comoving area at $z = 3.1$, which is large enough to cover the protocluster.

Source Extraction

The 1.1-mm sources are extracted from the signal-to-noise map, made from the signal map divided by the noise map, with a detection threshold of $\geq 3.5\sigma$. Each source position is defined by flux-squared weighting of the pixels of the nominal peak within a radius of 15 arcsec. We detected 125 sources in the 30% coverage area, which are listed in Table 2.2 – Table 2.5. Seventeen $\geq 3.5\sigma$ sources were detected in the 10–30% coverage area.

Deboosting

For a source population whose number counts decrease rapidly with increasing flux density, the measured flux of a low signal-to-noise-ratio (S/N) source can be boosted by random noise. The flux densities of the detected sources are de-boosted to correct for this flux bias using the Bayesian recipe described in Coppin et al. (2006) and Scott et al. (2008). To compute the posterior probability distribution function (PDF) of the intrinsic flux densities, we simulated a prior distribution function and a likelihood function at each position where the actual source is detected. In order to estimate the prior distribution function, we made 10^4 maps of photon-noise-free random sky realizations that we would observe with the AzTEC/ASTE kernel according to the best-estimate of the 1.1-mm source counts (Scott et al. 2012). By creating a flux histogram across the maps we arrived at the prior distribution

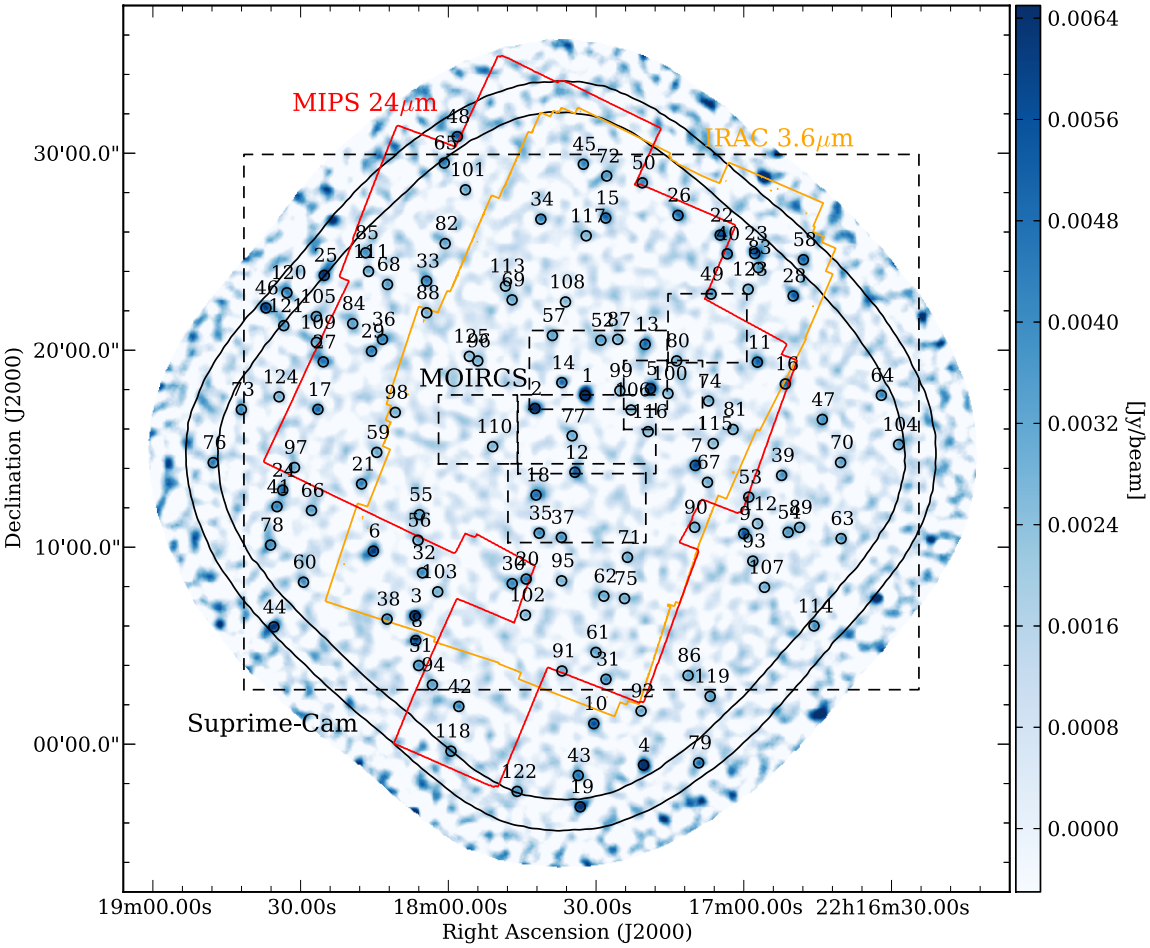

Fig. 2.1 AzTEC/ASTE 1.1 mm image and observation areas of each instrument. The background image is the AzTEC 1.1 mm signal map of the SSA22 field with a 10% uniform coverage region. The side bar represents flux density in unit of Jy/beam. The 30% and 50% coverage regions are shown using black contours. The black circles indicate the positions of $\geq 3.5\ \sigma$ sources and the diameter is 30 $''$, which correspond to the FWHM of AzTEC/ASTE. In addition, the area of Suprime-Cam (large dashed rectangle), MIPS 24 μm (red line), IRAC 3.6 μm (yellow line), and MOIRCS (small dashed rectangle) are shown. UKIRT/DXS survey and VLA 1.4 GHz observations contains all AzTEC sources.

ID	R.A. [$^{h\ m\ s}$]	Dec. [$^{\circ\ \prime\ \prime\prime}$]	$S_{observed}$ [mJy]	$S_{deboosted}$ [mJy]	S/N
SSA22-AzTEC1	22 17 32.21	+00 17 42.1	11.9 ± 0.7	$11.3\ ^{+0.9}_{-0.7}$	16.2
SSA22-AzTEC2	22 17 42.42	+00 17 02.5	7.5 ± 0.7	$6.9\ ^{+0.9}_{-0.7}$	10.1
SSA22-AzTEC3	22 18 06.78	+00 06 30.6	7.4 ± 0.8	$6.9\ ^{+0.8}_{-0.9}$	9.4
SSA22-AzTEC4	22 17 20.36	−00 01 03.6	9.4 ± 1.0	$8.5\ ^{+1.1}_{-1.1}$	9.2
SSA22-AzTEC5	22 17 18.95	+00 18 03.0	6.6 ± 0.7	$6.1\ ^{+0.8}_{-0.8}$	8.9
SSA22-AzTEC6	22 18 15.23	+00 09 48.0	6.5 ± 0.8	$5.9\ ^{+0.8}_{-0.8}$	8.5
SSA22-AzTEC7	22 17 09.85	+00 14 08.9	6.1 ± 0.7	$5.6\ ^{+0.8}_{-0.8}$	8.3
SSA22-AzTEC8	22 18 06.62	+00 05 15.7	6.2 ± 0.8	$5.7\ ^{+0.8}_{-0.9}$	7.7
SSA22-AzTEC9	22 17 00.00	+00 10 41.2	5.8 ± 0.8	$5.3\ ^{+0.8}_{-0.8}$	7.7
SSA22-AzTEC10	22 17 30.46	+00 01 02.5	5.9 ± 0.8	$5.3\ ^{+0.9}_{-0.9}$	7.3
SSA22-AzTEC11	22 16 57.24	+00 19 23.6	5.5 ± 0.8	$4.9\ ^{+0.9}_{-0.8}$	7.2
SSA22-AzTEC12	22 17 34.30	+00 13 48.2	5.4 ± 0.8	$4.9\ ^{+0.8}_{-0.8}$	7.1
SSA22-AzTEC13	22 17 20.03	+00 20 17.9	5.2 ± 0.7	$4.6\ ^{+0.8}_{-0.8}$	7.0
SSA22-AzTEC14	22 17 36.96	+00 18 21.3	5.0 ± 0.7	$4.5\ ^{+0.8}_{-0.8}$	6.9
SSA22-AzTEC15	22 17 28.04	+00 26 42.6	5.3 ± 0.8	$4.7\ ^{+0.9}_{-0.8}$	6.8
SSA22-AzTEC16	22 16 51.56	+00 18 17.2	5.2 ± 0.8	$4.6\ ^{+0.9}_{-0.8}$	6.7
SSA22-AzTEC17	22 18 26.48	+00 16 59.6	5.1 ± 0.8	$4.5\ ^{+0.8}_{-0.8}$	6.5
SSA22-AzTEC18	22 17 42.18	+00 12 38.8	4.8 ± 0.7	$4.3\ ^{+0.8}_{-0.8}$	6.5
SSA22-AzTEC19	22 17 33.21	−00 03 10.8	7.5 ± 1.2	$6.3\ ^{+1.2}_{-1.2}$	6.5
SSA22-AzTEC20	22 17 44.20	+00 08 22.9	4.5 ± 0.7	$4.0\ ^{+0.8}_{-0.8}$	6.2
SSA22-AzTEC21	22 18 17.62	+00 13 12.6	4.6 ± 0.7	$4.0\ ^{+0.8}_{-0.8}$	6.1
SSA22-AzTEC22	22 17 04.79	+00 25 50.6	5.7 ± 0.9	$4.8\ ^{+1.0}_{-1.0}$	6.1
SSA22-AzTEC23	22 16 57.77	+00 24 54.3	5.9 ± 1.0	$5.0\ ^{+1.0}_{-1.1}$	6.1
SSA22-AzTEC24	22 18 33.64	+00 12 53.6	5.0 ± 0.8	$4.4\ ^{+0.9}_{-0.9}$	6.1
SSA22-AzTEC25	22 18 25.20	+00 23 47.9	6.6 ± 1.1	$5.5\ ^{+1.2}_{-1.2}$	6.0
SSA22-AzTEC26	22 17 13.37	+00 26 50.8	5.1 ± 0.9	$4.4\ ^{+0.9}_{-1.0}$	5.9
SSA22-AzTEC27	22 18 25.40	+00 19 24.5	4.9 ± 0.8	$4.2\ ^{+0.9}_{-0.9}$	5.9
SSA22-AzTEC28	22 16 49.97	+00 22 45.2	5.5 ± 0.9	$4.7\ ^{+1.0}_{-1.1}$	5.8
SSA22-AzTEC29	22 18 15.60	+00 19 56.7	4.5 ± 0.8	$3.8\ ^{+0.9}_{-0.8}$	5.8
SSA22-AzTEC30	22 17 47.03	+00 08 09.0	4.2 ± 0.7	$3.7\ ^{+0.8}_{-0.8}$	5.8

Table 2.2 The AzTEC/ASTE SSA22 source catalog. The columns give: 1) source name; 2) AzTEC source ID; 3) Right ascension; 4) Declination; 5) observed 1.1 mm flux density and 1σ error; 6) deboosted 1.1 mm flux density and 68% confidence interval; and 7) signal to noise ratio of the detection in the AzTEC map.

ID	R.A. [$^{h\ m\ s}$]	Dec. [$^{\circ\ \prime\ \prime\prime}$]	$S_{observed}$ [mJy]	$S_{deboosted}$ [mJy]	S/N
SSA22-AzTEC31	22 17 27.99	+00 03 17.6	4.3 ± 0.8	$3.7\ ^{+0.8}_{-0.8}$	5.7
SSA22-AzTEC32	22 18 05.25	+00 08 41.8	4.2 ± 0.8	$3.7\ ^{+0.8}_{-0.9}$	5.6
SSA22-AzTEC33	22 18 04.42	+00 23 30.4	4.4 ± 0.8	$3.8\ ^{+0.9}_{-0.9}$	5.6
SSA22-AzTEC34	22 17 41.21	+00 26 39.0	4.3 ± 0.8	$3.7\ ^{+0.8}_{-0.8}$	5.6
SSA22-AzTEC35	22 17 41.56	+00 10 42.7	4.1 ± 0.7	$3.5\ ^{+0.8}_{-0.8}$	5.5
SSA22-AzTEC36	22 18 13.38	+00 20 32.9	4.2 ± 0.8	$3.6\ ^{+0.8}_{-0.9}$	5.4
SSA22-AzTEC37	22 17 37.05	+00 10 29.7	4.0 ± 0.7	$3.4\ ^{+0.8}_{-0.8}$	5.4
SSA22-AzTEC38	22 18 12.44	+00 06 20.8	4.3 ± 0.8	$3.6\ ^{+0.9}_{-0.9}$	5.3
SSA22-AzTEC39	22 16 52.32	+00 13 38.6	3.9 ± 0.8	$3.3\ ^{+0.8}_{-0.8}$	5.2
SSA22-AzTEC40	22 17 03.36	+00 24 53.6	4.6 ± 0.9	$3.8\ ^{+1.0}_{-1.0}$	5.2
SSA22-AzTEC41	22 18 34.80	+00 12 03.5	4.5 ± 0.9	$3.7\ ^{+0.9}_{-1.0}$	5.2
SSA22-AzTEC42	22 17 57.87	+00 01 54.9	4.5 ± 0.9	$3.7\ ^{+0.9}_{-1.0}$	5.1
SSA22-AzTEC43	22 17 33.63	−00 01 35.4	4.8 ± 1.0	$3.9\ ^{+1.0}_{-1.0}$	5.1
SSA22-AzTEC44	22 18 35.43	+00 05 57.3	6.8 ± 1.3	$5.0\ ^{+1.5}_{-1.4}$	5.0
SSA22-AzTEC45	22 17 32.59	+00 29 26.4	4.3 ± 0.9	$3.5\ ^{+1.0}_{-0.9}$	5.0
SSA22-AzTEC46	22 18 37.04	+00 22 08.7	6.5 ± 1.3	$4.8\ ^{+1.5}_{-1.4}$	5.0
SSA22-AzTEC47	22 16 44.05	+00 16 29.1	3.9 ± 0.8	$3.2\ ^{+0.9}_{-0.9}$	4.8
SSA22-AzTEC48	22 17 58.17	+00 30 50.5	5.7 ± 1.2	$4.3\ ^{+1.3}_{-1.3}$	4.8
SSA22-AzTEC49	22 17 06.64	+00 22 50.9	3.8 ± 0.8	$3.1\ ^{+0.9}_{-0.9}$	4.8
SSA22-AzTEC50	22 17 20.60	+00 28 29.8	4.3 ± 0.9	$3.4\ ^{+1.0}_{-1.0}$	4.8
SSA22-AzTEC51	22 18 06.03	+00 03 59.6	4.1 ± 0.9	$3.3\ ^{+0.9}_{-1.0}$	4.7
SSA22-AzTEC52	22 17 29.02	+00 20 30.2	3.5 ± 0.7	$2.9\ ^{+0.8}_{-0.8}$	4.7
SSA22-AzTEC53	22 16 58.98	+00 12 32.7	3.5 ± 0.7	$2.8\ ^{+0.9}_{-0.8}$	4.7
SSA22-AzTEC54	22 16 50.99	+00 10 45.2	3.7 ± 0.8	$3.0\ ^{+0.9}_{-0.9}$	4.6
SSA22-AzTEC55	22 18 05.86	+00 11 39.0	3.3 ± 0.7	$2.7\ ^{+0.8}_{-0.8}$	4.6
SSA22-AzTEC56	22 18 06.15	+00 10 21.2	3.3 ± 0.7	$2.7\ ^{+0.8}_{-0.8}$	4.5
SSA22-AzTEC57	22 17 38.86	+00 20 44.8	3.3 ± 0.7	$2.7\ ^{+0.8}_{-0.8}$	4.5
SSA22-AzTEC58	22 16 47.90	+00 24 35.6	5.2 ± 1.2	$3.8\ ^{+1.3}_{-1.4}$	4.4
SSA22-AzTEC59	22 18 14.53	+00 14 48.8	3.2 ± 0.7	$2.6\ ^{+0.8}_{-0.8}$	4.4
SSA22-AzTEC60	22 18 29.42	+00 08 13.4	4.1 ± 0.9	$3.1\ ^{+1.1}_{-1.0}$	4.4
SSA22-AzTEC61	22 17 30.02	+00 04 39.6	3.3 ± 0.7	$2.6\ ^{+0.8}_{-0.8}$	4.4
SSA22-AzTEC62	22 17 28.42	+00 07 30.7	3.2 ± 0.7	$2.6\ ^{+0.8}_{-0.9}$	4.4
SSA22-AzTEC63	22 16 40.23	+00 10 26.1	4.0 ± 0.9	$3.0\ ^{+1.1}_{-1.0}$	4.4
SSA22-AzTEC64	22 16 32.06	+00 17 42.5	4.4 ± 1.0	$3.3\ ^{+1.2}_{-1.2}$	4.3
SSA22-AzTEC65	22 18 00.83	+00 29 30.1	4.6 ± 1.1	$3.4\ ^{+1.2}_{-1.2}$	4.3

Table 2.3 AzTEC/ASTE source catalog (2/4)

ID	R.A. [h m s]	Dec. [° ′ ″]	$S_{observed}$ [mJy]	$S_{deboosted}$ [mJy]	S/N
SSA22-AzTEC66	22 18 27.80	+00 11 51.7	3.4 ± 0.8	$2.7^{+0.9}_{-0.9}$	4.3
SSA22-AzTEC67	22 17 07.38	+00 13 17.5	3.1 ± 0.7	$2.5^{+0.8}_{-0.8}$	4.3
SSA22-AzTEC68	22 18 12.36	+00 23 20.2	3.6 ± 0.8	$2.8^{+0.9}_{-1.0}$	4.3
SSA22-AzTEC69	22 17 47.05	+00 22 33.2	3.1 ± 0.7	$2.5^{+0.8}_{-0.8}$	4.3
SSA22-AzTEC70	22 16 40.34	+00 14 17.9	3.5 ± 0.8	$2.7^{+0.9}_{-0.9}$	4.3
SSA22-AzTEC71	22 17 23.62	+00 09 29.1	3.1 ± 0.7	$2.5^{+0.8}_{-0.8}$	4.2
SSA22-AzTEC72	22 17 27.84	+00 28 50.6	3.6 ± 0.9	$2.8^{+0.9}_{-1.0}$	4.2
SSA22-AzTEC73	22 18 42.03	+00 16 59.3	4.2 ± 1.0	$3.1^{+1.1}_{-1.1}$	4.2
SSA22-AzTEC74	22 17 07.16	+00 17 25.2	3.1 ± 0.7	$2.4^{+0.9}_{-0.8}$	4.2
SSA22-AzTEC75	22 17 24.22	+00 07 23.5	3.1 ± 0.7	$2.4^{+0.8}_{-0.8}$	4.2
SSA22-AzTEC76	22 18 47.75	+00 14 17.5	4.7 ± 1.1	$3.3^{+1.3}_{-1.4}$	4.1
SSA22-AzTEC77	22 17 34.86	+00 15 39.2	3.2 ± 0.8	$2.4^{+0.9}_{-0.8}$	4.1
SSA22-AzTEC78	22 18 36.10	+00 10 06.5	3.9 ± 1.0	$2.9^{+1.1}_{-1.1}$	4.1
SSA22-AzTEC79	22 17 09.16	−00 00 57.0	5.1 ± 1.3	$3.4^{+1.5}_{-1.5}$	4.1
SSA22-AzTEC80	22 17 13.64	+00 19 27.5	3.0 ± 0.7	$2.3^{+0.9}_{-0.8}$	4.1
SSA22-AzTEC81	22 17 02.19	+00 15 58.6	3.0 ± 0.7	$2.3^{+0.9}_{-0.8}$	4.1
SSA22-AzTEC82	22 18 00.65	+00 25 24.7	3.3 ± 0.8	$2.5^{+0.9}_{-0.9}$	4.1
SSA22-AzTEC83	22 16 57.04	+00 24 11.5	3.8 ± 0.9	$2.7^{+1.1}_{-1.0}$	4.0
SSA22-AzTEC84	22 18 19.43	+00 21 20.9	3.3 ± 0.8	$2.5^{+1.0}_{-0.9}$	4.0
SSA22-AzTEC85	22 18 16.78	+00 24 56.6	3.9 ± 1.0	$2.8^{+1.2}_{-1.1}$	4.0
SSA22-AzTEC86	22 17 11.31	+00 03 29.2	3.3 ± 0.8	$2.5^{+1.0}_{-1.0}$	4.0
SSA22-AzTEC87	22 17 25.60	+00 20 32.9	2.9 ± 0.7	$2.3^{+0.8}_{-0.9}$	4.0
SSA22-AzTEC88	22 18 04.39	+00 21 54.0	3.0 ± 0.8	$2.3^{+0.9}_{-0.9}$	4.0
SSA22-AzTEC89	22 16 48.67	+00 11 00.2	3.2 ± 0.8	$2.4^{+0.9}_{-0.9}$	3.9
SSA22-AzTEC90	22 17 09.98	+00 11 00.5	2.9 ± 0.7	$2.2^{+0.9}_{-0.8}$	3.9
SSA22-AzTEC91	22 17 36.92	+00 03 42.9	2.9 ± 0.8	$2.2^{+0.9}_{-0.8}$	3.9
SSA22-AzTEC92	22 17 20.86	+00 01 41.0	3.2 ± 0.8	$2.4^{+1.0}_{-1.0}$	3.9
SSA22-AzTEC93	22 16 58.17	+00 09 17.7	3.0 ± 0.8	$2.3^{+0.9}_{-0.9}$	3.9
SSA22-AzTEC94	22 18 03.24	+00 03 00.6	3.4 ± 0.9	$2.5^{+1.0}_{-1.0}$	3.9
SSA22-AzTEC95	22 17 36.99	+00 08 17.5	2.8 ± 0.7	$2.2^{+0.8}_{-0.9}$	3.9
SSA22-AzTEC96	22 17 54.02	+00 19 27.4	2.8 ± 0.7	$2.2^{+0.8}_{-0.9}$	3.9
SSA22-AzTEC97	22 18 31.24	+00 14 02.7	3.1 ± 0.8	$2.3^{+0.9}_{-0.9}$	3.9
SSA22-AzTEC98	22 18 10.78	+00 16 50.5	2.9 ± 0.7	$2.2^{+0.8}_{-0.9}$	3.9
SSA22-AzTEC99	22 17 25.16	+00 17 56.8	2.9 ± 0.7	$2.2^{+0.8}_{-0.9}$	3.9
SSA22-AzTEC100	22 17 15.40	+00 17 47.9	2.8 ± 0.7	$2.2^{+0.8}_{-0.9}$	3.8

Table 2.4 AzTEC/ASTE source catalog (3/4)

ID	R.A. [h m s]	Dec. [° ′ ″]	$S_{observed}$ [mJy]	$S_{deboosted}$ [mJy]	S/N
SSA22-AzTEC101	22 17 56.53	+00 28 08.6	3.4 ± 0.9	$2.5^{+1.0}_{-1.1}$	3.8
SSA22-AzTEC102	22 17 44.34	+00 06 33.1	2.8 ± 0.7	$2.1^{+0.9}_{-0.8}$	3.8
SSA22-AzTEC103	22 18 02.15	+00 07 44.0	2.9 ± 0.8	$2.2^{+0.9}_{-0.9}$	3.8
SSA22-AzTEC104	22 16 28.56	+00 15 12.6	4.0 ± 1.0	$2.7^{+1.3}_{-1.3}$	3.8
SSA22-AzTEC105	22 18 26.81	+00 21 42.5	3.6 ± 1.0	$2.5^{+1.1}_{-1.1}$	3.8
SSA22-AzTEC106	22 17 22.90	+00 16 57.8	2.8 ± 0.7	$2.1^{+0.8}_{-0.9}$	3.8
SSA22-AzTEC107	22 16 55.79	+00 07 57.7	3.1 ± 0.8	$2.3^{+1.0}_{-1.0}$	3.8
SSA22-AzTEC108	22 17 36.21	+00 22 26.9	2.8 ± 0.7	$2.1^{+0.8}_{-0.9}$	3.8
SSA22-AzTEC109	22 18 26.80	+00 20 23.9	3.3 ± 0.9	$2.3^{+1.1}_{-1.0}$	3.7
SSA22-AzTEC110	22 17 51.00	+00 15 06.4	2.7 ± 0.7	$2.1^{+0.8}_{-0.9}$	3.7
SSA22-AzTEC111	22 18 16.21	+00 23 59.9	3.4 ± 0.9	$2.4^{+1.0}_{-1.1}$	3.7
SSA22-AzTEC112	22 16 57.21	+00 11 11.6	2.8 ± 0.8	$2.1^{+0.9}_{-0.9}$	3.7
SSA22-AzTEC113	22 17 48.40	+00 23 15.2	2.7 ± 0.7	$2.0^{+0.9}_{-0.9}$	3.7
SSA22-AzTEC114	22 16 45.74	+00 06 00.1	4.2 ± 1.1	$0.0^{+1.5}_{-1.4}$	3.7
SSA22-AzTEC115	22 17 06.21	+00 15 15.6	2.7 ± 0.7	$2.0^{+0.9}_{-0.9}$	3.6
SSA22-AzTEC116	22 17 19.43	+00 15 52.0	2.7 ± 0.7	$2.0^{+0.8}_{-0.9}$	3.6
SSA22-AzTEC117	22 17 32.01	+00 25 48.4	2.8 ± 0.8	$2.0^{+0.9}_{-0.9}$	3.6
SSA22-AzTEC118	22 17 59.46	−00 00 21.4	4.0 ± 1.1	$2.6^{+1.3}_{-1.4}$	3.6
SSA22-AzTEC119	22 17 06.83	+00 02 25.8	3.4 ± 0.9	$2.3^{+1.2}_{-1.1}$	3.6
SSA22-AzTEC120	22 18 32.78	+00 22 54.9	4.5 ± 1.2	$0.0^{+1.6}_{-1.6}$	3.6
SSA22-AzTEC121	22 18 33.42	+00 21 14.9	3.9 ± 1.1	$0.0^{+1.3}_{-1.4}$	3.6
SSA22-AzTEC122	22 17 46.04	−00 02 23.9	3.9 ± 1.1	$0.0^{+1.3}_{-1.4}$	3.6
SSA22-AzTEC123	22 16 59.11	+00 23 05.5	3.0 ± 0.8	$2.1^{+1.0}_{-1.1}$	3.5
SSA22-AzTEC124	22 18 34.38	+00 17 38.1	3.1 ± 0.9	$2.1^{+1.1}_{-1.1}$	3.5
SSA22-AzTEC125	22 17 55.73	+00 19 41.3	2.6 ± 0.7	$1.9^{+0.9}_{-0.9}$	3.5

Table 2.5 AzTEC/ASTE source catalog (4/4)

function. We approximated the likelihood function with a normal distribution with σ being the local noise level at each source position. The PDF was obtained by multiplying the prior and likelihood functions. The de-boosted flux is then given by the flux that gives a local maximum of the PDF closest to the measured flux. The de-boosted flux and error bars (68% confidence intervals) are also listed in Table 2.

False Detections

Some fraction of the AzTEC sources were expected to be spurious sources due to positive noise fluctuation, especially when the source had a modest value of S/N. To estimate the number of such non-real sources in the SSA22 map, we extracted sources from a set of jackknifed noise maps. The standard source extraction procedures were performed for 100 simulated maps within the 30% coverage region. Figure 2.2 represents the obtained cumulative false detection rate. The computed number of false detections is shown as a function of S/N. At S/N $\approx$ 3.5, approximately 8 out of 125 sources (6%) were predicted to be spurious.

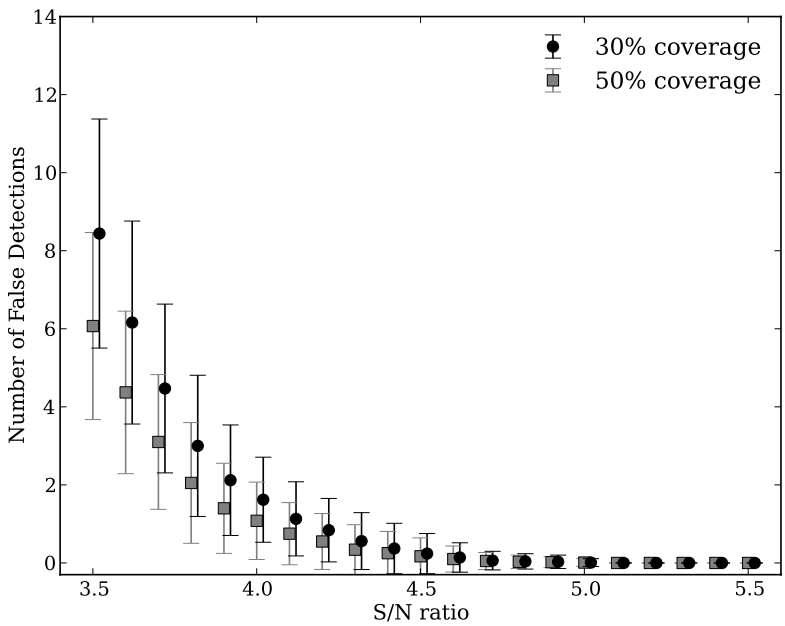

Fig. 2.2 Cumulative number counts of false detections as a function of the signal to noise ratio. The error bars represent 1σ Poisson uncertainties. Circles and squares represent the 50 % and 30 % coverage field, respectively. Data points for the 30 % coverage field are displaced by $+0.02$ in the S/N ratio for clarity.

Completeness

The survey completeness is defined as the probability that a real source will result in a measurement above the detection threshold. To evaluate it, we measured the recovery rate of point sources with known flux densities that were embedded into the signal map. The sources were embedded one at the time, using flux densities ranging from 0.5 mJy to 8.0 mJy. The input positions were selected randomly within the 30% coverage region. To avoid source blending, the area around a real source (within 20″) was not permitted for embedding sources. If an input source was detected within 20″ of its embedded position with S/N $\gg$3.5, it was approved to be recovered. We performed 1000 trials and found that the survey completeness was 50% at a flux density of 2.75 mJy. Figure 2.3 shows the differential completeness as a function of flux density. The error bars were calculated assuming a binomial distribution.

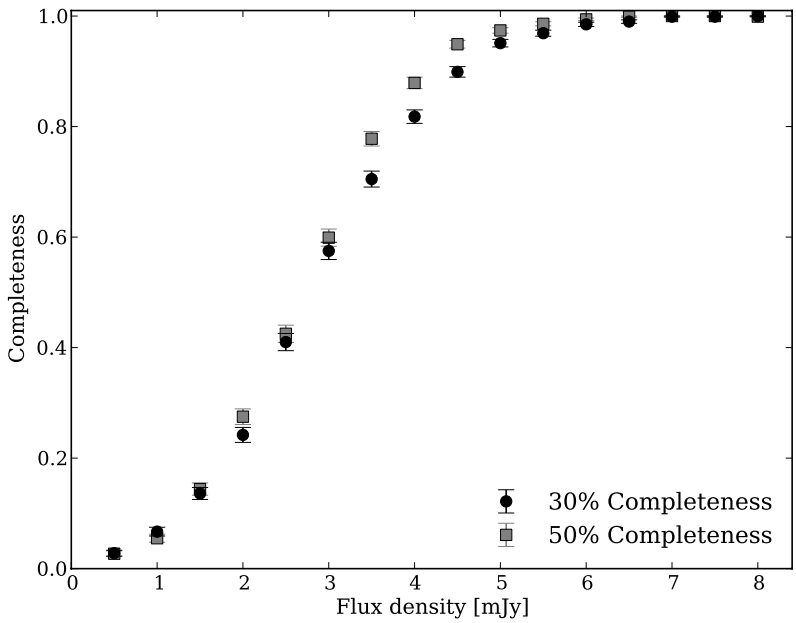

Fig. 2.3 Completeness of the AzTEC/ASTE survey in the 50 % and 30 % coverage field. The error bars represent 1σ estimated from the binomial distribution.

Positional Uncertainty

The detected position of a 1.1 mm source is affected by random and confusion noise in the map, which leads to a large positional error. We estimated such positional uncertainty in a way similar to the one in Section 2.4.2. A point source was inserted with known flux

density into the SSA22 signal map. We extracted it using a standard algorithm and measured the distribution of input to output source distances as a function of S/N. We repeated these processes for three sample S/N bins (3.5≤S/N<4.5, 4.5≤S/N<5.5, and 5.5≤S/N <9.0). Figure. 2.4 shows the probability that a source detected with a given S/N will be found outside a radial distance θ from its intrinsic position.

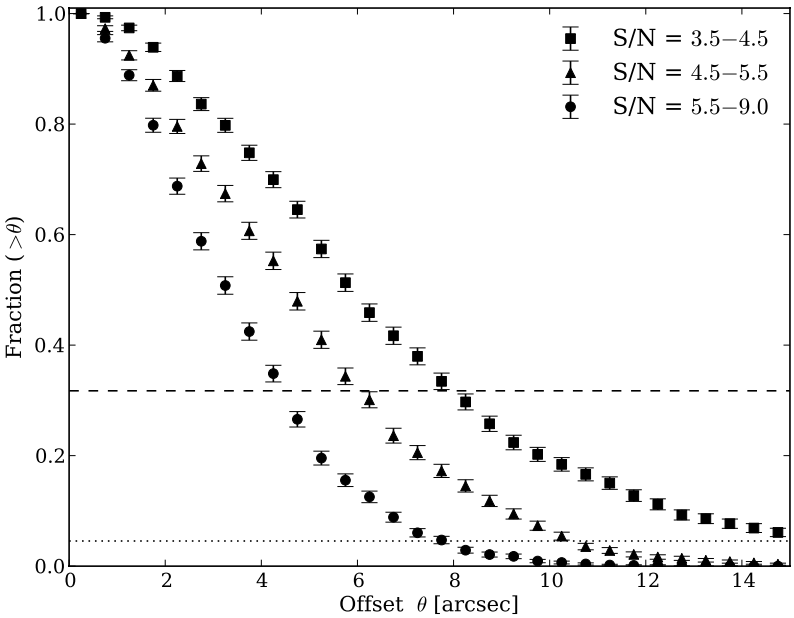

Fig. 2.4 Positional uncertainties estimated from the cumulative probability distribution for a source being detected at a position θ arcsec away from the true position. The probability was calculated for sources with 3.5≤S/N<4.5 (squares with error bars), 4.5≤S/N<5.5 (triangles with error bars), and 5.5≤S/N <9.0 (circles with error bars). The horizontal dashed and dotted lines represent 68.3% and 99.5% confidence levels, respectively.

2.2 The 1.1 mm Mapping with ALMA Band 6

2.2.1 Observations

The ALMA observations of Cycle 1 #2012.1.00608.S (PI. Umehata) were carried out on 2014 May 5 and 2014 May 6. The targets were the 45 out of 125 submillimeter sources originally detected by the AzTEC/ASTE survey in the SSA22 filed. Our Monte-Carlo simulations indicate that only 8 out of 125 AzTEC sources with S/N $\geq$ 3.5 can be false detections. The 45 targets were selected for the follow-up campaign with ALMA. One of our

primary motivations is to reveal the relation between SMGs and the large scale structure at $z = 3.1$ and therefore we selected the possible candidates based on counterpart identification using radio, MIPS, and IRAC data and optical to near-IR photo$-z$ estimates. First we extracted 10 sources of which counterpart candidates have photometric redshifts of $2.6 \geq z_{\rm phot} \geq 3.6$, which is considered to be roughly consistent with the redshift of the large-scale structure, $z = 3.1$. Second we extracted additional 35 sources which are the brighter than the 1.1 mm flux densities measured by AzTEC/ASTE of $S_{1.1\rm mm} > 1.6$ mJy[1] and observed by *Spitzer*/IRAC in order to pick up the $z = 3.1$ SMGs which might be missed.

We observed the AzTEC sources with ALMA band 6 centered at 263 GHz (1.14 mm), which is the almost same frequency of the AzTEC/ASTE survey (270 GHz) and suitable for direct comparison of the measured flux densities. The observations were carried out with 32 – 33 usable 12 m antennas under good 1.1 mm weather conditions (precipitable water vapor of 0.78–2.08 mm). The elevation angles during the observations were also good (54–67 deg). Considering the practical restrict in observing with ALMA, we were force to adopt four spectral windows. We utilized the Time Division Modes (TDM) correlator, with 4×128 dual polarization channels over the full 8 GHz bandwidth, or an effective bandwidth of 7.5 GHz after flagging edge channels. The correlator was set up to target two spectral windows of 1.875 GHz bandwidth each at 15.6 MHz ($\sim$ 18 km s^{-1}) resolution in each sideband. The central frequencies of the four spectral window are 254.0, 256.0, 270.0, and 272.0 GHz. The observations were taken in C32-4 configuration (the longest baseline of 558 m).

The 45 sources were split into 3 scheduling blocks (SBs) of sb0, sb1, sb2, according to the AzTEC/ASTE 1.1 mm flux densities; sb0 has the brightest 15 sources and sb2 the faintest 15. To minimize the observing time, we change the on source time for each SB. Each field was observed for $\sim$ 1, 2, and 3.5 min in total, not including overheads. The primary beam was centered on the positions of the AzTEC sources (Table 2.2– Table 2.5 , also shown in Umehata et al. (2014)). The primary beam of ALMA at the frequency of our observations is $22''.9$ (FWHM). Although the FWHM beam size is slightly smaller than that of the AzTEC/ASTE beam, it is expected that we can detect most of SMGs contributing the AzTEC sources considering the positional error refined with the signal to noise ratio. Furthermore ALMA has sensitivity relatively outside of the FWHM area though the sensitivity decrease following Gaussian. If we consider the 20% sensitivity area, we can cover the circle area of which radius is $32''.9$. Thus the sky area observed by ALMA are thought to be enough large to cover the AzTEC sources.

[1] Since the analysis pipeline for the AzTEC data was updated after submitted the proposal, flux densities at the time is different from Table 2.2– Table 2.5

SB [a]	Date [b]	Antennas [c]	Fields [d]	PWV (mm) [e]
SB1	2014 May 5	32	15	2.0
SB2	2014 May 6	33	15	0.9
SB3	2014 May 6	33	15	0.8

Table 2.6 Summary of ALMA Observations.
[a]: each scheduling block ID.
[b]: The day the observation was executed.
[c]: The number of usable antennas for each observation.
[d]: The number of observed fields. All were single pointing observation.
[e]: The Precipitable Water Vapour

The quasar J2134-0153 or J2148+0657 was utilized for bandpass calibration. The flux calibrator was Neptune. The phase calibrator, J2148+0657, was observed before and after each track.

2.2.2 Data Reduction

The common Astronomy Software Applications (CASA)[2] version 4.2.1 was used for data reduction and analysis. The visibility data were calibrated and converted into an ALMA measurement set (MS) for each SB. For 30 fields in SB1 and SB2, jail patterns contaminated the fields severely and increased the noise revel especially at the center. To remove this artificial effect, we then visually inspected the *uv*-distance to amplitude diagram, flagging the spike-like spurious data.

The final visibility data were Fourier-transformed and the dirty image was generated. Then the dirty image was deconvolved from synthesized beam, or the point spread function (PSF) of an interferometer, and mapped using the CLEAN algorithm with the "natural" weighting to maximize the sensitivity. The resulting image has 360 pixels per side and a pixel scale of $0''.1$ (i.e., the map size is $36'' \times 36''$.). All images were cleaned to a depth of 3σ over the entire image.

Final cleand maps before primary beam correction are shown in Figure. A.7 – A.11. The FWHM of the primary beam ($22''.9$) is superposed in each map. The map properties such as rms noise and beam shape are summarized in Table 2.7 – 2.8. The analysis resulted in typical synthesized beams of $0''.7 \times 0''.6$ (FWHM). This means that we achieved $\times 50$ better angular resolution than the AzTEC 1.1 mm map. In calculating for the beam area, the improvement reaches $\times 2500$. This especially means the big jump in source identification from AzTEC/ASTE. The rms noise revels were measured on the map before primary beam

[2]http://casa.nrao.edu

correction by CASA's task IMSTAT. We divided the central $18'' \times 18''$ square field into four $9'' \times 9''$ fields and measure rms revel for each square. The rms noise of each field are defined as the minimum value of the four measurements to suppress the impact of bright sources. The final rms noise when averaging over all four spectral windows (i.e., 7.5 GHz) is $\sim$160, 100, and 70 μJy beam^{-1} in the phase centers for each SB, which is 4 – 10 times deeper than the original AzTEC/ASTE image. Fifteen fields in each SB have similar rms noise revel. The measured sensitivity revel is almost consistent with the theoretical predictions from the system noise temperature, phase noises, and the number and efficiencies of antennas.

Though some sources are enough bright to apply self-calibration, we haven't applied it in this thesis.

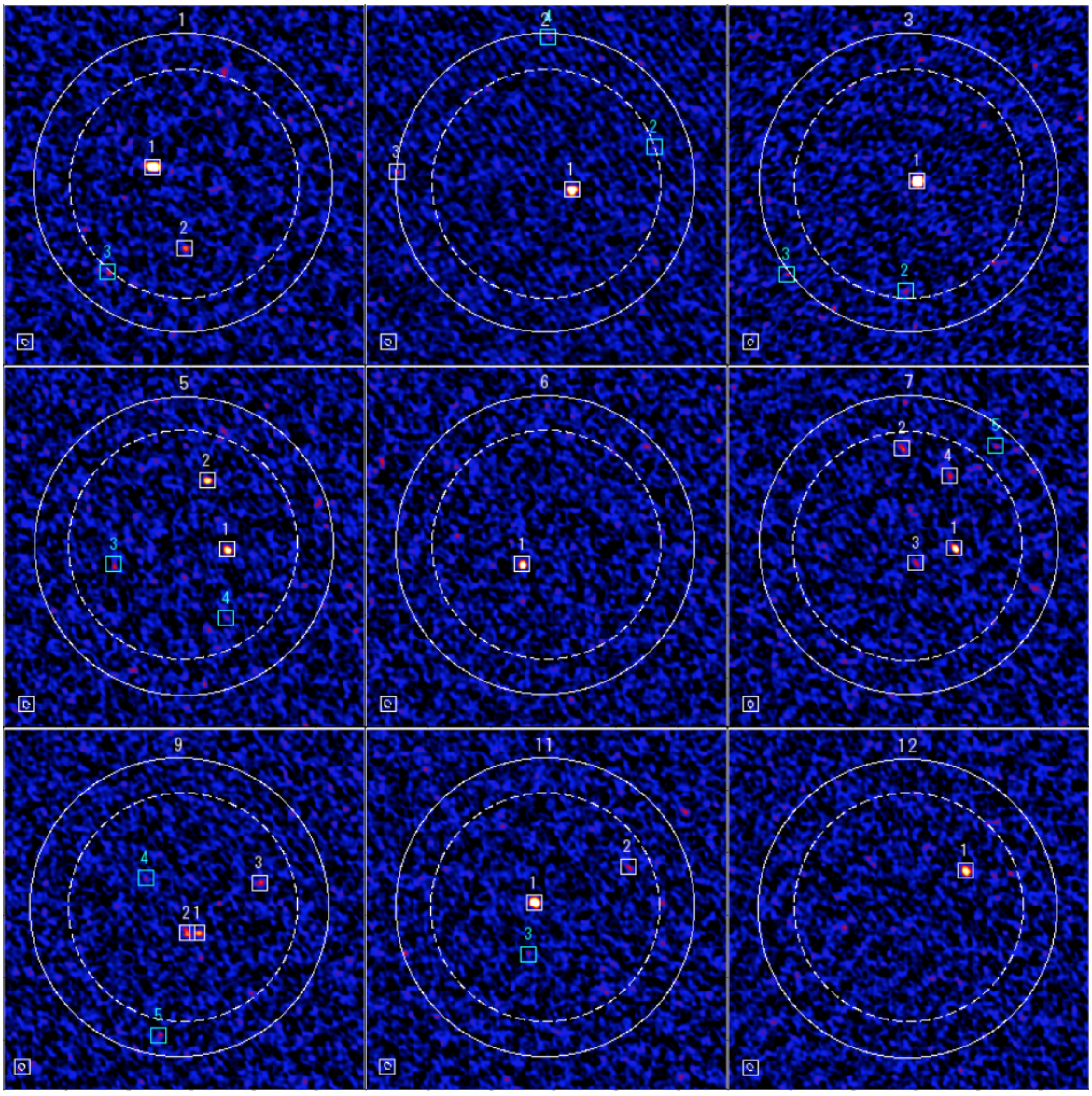

Fig. 2.5 ALMA 1.1 mm images in order of AzTEC ID (AzTEC1–AzTEC12). Each image is $36'' \times 36''$ in size. Large circles with AzTEC ID number represent the AzTEC/ASTE beam (FWHM=30″) and inner dashed circles stand for the size of the ALMA primary beam FWHM at 263 GHz. White squares with numbers show MAIN detected sources ($\geq 4.5\sigma$ within 50% sensitivity area or $\geq 5.0\sigma$ within 20–50% sensitivity area). Cyan squares stand for supplementary sources, which are detected with S/N = 4.1 – 4.5 and locate in 50% sensitivity coverage. The size of synthesized beam is also shown at the bottom left corner in each map.

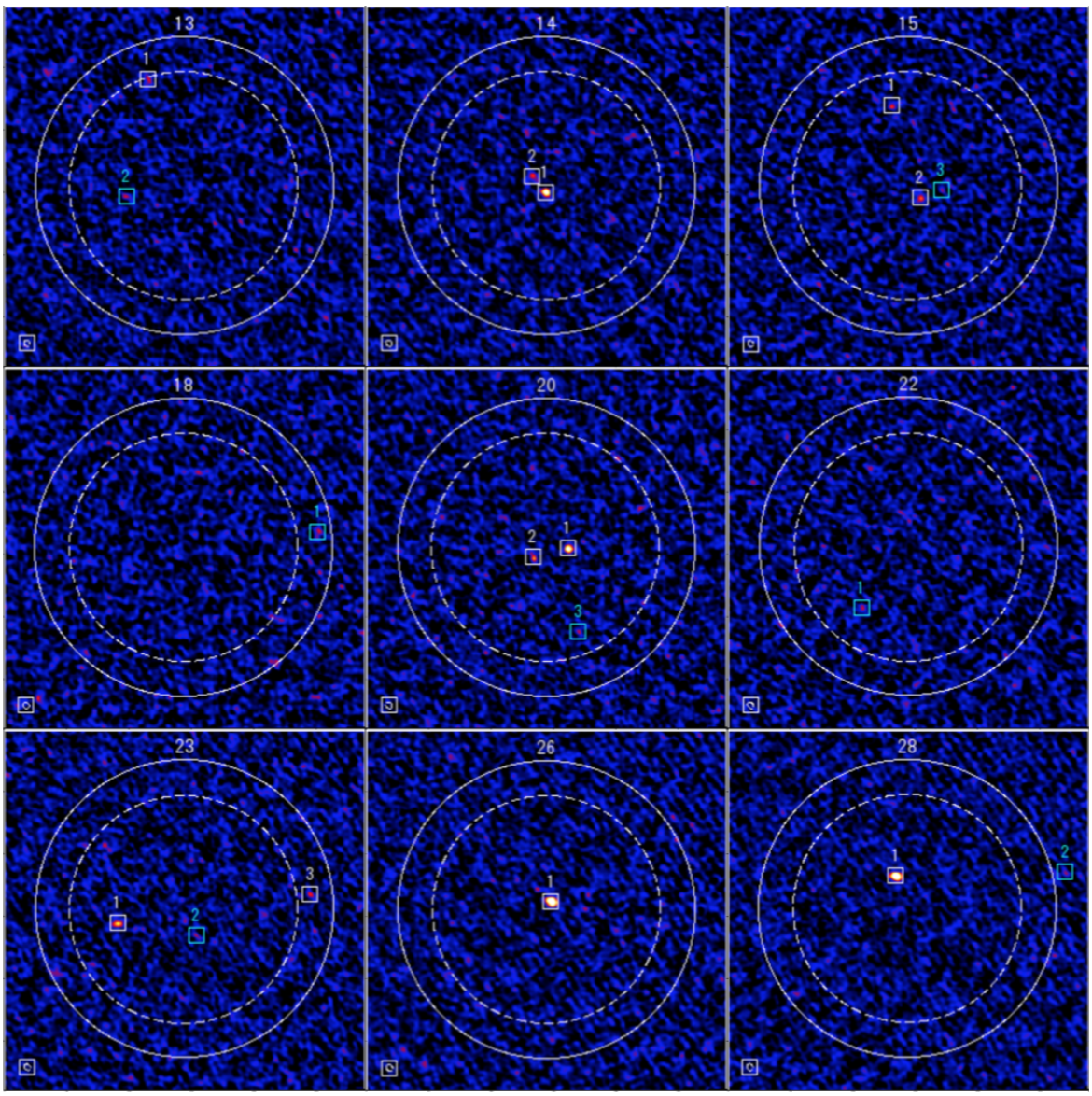

Fig. 2.6 ALMA 1.1 mm images in order of AzTEC ID (AzTEC13–AzTEC28).

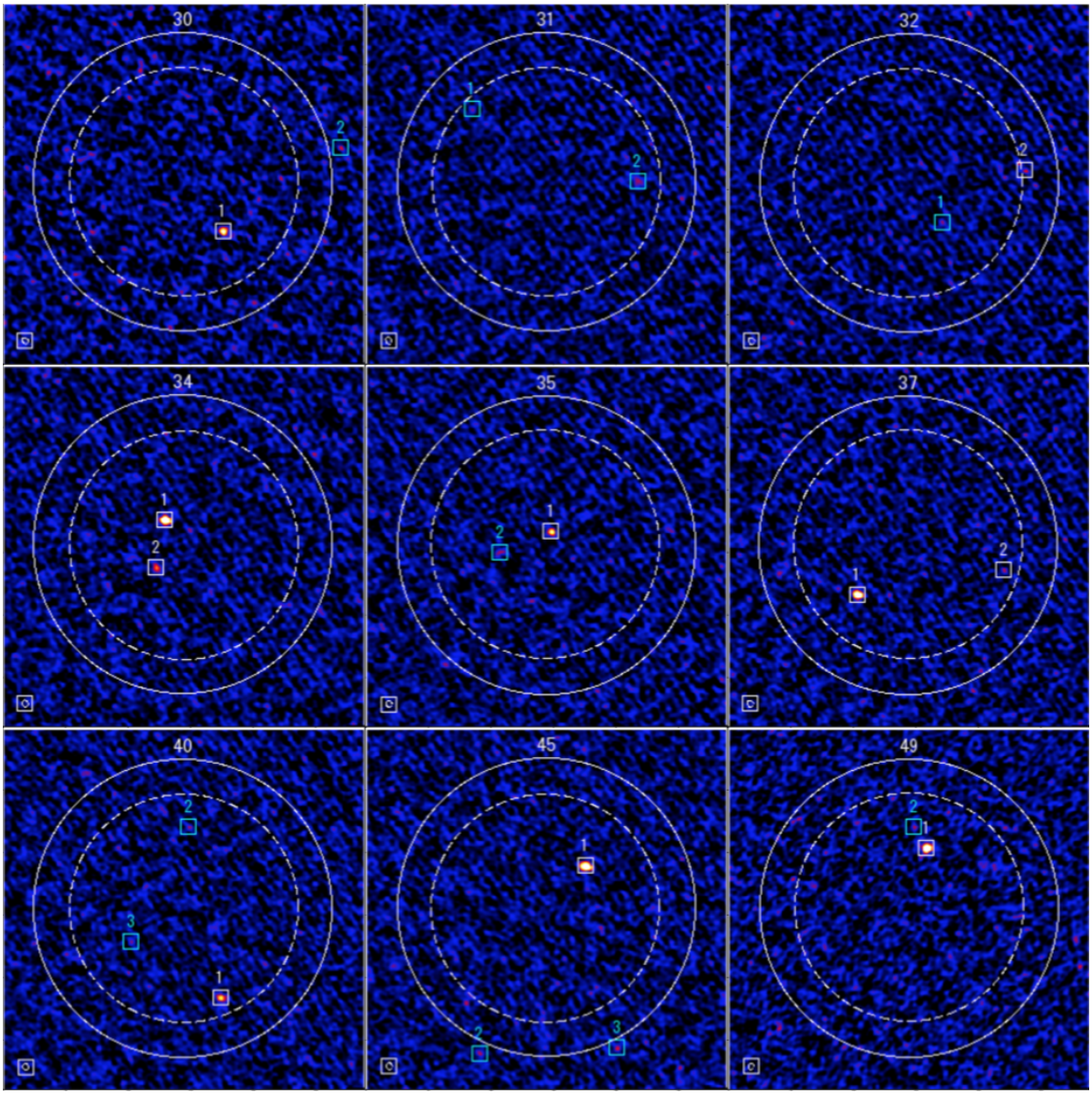

Fig. 2.7 ALMA 1.1 mm images in order of AzTEC ID (AzTEC30–AzTEC49).

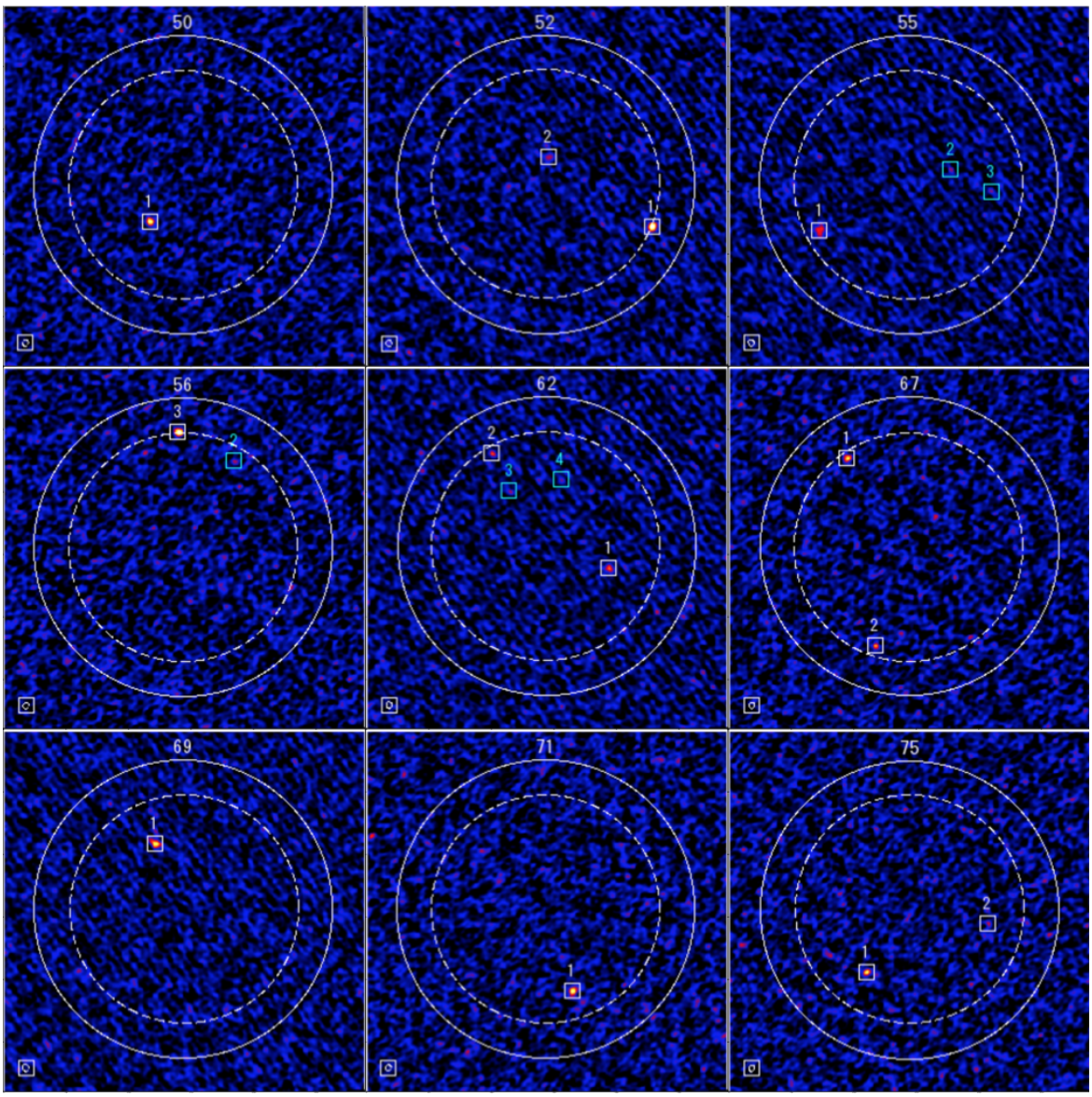

Fig. 2.8 ALMA 1.1 mm images in order of AzTEC ID (AzTEC50–AzTEC75).

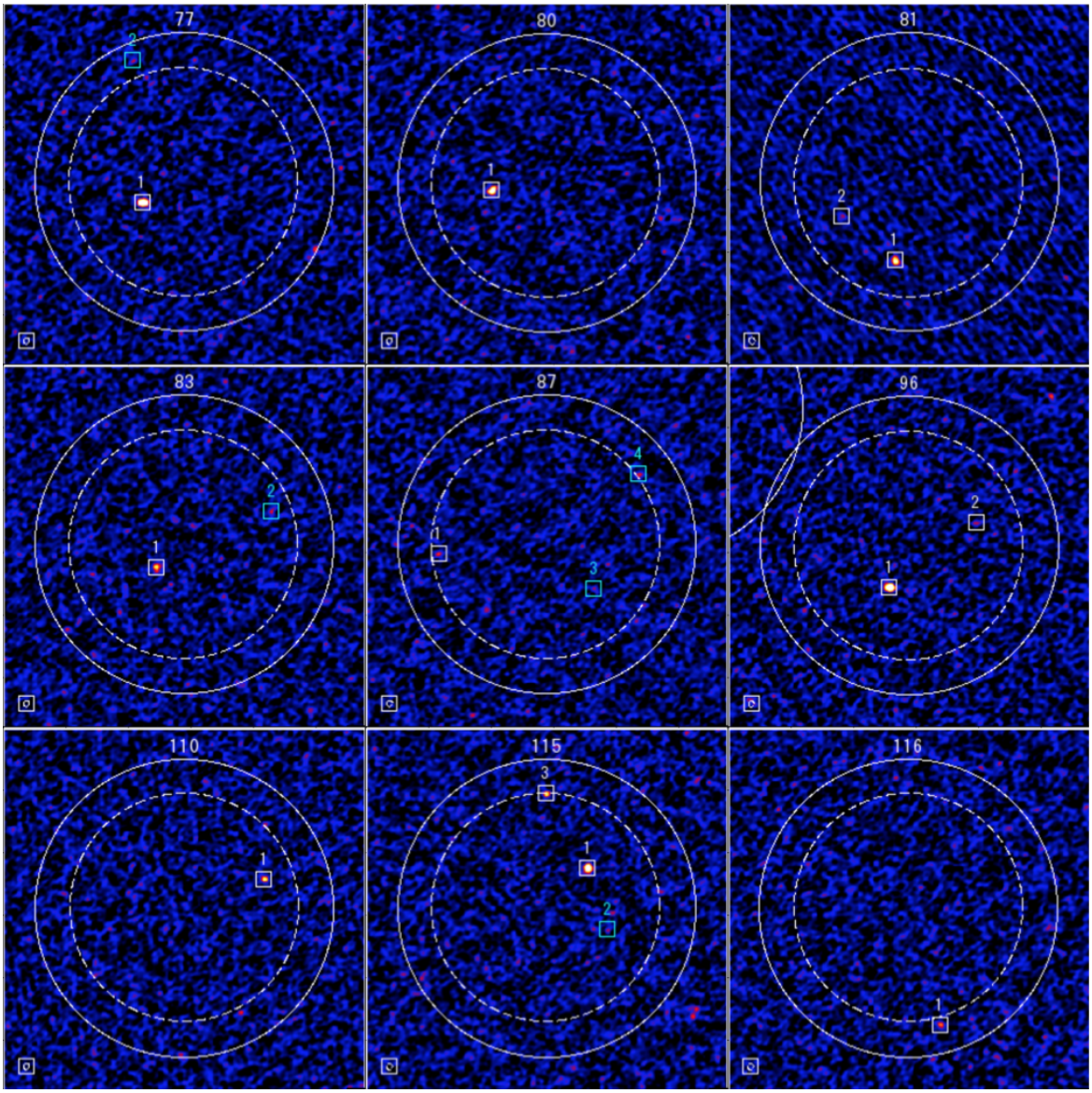

Fig. 2.9 ALMA 1.1 mm images in order of AzTEC ID (AzTEC77–AzTEC116).

AzTEC ID	Center Coordinates J2000	S_{AzTEC} (mJy)	$\mathrm{S/N}_{\mathrm{AzTEC}}$	σ_{ALMA} (mJy/Beam)	ALMA Beam ($''$)	PA (deg)	SB
AzTEC 1	22:17:32.21 +00:17:42.12	11.3 ± 0.9	16.2	0.159	0.69×0.55	50.62	sb0
AzTEC 2	22:17:42.42 +00:17:2.52	6.9 ± 0.9	10.1	0.093	0.68×0.57	63.39	sb1
AzTEC 3	22:18:06.78 +00:06:30.63	6.9 ± 0.8	9.4	0.069	0.65×0.54	-64.35	sb2
AzTEC 5	22:17:18.95 +00:18:3.00	6.1 ± 0.8	8.9	0.166	0.69×0.55	50.98	sb0
AzTEC 6	22:18:15.23 +00:09:48.05	5.9 ± 0.8	8.5	0.153	0.69×0.56	50.77	sb0
AzTEC 7	22:17:09.85 +00:14:8.93	5.6 ± 0.8	8.3	0.157	0.70×0.55	50.71	sb0
AzTEC 9	22:16:60.00 +00:10:41.21	5.3 ± 0.8	7.7	0.149	0.69×0.55	51.38	sb0
AzTEC 11	22:16:57.24 +00:19:23.55	4.9 ± 0.9	7.2	0.156	0.69×0.55	50.05	sb0
AzTEC 12	22:17:34.30 +00:13:48.15	4.9 ± 0.8	7.1	0.161	0.69×0.55	50.69	sb0
AzTEC 13	22:17:20.03 +00:20:17.89	4.6 ± 0.8	7.0	0.159	0.69×0.55	50.49	sb0
AzTEC 14	22:17:36.96 +00:18:21.28	4.5 ± 0.8	6.9	0.164	0.69×0.56	50.63	sb0
AzTEC 15	22:17:28.04 +00:26:42.56	4.7 ± 0.9	6.8	0.161	0.70×0.55	50.47	sb0
AzTEC 18	22:17:42.18 +00:12:38.80	4.3 ± 0.8	6.5	0.161	0.69×0.55	50.73	sb0
AzTEC 20	22:17:44.20 +00:08:22.87	4.0 ± 0.8	6.2	0.165	0.69×0.55	50.89	sb0
AzTEC 22	22:17:04.79 +00:25:50.62	4.8 ± 1.0	6.1	0.162	0.70×0.55	50.40	sb0
AzTEC 23	22:16:57.77 +00:24:54.32	5.0 ± 1.0	6.1	0.149	0.69×0.56	50.51	sb0
AzTEC 26	22:17:13.37 +00:26:50.76	4.4 ± 0.9	5.9	0.106	0.69×0.58	64.97	sb1
AzTEC 28	22:16:49.97 +00:22:45.21	4.7 ± 1.0	5.8	0.095	0.68×0.57	62.93	sb1
AzTEC 30	22:17:47.03 +00:08:9.02	3.7 ± 0.8	5.8	0.164	0.69×0.56	50.90	sb0
AzTEC 31	22:17:27.99 +00:03:17.62	3.7 ± 0.8	5.7	0.097	0.69×0.58	65.26	sb1
AzTEC 32	22:18:05.25 +00:08:41.78	3.7 ± 0.8	5.6	0.097	0.69×0.58	65.12	sb1
AzTEC 34	22:17:41.21 +00:26:39.01	3.7 ± 0.8	5.6	0.099	0.68×0.57	63.06	sb1

Table 2.7 ALMA Observations of SSA22 Field (1/2)

AzTEC ID	Center Coordinates J2000	S_{AzTEC} (mJy)	$\mathrm{S/N}_{\mathrm{AzTEC}}$	σ_{ALMA} (mJy/Beam)	ALMA Beam ($''$)	PA (deg)	SB
AzTEC 35	22:17:41.56 +00:10:42.66	3.5 ± 0.8	5.5	0.098	0.68×0.57	63.20	sb1
AzTEC 37	22:17:37.04 +00:10:29.69	3.4 ± 0.8	5.4	0.100	0.69×0.59	65.20	sb1
AzTEC 40	22:17:03.36 +00:24:53.56	3.8 ± 1.0	5.2	0.094	0.68×0.57	63.31	sb1
AzTEC 45	22:17:32.59 +00:29:26.42	3.5 ± 1.0	5.0	0.095	0.68×0.57	62.75	sb1
AzTEC 49	22:17:06.64 +00:22:50.87	3.1 ± 0.9	4.8	0.068	0.64×0.54	-64.48	sb2
AzTEC 50	22:17:20.60 +00:28:29.77	3.4 ± 1.0	4.8	0.069	0.64×0.54	-64.87	sb2
AzTEC 52	22:17:29.02 +00:20:30.16	2.9 ± 0.8	4.7	0.106	0.69×0.58	65.00	sb1
AzTEC 55	22:18:05.86 +00:11:38.99	2.7 ± 0.8	4.6	0.092	0.68×0.57	62.95	sb1
AzTEC 56	22:18:06.15 +00:10:21.21	2.7 ± 0.8	4.5	0.071	0.65×0.54	-65.46	sb2
AzTEC 62	22:17:28.42 +00:07:30.74	2.6 ± 0.8	4.4	0.098	0.69×0.58	64.77	sb1
AzTEC 67	22:17:07.38 +00:13:17.51	2.5 ± 0.8	4.3	0.074	0.65×0.54	-64.15	sb2
AzTEC 71	22:17:23.62 +00:09:29.14	2.5 ± 0.8	4.2	0.071	0.64×0.54	-64.51	sb2
AzTEC 75	22:17:24.22 +00:07:23.49	2.4 ± 0.8	4.2	0.070	0.64×0.54	-65.11	sb2
AzTEC 77	22:17:34.86 +00:15:39.21	2.4 ± 0.9	4.1	0.069	0.64×0.54	-65.81	sb2
AzTEC 80	22:17:13.64 +00:19:27.48	2.3 ± 0.9	4.1	0.071	0.64×0.55	-65.07	sb2
AzTEC 81	22:17:02.19 +00:15:58.61	2.3 ± 0.9	4.1	0.097	0.68×0.57	63.41	sb1
AzTEC 83	22:16:57.04 +00:24:11.52	2.7 ± 1.1	4.0	0.070	0.64×0.54	-64.68	sb2
AzTEC 87	22:17:25.60 +00:20:32.92	2.3 ± 0.8	4.0	0.066	0.64×0.54	-64.33	sb2
AzTEC 96	22:17:54.02 +00:19:27.37	2.2 ± 0.8	3.9	0.070	0.64×0.54	-65.65	sb2
AzTEC 110	22:17:51.00 +00:15:6.42	2.1 ± 0.8	3.7	0.070	0.64×0.55	-65.32	sb2
AzTEC 115	22:17:06.21 +00:15:15.57	2.0 ± 0.9	3.6	0.069	0.64×0.54	-64.46	sb2
AzTEC 116	22:17:19.43 +00:15:51.97	2.0 ± 0.8	3.6	0.071	0.65×0.54	-63.78	sb2

Table 2.8 ALMA Observations of SSA22 Field (2/2)

2.2.3 Cataloging the SMGs in the ALMA maps

Source Extraction and Measurement

Source extraction and characterization were carried out using a custom-developped Python code and CASA's task IMFIT. First we identified connected pixels which have above 3.5σ S/N using the Python code and performed Gaussian fitting at each position with IMFIT. We define the S/N as the ratio between the peak flux density measured by IMFIT and the rms noise revel for each map. The box size of ($1''.5$,$1''.5$) was adopted for all targets but ASA 1.1. This size is generally adequate to measure the flux considering the size of synthesized beam, $\sim 0.7'' \times 0.6''$). For ASA 1.1, we utilized the $2''.5 \times 2''.5$ box since it has exceptionally extended emission.

False Detection Rate and Criteria in Cataloging

It is expected that as the S/N of detected sources become low, the probability of fake sources would increase. In order to estimate the fraction of contaminants of non-real sources and determine the detection threshold, we calculated the number of spurious sources utilizing the inverted map for all 45 ALMA fields. The inverted map, which is a map multiplied by -1, was generated using IRAF (Tody 1986) task IMARITH for each field. Source extraction and flux measurement were conducted in a same way for the ALMA FoV, which is defined by the FWHM of the primary beam. The results are shown in Figure 2.10 for both of positive and negative maps. The cumulative distribution of negative detections per field indicates that the number of false detections reaches almost one at S/N$\sim$4.0.

First we define the detection threshold of 4.5σ for sources within the FWHM of primary beam and consider the selected sources as primary sources and include them in "main" ALMA source catalog. Figure 2.10 indicates that each filed have less than 0.3 fake sources at the threshold. In addition, we also need to focus on the sources without the central field since the beam size of AzTEC/ASTE is larger than the ALMA's primary beam FWHM and some sources related to the AzTEC sources can lie such outskirt area. Therefore we also include above 5.0σ sources located in 20 – 50% sensitivity area in the main catalog. We have raised the threshold because the lower sensitivity at the outskirt area should lead the higher fraction of spurious sources.

Second we construct a supplementally catalog to list up sources with the S/N of just below the above threshold. Similarly we define the secondary threshold for both of central and out side fields as S/N = 4.1–4.5 and 4.5–5.0, respectively.

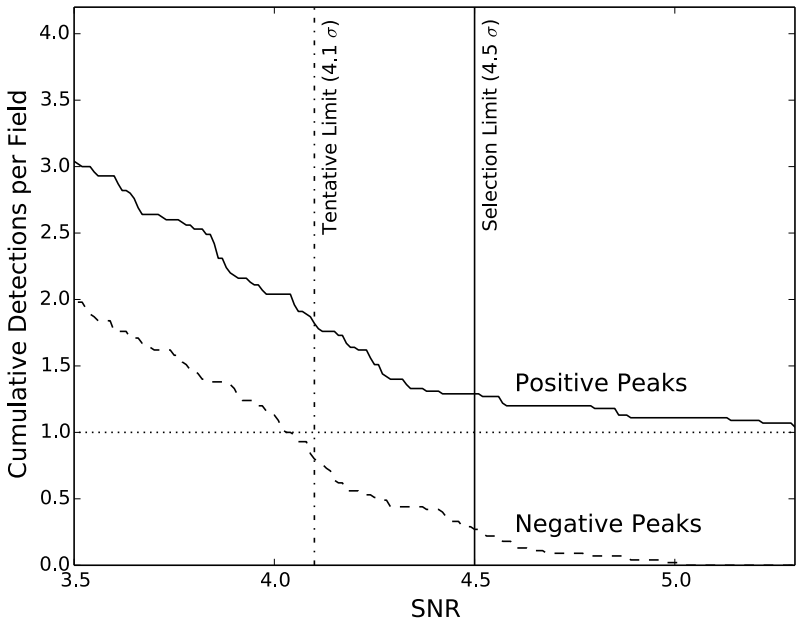

Fig. 2.10 The averaged number of detected positive and negative sources as a function of S/N. Both of positive and negative peaks are assembled from all 45 ALMA fields. The vertical axis shows the number of detections per single field. The two threshold of 4.1σ and 4.5σ are also shown.

Completeness

The completeness is also needed to evaluate the reliability of extracted sources. The effect of noise fluctuation becomes obvious as the S/N of sources is decreased. We calculate the completeness using SExtractor version 2.5 (Bertin & Arnouts (1996)) in a similar way reported in Hatsukade et al. (2013). Through the process we utilized a primary-beam-uncorrected map to satisfy the same condition in extracting sources described above. First we subtracted $\geq 3.0\sigma$ sources from a map and then inserted a flux-scaled synthesized beam into the map. The positions to inject sources were selected completely randomly since the noise level of the map is considered to be almost uniform. The completeness is defined as a recovery rate of injected sources as a function of S/N. If the artificial source is extracted within $1''.0$ from the inserted position with S/N$\geq$ 4.1, we recognize that the source is recovered. For each source, S/N is calculated using a noise level measured by IMSTAT to be fair. We calculated the completeness 100 times for a bin per map and five fields were processed. In total, we insert 15000 sources. Figure 2.11 shows the result. We can find that the completeness is over 0.5 at the supplement limit, S/N=4.1 and reaches > 0.7 at S/N=4.5.

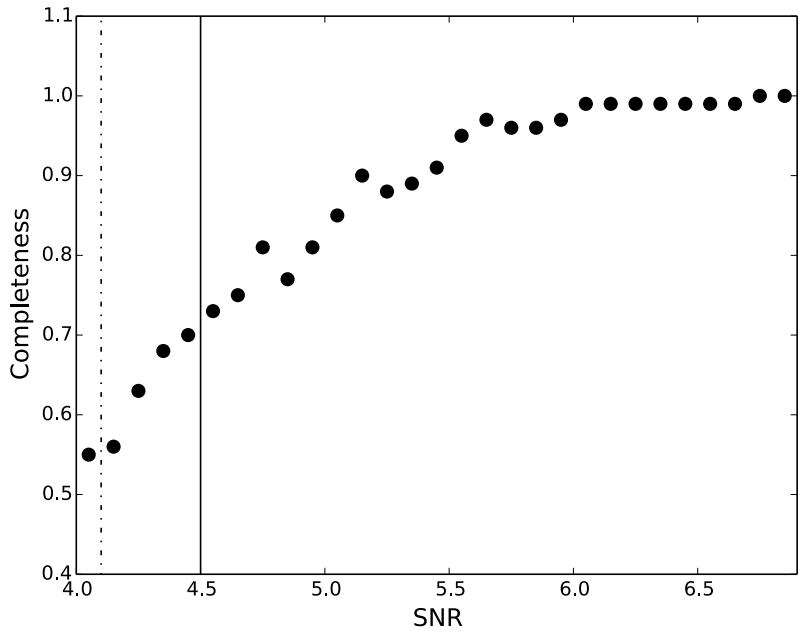

Fig. 2.11 Completeness as a function of S/N. We averaged the results for example five fields. The dotted – dashed line shows the S/N of 4.1, which is the detection limit of supplementary sources. The solid line represents the 4.5 σ threshold for the main catalog.

Flux Scale Compared to AzTEC

Whilst ALMA allows us to resolve the AzTEC sources into individual sources, we are forced to have significant questions. Is ALMA measurement consistent with that of AzTEC? Or does ALMA sources represent the whole of the 1.1 mm flux density measured by AzTEC/ASTE?

In order to check the absolute flux scale and obtain an answer for such questions, we compared flux densities measured by ALMA with those of the AzTEC / ASTE survey (Umehata et al. (2014)). Broadly there are two critical differences between the two surveys. The first one is a bandwidth. Though both surveys were conducted at almost same (but not exactly the same) frequency (263 GHz for ALMA, 270 GHz for AzTEC), the two have a crucially different bandwidth. While ALMA has a 7.5 GHz bandwidth which is composed of 4 separated bands, AzTEC/ASTE has a 50 GHz continuous bandwidth. The difference can result in producing a systematic difference since SEDs of SMGs have a steep Rayleigh-Jeans tail. The second one is found in an angular resolution. The AzTEC/ASTE survey has coarse angular resolution ($\sim 30''$). Hence it can detect the extended emission and have a sensitivity for very faint sources.

In Figure 2.12, we show the result of the comparison. We utilize the deboosted flux den-

sity as AzTEC measurements (Table 2.2–2.5), which is the best estimate for the survey. For the ALMA survey, we adopt the sum of individually detected sources. Both of the estimate are generally consistent within error bars and one implication is that we can deconvolve the AzTEC sources successfully. However, it is also notable that the ALMA flux density tends to be lower than that of the AzTEC flux density. The median value of ALMA to AzTEC flux density ratio is $S_{ALMA}/S_{AzTEC} = 0.73$. If we consider all sources including supplementary ones, the median go up to $S_{ALMA}/S_{AzTEC} = 0.82$. The contribution of fainter sources to AzTEC flux may be so important.

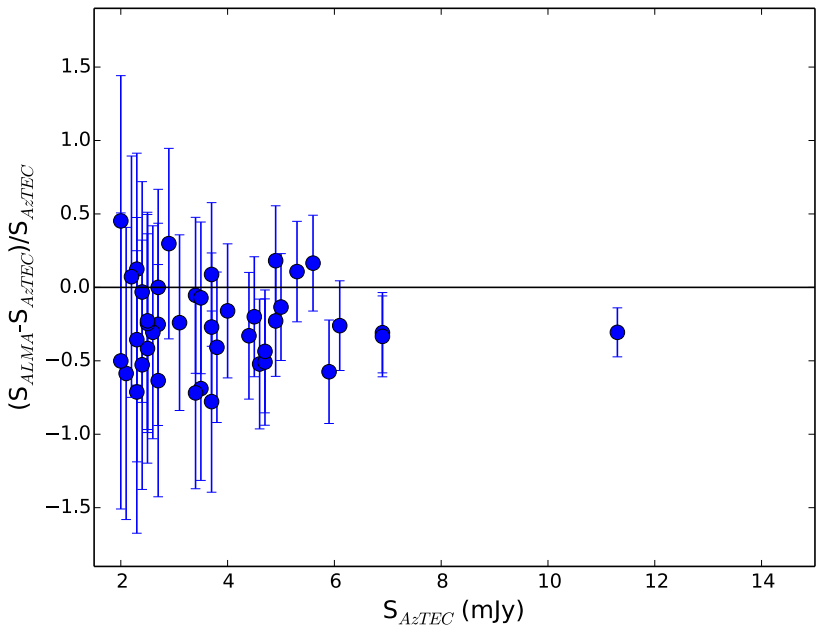

Fig. 2.12 The flux ratio of the AzTEC and ALMA survey. The horizontal axis shows flux densities measured by AzTEC/ASTE and the vertical axis represents the relation between the two. We considered only ALMA sources in the main catalog here. Both measurements indicate good agreement within errors, though it is likely that the ALMA survey tends to show lower flux densities.

Astrometry

In oder to examine the achieved astrometric accuracies, we compared the positions of ALMA sources with those of VLA 1.4 GHz counterparts (Chapman et al. 2004, Umehata et al. 2014). In the comparison, the $> 4\sigma$ 1.4 GHz sources and $> 4.5\sigma$ 1.1 mm sources were utilized. We matched both catalog and extracted if the offset between the two is smaller than $1''.0$. ASA 9.1 and ASA 9.2 were not considered since the separation of the two is too small

and the 1.4 GHz counterparts to ASA 9.1/2 are blended into a single source. We measured the offset in the sense ALMA-VLA and Figure 2.13 stands for the results. The mean offsets in R.A. and Dec are $0''.036$ and $0''.001$, respectively. The scatter considering all cases is $0''.08$. This measurement is roughly consistent with the expected value based on the size of synthesized beam (Θ) and S/N ($\sim \Theta$ / (S/N), 0.02–0.13). The two large offset ($> 0''.5$) sources are recognized in Figure 2.13. For both case, There are two clear Spitzer/IRAC counterparts to the two ALMA sources that also offset from the VLA positions, suggesting that the offset between them may be intrinsic. Hence the offset between ALMA and VLA data for the two sources may be intrinsic and VLA is looking at objects different from the ALMA sources. In conclusion, the ALMA data has good astrometry and the estimated positional uncertainty is $< 0''.1$.

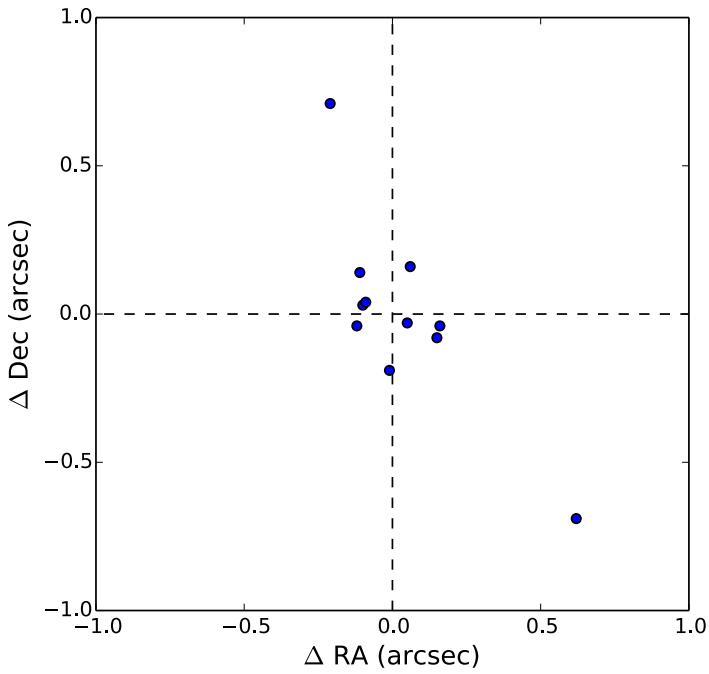

Fig. 2.13 The diagram of astrometric offset between the ALMA 1.1 mm data and the VLA 1.4 GHz data in a sense of ALMA–VLA.

Final Catalog

Finally we compile a main ALMA source catalog and a supplementary ALMA source catalog as summarized in Table 2.9 – 2.11 and Table 2.11 – 2.13, respectively. We include AzTEC ID, ALMA ID, coordinates of ALMA source, flux densities, previous identification

based on VLA and Spitzer data, and flags. We named ALMA sources like ASA001.1, which originally means ALMA-SSA22-AzTEC001.1. Three types of flux density are shown in the tables: (i) peak flux density without primary-beam correction, (ii) integral flux density without primary beam correction, and (iii) primary beam corrected integral flux density. In the following analysis and discussion, the primary beam corrected integral flux densities are considered to be best estimates. The flags of 'c' and 'o' represent the source position. The former means sources located within the primary beam FWHM ($\geq$ 50% sensitivity area). The latter stands for sources discovered at outskirt area (20–50% sensitivity area). The main catalog comprises of 64 sources, which have flux density of $S_{263\mathrm{GHz}}$ =0.3 – 6.4 mJy. The supplementary catalog contains 38 sources, the flux density of which is $S_{263\mathrm{GHz}}$ =0.2 – 1.4 mJy. Totally 102 ALMA sources are listed up.

AzTEC ID	ALMA ID	RA (J2000)	DEC (J2000)	S_{pk} (mJy / Beam)	S_{int} (mJy)	S/N_{pk}	$S_{BEST,pbcorr}$ (mJy)	ID	Flag
SSA22-AzTEC 001	ASA 001 . 1	22:17:32.42	+00:17:43.83	3.10 ± 0.13	6.03 ± 0.25	19.5	6.40 ± 0.27	r	c
SSA22-AzTEC 001	ASA 001 . 2	22:17:32.21	+00:17:35.67	1.01 ± 0.15	1.17 ± 0.17	6.4	1.44 ± 0.20	–	c
SSA22-AzTEC 002	ASA 002 . 1	22:17:42.25	+00:17:1.94	2.13 ± 0.08	3.02 ± 0.11	22.9	3.10 ± 0.12	r	c
SSA22-AzTEC 003	ASA 003 . 1	22:18:06.72	+00:06:30.93	3.35 ± 0.04	4.59 ± 0.05	48.6	4.60 ± 0.06	–	c
SSA22-AzTEC 005	ASA 005 . 1	22:17:18.66	+00:18:2.65	1.86 ± 0.11	2.20 ± 0.13	11.2	2.40 ± 0.15	r	c
SSA22-AzTEC 005	ASA 005 . 2	22:17:18.80	+00:18:9.62	1.72 ± 0.16	1.65 ± 0.16	10.4	2.11 ± 0.21	–	c
SSA22-AzTEC 006	ASA 006 . 1	22:18:15.39	+00:09:46.18	2.14 ± 0.11	2.42 ± 0.12	14.0	2.51 ± 0.13	t	c
SSA22-AzTEC 007	ASA 007 . 1	22:17:09.54	+00:14:8.69	2.06 ± 0.13	2.12 ± 0.13	13.1	2.33 ± 0.14	–	c
SSA22-AzTEC 007	ASA 007 . 2	22:17:09.89	+00:14:18.71	0.87 ± 0.10	1.29 ± 0.15	5.6	2.16 ± 0.27	–	c
SSA22-AzTEC 007	ASA 007 . 3	22:17:09.80	+00:14:7.25	0.82 ± 0.17	0.93 ± 0.20	5.2	0.93 ± 0.20	–	c
SSA22-AzTEC 007	ASA 007 . 4	22:17:09.58	+00:14:15.98	0.81 ± 0.11	0.78 ± 0.11	5.1	1.10 ± 0.16	–	c
SSA22-AzTEC 009	ASA 009 . 1	22:16:59.88	+00:10:38.73	1.14 ± 0.12	1.71 ± 0.17	7.7	1.77 ± 0.18	r	c
SSA22-AzTEC 009	ASA 009 . 2	22:16:59.95	+00:10:38.77	0.87 ± 0.13	2.44 ± 0.38	5.9	2.49 ± 0.38	r	c
SSA22-AzTEC 009	ASA 009 . 3	22:16:59.47	+00:10:43.79	0.80 ± 0.10	1.17 ± 0.14	5.4	1.61 ± 0.20	–	c
SSA22-AzTEC 011	ASA 011 . 1	22:16:57.32	+00:19:24.12	2.72 ± 0.13	4.46 ± 0.22	17.4	4.48 ± 0.22	r	c
SSA22-AzTEC 011	ASA 011 . 2	22:16:56.69	+00:19:27.64	0.76 ± 0.18	0.85 ± 0.20	4.9	1.31 ± 0.33	–	c
SSA22-AzTEC 012	ASA 012 . 1	22:17:33.92	+00:13:51.99	1.73 ± 0.09	2.99 ± 0.15	10.7	3.78 ± 0.19	r	c
SSA22-AzTEC 013	ASA 013 . 1	22:17:20.28	+00:20:28.55	0.73 ± 0.13	1.13 ± 0.21	4.6	2.20 ± 0.42	–	c
SSA22-AzTEC 014	ASA 014 . 1	22:17:36.97	+00:18:20.65	2.24 ± 0.13	2.24 ± 0.13	13.7	2.24 ± 0.13	r	c
SSA22-AzTEC 014	ASA 014 . 2	22:17:37.05	+00:18:22.24	0.75 ± 0.12	1.35 ± 0.22	4.6	1.36 ± 0.22	r	c

Table 2.9 ALMA Main Source Catalog (1/3).
S_{pk}, S_{int}: Peak and Integral flux density and errors measured by CASA IMFIT,
S/N_{pk}: The ratio between peak flux density and the rms noise measured by CASA IMSTAT,
$S_{BEST,pbcorr}$: Primary beam corrected integral flux density.
ID: Classification of VLA/MIPS/IRAC counterpart identification (Umehata et al. 2014). ‘r’ and ‘t’ are robust and tentative counterparts, respectively.

AzTEC ID	ALMA ID	RA (J2000)	DEC (J2000)	$S_{\rm pk}$ (mJy / Beam)	$S_{\rm int}$ (mJy)	S/N$_{\rm pk}$	$S_{\rm BEST,pbcorr}$ (mJy)	ID	Flag
SSA22-AzTEC 015	ASA 015 . 1	22:17:28.15	+00:26:50.61	0.86 ± 0.12	0.71 ± 0.10	5.3	1.02 ± 0.14	–	c
SSA22-AzTEC 015	ASA 015 . 2	22:17:27.96	+00:26:41.38	0.85 ± 0.12	1.28 ± 0.18	5.3	1.29 ± 0.18	–	c
SSA22-AzTEC 020	ASA 020 . 1	22:17:44.05	+00:08:22.79	1.99 ± 0.11	2.21 ± 0.12	12.1	2.25 ± 0.12	r	c
SSA22-AzTEC 020	ASA 020 . 2	22:17:44.29	+00:08:21.91	0.98 ± 0.12	1.10 ± 0.13	6.0	1.11 ± 0.13	r	c
SSA22-AzTEC 023	ASA 023 . 1	22:16:58.22	+00:24:52.95	1.11 ± 0.09	1.90 ± 0.14	7.5	2.41 ± 0.18	t	c
SSA22-AzTEC 026	ASA 026 . 1	22:17:13.34	+00:26:51.66	2.10 ± 0.04	2.95 ± 0.06	19.8	2.95 ± 0.06	–	c
SSA22-AzTEC 028	ASA 028 . 1	22:16:50.06	+00:22:48.60	2.06 ± 0.06	2.50 ± 0.07	21.7	2.65 ± 0.07	t	c
SSA22-AzTEC 030	ASA 030 . 1	22:17:46.77	+00:08:4.20	1.82 ± 0.17	2.22 ± 0.21	11.1	2.70 ± 0.25	r	c
SSA22-AzTEC 034	ASA 034 . 1	22:17:41.34	+00:26:41.58	2.00 ± 0.07	2.86 ± 0.10	20.2	2.99 ± 0.11	r	c
SSA22-AzTEC 034	ASA 034 . 2	22:17:41.40	+00:26:36.80	0.64 ± 0.04	0.98 ± 0.07	6.5	1.03 ± 0.07	–	c
SSA22-AzTEC 035	ASA 035 . 1	22:17:41.53	+00:10:44.08	1.08 ± 0.07	1.08 ± 0.07	11.0	1.09 ± 0.07	–	c
SSA22-AzTEC 037	ASA 037 . 1	22:17:37.39	+00:10:24.82	1.69 ± 0.09	2.17 ± 0.11	16.9	2.80 ± 0.14	r	c
SSA22-AzTEC 037	ASA 037 . 2	22:17:36.41	+00:10:27.22	0.48 ± 0.07	0.25 ± 0.04	4.8	0.42 ± 0.07	–	c
SSA22-AzTEC 040	ASA 040 . 1	22:17:03.12	+00:24:44.65	0.81 ± 0.06	1.37 ± 0.10	8.6	2.25 ± 0.16	–	c
SSA22-AzTEC 045	ASA 045 . 1	22:17:32.33	+00:29:30.66	1.78 ± 0.08	2.76 ± 0.12	18.7	3.25 ± 0.14	t	c
SSA22-AzTEC 049	ASA 049 . 1	22:17:06.52	+00:22:56.96	1.44 ± 0.05	1.93 ± 0.06	21.2	2.35 ± 0.08	–	c
SSA22-AzTEC 050	ASA 050 . 1	22:17:20.83	+00:28:26.17	0.66 ± 0.04	0.85 ± 0.06	9.6	0.96 ± 0.07	t	c
SSA22-AzTEC 052	ASA 052 . 1	22:17:28.32	+00:20:26.05	1.33 ± 0.06	1.57 ± 0.07	12.5	3.12 ± 0.13	t	c
SSA22-AzTEC 052	ASA 052 . 2	22:17:29.01	+00:20:32.99	0.48 ± 0.07	0.63 ± 0.09	4.5	0.64 ± 0.10	t	c
SSA22-AzTEC 055	ASA 055 . 1	22:18:06.46	+00:11:34.50	0.55 ± 0.06	1.58 ± 0.16	6.0	2.70 ± 0.26	t	c
SSA22-AzTEC 062	ASA 062 . 1	22:17:28.01	+00:07:28.61	0.63 ± 0.05	0.79 ± 0.06	6.5	0.98 ± 0.08	–	c
SSA22-AzTEC 062	ASA 062 . 2	22:17:28.79	+00:07:40.11	0.62 ± 0.04	0.44 ± 0.03	6.4	0.83 ± 0.05	–	c

Table 2.10 ALMA Source Catalog (2/3)

AzTEC ID	ALMA ID	RA (J2000)	DEC (J2000)	$S_{\rm pk}$ [a] (mJy / Beam)	$S_{\rm int}$ [a] (mJy)	S/N$_{\rm pk}$ [b]	$S_{\rm BEST,pbcorr}$ [c] (mJy)	ID	Flag
SSA22-AzTEC 067	ASA 067 . 1	22:17:07.80	+00:13:26.45	0.58 ± 0.07	0.60 ± 0.07	7.8	1.15 ± 0.13	–	c
SSA22-AzTEC 067	ASA 067 . 2	22:17:07.61	+00:13:7.68	0.42 ± 0.05	0.41 ± 0.05	5.7	0.73 ± 0.09	t	c
SSA22-AzTEC 069	ASA 069 . 1	22:17:47.25	+00:22:39.94	0.92 ± 0.08	1.46 ± 0.13	9.7	1.93 ± 0.17	–	c
SSA22-AzTEC 071	ASA 071 . 1	22:17:23.45	+00:09:21.04	0.59 ± 0.05	1.01 ± 0.08	8.3	1.46 ± 0.12	–	c
SSA22-AzTEC 075	ASA 075 . 1	22:17:24.51	+00:07:17.34	0.62 ± 0.04	0.61 ± 0.04	8.8	0.82 ± 0.06	t	c
SSA22-AzTEC 075	ASA 075 . 2	22:17:23.70	+00:07:22.18	0.34 ± 0.06	0.23 ± 0.04	4.9	0.31 ± 0.05	–	c
SSA22-AzTEC 077	ASA 077 . 1	22:17:35.14	+00:15:37.28	1.58 ± 0.05	2.10 ± 0.07	22.9	2.32 ± 0.07	r	c
SSA22-AzTEC 080	ASA 080 . 1	22:17:14.01	+00:19:26.79	1.04 ± 0.05	1.27 ± 0.06	14.7	1.48 ± 0.07	–	c
SSA22-AzTEC 081	ASA 081 . 1	22:17:02.29	+00:15:50.85	1.16 ± 0.09	1.47 ± 0.11	12.0	2.02 ± 0.15	t	c
SSA22-AzTEC 081	ASA 081 . 2	22:17:02.64	+00:15:55.28	0.44 ± 0.08	0.42 ± 0.08	4.6	0.56 ± 0.10	–	c
SSA22-AzTEC 083	ASA 083 . 1	22:16:57.23	+00:24:9.35	0.50 ± 0.04	0.93 ± 0.07	7.1	0.98 ± 0.08	t	c
SSA22-AzTEC 087	ASA 087 . 1	22:17:26.32	+00:20:32.10	0.36 ± 0.06	0.35 ± 0.06	5.4	0.66 ± 0.11	–	c
SSA22-AzTEC 096	ASA 096 . 1	22:17:54.16	+00:19:23.25	1.36 ± 0.06	1.80 ± 0.08	19.4	2.00 ± 0.09	–	c
SSA22-AzTEC 096	ASA 096 . 2	22:17:53.58	+00:19:29.69	0.34 ± 0.06	0.28 ± 0.05	4.9	0.36 ± 0.07	–	c
SSA22-AzTEC 110	ASA 110 . 1	22:17:50.47	+00:15:9.41	0.59 ± 0.04	0.60 ± 0.04	8.5	0.87 ± 0.07	t	c
SSA22-AzTEC 115	ASA 115 . 1	22:17:05.94	+00:15:19.69	1.11 ± 0.04	1.57 ± 0.06	16.1	1.85 ± 0.07	–	c
SSA22-AzTEC 002	ASA 002 . 3	22:17:43.42	+00:17:3.75	0.52 ± 0.06	0.46 ± 0.05	5.6	1.67 ± 0.19	–	o
SSA22-AzTEC 023	ASA 023 . 3	22:16:56.93	+00:24:55.85	0.76 ± 0.12	0.79 ± 0.12	5.1	1.92 ± 0.29	–	o
SSA22-AzTEC 032	ASA 032 . 2	22:18:04.48	+00:08:43.08	0.49 ± 0.11	0.41 ± 0.09	5.1	0.82 ± 0.17	–	o
SSA22-AzTEC 056	ASA 056 . 3	22:18:06.19	+00:10:32.79	0.80 ± 0.06	0.98 ± 0.07	11.3	2.02 ± 0.15	–	o
SSA22-AzTEC 115	ASA 115 . 3	22:17:06.22	+00:15:27.11	0.61 ± 0.05	0.52 ± 0.04	8.9	1.05 ± 0.09	–	o
SSA22-AzTEC 116	ASA 116 . 1	22:17:19.23	+00:15:40.36	0.43 ± 0.04	0.45 ± 0.05	6.0	1.00 ± 0.10	–	o

Table 2.11 ALMA Main Source Catalog (3/3)

AzTEC ID	ALMA ID	RA (J2000)	DEC (J2000)	$S_{\rm pk}$ (mJy / Beam)	$S_{\rm int}$ (mJy)	S/N$_{\rm pk}$	$S_{\rm BEST,pbcorr}$ (mJy)
SSA22-AzTEC 002	ASA 002 . 2	22:17:41.70	+00:17:6.17	0.38 ± 0.08	0.27 ± 0.06	4.1	0.55 ± 0.12
SSA22-AzTEC 003	ASA 003 . 2	22:18:06.80	+00:06:19.90	0.29 ± 0.06	0.39 ± 0.07	4.2	0.71 ± 0.14
SSA22-AzTEC 005	ASA 005 . 3	22:17:19.42	+00:18:1.14	0.70 ± 0.16	0.68 ± 0.16	4.2	0.88 ± 0.20
SSA22-AzTEC 005	ASA 005 . 4	22:17:18.67	+00:17:55.85	0.69 ± 0.10	0.36 ± 0.05	4.2	0.52 ± 0.07
SSA22-AzTEC 009	ASA 009 . 4	22:17:00.23	+00:10:44.20	0.61 ± 0.09	0.63 ± 0.09	4.1	0.70 ± 0.10
SSA22-AzTEC 011	ASA 011 . 3	22:16:57.36	+00:19:18.97	0.64 ± 0.14	0.30 ± 0.06	4.1	0.34 ± 0.07
SSA22-AzTEC 013	ASA 013 . 2	22:17:20.42	+00:20:16.81	0.65 ± 0.16	0.72 ± 0.17	4.1	0.85 ± 0.21
SSA22-AzTEC 015	ASA 015 . 3	22:17:27.82	+00:26:42.21	0.68 ± 0.20	0.34 ± 0.10	4.2	0.35 ± 0.10
SSA22-AzTEC 020	ASA 020 . 3	22:17:43.98	+00:08:14.44	0.71 ± 0.11	0.47 ± 0.07	4.3	0.72 ± 0.11
SSA22-AzTEC 022	ASA 022 . 1	22:17:05.10	+00:25:44.55	0.71 ± 0.10	0.65 ± 0.09	4.4	0.88 ± 0.12
SSA22-AzTEC 023	ASA 023 . 2	22:16:57.69	+00:24:51.68	0.64 ± 0.14	0.52 ± 0.11	4.3	0.54 ± 0.11
SSA22-AzTEC 031	ASA 031 . 1	22:17:28.49	+00:03:24.98	0.42 ± 0.09	0.25 ± 0.05	4.3	0.46 ± 0.09
SSA22-AzTEC 031	ASA 031 . 2	22:17:27.38	+00:03:17.82	0.41 ± 0.06	0.90 ± 0.14	4.2	1.39 ± 0.22
SSA22-AzTEC 032	ASA 032 . 1	22:18:05.03	+00:08:37.86	0.41 ± 0.08	0.28 ± 0.05	4.3	0.33 ± 0.06
SSA22-AzTEC 035	ASA 035 . 2	22:17:41.87	+00:10:42.04	0.42 ± 0.06	0.70 ± 0.09	4.3	0.77 ± 0.10
SSA22-AzTEC 040	ASA 040 . 2	22:17:03.33	+00:25:1.79	0.40 ± 0.08	0.30 ± 0.06	4.3	0.42 ± 0.09
SSA22-AzTEC 040	ASA 040 . 3	22:17:03.71	+00:24:50.32	0.40 ± 0.08	0.28 ± 0.06	4.2	0.34 ± 0.07
SSA22-AzTEC 049	ASA 049 . 2	22:17:06.61	+00:22:59.10	0.29 ± 0.04	0.20 ± 0.03	4.2	0.29 ± 0.04
SSA22-AzTEC 055	ASA 055 . 2	22:18:05.59	+00:11:40.53	0.40 ± 0.09	0.25 ± 0.06	4.3	0.27 ± 0.06
SSA22-AzTEC 055	ASA 055 . 3	22:18:05.32	+00:11:38.37	0.38 ± 0.08	0.25 ± 0.05	4.2	0.35 ± 0.07
SSA22-AzTEC 056	ASA 056 . 2	22:18:05.82	+00:10:29.85	0.30 ± 0.05	0.20 ± 0.04	4.2	0.35 ± 0.06
SSA22-AzTEC 062	ASA 062 . 3	22:17:28.67	+00:07:36.34	0.43 ± 0.07	0.27 ± 0.04	4.4	0.34 ± 0.06
SSA22-AzTEC 062	ASA 062 . 4	22:17:28.33	+00:07:37.48	0.40 ± 0.09	0.22 ± 0.05	4.1	0.65 ± 0.32
SSA22-AzTEC 083	ASA 083 . 2	22:16:56.46	+00:24:14.97	0.29 ± 0.06	0.38 ± 0.07	4.2	0.60 ± 0.12
SSA22-AzTEC 087	ASA 087 . 3	22:17:25.29	+00:20:28.58	0.28 ± 0.07	0.20 ± 0.05	4.2	0.25 ± 0.06
SSA22-AzTEC 115	ASA 115 . 2	22:17:05.80	+00:15:13.50	0.29 ± 0.07	0.16 ± 0.04	4.3	0.20 ± 0.05

Table 2.12 ALMA Supplementary Source Catalog (1/2)

AzTEC ID	ALMA ID	RA (J2000)	DEC (J2000)	$S_{\rm pk}$ (mJy / Beam)	$S_{\rm int}$ (mJy)	S/N$_{\rm pk}$	$S_{\rm BEST,pbcorr}$ (mJy)
SSA22-AzTEC 001	ASA 001 . 3	22:17:32.72	+00:17:33.31	0.73 ± 0.13	0.68 ± 0.12	4.6	1.42 ± 0.25
SSA22-AzTEC 002	ASA 002 . 4	22:17:42.40	+00:17:17.20	0.44 ± 0.06	0.23 ± 0.03	4.8	0.82 ± 0.13
SSA22-AzTEC 003	ASA 003 . 3	22:18:07.59	+00:06:21.57	0.33 ± 0.05	0.18 ± 0.03	4.8	0.68 ± 0.10
SSA22-AzTEC 007	ASA 007 . 5	22:17:09.27	+00:14:18.90	0.75 ± 0.14	0.40 ± 0.08	4.8	1.06 ± 0.20
SSA22-AzTEC 009	ASA 009 . 5	22:17:00.14	+00:10:28.47	0.72 ± 0.15	0.62 ± 0.13	4.8	1.61 ± 0.33
SSA22-AzTEC 018	ASA 018 . 1	22:17:41.29	+00:12:40.42	0.73 ± 0.14	0.86 ± 0.17	4.5	2.33 ± 0.47
SSA22-AzTEC 028	ASA 028 . 2	22:16:48.92	+00:22:48.98	0.46 ± 0.08	0.31 ± 0.06	4.9	1.39 ± 0.26
SSA22-AzTEC 030	ASA 030 . 2	22:17:45.98	+00:08:12.50	0.77 ± 0.08	0.47 ± 0.05	4.7	2.11 ± 0.23
SSA22-AzTEC 045	ASA 045 . 2	22:17:33.04	+00:29:11.89	0.45 ± 0.06	0.40 ± 0.05	4.7	1.77 ± 0.20
SSA22-AzTEC 045	ASA 045 . 3	22:17:32.12	+00:29:12.46	0.43 ± 0.07	0.46 ± 0.08	4.5	1.84 ± 0.30
SSA22-AzTEC 077	ASA 077 . 2	22:17:35.21	+00:15:51.48	0.33 ± 0.05	0.23 ± 0.03	4.8	0.63 ± 0.09
SSA22-AzTEC 087	ASA 087 . 4	22:17:24.99	+00:20:40.03	0.33 ± 0.04	0.34 ± 0.04	4.9	0.71 ± 0.09

Table 2.13 ALMA Supplementary Source Catalog (2/2)

2.3 The 870 μm Mapping with ALMA Band 7

2.3.1 Observations

In this field, one ALMA Cycle 0 project, # 2011.0.00725.S (PI. D. Alexander), was conducted and all products have been opened to all astronomers. They observed eight X-ray luminous AGNs and all of which have spec-z=3.09 with ALMA band 7. These data is also really useful for our study and we obtained these archive data from ALMA archive.

The observations were carried out on 2012 November 20 with 24 working 12 m antennas. The weather condition was excellent (PWV$\sim$0.4 mm), though the elevation condition was not ideal ($\sim$ 20–40 deg). The single continuum spectral mode with 7.5 GHz band width was utilized. The observed frequency was tuned to 345 GHz (870 μm), which comprises of four spectral windows (337–339, 339–341, 349–351, 351–353 GHz). Hence their frequency set-up is similar with that of ALESS survey of which central frequency is 344 GHz. The FoV is $17''.5$ (FWHM of ALMA's primary beam) and the center of the beam is adjusted to the known AGN positions. The longest baseline of the observations was 375 m, which is the extended configuration of ALMA cycle0, resulting in an angular resolution of $\sim 1''.0$. The integration time for each field is about five minutes. The flux calibrator was Neptune. The phase calibrator of J2225-049, which was also the bandpass calibrator, was observed before and after each track.

2.3.2 Data Reduction

The data of this ALMA cycle0 observations were reduced as well as the ALMA cycle1 data using CASA version 4.2.1. All eight field data were mapped using the CLEAN algorithm with natural weighting. The generated maps have 360 pixels per side and a pixel scale of $0''.11$. All maps were cleaned to around 3 σ depth over the whole fields. We show the final cleaned maps without primary beam correction in Figure 2.14 and summarize the information in Table 2.14.

2.3.3 Catalog

We performed source extraction and flux measurement in a same way described in the previous section. Here above 5σ sources are listed up. In addition, the AGN4 field is overlapped with AzTEC13 field in the 1.1 mm survey and we found that ASA 013.1 has a 4.6σ 870 μm counterpart just outside of the FoV. The results are shown in Table 2.15.

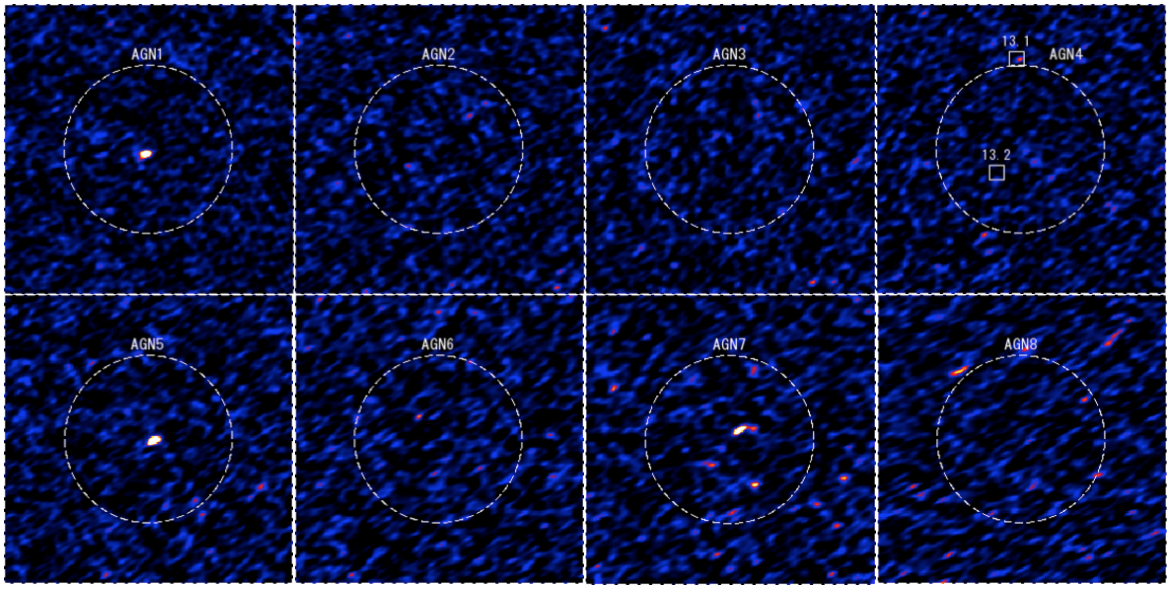

Fig. 2.14 ALMA 870 μm images for eight $z = 3.09$ AGN fields. The target ID named by Alexander et al. are shown within each panel. The dashed circles represent the FWHM of the primary beam. Each panel has a $30'' \times 30''$ size. The primary beam attenuation is not corrected in these images. We also shown the positions of ASA13.1 and ASA13.2, which are discovered by the 1.1 mm survey.

Target	Center Coordinates J2000	$\sigma_{\rm ALMA}$ (mJy/Beam)	ALMA Beam ($''$)	PA (deg)
AGN1	22:17:36.52 +00:16:23.0	0.205	1.00×0.68	-71.44
AGN2	22:17:39.05 +00:13:30.2	0.215	1.05×0.68	-70.81
AGN3	22:17:09.65 +00:18:00.8	0.234	1.01×0.63	-59.22
AGN4	22:17:20.25 +00:20:19.2	0.227	1.06×0.61	-60.42
AGN5	22:17:35.86 +00:15:59.2	0.233	1.13×0.61	-61.53
AGN6	22:17:59.2 +00:15:29.5	0.255	1.22×0.61	-62.65
AGN7	22:17:16.17 +00:17:45.9	0.266	1.34×0.62	-63.66
AGN8	22:17:32.01 +00:16:55.7	0.254	1.45×0.59	-64.77

Table 2.14 ALMA Observations of #2011.0.00725.S

Field	ALMA ID	RA (J2000)	DEC (J2000)	$S_{\rm pk}$ (mJy / Beam)	$S_{\rm int}$ (mJy)	S/N$_{\rm pk}$	$S_{\rm BEST,pbcorr}$ (mJy)	Other ID
AGN1	AS-AGN 001 . 1	22:17:36.55	+00:16:22.57	1.84 ± 0.14	2.52 ± 0.18	9.0	2.52 ± 0.18	1
AGN5	AS-AGN 005 . 1	22:17:35.83	+00:15:59.12	2.60 ± 0.13	3.08 ± 0.15	11.2	3.08 ± 0.15	2,3,4
AGN7	AS-AGN 007 . 1	22:17:16.10	+00:17:46.98	1.73 ± 0.20	2.38 ± 0.28	6.8	2.38 ± 0.28	5,6
AGN4	AS-AGN 004.1	22:17:20.26	+00:20:28.61	1.05 ± 0.20	0.63 ± 0.12	4.6	1.48 ± 0.26 $(2.44 \pm 0.44)^a$	7,8

Table 2.15 ALMA 870 μm Source Catalog ($\geq 5\sigma$).
a) primary beam corrected peak flux density.
1. SDSS J221736.54+001622.6 (QSO) (Evans et al. 2010)
2. SMMJ221735.84+001558.9 (Chapman et al. 2005)
3. CXO J221735.8+001559 (Evans et al. 2010)
4. LAB14 (Matsuda et al. 2005)
5. CXOSSA22 J221716.1+001745 (Lehmer et al. 2009b)
6. SSA22-AzTEC100 (Umehata et al. 2014)
7. ASA 013.1 (this work)
8. SSA22-AzTEC13 (Umehata et al. 2014)

Chapter 3

The Nature of SMGs: Submillimeter/Millimeter

3.1 Number Counts

Until today a number of deep and wide surveys at submm/mm wavelengths have generated the number counts, which are the number of sources per unit area as a function of flux density (e.g.,Coppin et al. 2006, Bertoldi et al. 2007,Weiß et al. 2009, Scott et al. 2010, Austermann et al. 2010, Vieira et al. 2010, Hatsukade et al. 2011, Scott et al. 2012). These submm/mm number counts represent basic properties of SMGs, which allows us to characterize the nature of this galaxy population and to give a constraint on galaxy formation theories. Some difficulties have, however, prevented us from constructing the accurate number counts.

The all previous works listed above were based on the surveys taken with single dish-telescopes such as LABOCA, MAMBO, AzTEC/ASTE or JCMT, and SPT, the angular resolution of which is quite coarse ($\sim$20-30$''$, FWHM). Hence the measurement including source counts must be affected by the source confusion limit (Condon, 1974). In the case of AzTEC/ASTE surveys, the faint population below $\sim$1mJy at 1.1 mm are undetectable due to this limit (Scott et al., 2010). In addition, the lough beam can increase the possibility that two or more submm sources locates within a beam, which produces 'artificial' bright sources and warps the intrinsic shape of the number counts.

In the last several years, some tried to conduct follow-up imaging surveys, targeting SMGs selected by single-dish surveys, using interferometers such as SMA and PdBI to obtain high-angular resolution maps (e.g., Barger et al. (2012), Smolčić et al. (2012)). But the number of sources identified by such pre-ALMA interferometers wasn't large. The limited

sensitivity of the telescopes also restrict our knowledge only for exceptional bright populations. Thus our understanding about the source counts of SMGs didn't change dramatically yet.

After the ALMA early science observations started, this academic disciplines have experienced great advance. Karim et al. (2013) reported the sophisticated results using ALMA. They obtained the 870 μm number counts for 88 ALMA fields with arcsecond-resolution as a product of the ALESS survey. In addition, Hatsukade et al. (2013) and Ono et al. (2014) assembled deep ALMA data at 1.2–1.3 mm and opened the way to derive the source counts of sub-mJy sources, which are thought to contribute the submm/mm extragalactic background light (EBL) mainly.

While the significant improvement has been achieved, we are, however, left with a number of uncertainties. Does the ALESS number counts actually stand for the common properties of SMGs? Aren't there any difference between 870 μm selected populations and 1.1 mm selected populations? How can we link the bright source counts and the faint counts? How accurate are the faint source counts obtained at this moments based on the small statistics?

To approach such questions, we present the first results of the 1.1 mm number counts with meaningful number of sources taken with ALMA in this section. Our observations achieved the high angular resolution ($> 2\times$ of the ALESS) and the high sensitivity (at most $> 3\times$ of the ALESS). Therefore we can discuss both of bright and faint end in a same field and at same wavelength firstly.

3.1.1 The ALMA 1.1 mm Number Counts

Here we only consider bright part ($\geq$ 1mJy), though we detected a number of fainter submm sources. Whilst our ALMA source catalog contain sources with a wide range of flux densities, $S_{263\mathrm{GHz}}$=0.2–6.4 mJy, we also need to the patchiness of the observing coverage and the heterogeneity of the sensitivities.

Effective Area

In the previous AzTEC/ASTE survey, we discovered 125 sources with $S/N \geq 3.5$ across the 950 arcmin^2. The ALMA survey was conducted for 45 AzTEC sources, all of which have been discovered within central 50% sensitivity area. As shown in Table 2.1, 107 out of 125 sources locates this area. We cannot find any way to divide this 107 sources into more specific groups since the 45 sources chosen for ALMA have various flux densities in the AzTEC map and it is revealed that AzTEC sources have multiple ALMA sources and

there is no strong correlation between the AzTEC-measured flux density and that of ALMA. Considering these conditions, we define the effective area simply as follows.

$$A_{\rm eff} = \frac{N_{\rm fields}({\rm ALMA})}{N_{\rm sources}({\rm AzTEC})} \times A_{\rm AzTEC} \tag{3.1}$$

Where $A_{\rm eff}$ is the effective this ALMA survey area, $N_{\rm fields}({\rm ALMA}) = 45$ is the number of observed ALMA fields, $N_{\rm sources}({\rm AzTEC}) = 107$ is the total number of submillimeter sources in the AzTEC/ASTE catalog, $A_{\rm AzTEC} = 749$ arcmin^2 is the area of the 50% sensitivity area.

The inevitable uncertainties

Though we consider above 1 mJy side of source counts here, the fainter part of this side ($\leq\sim$ 3 mJy) contain large uncertainties. One difficulty is from the incompleteness of the AzTEC/ASTE survey. In the 50 % area, the noise revel of the AzTEC map is $\sigma = 0.72 - 1.00$mJy beam^{-1} and the source detection limit is 3.5σ. After flux deboosting, we detected $>$1.9 mJy sources. Therefore our AzTEC sample is originally a incomplete sample in the fainter flux range ($\leq\sim$ 3 mJy) and we can overestimate the effective area, leading an underestimated source counts. The ALMA's sensitivity can also cause a problem. Among the three scheduling blocks, sb1 and sb2 are thought to have no problem for the $\geq$ 1mJy source counts since the 4.5σ sensitivity limit is below 1.0 mJy at the edge of the primary beam FWHM. For SB0, the 4.5σ sensitivity limit is, however, about 1.4 mJy at the edge, and therefore some $\sim$1 mJy sources might be missed. We should note about such issues in the later discussion.

Error Estimate

We calculate the errors as Poisson confidence limits of 84.13%, which correspond to 1σ for Gaussian statistics (Gehrels 1986) because the number of sources for each bin isn't large. The upper and lower limits for a given event number n are given by

$$\lambda_u = (n+1)\left[1 - \frac{1}{9(n+1)} + \frac{1}{3\sqrt{n+1}}\right]^3 \tag{3.2}$$

$$\lambda_l = n\left(1 - \frac{1}{9n} - \frac{1}{3\sqrt{n}}\right)^3 \tag{3.3}$$

Results

We calculate the source counts considering both of main and supplementary catalogs. (There is nine source from the supplementary catalogs) The results are summarized in Table 3.1

Flux density (mJy)	dN/dS (mJy^{-1} deg^{-2})	Flux density (mJy)	N(>S) (deg^{-2}
1.5	$308.57^{+71.50}_{-58.98}$	1.0	$651.43^{+98.19}_{-86.00}$
2.5	$262.86^{+66.99}_{-54.37}$	2.0	$342.86^{+74.68}_{-62.21}$
3.5	$45.71^{+36.05}_{-21.82}$	3.0	$80.00^{+43.01}_{-29.45}$
4.5	$22.86^{+30.03}_{-14.72}$	4.0	$34.29^{+33.24}_{-18.60}$
5.5	$0.00^{+0.00}_{-0.00}$	5.0	$11.43^{+26.14}_{-9.47}$
6.5	$11.43^{+26.14}_{-9.47}$	6.0	$11.43^{+26.14}_{-9.47}$

Table 3.1 263 GHz (1.14 mm) number counts derived from our ALMA survey. The first two columns stand for the center flux for each bin and corresponding differential number counts. The last two columns show the minimum flux for each bin and cumulative number counts. The errors are the 1σ uncertainties calculated from Poisson confidence limits.

Figure 3.1 and 3.1 stand for differential number counts and cumulative number counts, respectively. We compare the obtained number counts with two previous results. One is the total AzTEC/ASTE 1.1mm number counts combining six blank fields to investigate the relation between the single dish survey and the ALMA survey directly. The covered area reaches 1.6 deg^2 in total (Scott et al. 2012). The other is the ALESS 870 μm number counts, which is useful to examine the cosmic variance and the disparity in wavelengths. The model counts arising from a semi-analytical/hydrodynamic approach by Hayward et al. (2013) are also shown. So as to compensate the difference in observing wavelengths, we scale these counts assuming a modified blackbody with representative values. We adopt spectral index of β=1.5, dust temperature of 35 K (e.g., Coppin et al. 2008), and redshift of 2.5 (e.g., Chapman et al. 2005). The derived scaling factors are $S_{263GHz(1.14\mathrm{mm})}/S_{1.1\mathrm{mm}} = 0.93$ and $S_{263GHz(1.14\mathrm{mm})}/S_{870\mu\mathrm{m}} = 0.50$.

3.1.2 Discussion

The deficit of the bright end

It is argued that there is a clear break at the bright end in the ALMA number counts (Karim et al. 2013). Whilst they observed 12 sources with $S_{870\mu\mathrm{m}}$ >9 mJy, no ALMA source have the flux density of > 9 mJy (According to Hodge et al. (2013), the brightest one has just 9 mJy). As a result, they recognized a abysmal decrease at the bright end of their number count and suspected that the absence of the brightest population ($S_{870\mu\mathrm{m}}$ >9 mJy) is ubiquitous and a natural limit to the star formation rate (SFR) in an SMG of $\leq 1000\mathrm{M}_\odot$ yr^{-1} can exist. If their argument is real, galaxy formation models are forced to modify so as to reproduce the cliff, suppressing the most active and massive dusty starbursts.

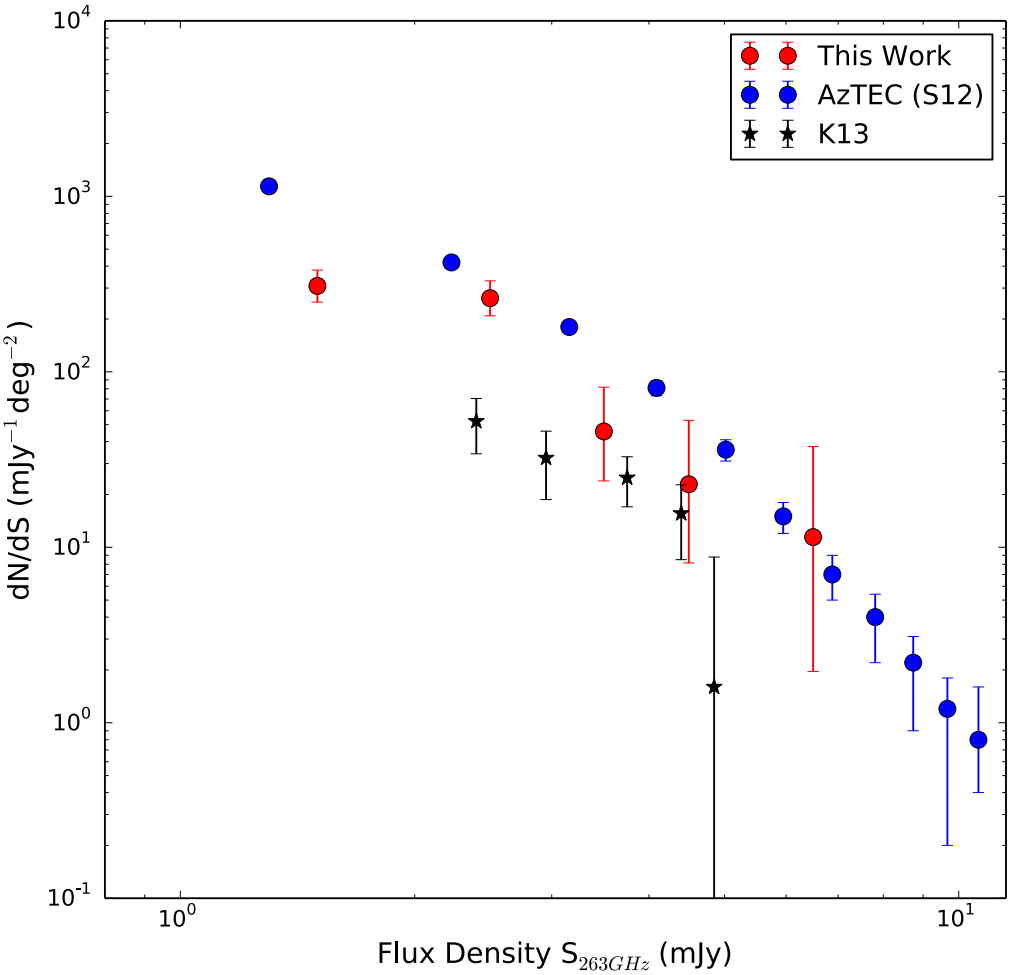

Fig. 3.1 Bright side of differential number counts of our ALMA observations ($S_{263GHz} \geq$1.0 mJy). For comparison, we also show the counts of ALESS survey (Karim et al. 2013) and those of AzTEC survey (Scott et al. 2012).

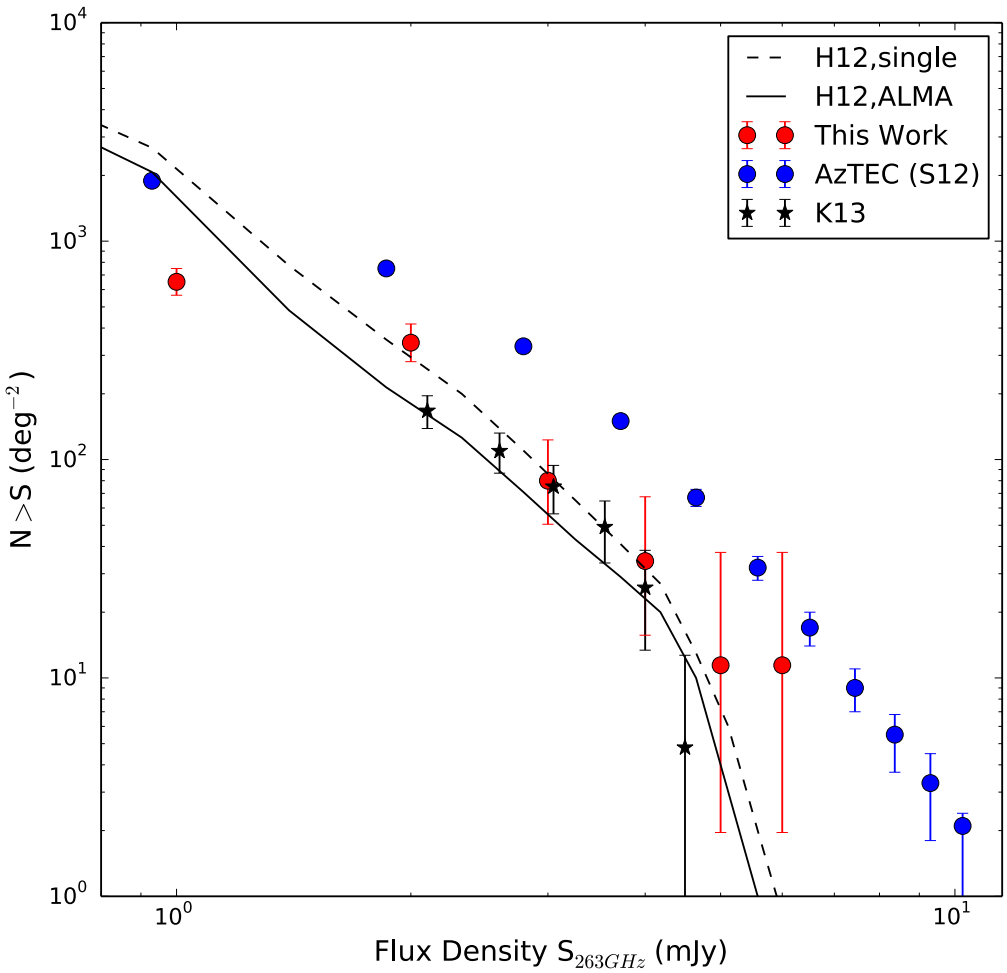

Fig. 3.2 Bright side of differential number counts of our ALMA observations ($S_{263GHz} \geq$1.0 mJy). In addition to the ALESS counts and the AzTEC counts, the model prediction by Hayward et al. (2013) is also shown.

Our survey provides us with the first opportunity to verify this critical issue. And our results indicate somewhat different characteristics. First the trend that most of the brightest populations comprise multiple sources is similar in this 1.1 mm survey. Though six $S_{1.1\mathrm{mm}} >$ 6 mJy sources in the AzTEC catalog were observed by ALMA, just one ALMA source (ASA 1.1) have flux density of >6 mJy. And flux density of AzTEC1 is 11.3 mJy and therefore the brightest source is also affected by the effect of the multiplicity. On the other hand, the brightest one in our survey is more luminous than that of ALESS survey after flux scaling as shown in Figure 3.1, though the source with $S_{1.1\mathrm{mm}} > 7$ mJy is still absent. The number counts of our survey suggest that the counts can decrease more moderately at the bright end compared to the "clear" drop reported by Karim et al. (2013). Our results imply that the bright end of the number count in the ECDF-S might not represent a general picture.

It is sure that we need larger samples to obtain well-restricted statistics. A SMG survey to observe 333 AzTEC sources in the AKARI Deep filed, SSA22, and SXDF is approved in ALMA Cycle2 (PI. Hatsukade) and this survey should make the situation clear.

Comparison with model prediction

There is no model counts that reproduce both of single-dish and ALMA number counts. Hayward et al. (2013) reproduced the AzTEC number counts and predicted the ALMA source counts. But the pipeline to analyze the AzTEC/ASTE data was updated (Downes et al. 2012), which makes their counts underestimated. Though their prediction for the ALMA survey is generally consistent with the ALESS survey and our survey as shown in Figure 3.2, the offset between the single-dish counts and the ALMA counts is not consistent with observations. Shimizu et al. (2012) presented source counts which is well-fitted to the AzTEC source counts (Scott et al. 2012), but our survey reveals that such counts are overestimated. Our results therefore might be a trigger to sophisticate the model predictions.

The possible excess in intermediate flux range

As shown in Figure 3.1, the differential number counts of our survey show significant excess ($\sim 5\times$) at $S_{263GHz} \sim 2.5$ mJy compared to the ALESS counts, though both surveys might be suffered from the effect of incompleteness. One explanation is that the SMGs associated with the $z = 3.1$ large-scale structure contribute this excess. We will discuss more in the later chapter. Another possibility is that the ALMA counts have universally steeper profile compared to the AzTEC counts. Although our field is a protocluster field, Hatsukade et al. (2011) reported that the AzTEC count in the SSA22 is generally agree with that of blank fields. The absence of the single extremely bright source implies that these multiple com-

ponents can increase the number of fainter sources compared to the single dish counts. The upcoming large survey is expected to resolve this problem.

3.2 Accuracy of Multi-wavelength Identification

3.2.1 Counterpart Identification Methods

Metheology

The majority of SMGs discovered by a single survey have been forced to have a trouble in pinpointing the accurate position due to the lough angular resolution. Traditionally radio and mid-infrared data have been utilized to suspect the coordinates of SMGs accurately and to derive their nature (e.g., Ivison et al. 2007, Wardlow et al. 2011, Biggs et al. 2011,Yun et al. 2012, Michałowski et al. 2012).

As well as these previous works, we also conducted a counterpart identification survey in Umehata et al. (2014). We utilized VLA 1.4 GHz, MIPS 24 μm, and IRAC 3.6, 4.5, 5.8, and 8.0 μm imaging data. These wavelength data, which are expected to select SMGs effectively, have better angular resolution than the AzTEC/ASTE survey. The VLA 1.4 GHz map have the best angular resolution among them ($\theta_{\rm FWHM} \sim 3''$) and the tight far-infrared – radio correlation of star-forming galaxies (Condon 1992) supports the validity. Though the MIPS μm data is slightly less-useful in terms of the angular resolution ($\theta_{\rm FWHM} \sim 6''$), the resolution is significantly better than that of the AzTEC/ASTE map. Yun et al. (2008) developed an identification method using the IRAC data. They found that SMGs usually have a characteristic IRAC color in the ([5.8μm]/[3.6μm] vs [8.0μm/4.5μm]) diagram based on a small subset of SMGs observed by SMA. The IRAC observations achieve $\theta_{\rm FWHM} \sim 2'' - 4''$ corresponding to channels. Sources which lie within a 2σ positional uncertainty, i.e., within a radius R_S from an AzTEC/ASTE centroid position were extracted for each data set. R_Ss were calculated as functions of S/Ns through Monte Carlo simulations (more details about this process are described in the supplementary information of Tamura et al. 2009 and Hatsukade et al. 2011). Then we calculated the corrected Poisson probability ("p-value", hereafter p), the probability of chance association, for all selected candidates. We classified the sources with $p \leq 0.05$ as robust counterparts. In addition, we have listed also tentative sources ($0.05 < p \leq 0.20$). These criteria is similar with other works.

Radio Data

The region centered on the coordinate (RA, Dec)$_{J2000}$ =(22h17m48.0s, +00°17′13″) was observed for a total of 48 hours at 1.4 GHz using the National Radio Astronomy Observatory's (NRAO's) Very Large Array (VLA) in its A and B configurations (Chapman et al. 2004). Our imaging applied a 50 kλ Gaussian taper to reduce the band width smearing. This produced a well-behaved synthesized beam of $3.0'' \times 2.9''$ at a position angle of -80 deg. Generally, a root-mean-square (r.m.s.) noise level of ~ 8.5 μJy/beam was achieved near the phase center and ~ 20 μJy at $15'$ from the phase center. Unfortunately, the radio map was partly contaminated by remarkable side lobes, which were generated by nearby radio-loud sources. Therefore, to avoid misidentification when cataloguing the radio sources we eliminated areas with a local noise level of ≥ 20 μJy/beam in cataloging radio sources. The local noise was estimated using the *AIPS* task, RMSD, in a 100 $\times$100 pixel region centered on each pixel. To generate a source catalog and to measure source properties, we used the task of SAD. Finally 40 radio sources were detected with S/N of ≥ 4 for 66 SMGs.

MIPS Data

We obtained MIPS ch1 (24 μm) images from the *Spitzer* Science Center (SSC) web site. As shown in Figure. 2.1, the area observed with MIPS corresponds to about a half of the area of AzTEC/ASTE. The FWHM of the PSF was $6''$. We extracted sources with S/N ≥ 5 and measured the flux densities using the APEX module within the MOPEX software package ver. 18.4.9 (Makovoz & Marleau 2005) through point-response-function (PRF) fitting. The 5σ limit magnitude is 18.3 mag$_{AB}$ (Hainline et al. 2009). We also utilized the archival IRAC data. For these, we address the nature and analysis in section 4.1.

Results

As a result, we found at least one robust counterpart for 19 AzTEC SMGs. It is also found that additional 40 AzTEC SMGs have only tentative counterparts.

3.2.2 ALMA's Answer

The large interferometric survey taken with ALMA provide us with a new position. Now that we have the intrinsic 'answer' of the previous speculation for the 45 AzTEC sources. Here we consider 58 main ALMA sources which lie in ALMA FoV. We find that 15 have robust counterparts considering all methods, VLA, MIPS, and IRAC. Additionally 13 have tentative counterparts. The remaining 32 sources weren't referred in Umehata et al. (2014).

Considering both of robust and tentative identification, around 45 % of ALMA sources were therefore predicted by the conventional scheme. The result of each classification is summarized in Table 2.9 – 2.11. On the other hand, we cannot find any previously identified objects among all 44 ALMA sources. This may be not a surprising result since the majority of these supplemental sources have flux density of $<$1 mJy and therefore they are not necessarily the classical SMGs on which the identification methods focus.

In Figure 3.3 we show the relationship between the distribution of flux density and the fraction of robust/tentative counterparts. It is salient that brighter ALMA sources tend to have identified counterparts with high probability. If we only consider ALMA sources with $\geq$ 2 mJy, 19/27 (70%) have robust/tentative counterparts. The fraction reaches 12/14 (86%) for $\geq$ 2.5 mJy sources. Thus the conventional method is valid especially for such bright sources.

The high angular resolution of ALMA maps manifest the necessity to take the probability of source blending into account in identifying submm/mm sources as some previous works suggested (e.g., Smolčić et al. 2012). For instance, ASA 9.1 and ASA 9.2 had been recognized one bright radio source. ALMA revealed that there are two SMGs, which might be to interact. We also have a trouble to distinguish ASA 14.1 and 14.2 in IRAC bands. We should note that the above statistics contain such cases.

Hodge et al. (2013) indicate that the S/N-dependent search radius is not always useful since the brighter sources selected by single dish surveys have well-restricted the radius but some bright (sometimes the most bright in a field) sources lie outside it. In our survey, the search radius considering the S/N in the AzTEC map seems to be generally effective. It is found that the majority of ALMA sources reside within the error circles. For example, six fields of AzTEC1 – AzTEC7 have relatively small search radius due to high S/N ($>$ 8) in the AzTEC map but at least the brightest source lie within the error circle. Whereas the situation is slightly different for secondary sources. The small searching area correspond to the high S/N leads us to miss some ALMA sources like ASA 5.2. Thus it is sure that we should be careful for the outside region in identifying SMG counterpart in radio/infrared images.

The depth of the radio and MIPS/IRAC observations can be a critical factor to determine the success rate of the identification. Barger et al. (2012) reported that all 16 SMGs identified by SMA in a SCUBA selected sample, have radio counterparts utilizing the ultra deep ($1\sigma = 2.5$ μJy) 1.4 GHz image obtained by JVLA. They found that 10 out of 16 these SMGs have the relatively low radio flux density ($S_{1.4\mathrm{GHz}} < 40$ μJy), which is undetectable in our VLA 1.4 GHz map. Therefore surely we missed a number of faint radio counterparts. Indeed, ASA 15.1 and ASA 15.2 have faint radio sources (Figure 3.5) just below the detec-

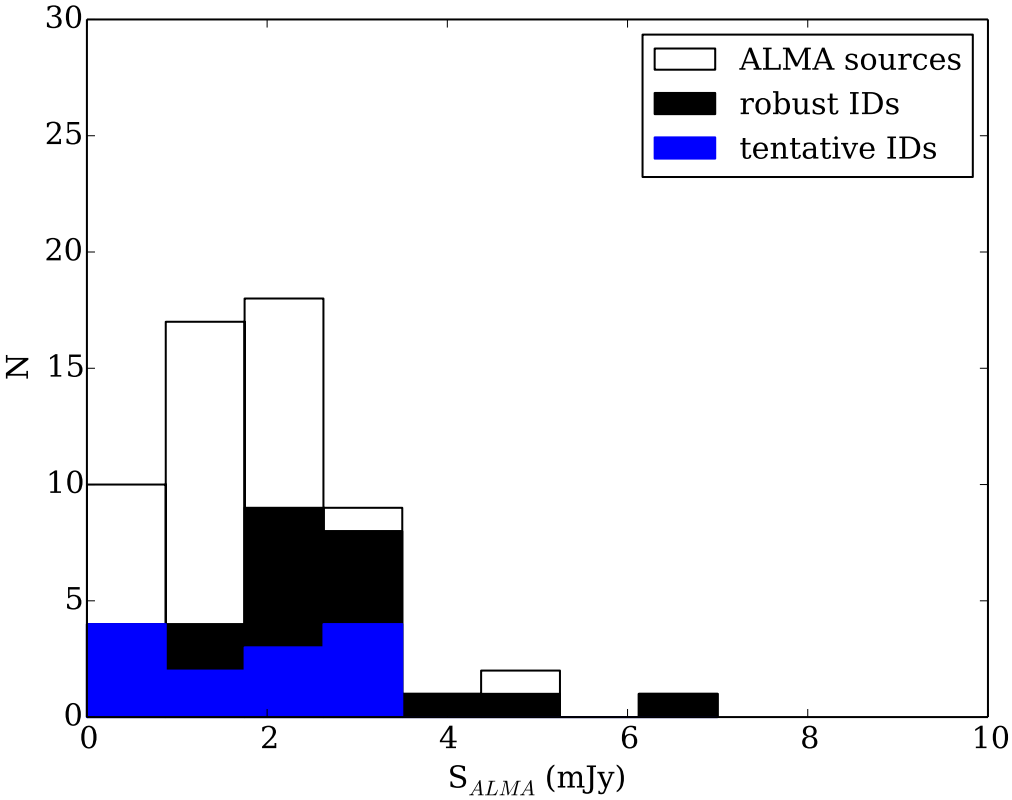

Fig. 3.3 Histogram of ALMA flux densities in the unit of mJy. Here only sources in the MAIN catalog are reflected. In addition to the $\geq 4.5\sigma$ ALMA sources, the sources identified in Umehata et al. (2014) among them are also shown. The large number of ALMA sources with $\geq$3 mJy were identified in our previous work.

tion limit (4σ). And undoubtedly we also face a same difficulty in utilizing IRAC images. Though sources aren't identified as counterparts unless they are detected in all four IRAC bands, the IRAC observations in the SSA22 field are slightly shallow especially in the case of ch3 and ch4 (see chapter 4).

The ALMA survey also reveals the percentage of the correct answer in the robust/tentative catalog reported in Umehata et al. (2014). In the previous work, we proposed 54 counterparts totally. Among them 27 has been detected in ALMA maps, which means total accuracy is 50 %. In calculating a breakdown of the accuracy, the most reliable way is to utilize the radio data. Eleven out of 14 robust/tentative counterparts are ALMA sources (79%), which is in agreement with the formally predicted fraction. Meanwhile MIPS 24 μm data is likely to be the most useless one for the purpose. Although we listed up 27 candidates for both of robust and tentative identification, only 9 (33 %) are verified by ALMA. One promising reason is that MIPS sources traces relatively low-z dusty sources compared to 1 mm selected SMGs. In the case of IRAC identification, 14 out of 29 (52%) proposed sources are confirmed. This might be also not surprising because the IRAC criteria should contain not only SMGs but also various populations.

To summarize, the combination of our ALMA survey and previous identification reveals a completeness of about 45 % and a reliability of 50 %. These results strongly suggest that the interferometric follow up observation is essential to identify the accurate position of SMGs. ALMA is almost only the way to pinpoint a lot of SMGs at the moment.

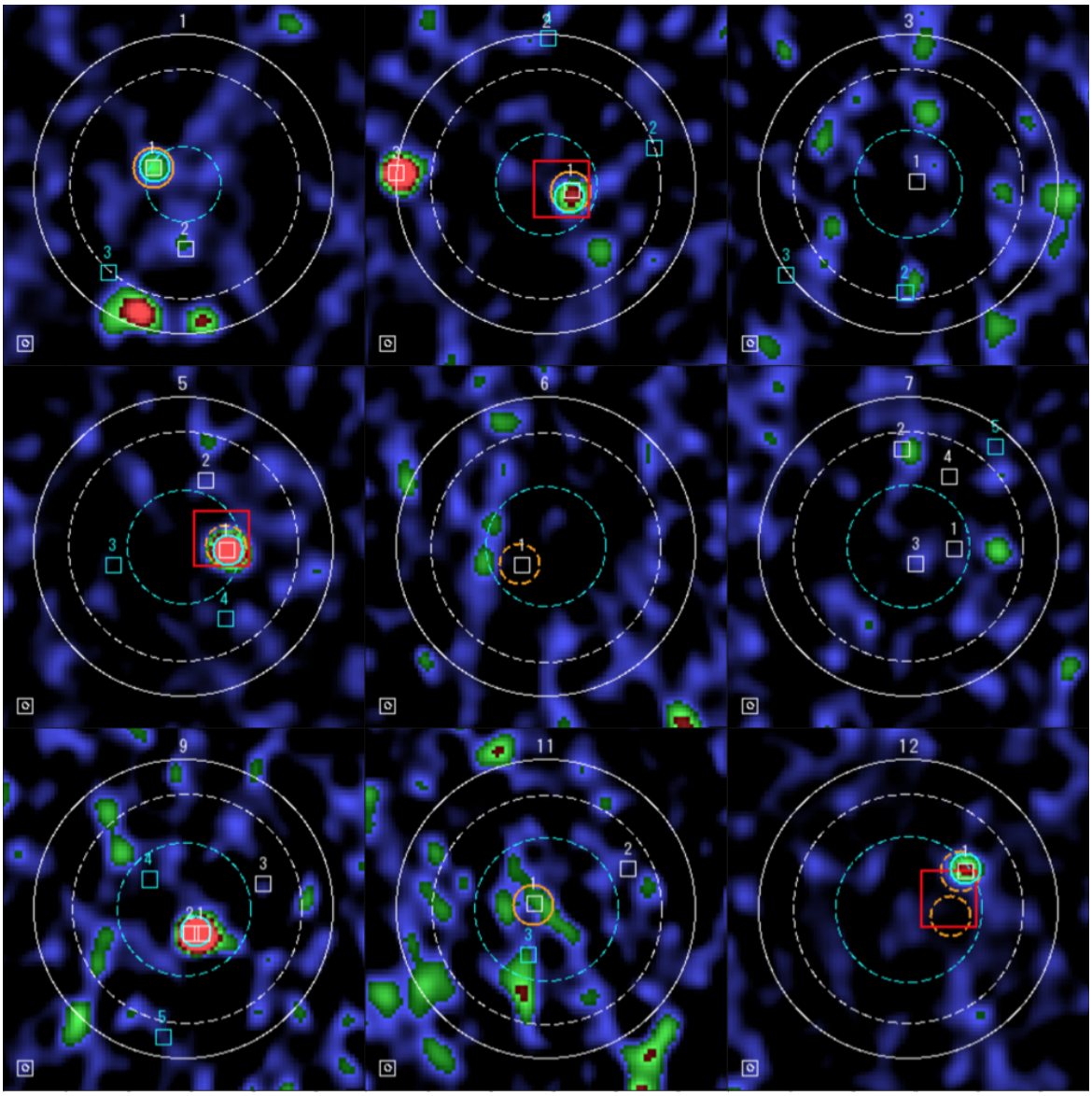

Fig. 3.4 The VLA 1.4 GHz map in positions of ALMA fields. The ALMA sources are shown in a same way displayed in Figure A.7– A.11. Radio, MIPS, IRAC counterparts identified in Umehata et al. (2014) are plotted using cyan circles, red squares, orange circles. Robust and tentative candidates are shown with solid and dashed lines, respectively. The size of each markers correspond to the angular resolution of each original maps. Big cyan dashed circles stand for the 2σ error circles derived in Umehata et al. (2014). We also show the AzTEC/ASTE beam ($30''$) and the ALMA's primary beam (FWHM, $22.9''$) with white solid circles and dashed circles.

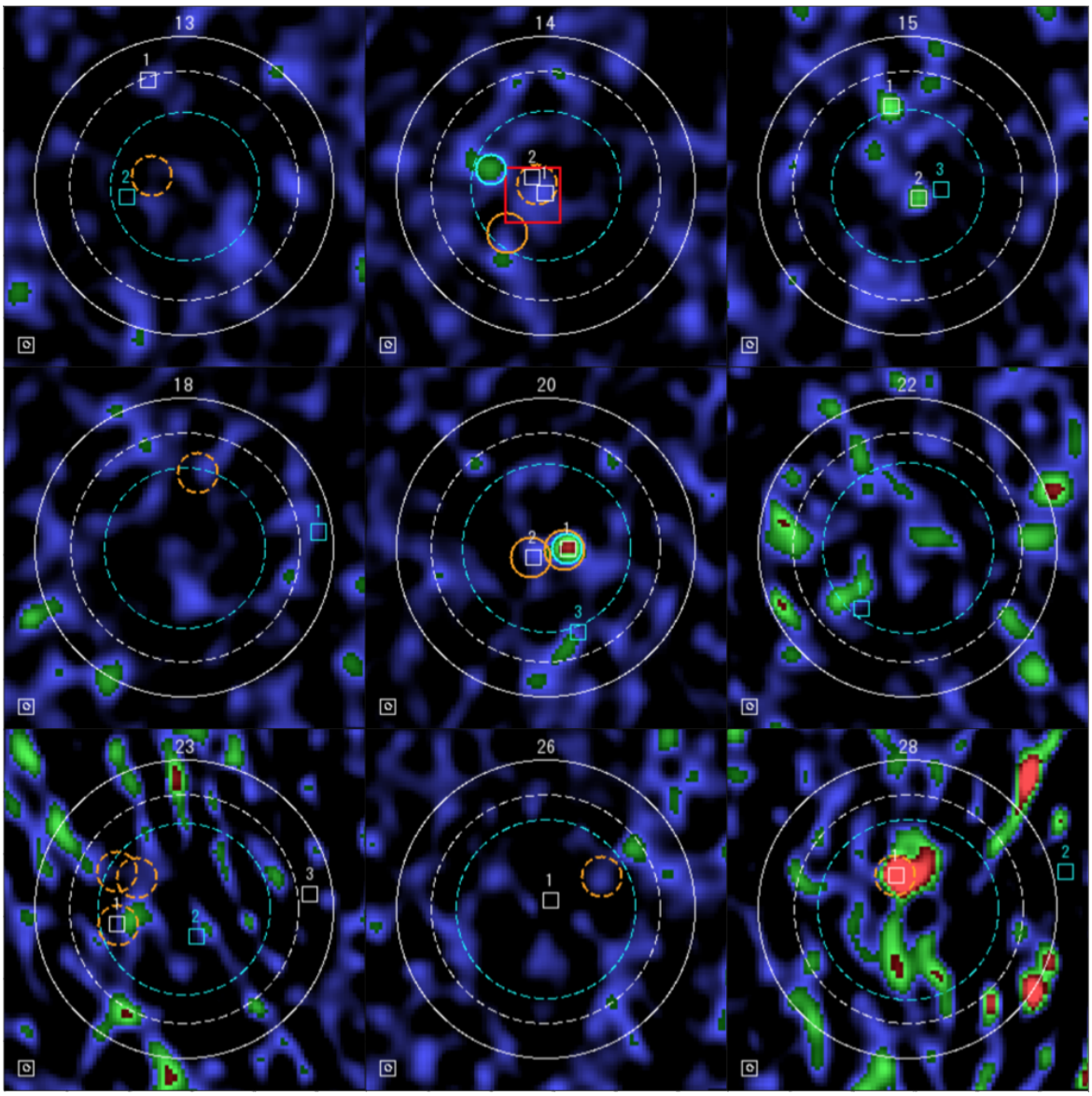

Fig. 3.5 VLA 1.4 GHz images in order of AzTEC ID (AzTEC13–AzTEC28).

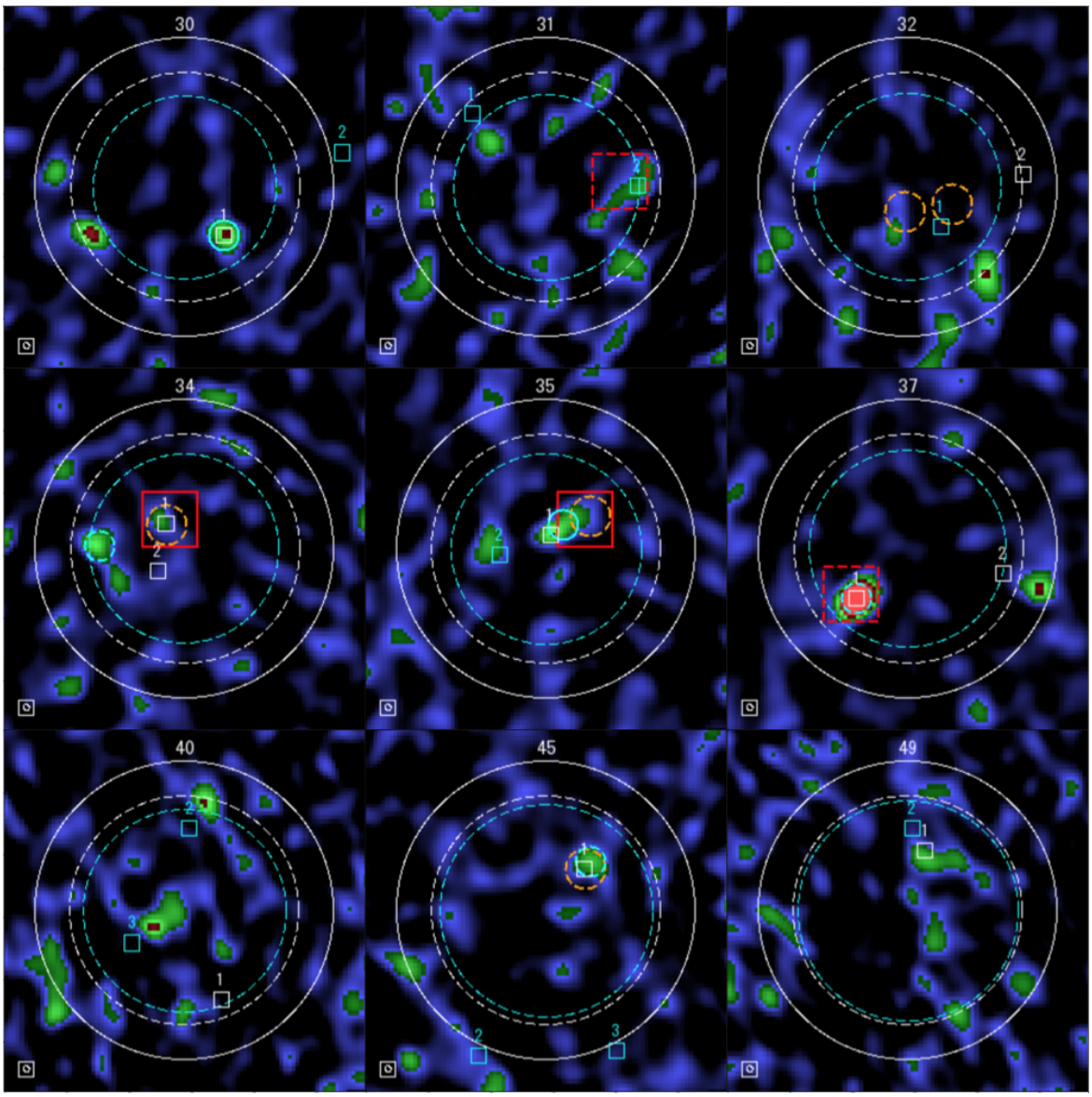

Fig. 3.6 VLA 1.4 GHz images in order of AzTEC ID (AzTEC30–AzTEC49).

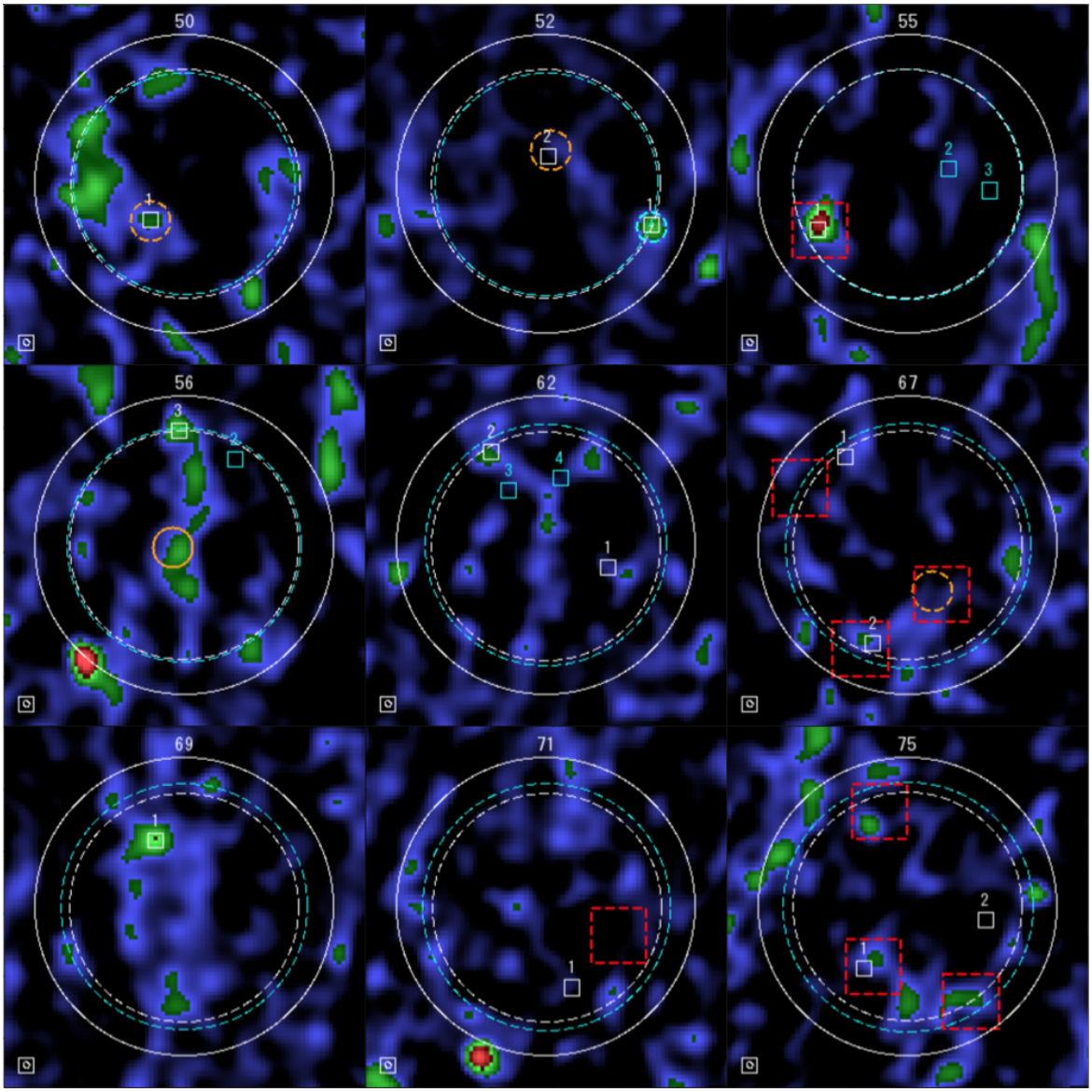

Fig. 3.7 VLA 1.4 GHz images in order of AzTEC ID (AzTEC50–AzTEC75).

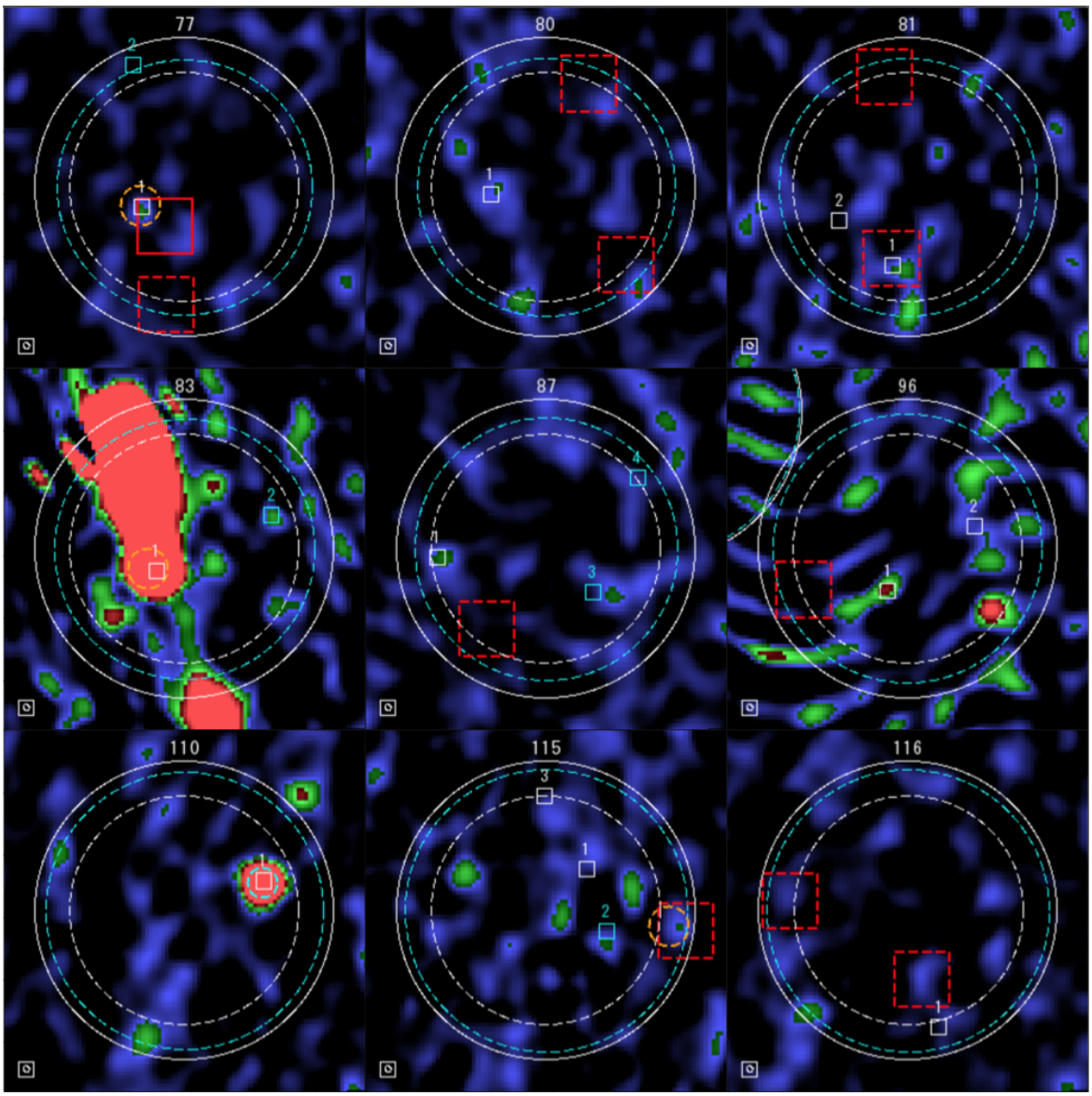

Fig. 3.8 VLA 1.4 GHz images in order of AzTEC ID (AzTEC77–AzTEC116).

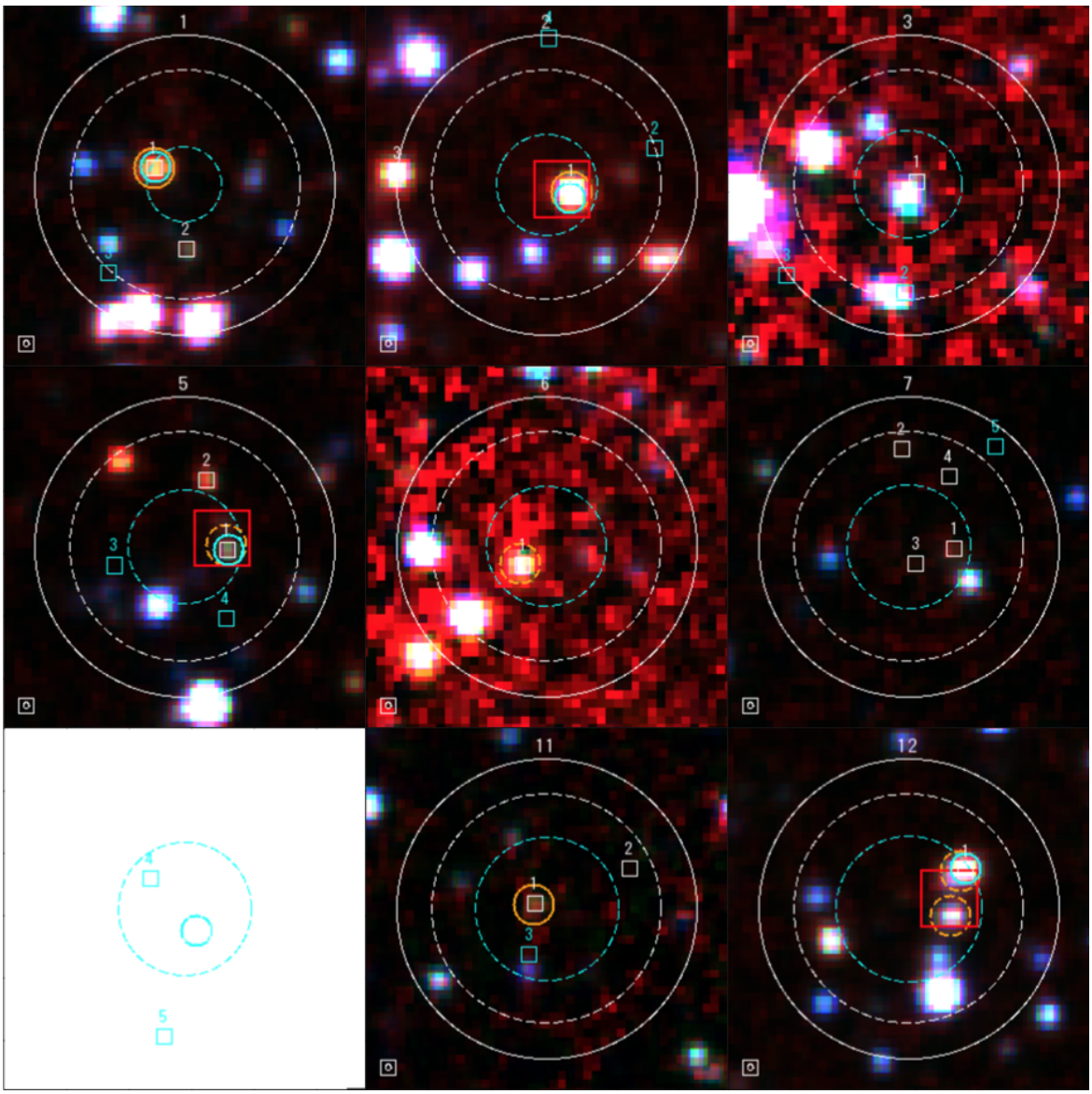

Fig. 3.9 IRAC false color image, produced using the 3.6 μm (blue), 4.5 μm (green), and 5.8 μm (red) band images, for each ALMA field. All marks are same as Figure 3.4 – 3.8.

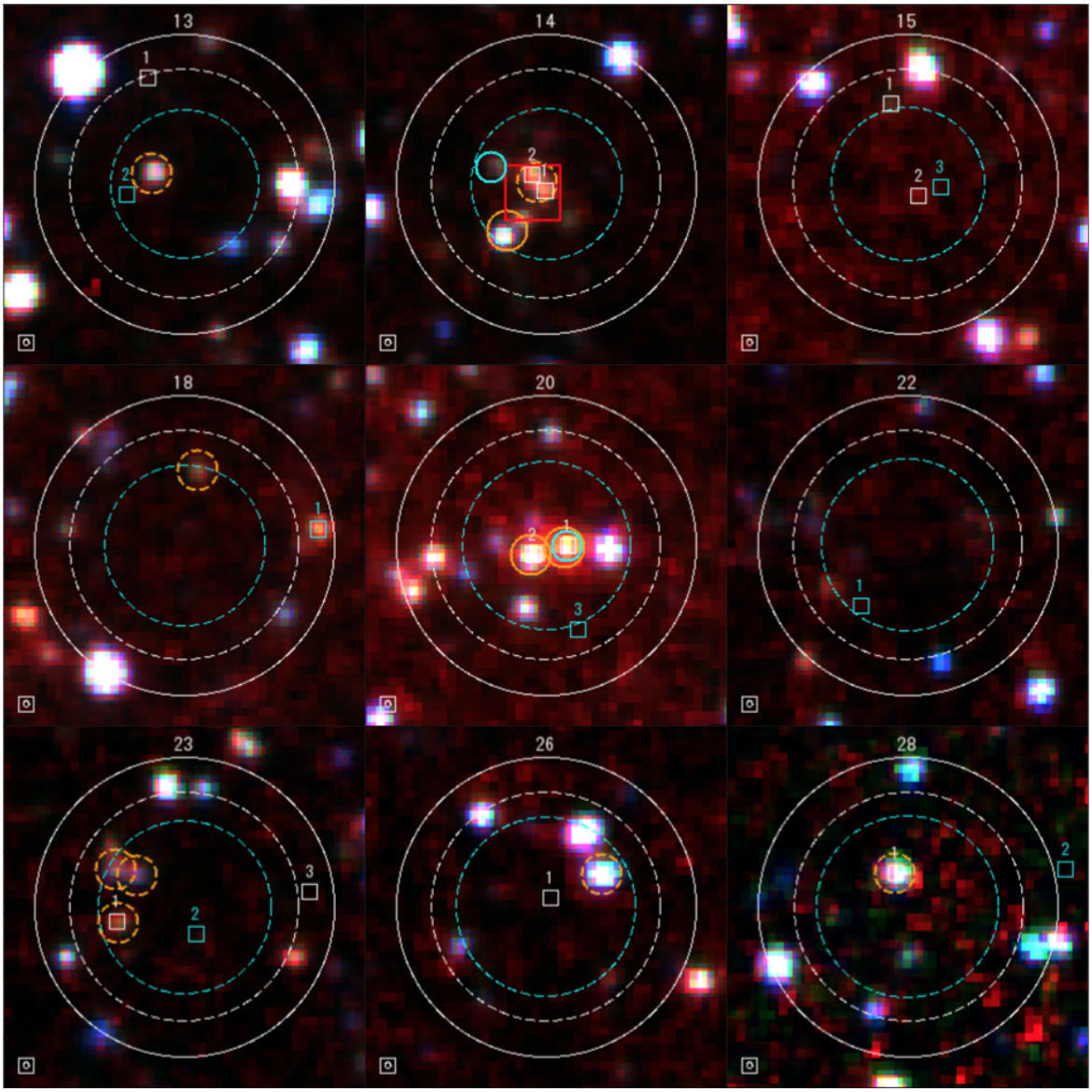

Fig. 3.10 IRAC color images in order of AzTEC ID (AzTEC13–AzTEC28).

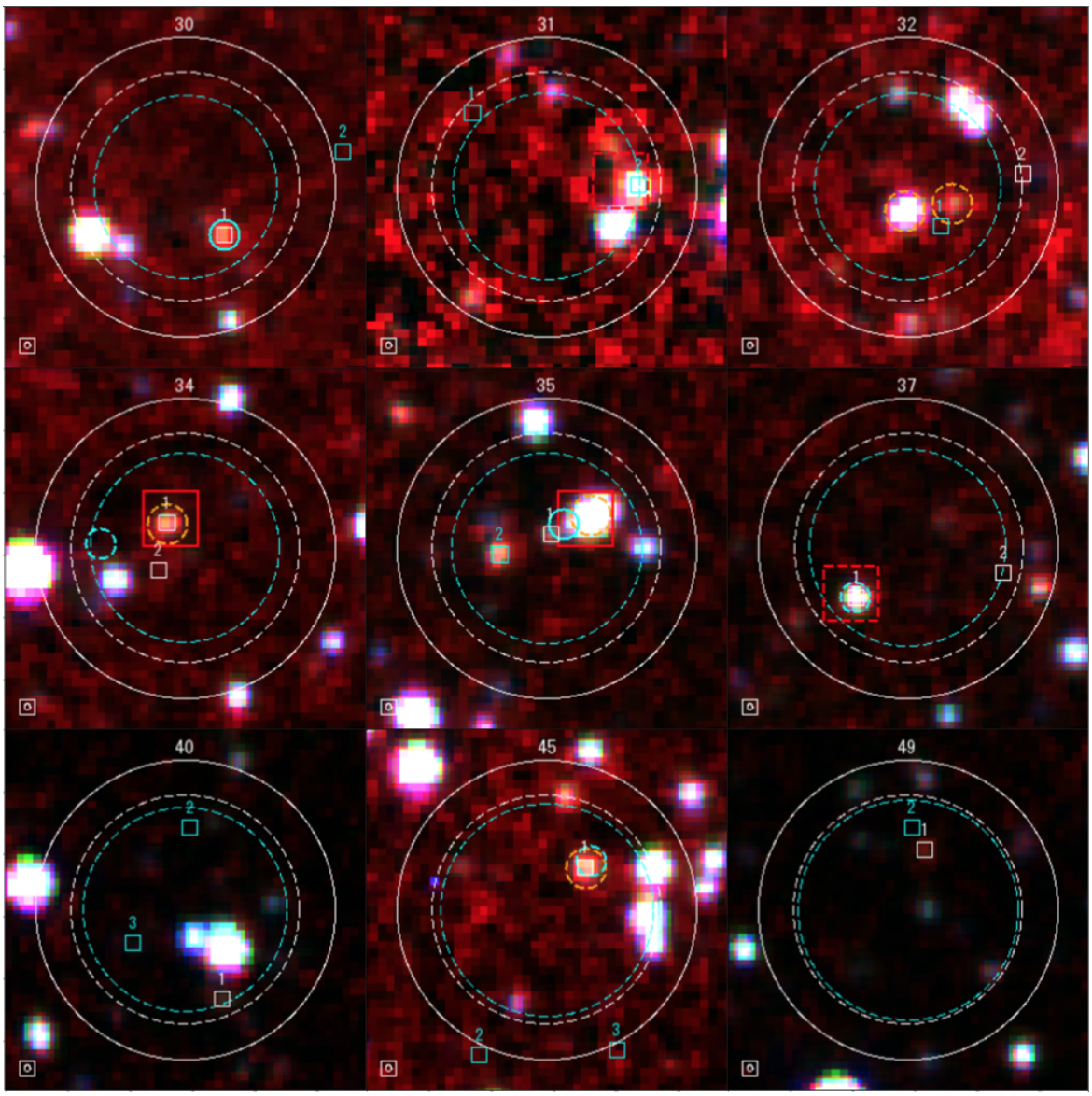

Fig. 3.11 IRAC color images in order of AzTEC ID (AzTEC30–AzTEC49).

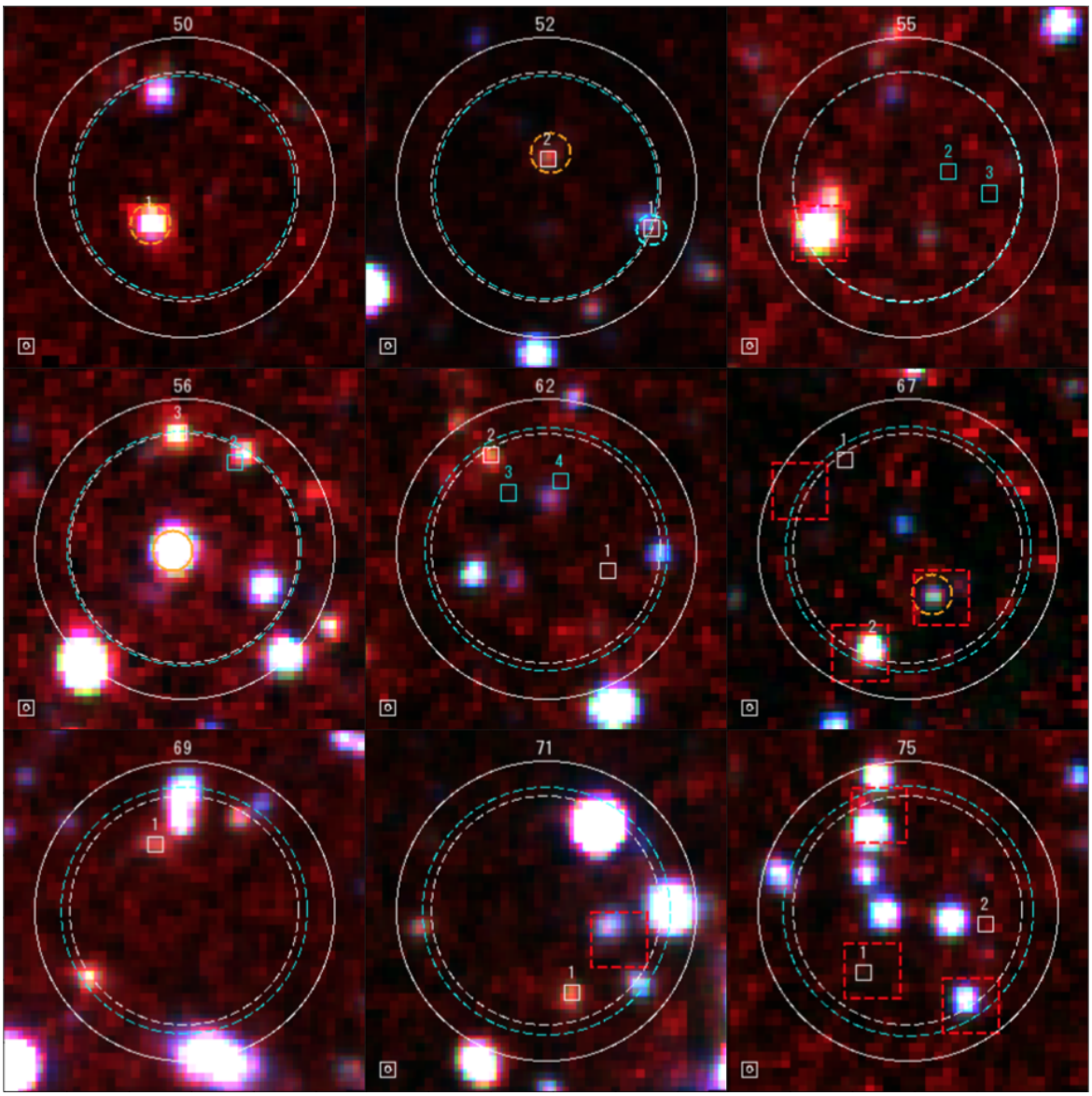

Fig. 3.12 IRAC color images in order of AzTEC ID (AzTEC50–AzTEC75).

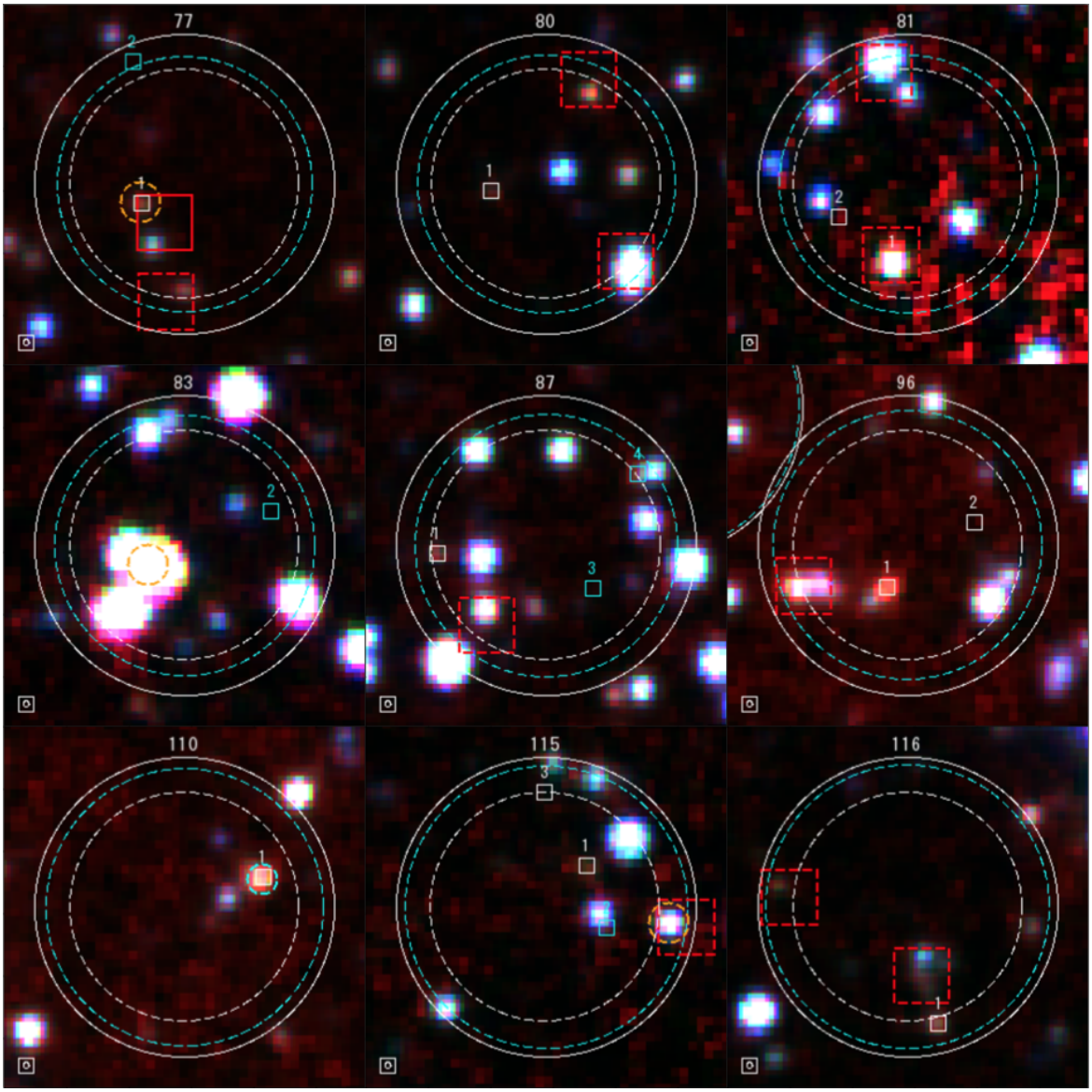

Fig. 3.13 IRAC color images in order of AzTEC ID (AzTEC77–AzTEC116).

Chapter 4

The Nature of SMGs: Optical to Near-IR

4.1 Photometric Redshift

The redshift information is one of the most crucial parameter in characterizing the SMG populations. We, however, are left with large uncertainties about it.

Chapman et al. (2005) pave the way to derive the redshift distribution of SMGs spectroscopically. They obtained the result that this dusty populations peaks at the redshift of 2–2.5, which is consistent with the peak of black hole accretion and star formation rate density derived from the rest-flame UV to optical observations (e.g., Madau & Dickinson 2014). However they relied on radio counterparts seriously, which are not only highly biased samples but expected to contain a number of contaminants (i.e., not real SMG counterpart). Smolčić et al. (2012) assembled 50 interferometric images at $< 2''$ taken with PdBI and SMA and estimated the mean photometric redshift of 2.6±0.4 and 3.1±0.4 for 870 μm selected SMGs and 1.1 mm selected SMGs, respectively. Though their work provided a large number of photometric redshifts based on SMGs identified interferometrically for the first time, their targets are biased to bright populations ($S_{1.1\mathrm{mm}} >\sim 4$ mJy). And their achieved angular resolution had been relatively rough yet, which might cause problems in identifying optical to near-infrared counterparts and deriving photometric redshifts for some cases.

ALMA has been enabled us to make impressive progress in some ways. Weiß et al. (2013) conducted a blind spectroscopic redshift survey for extremely bright SPT sources selected in 1.4 mm and 2.0 mm, almost all of which are considered to be magnified by the gravitational lensing effect. They present that mean redshift of 3.5, which strongly argues that the previous redshift distributions for radio-bright SMGs don't stand for the representative nature of SMGs. But the SPT-ALMA survey have a problem in deriving optical to near-infrared properties because of the shortage of such observations with enough sensitivity. Simpson et al. (2014b) performed photometric redshift search for the 96 ALESS SMGs

utilizing optical to near-infrared data. Their survey reduced the uncertainties in counterpart identification dramatically and provided the largest sample of photometric redshifts of ALMA-identified SMGs. The median redshift derived by their work is 2.5±0.2, which is consistent with suggestions from Chapman et al. (2005) and Smolčić et al. (2012).

Our ALMA survey at 1.1 mm have kept the uniqueness yet, in terms of the observed wavelength, angular resolution, and the number of sources. The SSA22 ALMA survey provides us with 64 ALMA sources without supplementary sources, which is the largest sample of 1.1 mm selected SMGs at this moment. Previous works indicate that the 870 μm-, 1.1 mm-, and 1.4 mm- selected SMGs have different redshift distributions. Our survey can be a key to examine this issue. Our achieved angular resolution is really good ($\sim 0.6''$) and it is expected to distinguish the real counterparts and the apparently conjunct sources.

In this section, we report the estimate of photometric redshifts based on optical to near-infrared photometries and discuss the results, comparing the previous works especially obtained by ALMA. Unless especially stated, errors are estimated as a 95% confidence interval from a bootstrap analysis.

4.1.1 Data Preparation

Optical to Near-infrared Data

The SSA22 filed have rich optical to near-infrared imaging data, the majority of which had been taken with Subaru Telescope. Deep optical imaging with Suprime-Cam (Miyazaki et al. 2002) using five broad band filters (*B, V, R, i', and z'*) were obtained by Hayashino et al. (2004). The series of Suprime-Cam images have the area of $27' \times 34'$ and contain all of the ALMA fields in 1.1 mm and 870 μm as shown in Figure 2.1. Additionally we have obtained archival CFHT/MegaCam U band data (P.I. L.Cowie) similarly over the entire ALMA field. Subaru also provide us with deep near-infrared imaging data for a portion of the ALMA sources. There are J, H, and Ks band images taken with MOIRCS (Suzuki et al. 2008), which covers the central part of the SSA22 fields displayed in Figure 2.1(Uchimoto et al. 2008 and Uchimoto et al. 2012). Though these MOIRCS data set is the deepest one at the wavelengths of $J - K$ bands, only 20 out of 45 ALMA fields were observed and the remaining 25 fields cannot receive the great favors. For these cases, we also utilize the archival J and K band Deep Extragalactic Survey (DXS) catalogs, which is constructed using UKIRT/Wide Field Camera (WFCAM) (Lawrence et al. 2007). Although these data are $\sim$ 1.5 mag shallower than the MOIRCS images, all ALMA fields are covered and still useful in investigating the characteristics of SMGs.

We have also obtained the *Spitzer*/IRAC observations of #3473 (PI. A. Blain) and #64

Band	$\lambda_{\rm effective}$ (μm)	Detection Limit (3σ,AB mag)	Reference
CFHT MegaCam Un	0.28	26.6	Archival data
Subaru Suprime-Cam B	0.44	27.0	Hayashino et al. (2004)
Subaru Suprime-Cam V	0.54	27.1	Hayashino et al. (2004)
Subaru Suprime-Cam R	0.65	27.2	Hayashino et al. (2004)
Subaru Suprime-Cam i'	0.77	26.9	Hayashino et al. (2004)
Subaru Suprime-Cam z'	0.92	26.2	Hayashino et al. (2004)
Subaru MOIRCS J	1.25	24.2	Uchimoto et al. (2012)
UKIRT/WFCAM J	1.26	23.3 (5σ)	Lawrence et al. (2007)
Subaru MOIRCS H	1.64	24.1	Uchimoto et al. (2012)
Subaru MOIRCS Ks	2.15	24.1	Uchimoto et al. (2012)
UKIRT/WFCAM K	2.24	22.7 (5σ)	Lawrence et al. (2007)
Spitzer IRAC ch1[a]	3.56	24.9	Hainline et al. (2009)
Spitzer IRAC ch2 [a]	4.51	24.1	Hainline et al. (2009)
Spitzer IRAC ch3	5.76	22.0	Hainline et al. (2009)
Spitzer IRAC ch4	7.96	21.6	Hainline et al. (2009)

Table 4.1 Summary of optical to near/mid infrared photometry employed in this paper.
a) The depth of the IRAC campaign of # 90045 (SpIES: The Spitzer-IRAC Equatorial Survey) is estimated to be 4.9 μJy ($\sim$ 22.2 AB mag) and 7.2 μJy ($\sim$ 21.8 AB mag) at 3.6 μm and 4.5μm in their proposal.

(PI. F. Giovanni) through the *Spitzer* Science Center (SSC) archive[1]. Almost all ALMA fields but SSA22-AzTEC9 were observed in all four wavelength bands (3.6, 4.5, 5.8, 8.0 μm) as shown in Figure 2.1. There is another new IRAC projects, # 90045 (PI. R. Gordon), which is a wide and shallow survey in the *Spitzer* warm mission using the 3.6 and 4.5 μm channels. The field of SSA22-AzTEC9 were observed by this survey.

In summary we can utilize 12 or 13 bands for deriving photometric redshifts. We summarized the observations in Table 4.1 and present postage stamps of B, R, $K(Ks)$, and IRAC 4 channels in Figure A.7 – A.13.

Photometry

We utilize the well-aligned optical to near-infrared images for aperture photometry. Though it is not easy to evaluate the uncertainty in matching these coordinates and ALMA positions, the comparison between ALMA and VLA observations indicate the two images are well aligned as described in Chapter 2 (2.3.3). It is found that the ALMA observations achieve the angular resolution of $\sim 0''.6$ and the positional uncertainty of $< 0''.1$. The ALMA and

[1] http://ssc.spitzer.caltech.edu

VLA coordinates are defined in the International Celestial Reference Frame determined using distant QSOs and all optical to near-infrared positional information is in accordance with the FK5 reference system. Both coordinate systems are known to be well-matched ($< \pm 0''.05$, e.g., Arias et al. 1995). These support that we can compare ALMA maps with optical to near-infrared images directly and identify counterparts at these wavelengths securely.

Although it is ideal to utilize PSF-matched images for all survey data, we performed the PSF-matching only for $U-K(Ks)$ band images since the PSF size of IRAC images are much worse than that of other data. The all $U-K$ band images except for those of MOIRCS three bands have $1''$ PSF (FWHM). Therefore we convolved the MOIRCS images, which have $\sim 0''.5$ PSF, to the lower resolution, $1''$ PSF using the task of GAUSS in the IRAF packages. We use APPHOT in IRAF to measure flux densities in $2''$-diameter apertures whose center are at the ALMA source position. We adopt the centering algorithm "none" and fix the aperture position not to shift the position to the near bright (but not ALMA counterpart) sources. (We found that IRAF tends to measure the bright nearby sources by mistake if we allow to shift the center position, even if the maximum shift is set to be sub-arcsec).

IRAC images have the effective PSF size of 1.9, 2.0, 1.9, and $2''.2$ for 3.6, 4.5, 5.8, and 8.0 μm data, respectively (Surace 2005). We measure photometry for IRAC four band images in $3''.8$-diameter apertures using IRAF/APPHOT. Similarly we fix the aperture position. The final IRAC mosaic images have a scale of $0''.6$/pixel and we adopt the conversion factor from MJy/str to μJy/pixel of 8.461595 (IRAC Instrument Handbook[2]). Finally we apply aperture corrections derived in (Surace 2005). The total measured flux is divided by 0.736, 0.716, 0.606, and 0.543 for 3.6, 4.5, 5.8, and 8.0 μm images. Uncertainties in flux densities are determined based on the sky background revel around the aperture in a similar way reported in Webb et al. (2009). Here we measure the standard deviation of sky flux within an area of PSF's FWHM as flux error.

We list up above 3σ detections for all bands and also utilize 5σ UKIDSS catalogs. The limiting magnitudes are shown in Table 4.1. The photometry is given in Table 4.2 – 4.7.

Blending Effect

As Figure A.7 – A.13 show, source blending causes critical problem in identifying counterparts and deriving photometries. We checked all ALMA sources visually and divided the candidates affected by the blending into three representative cases.

Case1: ALMA sources seems to be detected at several bands. However they are accom-

[2]http://irsa.ipac.caltech.edu/data/SPITZER/docs/irac/iracinstrumenthandbook/25/

panied by another bright sources, which ubiquitously prevents us from measuring the flux density of ALMA's counterparts correctly especially in $U - K(Ks)$ bands (ASA 3.1, ASA12.1, ASA28.1).

Case2: Though the aperture photometries at a fixed position indicate source detection above the threshold, it can be just a tail of nearby bright sources. Though it is hard to exclude the possibility that the ALMA source indeed associates with the optical bright sources, the apparent separation is larger than $1''.0$ (ASA7.4, ASA37.2, ASA81.2, ASA32.2).

Case3: Whilst ALMA sources have possibly secure IRAC counterparts, they appear to have Suprime-Cam sources within the aperture by accident (ASA52.1, ASA35.1, ASA14.1, ASA77.1, ASA110.1).

In addition, IRAC sources tend to be affected this effect frequently.

Thus the blending effect may be critical for some cases. In Wardlow et al. (2011) they evaluated that fewer than ten percent of counterparts are affected. This estimate may be optimistic. But it is impossible to distinguish the contribution of the ALMA counterparts securely based on currently existing data and in general we simply adopt the derived photometries at the ALMA position.

The magnitude distributions

We find 32/64 (50%), 27/64 (42%), 55/61 (90%) counterparts of V, $K(Ks)$, 3.6μm bands sources. Here we exclude three sources (ASA 9.1, ASA9.2, and ASA9.3) in calculating the fraction of 3.6 μm since they don't have deep IRAC observations. The median AB magnitudes are >27.1, >22.7, and 22.26 for V, $K(Ks)$, 3.6μm bands, respectively. While IRAC data show extremely high detection rate, ALMA sources are very faint in optical to near-infrared wavelength even if at K band, which is generally consistent with the traditional picture. Three ALMA sources (ASA11.2, ASA96.2, and ASA23.3) have no optical to near-infrared counterpart while they are detected with the S/N of 4.9, 4.9, and 5.1.

The ALESS survey reported that their 870 μm-selected SMGs have brighter optical to near-infrared counterparts for all the three bands. The median values of V, $K(Ks)$, 3.6μm band counterparts in the survey are 26.09, 23.0, 21.80 (AB magnitude). There are some possible scenarios to give the reason about the disparity. Firstly our ALMA survey is much deeper than the ALESS and we detect a number of more faint mm sources, which might contribute to generate the gap. However, the median values are not dramatically change if we only focus on >1mJy sources ($m_{V,med}$=27.03, $m_{3.6\mu m}$=22.19). Secondly the ALESS

photometry can be affected by brighter sources which lie within the aperture accidentally. The diameter of their photometric aperture is 1.5 times larger than us, which raises the probability of the coincidence. At last Chapman et al. (2005) reported the median magnitude of radio-selected SMGs of $m_{3.6\mu m}$=20.63. This substantiates that the traditional radio-identified SMGs are highly biased sample.

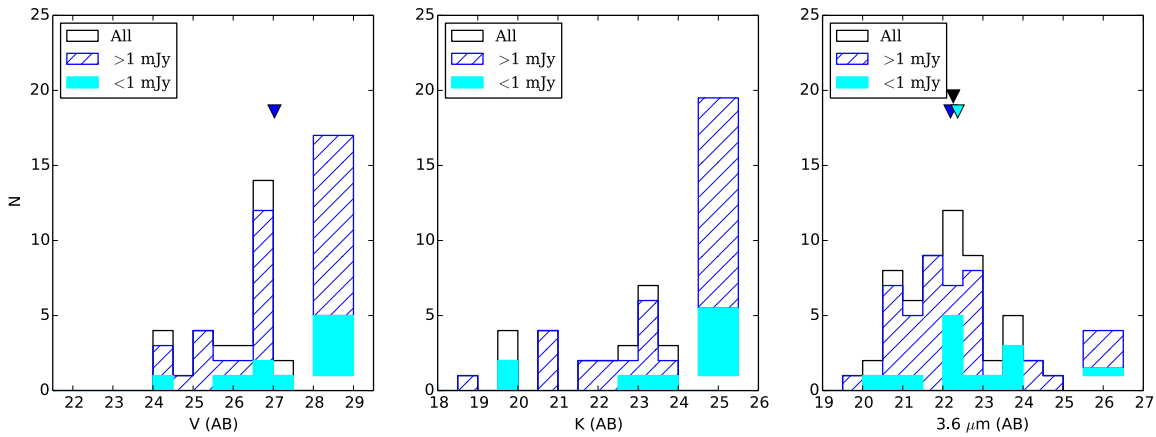

Fig. 4.1 Apparent AB magnitude distributions of ALMA sources in the V, $K(Ks)$, and 3.6μm bands. As well as all MAIN catalog sources, we also plot the sub-samples of $S_{263GHz} \geq 1$ mJy and $S_{263GHz} < 1$ mJy sources. The right rectangle on each panel stands for the undetected sources at each band. The median value for each band are shown using down-pointing triangles if it is above the detection limit.

ALMA ID	U	B	V	R	i'	z'
ASA 1.1	>26.6	>27.0	>27.2	>27.2	>26.9	>26.2
ASA 1.2	>26.6	>27.0	26.72 ±0.07	26.26 ±0.05	25.98 ±0.05	>26.2
ASA 2.1	>26.6	>27.0	26.57 ±0.07	26.22 ±0.05	25.83 ±0.04	25.28 ±0.04
ASA 3.1	>26.6	25.49 ±0.03	24.42 ±0.02	23.59 ±0.01	23.41 ±0.02	23.12 ±0.01
ASA 5.1	>26.6	>27.0	>27.2	27.02 ±0.09	>26.9	26.14 ±0.07
ASA 5.2	>26.6	>27.0	>27.2	>27.2	>26.9	>26.2
ASA 6.1	>26.6	>27.0	>27.2	>27.2	>26.9	>26.2
ASA 7.1	>26.6	>27.0	>27.2	26.73 ±0.07	26.48 ±0.23	26.14 ±0.07
ASA 7.2	>26.6	>27.0	>27.2	>27.2	>26.9	>26.2
ASA 7.3	>26.6	>27.0	>27.2	>27.2	>26.9	>26.2
ASA 7.4	>26.6	26.64 ±0.07	26.01 ±0.04	25.97 ±0.04	26.00 ±0.16	25.96 ±0.06
ASA 9.1	>26.6	26.08 ±0.05	25.62 ±0.03	25.12 ±0.03	25.00 ±0.06	24.79 ±0.02
ASA 9.2	>26.6	>27.0	26.64 ±0.07	26.08 ±0.05	25.85 ±0.12	25.52 ±0.04
ASA 9.3	25.70 ±0.05	25.49 ±0.03	25.09 ±0.03	24.95 ±0.02	25.09 ±0.05	24.86 ±0.03
ASA 11.1	>26.6	>27.0	>27.2	>27.2	>26.9	>26.2
ASA 11.2	>26.6	>27.0	>27.2	>27.2	26.72 ±0.07	>26.2
ASA 12.1	26.35 ±0.09	25.42 ±0.03	24.39 ±0.02	23.96 ±0.01	23.82 ±0.02	23.63 ±0.01
ASA 13.1	>26.6	>27.0	>27.2	26.38 ±0.06	26.60 ±0.19	>26.2
ASA 14.1	24.33 ±0.02	24.34 ±0.02	24.12 ±0.01	23.71 ±0.01	23.52 ±0.01	23.57 ±0.01
ASA 14.2	>26.6	>27.0	27.03 ±0.09	26.73 ±0.07	>26.9	>26.2
ASA 15.1	>26.6	>27.0	>27.2	>27.2	>26.9	>26.2
ASA 15.2	>26.6	>27.0	>27.2	>27.2	>26.9	>26.2

Table 4.2 Photometry ($U - z'$) (1/3)

ALMA ID	U	B	V	R	i'	z'
ASA 20.1	>26.6	26.62 ±0.07	26.66 ±0.07	25.76 ±0.04	25.45 ±0.03	25.22 ±0.03
ASA 20.2	>26.6	>27.0	26.99 ±0.09	26.23 ±0.05	26.06 ±0.05	25.59 ±0.04
ASA 23.1	>26.6	>27.0	>27.2	>27.2	>26.9	>26.2
ASA 26.1	>26.6	>27.0	>27.2	>27.2	>26.9	>26.2
ASA 28.1	26.07 ±0.07	25.42 ±0.03	24.74 ±0.02	24.39 ±0.02	23.69 ±0.01	23.07 ±0.01
ASA 30.1	>26.6	>27.0	>27.2	>27.2	>26.9	>26.2
ASA 34.1	>26.6	>27.0	>27.2	26.73 ±0.07	26.30 ±0.11	25.78 ±0.05
ASA 34.2	>26.6	>27.0	>27.2	>27.2	>26.9	>26.2
ASA 35.1	>26.6	26.82 ±0.10	26.21 ±0.06	25.42 ±0.04	25.45 ±0.09	25.25 ±0.04
ASA 37.1	>26.6	25.52 ±0.03	25.31 ±0.03	25.00 ±0.02	24.91 ±0.02	24.58 ±0.02
ASA 37.2	>26.6	>27.0	26.85 ±0.08	27.08 ±0.09	>26.9	>26.2
ASA 40.1	>26.6	>27.0	>27.2	26.66 ±0.07	26.41 ±0.06	>26.2
ASA 45.1	>26.6	>27.0	>27.2	>27.2	>26.9	>26.2
ASA 49.1	>26.6	>27.0	>27.2	>27.2	>26.9	>26.2
ASA 50.1	>26.6	26.86 ±0.09	26.31 ±0.05	26.26 ±0.05	25.57 ±0.04	25.04 ±0.03
ASA 52.1	25.70 ±0.05	25.74 ±0.04	25.46 ±0.03	25.15 ±0.03	24.59 ±0.02	24.00 ±0.02
ASA 52.2	>26.6	>27.0	>27.2	>27.2	26.25 ±0.05	25.40 ±0.05
ASA 55.1	26.30 ±0.08	25.81 ±0.04	25.33 ±0.03	24.99 ±0.03	24.64 ±0.02	24.13 ±0.02
ASA 62.1	>26.6	>27.0	>27.2	>27.2	>26.9	>26.2
ASA 62.2	>26.6	>27.0	26.85 ±0.08	26.31 ±0.05	26.08 ±0.05	25.97 ±0.06
ASA 67.1	>26.6	26.84 ±0.08	26.57 ±0.06	26.54 ±0.06	26.61 ±0.07	>26.2
ASA 67.2	>26.6	>27.0	>27.2	>27.2	26.56 ±0.21	25.69 ±0.05

Table 4.3 Photometry ($U - z'$) (2/3)

ALMA ID	U	B	V	R	i'	z'
ASA 55.1	26.30 ±0.08	25.81 ±0.04	25.33 ±0.03	24.99 ±0.03	24.64 ±0.02	24.13 ±0.02
ASA 69.1	>26.6	26.72 ±0.07	25.68 ±0.03	25.21 ±0.03	24.94 ±0.02	24.72 ±0.02
ASA 71.1	>26.6	>27.0	26.56 ±0.07	26.09 ±0.06	26.27 ±0.07	25.94 ±0.07
ASA 75.1	>26.6	>27.0	>27.2	>27.2	>26.9	>26.2
ASA 75.2	>26.6	>27.0	>27.2	27.05 ±0.09	26.29 ±0.10	25.80 ±0.05
ASA 77.1	>26.6	26.77 ±0.08	26.56 ±0.06	26.12 ±0.04	25.98 ±0.04	25.83 ±0.05
ASA 80.1	>26.6	>27.0	26.76 ±0.07	26.02 ±0.04	25.96 ±0.13	25.56 ±0.05
ASA 81.1	>26.6	27.00 ±0.09	26.70 ±0.06	26.17 ±0.04	25.93 ±0.04	25.32 ±0.04
ASA 81.2	>26.6	>27.0	>27.2	>27.2	>26.9	>26.2
ASA 83.1	20.43 ±0.00	20.51 ±0.00	20.38 ±0.00	20.40 ±0.00	19.20 ±0.00	20.37 ±0.00
ASA 87.1	>26.6	>27.0	27.10 ±0.10	26.44 ±0.06	>26.9	>26.2
ASA 96.1	>26.6	>27.0	26.92 ±0.09	26.97 ±0.09	26.15 ±0.05	25.88 ±0.06
ASA 96.2	>26.6	>27.0	>27.2	>27.2	>26.9	>26.2
ASA 110.1	>26.6	26.39 ±0.06	25.71 ±0.04	25.48 ±0.03	25.45 ±0.03	25.25 ±0.04
ASA 115.1	>26.6	>27.0	>27.2	>27.2	>26.9	>26.2
ASA 2.3	>26.6	>27.0	>27.2	>27.2	26.85 ±0.11	25.99 ±0.06
ASA 23.3	>26.6	>27.0	>27.2	>27.2	>26.9	>26.2
ASA 32.2	25.08 ±0.03	24.70 ±0.02	24.24 ±0.01	24.04 ±0.01	23.97 ±0.01	23.82 ±0.01
ASA 56.3	>26.6	>27.0	>27.2	26.96 ±0.08	26.76 ±0.08	26.15 ±0.06
ASA 115.3	>26.6	>27.0	>27.2	>27.2	>26.9	>26.2
ASA 116.1	>26.6	>27.0	26.64 ±0.06	26.44 ±0.05	26.15 ±0.05	25.94 ±0.06

Table 4.4 Photometry ($U - z'$) (3/3)

ALMA ID	J	H	K	3.6 μm	4.5 μm	5.8 μm	8.0 μm
ASA 1.1	>24.2	23.84 ±0.39	23.28 ±0.30	21.56 ±0.02	20.90 ±0.01	20.36 ±0.03	19.98 ±0.02
ASA 1.2	>24.2	23.59 ±0.34	23.04 ±0.27	22.19 ±0.05	21.86 ±0.05	22.11 ±0.13	21.31 ±0.07
ASA 2.1	23.39 ±0.33	22.49 ±0.22	21.56 ±0.15	20.30 ±0.00	19.95 ±0.00	19.66 ±0.01	19.91 ±0.02
ASA 3.1	>23.3	...	>22.5	20.70 ±0.02	20.74 ±0.02	21.09 ±0.14	20.26 ±0.06
ASA 5.1	>24.2	23.21 ±0.29	22.79 ±0.24	21.72 ±0.02	21.47 ±0.02	21.43 ±0.06	21.29 ±0.06
ASA 5.2	>24.2	>24.1	23.87 ±0.40	22.41 ±0.03	21.77 ±0.02	21.18 ±0.05	20.82 ±0.04
ASA 6.1	>23.3	...	20.69 ±0.15	21.17 ±0.02	20.67 ±0.01	20.02 ±0.06	20.25 ±0.04
ASA 7.1	>23.3	...	>22.5	22.53 ±0.03	22.14 ±0.03	21.70 ±0.10	21.38 ±0.07
ASA 7.2	>23.3	...	>22.5	23.61 ±0.07	22.99 ±0.06	>22.0	21.90 ±0.11
ASA 7.3	>23.3	...	>22.5	23.94 ±0.10	23.17 ±0.08	>22.0	>21.6
ASA 7.4	>23.3	...	>22.5	24.73 ±0.21	>24.1	>22.0	>21.6
ASA 9.1	>23.3	...	20.68 ±0.15	...	...	...	...
ASA 9.2	>23.3	...	>22.5	...	...	...	...
ASA 9.3	>23.3	...	>22.5	...	...	...	...
ASA 11.1	>23.3	...	>22.5	22.74 ±0.06	21.87 ±0.07	21.29 ±0.10	21.36 ±0.20
ASA 11.2	>23.3	...	>22.5	>24.9	>24.1	>22.0	>21.6
ASA 12.1	22.74 ±0.24	21.88 ±0.17	21.63 ±0.15	20.63 ±0.01	20.37 ±0.01	20.04 ±0.01	19.89 ±0.01
ASA 13.1	>24.2	>24.1	>24.1	22.95 ±0.05	22.97 ±0.07	>22.0	>21.6
ASA 14.1	23.33 ±0.30	23.15 ±0.28	22.87 ±0.25	21.61 ±0.01	21.17 ±0.01	20.68 ±0.03	20.31 ±0.02
ASA 14.2	>24.2	>24.1	23.21 ±0.29	21.50 ±0.01	21.09 ±0.01	20.61 ±0.03	20.41 ±0.03
ASA 15.1	>23.3	...	>22.5	22.79 ±0.05	22.27 ±0.05	>22.0	21.61 ±0.10
ASA 15.2	>23.3	...	>22.5	23.98 ±0.11	23.84 ±0.15	22.14 ±0.13	>21.6

Table 4.5 Photometry (J – 8.0 μm) (1/3)

ALMA ID	J	H	K	3.6 μm	4.5 μm	5.8 μm	8.0 μm
ASA 20.1	>23.3	...	20.78 ±0.16	21.26 ±0.01	20.77 ±0.01	19.89 ±0.02	19.14 ±0.01
ASA 20.2	>23.3	...	19.95 ±0.08	20.87 ±0.01	20.59 ±0.01	20.15 ±0.02	20.03 ±0.03
ASA 23.1	>23.3	...	>22.5	22.43 ±0.04	21.89 ±0.04	21.31 ±0.07	20.88 ±0.07
ASA 26.1	>23.3	...	>22.5	24.37 ±0.22	24.17 ±0.26	>22.0	>21.6
ASA 28.1	>23.3	...	>22.5	20.75 ±0.01	20.47 ±0.04	20.48 ±0.07	19.91 ±0.11
ASA 30.1	>23.3	...	>22.5	21.91 ±0.01	21.50 ±0.02	20.93 ±0.04	21.23 ±0.07
ASA 34.1	>23.3	...	>22.5	21.68 ±0.01	21.25 ±0.02	20.89 ±0.05	20.52 ±0.04
ASA 34.2	>23.3	...	>22.5	22.91 ±0.05	22.97 ±0.09	22.04 ±0.13	>21.6
ASA 35.1	>24.2	23.34 ±0.32	23.07 ±0.29	21.52 ±0.02	21.37 ±0.02	21.55 ±0.10	20.53 ±0.04
ASA 37.1	23.40 ±0.32	22.52 ±0.22	22.07 ±0.18	20.98 ±0.01	20.69 ±0.01	20.40 ±0.03	20.14 ±0.02
ASA 37.2	>24.2	>24.1	>24.1	23.70 ±0.09	23.90 ±0.16	>22.0	>21.6
ASA 40.1	>23.3	...	>22.5	22.35 ±0.04	22.10 ±0.05	21.84 ±0.11	21.46 ±0.10
ASA 45.1	>23.3	...	>22.5	21.39 ±0.02	20.98 ±0.02	20.78 ±0.06	20.90 ±0.07
ASA 49.1	>24.2	>24.1	>24.1	23.42 ±0.08	22.67 ±0.06	21.53 ±0.07	21.16 ±0.06
ASA 50.1	22.23 ±0.19	...	19.58 ±0.06	20.57 ±0.01	20.31 ±0.01	19.94 ±0.02	20.51 ±0.05
ASA 52.1	>23.3	...	>22.5	21.45 ±0.01	21.53 ±0.01	21.55 ±0.07	21.09 ±0.04
ASA 52.2	>24.2	23.60 ±0.35	23.19 ±0.29	22.27 ±0.02	21.89 ±0.02	21.33 ±0.05	21.22 ±0.04
ASA 55.1	21.31 ±0.08	...	18.84 ±0.03	19.71 ±0.00	19.40 ±0.00	19.18 ±0.01	19.55 ±0.01
ASA 62.1	>23.3	...	>22.5	23.58 ±0.10	23.39 ±0.10	>22.0	21.86 ±0.11
ASA 62.2	>23.3	...	>22.5	22.13 ±0.03	21.65 ±0.02	21.19 ±0.07	21.14 ±0.06
ASA 67.1	>23.3	...	>22.5	24.05 ±0.23	>24.1	>22.0	>21.6
ASA 67.2	>23.3	...	19.68 ±0.07	20.48 ±0.01	20.19 ±0.01	20.22 ±0.05	20.48 ±0.07

Table 4.6 Photometry (J – 8.0 μm) (2/3)

ALMA ID	J	H	K	3.6 μm	4.5 μm	5.8 μm	8.0 μm
ASA 69.1	>23.3	...	>22.5	21.67 ±0.01	21.46 ±0.02	21.16 ±0.05	20.94 ±0.05
ASA 71.1	>23.3	...	>22.5	22.20 ±0.07	21.64 ±0.04	21.16 ±0.07	21.54 ±0.12
ASA 75.1	>23.3	...	>22.5	23.38 ±0.10	23.14 ±0.10	>22.0	>21.6
ASA 75.2	>23.3	...	>22.5	22.37 ±0.04	23.21 ±0.12	21.97 ±0.14	>21.6
ASA 77.1	>24.2	23.84 ±0.41	23.44 ±0.35	22.33 ±0.02	21.90 ±0.02	21.70 ±0.06	21.26 ±0.05
ASA 80.1	>24.2	23.87 ±0.41	23.53 ±0.34	22.74 ±0.04	22.42 ±0.04	21.90 ±0.09	21.64 ±0.07
ASA 81.1	>23.3	...	19.64 ±0.06	20.51 ±0.01	20.21 ±0.01	19.75 ±0.04	20.31 ±0.08
ASA 81.2	>23.3	...	>22.5	22.46 ±0.07	22.79 ±0.15	22.18 ±0.32	21.29 ±0.16
ASA 83.1	18.85 ±0.02	...	17.08 ±0.01	18.28 ±0.00	18.09 ±0.00	17.84 ±0.00	17.48 ±0.00
ASA 87.1	>24.2	>24.1	23.86 ±0.40	22.25 ±0.04	22.01 ±0.04	21.85 ±0.09	21.53 ±0.08
ASA 96.1	>23.3	...	>22.5	21.69 ±0.01	21.31 ±0.01	20.74 ±0.03	20.80 ±0.04
ASA 96.2	>23.3	...	>22.5	>24.9	>24.1	>22.0	>21.6
ASA 110.1	>24.2	23.43 ±0.33	22.95 ±0.27	21.39 ±0.01	21.03 ±0.01	20.66 ±0.03	20.59 ±0.03
ASA 115.1	>23.3	...	>22.5	22.57 ±0.04	22.02 ±0.04	21.75 ±0.14	21.34 ±0.10
ASA 2.3	23.65 ±0.38	23.64 ±0.38	22.37 ±0.21	20.73 ±0.01	20.25 ±0.01	19.96 ±0.01	20.46 ±0.03
ASA 23.3	>23.3	...	>22.5	>24.9	>24.1	>22.0	>21.6
ASA 32.2	>23.3	...	>22.5	22.55 ±0.08	23.10 ±0.12	>22.0	21.84 ±0.14
ASA 56.3	>23.3	...	20.50 ±0.13	21.21 ±0.01	20.71 ±0.01	20.41 ±0.04	20.53 ±0.04
ASA 115.3	>23.3	...	>22.5	22.93 ±0.05	22.73 ±0.07	>22.0	>21.6
ASA 116.1	>24.2	24.04 ±0.45	23.32 ±0.33	22.15 ±0.02	21.83 ±0.02	21.42 ±0.06	21.30 ±0.06

Table 4.7 Photometry (J – 8.0 μm) (3/3)

4.1.2 SED Fitting

We derive photometric redshifts of the ALMA sources through SED fitting with the code of HYPERZ (Bolzonella et al. 2000). The usable photometric bands are 12 or 13 (U,B,V,R,i',z', $J,H,K(Ks),3.6,4.5,5.8,8.0\mu$m), which is depend on whether a given ALMA source have MOIRCS observations or not. In the case of non-detections, we regard the flux density at the band as zero with errors between zero and the limiting magnitude listed in Table 4.1. We adopt eight spectral templates of Bruzual & Charlot (2003) that have different star formation history (SFH). One is single burst model (Burst) and the other one is constant star formation model (Im). We also consider six templates with exponentially decaying SFHs with timescales τ of 1, 2,3,5,15,30 Gyr (E, S0, Sa, Sb, Sc, Sd) like

$$\mathrm{SFR(t)} \propto \exp(-\mathrm{t}/\tau) \tag{4.1}$$

We assume Chabrier IMF (Chabrier 2003) and solar metallicity. The reddening raw for starburst galaxies from Calzetti et al. (2000) is utilized to calculate the amount of internal reddening in the range of $A_V = 0-5$ in steps of 0.5. The considered redshift range is limited to $z = 0-6$ and we validate the age check not to adopt over cosmic age.

4.1.3 Results

We running HYPERZ for 59 ALMA sources. (ASA9.1, 9.2, 9.3 were excluded because of the shortage of IRAC data. ASA11.2, ASA 96.2 and ASA23.3 were also ruled out since they have no valid detection.) Table 4.8–4.9 shows the results of the SED fitting. We also present the photometries and the best-fit SEDs in Figure A.1 – A.6.

Five ALMA sources, ASA14.1, ASA20.1, ASA35.1, ASA52.1, and ASA83.1, have the minimum $\chi^2_{\mathrm{red}} > 10$. There are roughly two main suspects. The one is the contamination of apparent nearby sources. ASA14.1, ASA35.1, and ASA52.1 are detected in Suprime-Cam bands, but the MOIRCS maps with high angular resolution ($\sim 0''.5$) suggest the optical emission is not from ALMA sources. ASA14.1 and ASA52.1 don't have Ks-band counterpart at the position of IRAC sources and inversely ASA35.1 have clear Ks-band counterpart and we cannot recognize any optical source there. The other is the excess at 8.0 μm, which is considered to be attributed to hot-dust, power-law component. ASA20.1 shows remarkable this excess. Such excess is also shown in some other candidates of AGN-hosts such as ASA1.2 and ASA14.1, both of which have X-ray counterparts. ASA83.1 is one of SDSS galaxies and clear radio jet are shown in the 1.4 GHz image. Hence ASA83.1 is likely to be an active radio galaxy.

ALMA ID	$S_{\rm ALMA}$ mJy	$z_{\rm phot}$	$z_{\rm spec}$	$\chi^2_{\rm red}$	M_H (AB)	$M_{\rm stellar}$ $10^{10}M_\odot$	Coverage	$N_{\rm det}$
ASA 001 . 1	6.4	$2.96^{+0.79}_{-0.25}$	...	0.18	-25.36	16.00	MO	6
ASA 001 . 2	1.4	$3.08^{+0.17}_{-0.15}$	...	2.51	-23.64	3.28	MO	9
ASA 002 . 1	3.1	$2.17^{+0.06}_{-0.05}$	2.28[1]	0.29	-25.18	13.55	MO	11
ASA 003 . 1	4.6	$2.77^{+0.04}_{-0.03}$	...	9.66	-24.29	5.97	UK	9
ASA 005 . 1	2.4	$2.89^{+0.12}_{-0.11}$	...	1.11	-24.12	5.11	MO	7
ASA 005 . 2	2.1	$2.85^{+3.15}_{-0.24}$	...	0.10	-24.43	6.79	MO	5
ASA 006 . 1	2.5	$2.19^{+0.38}_{-0.19}$	...	0.84	-24.80	9.55	UK	5
ASA 007 . 1	2.3	$3.76^{+0.16}_{-0.24}$	...	0.42	-24.53	7.45	UK	7
ASA 007 . 2	2.2	$5.64^{+0.36}_{-3.14}$	...	0.04	-25.08	12.36	UK	3
ASA 007 . 3	0.9	$1.78^{+4.22}_{-0.33}$	...	0.03	-21.43	0.43	UK	2
ASA 007 . 4	1.1	$3.13^{+0.07}_{-0.12}$	...	0.10	-21.13	0.33	UK	6
ASA 011 . 1	4.5	$2.19^{+0.35}_{-0.20}$	...	0.15	-23.50	2.88	UK	4
ASA 012 . 1	3.8	$2.77^{+0.04}_{-0.03}$	2.56[2]	2.10	-25.38	16.30	MO	13
ASA 013 . 1	2.2	$2.38^{+0.37}_{-0.42}$	...	1.50	-22.24	0.90	MO	4
ASA 014 . 1	2.2	$2.19^{+0.04}_{-0.02}$	...	27.97	-24.24	5.70	MO	13
ASA 014 . 2	1.4	$2.88^{+0.25}_{-0.10}$	3.09[4]	1.55	-24.97	11.17	MO	7
ASA 015 . 1	1.0	$3.57^{+2.43}_{-1.44}$	...	0.11	-24.19	5.45	UK	3
ASA 015 . 2	1.3	$5.88^{+0.12}_{-0.79}$	...	1.83	-26.14	32.82	UK	3
ASA 020 . 1	2.2	$2.69^{+0.10}_{-0.11}$	2.95[3]	31.21	-25.52	18.54	UK	10
ASA 020 . 2	1.1	$2.67^{+0.08}_{-0.12}$	...	2.47	-25.19	13.68	UK	9
ASA 023 . 1	2.4	$5.09^{+0.91}_{-1.23}$	...	0.03	-25.80	23.99	UK	4
ASA 026 . 1	3.0	$1.25^{+4.75}_{-1.17}$	...	0.00	-19.52	0.07	UK	2
ASA 028 . 1	2.7	$1.41^{+0.05}_{-0.03}$	...	9.81	-23.41	2.66	UK	10
ASA 030 . 1	2.7	$2.35^{+0.12}_{-0.21}$	...	0.45	-24.09	4.97	UK	4
ASA 034 . 1	3.0	$3.44^{+0.50}_{-0.39}$	3.23[3]	0.29	-25.21	13.93	UK	7
ASA 034 . 2	1.0	$2.48^{+0.55}_{-0.34}$	...	1.51	-23.11	2.01	UK	3
ASA 035 . 1	1.1	$3.19^{+0.00}_{-0.03}$	...	11.74	-24.23	5.65	MO	11
ASA 037 . 1	2.8	$2.53^{+0.07}_{-0.12}$	2.61[2,3]	7.70	-24.84	9.91	MO	12
ASA 037 . 2	0.4	$1.55^{+0.92}_{-0.14}$	...	0.98	-20.36	0.16	MO	4
ASA 040 . 1	2.2	$2.96^{+0.52}_{-0.23}$	...	0.70	-23.78	3.73	UK	6
ASA 045 . 1	3.2	$1.75^{+0.80}_{-0.21}$	...	0.17	-23.51	2.91	UK	4
ASA 049 . 1	2.4	$4.96^{+0.50}_{-0.49}$	...	0.98	-25.61	20.14	MO	4
ASA 050 . 1	1.0	$1.80^{+0.05}_{-0.06}$	...	4.76	-24.27	5.86	UK	11

Table 4.8 Photometric properties (1/2)

ALMA ID[a]	$S^b_{\rm ALMA}$ mJy	$z^c_{\rm phot}$	$z^d_{\rm spec}$	$\chi^2_{\rm red}{}^e$	M^f_H (AB)	$M^g_{\rm stellar}$ $10^{10}M_\odot$	Coverage[h]	$N^i_{\rm det}$
ASA 052 . 1	3.1	$1.42^{+0.02}_{-0.04}$	...	17.92	-22.71	1.39	UK	10
ASA 052 . 2	0.6	$4.97^{+0.06}_{-0.06}$	...	1.06	-25.31	15.28	MO	7
ASA 055 . 1	2.7	$1.91^{+0.03}_{-0.05}$	...	1.71	-25.34	15.71	UK	12
ASA 062 . 1	1.0	$6.00^{+0.00}_{-0.60}$	...	0.48	-25.36	16.00	UK	3
ASA 062 . 2	0.8	$3.08^{+0.10}_{-0.18}$	...	2.57	-24.56	7.66	UK	8
ASA 067 . 1	1.1	$2.71^{+0.10}_{-0.24}$	...	0.31	-21.52	0.47	UK	5
ASA 067 . 2	0.7	$1.59^{+0.10}_{-0.23}$	...	0.36	-24.08	4.92	UK	7
ASA 069 . 1	1.9	$2.85^{+0.06}_{-0.05}$	...	1.31	-24.36	6.37	UK	9
ASA 071 . 1	1.5	$2.50^{+0.05}_{-0.11}$	...	5.56	-23.97	4.45	UK	8
ASA 075 . 1	0.8	$1.25^{+4.75}_{-0.38}$	...	0.01	-20.52	0.19	UK	2
ASA 075 . 2	0.3	$0.75^{+0.06}_{-0.05}$	...	4.64	-20.27	0.15	UK	7
ASA 077 . 1	2.3	$2.79^{+0.08}_{-0.07}$	3.10[2]	8.25	-23.77	3.70	MO	11
ASA 080 . 1	1.5	$3.58^{+0.07}_{-0.12}$	...	2.45	-24.19	5.45	MO	10
ASA 081 . 1	2.0	$2.19^{+0.07}_{-0.07}$	...	1.99	-25.16	13.31	UK	10
ASA 081 . 2	0.6	$6.00^{+0.00}_{-1.47}$	...	2.04	-25.62	20.33	UK	4
ASA 083 . 1	1.0	$2.50^{+0.00}_{-0.03}$	...	37.72	-27.30	95.52	UK	12
ASA 087 . 1	0.7	$3.27^{+0.13}_{-0.63}$	...	1.50	-24.12	5.11	MO	7
ASA 096 . 1	2.0	$2.62^{+0.09}_{-0.10}$	...	3.38	-24.55	7.59	UK	7
ASA 110 . 1	0.9	$2.79^{+0.00}_{-0.06}$	...	6.38	-24.76	9.21	MO	11
ASA 115 . 1	1.9	$3.55^{+2.45}_{-0.97}$	...	0.03	-24.46	6.98	UK	4
ASA 002 . 3	1.7	$1.81^{+0.12}_{-0.06}$	...	1.97	-24.33	6.20	MO	9
ASA 032 . 2	0.8	$2.48^{+0.07}_{-0.09}$	...	5.09	-22.26	0.92	UK	9
ASA 056 . 3	2.0	$2.27^{+0.15}_{-0.10}$	...	0.63	-24.52	7.38	UK	8
ASA 115 . 3	1.1	$1.25^{+4.75}_{-0.29}$	...	0.03	-20.96	0.28	UK	2
ASA 116 . 1	1.0	$2.94^{+0.10}_{-0.10}$	...	1.10	-24.21	5.55	MO	10

Table 4.9 Photometric properties (2/2).

[a] ALMA source ID

[b] The flux densities at 263 GHz

[c] Derived photometric redshifts with a 90% confidence interval.

[d] Spectroscopic redshifts from our observations and literatures

[e] The reduced χ^2 at the best-fit $z_{\rm phot}$

[f] The absolute AB magnitudes in the rest-flame H band.

[g] Stellar mass on the assumption of the mass to light ratio (M/L_H=0.15)

[h] The information about $J-K$ band observations. MO represent that the ALMA source have MOIRCS observations of J, H, and Ks bands. In the case of UK, we utilize J and K band photometries from the UKIDSS DXS survey.

[i] The number of photometric filters in which counterparts were detected.

1: Alaghband-Zadeh et al. (2012) 2: Chapman et al. (2005) 3: this work 4: Kubo et al. submitted to ApJ

Reliability

The most direct way to examine the reproducibility of our estimates is brought by the comparison between photometric redshift and spectroscopic redshift of same ALMA sources. Seven ALMA sources have spectroscopic redshifts, including four sources selected based on our work to measure $z_{\rm spec}$ (Alaghband-Zadeh et al. (2012), Kubo et al, and this thesis). (Among them, the information of ASA20.1 and ASA34.1 has not been published. Both are confirmed by our VLT/VIMOS observation (PI. Umehata). Since the details of the observation is out of focus here, we just show spectra of the two in Appendix B.)

We calculate Δz=$z_{\rm phot} - z_{\rm spec}$ and show the results of the comparison between the two in Figure 4.2. The median of $(\Delta z)/(1+z_{spec})$ is -0.033$^{+0.010}_{-0.042}$ and all sources don't represent catastrophic discrepancy of $|z_{photo} - z_{spec}|/(1+z_{spec}) > 0.15$ (e.g., Ilbert et al. 2009) even if a source is considered to be affected by the blending effect (e.g., ASA 77.1).

Optically undetected sources

For 64 ALMA sources in the main catalog, we find that three don't have significant detections at any optical to near-infrared wavelengths. In addition, four sources have just 2-band detections. This 'non-detection rate' does arise in calculating for 38 supplementary sources. It is found that 10/38 have no detection and 6/38 have $<$2 bands detection.

Though it is possible to be spurious detections for some cases, statistically it is also sure that there are such 'optically faint' populations. We have three possible explanation as Simpson et al. (2014b) pointed out. They might comprise of (i) extremely dust-obscured sources, (ii) sources with very small stellar masses, and/or (iii) high redshift sources. Though it is still open question, the upcoming observations including spectroscopy are expected to resolve their nature.

4.1.4 Redshift Distribution

Redshifts of ALMA sources in the SSA22

In Figure 4.3, we present the results of the estimate of photometric redshifts. We exclude 10 optically very faint sources, which don't have any optical to near-infrared detections or just have two band detections, in calculating the histograms since we cannot derive meaningful results. The remaining 54 sources with $\geq$ three band detections at optical to near-infrared wavelengths are considered in creating the histogram. As shown in Table 4.8 – 4.9, seven ALMA sources have spectroscopic redshifts and we adopt these $z_{\rm spec}$ for them. The distribution of 54 ALMA sources have median redshift of $z = 2.78^{+0.18}_{-0.28}$ and this value increase to

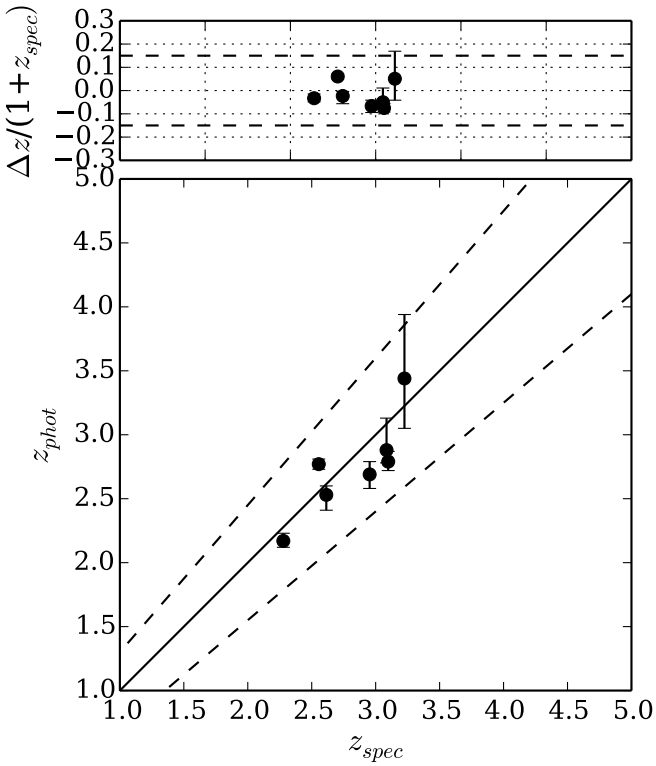

Fig. 4.2 The spectroscopic redshifts of ALMA sources compared to the photometric redshifts. Each error bar corresponds to a 90 % confidence interval. The dashed lines represent $z_{phot} = z_{spec} \pm 0.15(1+z_{spec})$ for reference. The upper panel stands for the values of $(z_{\rm phot} - z_{\rm spec})/(1+z_{\rm spec})$.

$z = 2.95_{-0.30} + 0.18$ if we include the 10 optically faint sources assuming they lie at $z \geq 4$.

While some previous works suggested that there is a correlation between observed flux density at submm/mm wavelengths and redshift – brighter SMGs tend to be at higher-redshift –(e.g., Ivison et al. 2002, Ivison et al. 2007, Pope et al. 2005, Biggs et al. 2011), recent studies (e.g., Wardlow et al. 2011, Simpson et al. 2014b) have put a query against it. Our ALMA survey supports that there is no significant correlation between the two as displayed in Figure 4.4. We confirmed this in also Figure 4.3. The bright ALMA sources with $S_{263\rm GHz} \geq 1.0$ mJy show median redshift of $z = 2.81^{+0.15}_{-0.31}$, which is consistent with that of the faint ($S_{263\rm GHz} < 1.0$ mJy) ALMA sources ($z = 2.65^{+1.23}_{-1.06}$) within the error.

One remarkable feature of the redshift distribution in the SSA22 is the peak at redshift of around 3. The SSA22 field have a remarkable large-scale structure at z=3.09 and one in-

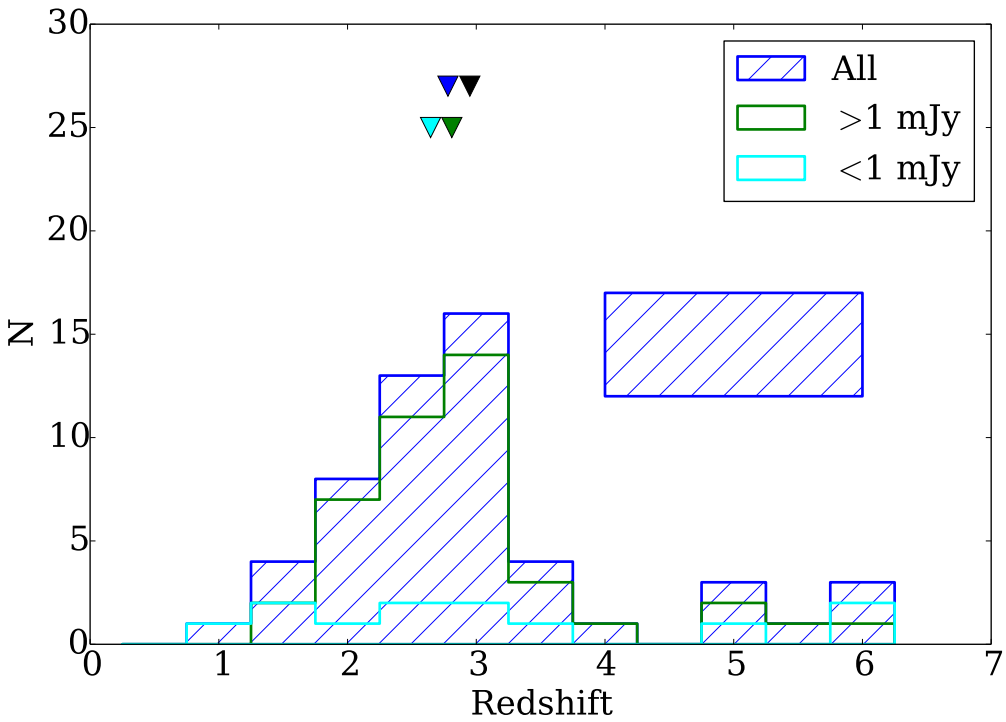

Fig. 4.3 Redshift distributions of ALMA sources in the SSA22. Sources with ≥ 3 band detections (54/64) are considered. Unless sources have spectroscopic redshifts, spectroscopic redshifts are utilized. For seven sources we adopt spectroscopic redshifts as best estimates. The blue histogram represents the distribution of all ALMA sources and the blue and black down-pointing triangles stand for the median value in the case of not including 10 optically (almost) non detections ($z = 2.78^{+0.18}_{-0.28}$) and including them as $z > 4$ sources ($z = 2.95^{+0.18}_{-0.30}$), respectively. We also show the redshift distributions of subsamples, $S \geq 1.0$ mJy and $S < 1.0$ mJy, using green and cyan histograms to investigate the dependence on 1.1 mm flux density. The two have median redshifts of $z = 2.81^{+0.15}_{-0.31}$ for the $S \geq 1.0$ mJy population and $z = 2.65^{+1.23}_{-1.06}$ for the $S \geq 1.0$ mJy population, which indicates there are no significant dependence on mm flux density.

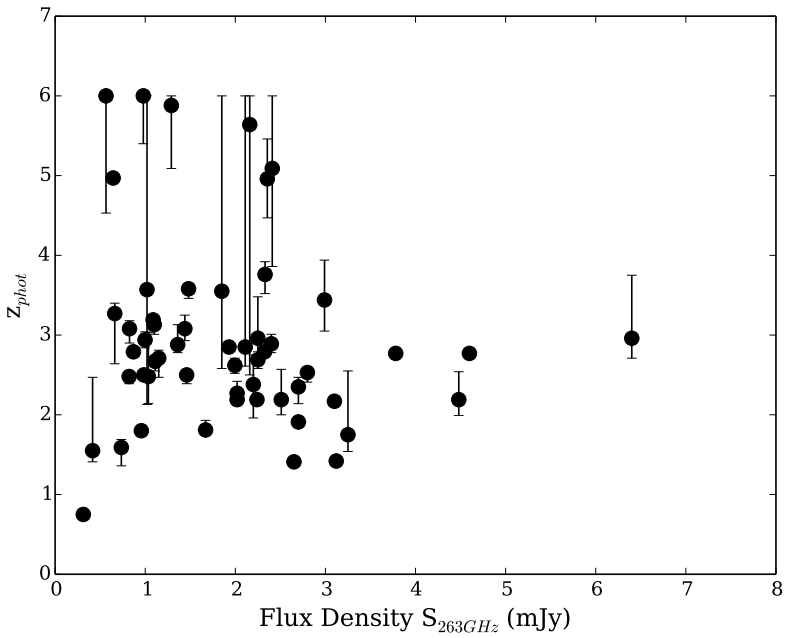

Fig. 4.4 Photometric redshifts as a function of observed ALMA flux density at 263 GHz. We cannot find any significant dependence.

teresting possibility is that the biased environment causes the peak. In the following section, we note that this field is not a general field and explore the origin of the peak.

Comparison with other surveys

The first largest spectroscopic survey of SMGs were conducted by Chapman et al. (2005). They obtained spectroscopic redshifts for 76 radio-identified counterparts of 73 SCUBA-selected SMGs. This survey has been the largest one in 2014 (zLESS: the spectroscopic survey of ALESS SMGs may became the largest in the near future.) The median redshift of the survey results in $z = 2.15^{+0.35}_{-0.16}$ considering all sources. One of the most remarkable feature of their distribution is the deficit of $z > 3$ populations ("high-z tail"). Their record of the highest redshift is $z = 3.6$ and just $< 10\%$ of sources lie at $z > 3$.

In the left panel of Figure 4.5, we compare the distributions of our work and the survey as well as our sub-sample of radio-detected sources. Totally 15 ALMA sources in the SSA22 have $\geq 3\sigma$ radio counterparts and the median redshift of them is $z = 2.56^{+0.29}_{-0.75}$. Though we should note that the depth of our VLA 1.4 GHz map ($1\sigma = 8.5 - 20\mu$Jy) are relatively shallower than that of their work ($1\sigma = 4 - 15\mu$Jy), the highest $z_{\rm phot}$ is $z = 3.57$, which stands for good agreement with Chapman's work. In contrast to their survey, it is likely that about

50% SMGs lie at $z > 3$ in our survey. As suggested in many previous works (e.g., Wardlow et al. 2011, Smolčić et al. 2012, Yun et al. 2012, Weiß et al. 2013, Umehata et al. 2014, Simpson et al. 2014b), the radio sensitivity limit seems to conceal the high-z tail in relying radio-identification. In addition, a valley at $z = 1-2$ seen in Chapman's distribution has been controversial. Now several photometric redshift survey based on ALMA identification have been carried out (Weiß et al. 2013, Simpson et al. 2014b, and this work), but no survey reports the bump of the $z <\sim 1$ populations (Weiß et al. (2013) is only considered $z > 1.5$ universe since their SMGs are affected by the gravitational lensing effect). Therefore the valley can have important meaning and the majority of the $z <\sim 1$ populations might be not SMGs. The spectroscopic redshift of these galaxies are obtained based on optical lines and their counterpart is selected using radio data, not submm/mm interferometric observations. As discussed in the section 3.4.2, radio data provide us with the most reliable tool in identifying counterparts of SMGs except for high resolution imaging at submm/mm, but they cannot evade the possibility of the miss-identification.

There are two photometric redshift surveys for ALMA populations that precede our survey. Simpson et al. (2014b) targeted 96 ALMA sources in the ALESS catalog and derived photometric redshifts for 77 sources which have larger than three band detections in optical to near-infrared wavelengths. It is also reported that ten ALMA sources have spectroscopic redshifts. The normalized redshift distributions of this ALESS survey and our survey are shown in the middle panel of Figure 4.5. The median redshift of 77 sources are $z = 2.28^{+0.16}_{-0.19}$ and if the remaining 19 sources are at $z > 3.0$, this raise to $z = 2.5 \pm 0.2$. Both estimates indicate that the ALESS survey tends to have lower redshift distribution significantly. Though $z = 3.09$ populations can partially contribute to make the number of $z > 3$ SMGs compared to that of 1.1 mm selected SMGs in general fields, the most reliable scenario is that 870 μm selected SMGs and 1.1 mm selected SMGs don't always overlap and the two wavelength trace somewhat different populations. The fact that the median redshifts of ALESS sources increases for the 250, 350, 500 μm peaker in Swinbank et al. (2014) supports the scenario. While both of the ALESS survey and our SSA22 survey show significant high-z tails, the distribution of this redshift range contain the large uncertainties and the comprehensive spectroscopic survey is required to reveal it and compare between both populations.

Weiß et al. (2013) conducted blind molecular spectroscopic survey for extremely bright ($S_{1.4\mathrm{mJy}} > 20$ mJy) SMGs selected by SPT. Their samples are selected in 1.4 mm and 2.0 mm and they also required 870 μm detections by LABOCA in order to restrict the source position. They detected at least one emission line for 23/26 SPT sources and concluded that the remaining three sources have redshifts of $z = 1.7-2.0$, which is the unobservable redshift range in their survey. We show their results in the middle panel of 4.5 adopting the

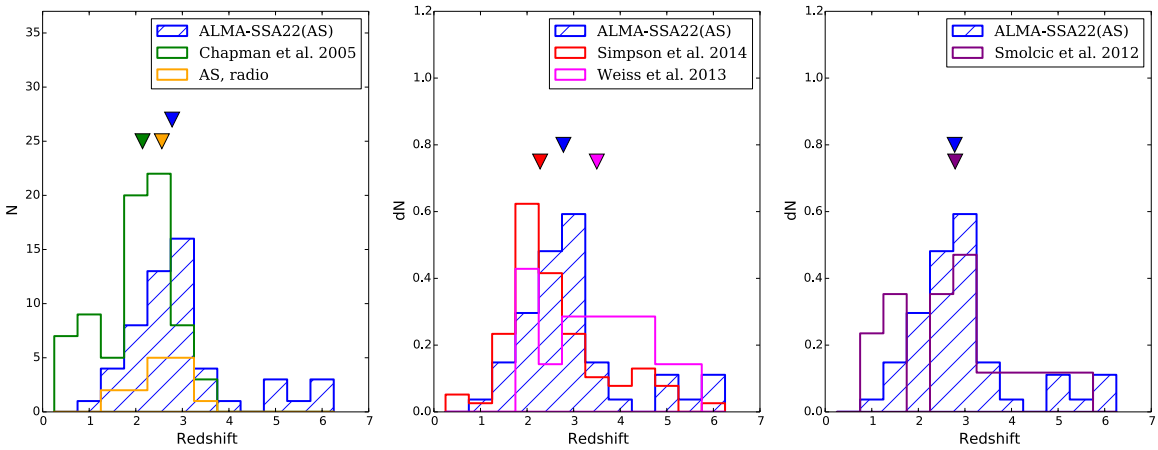

Fig. 4.5 The redshift distributions of SMGs. For all three diagram we plot the result of our survey using blue histograms. Note that we not include 10 optically faint SMGs here. For each panel the median redshifts are shown with triangles for each survey. **(left)** The green histogram stands for the spectroscopic redshift distributions of radio-identified SCUBA SMGs (Chapman et al. 2005). The orange one represent the distribution of radio-detected ALMA sources in the SSA22. **(middle)** The distributions for two ALMA surveys of 870 μm selected SMGs. The red histogram shows the results of ALESS survey (Simpson et al. 2014b) and the magenta one is from SPT-ALMA survey (Weiß et al. 2013). **(right)** The redshifts of 1.1 mm selected SMGs in Smolčić et al. (2012) are shown.

most plausible value derived in Weiß et al. (2013) for single line detection sources. They reported that $\geq 50\%$ of the SMGs lie at $z > 3$, which is consistent with our survey. On the other hand, their histogram represents flat profile at $z = 2.5 - 4.5$m which is very different with our survey as well as ALESS survey. As they referred in Weiß et al. (2013), this discrepancy can be generated by the fact that the SPT sources are though to be highly magnified lensed SMGs. Simpson et al. (2014b) indicate that the redshift distribution of SPT sources get closer to that of ALESS sources, applying the correction considering the probability of strong gravitational lensing. According to the estimate in Weiß et al. (2013), the probability increase from 5×10^{-5} at $z = 1.5$ to 20×10^{-5} at $z = 6$ assuming magnifications of μ=10 and no size evolution. In addition, recent studies suggest that the size of SMGs can also be a factor. Simpson et al. (2014a) and Ikarashi et al. (2014) report the compact nuclei (a diameter of 1-2 kpc) of dusty starbursts at $z \geq 3$. Though the dependence on redshift is still controversial, the size might decrease as the redshift increase. If so, the size evolution would also contribute to make the redshift distribution flatter.

Smolčić et al. (2012) reported the redshift distributions of 1.1 mm selected (and AzTEC selected) SMGs based on direct submm/mm identification and therefore the best sample for comparison with our survey. Their redshift information comprise of spectroscopic red-

shifts and optical to near-infrared photometric redshifts as well as mm to radio photometric redshifts. The mm/radio technique only provide with lower limits. As shown in the right panel of Figure 4.5, the distribution and derived median redshift ($z = 2.79^{+0.39}_{-1.43}$) appear to be similar. And we can also recognize a peak at $z \sim 3$ in their distribution. Thus it is not clear yet whether the $z = 3.1$ large-scale structure give a significant impact on the redshift distributions or not.

4.2 Stellar Mass

4.2.1 Importance

Stellar mass is one of the most important parameters to address the nature of SMGs. Firstly stellar mass can be a key to trace the evolution of massive galaxies through the cosmic history. The violent star-formation activity (SFR$\sim 10^3$) of SMGs suggests that these galaxies are at a rapid growth phase of stellar components. This makes them the most plausible candidates of the ancestors of local massive ellipticals which have uniformly old stellar populations(e.g., Bower et al. 1992, Kauffmann et al. 2003). Bell et al. (2003) pointed out that about 60 % of the stellar mass in ellipticals in the early universe. It has been also discovered that half of the most massive galaxies ($M_* > 10^{11}$ $M_\odot$) at $z \sim 2$ are old compact quiescent systems (e.g., van Dokkum et al. 2004, van Dokkum et al. 2008) and their evolved, dense stellar populations suggest formation within intense, compact starbursts 1–2 Gyr earlier (at $3 \leq z \leq 6$) (e.g., Whitaker et al. 2013, Bedregal et al. 2013). Therefore it is essential to understand the stellar mass assembly in SMGs in unveiling the evolutionally link.

Secondly stellar mass provides us with a unique tool to characterize the various physical properties of SMGs such as specific star formation rate (sSFR), the ratio of galaxy mass and SMBH mass, and gas mass fraction. Unless we derive stellar mass, we cannot calculate these important properties. The SSA22 field is a biased filed and stellar mass can be a key to parameterize the environmental dependence on the growth and assembly of stellar contents in SMGs.

4.2.2 Method

We calculate stellar mass of ALMA sources from their absolute H-band magnitudes as well as previous works (e.g., Hainline et al. 2011, Wardlow et al. 2011, and Simpson et al. 2014b). As illustrated in detail in Hainline et al. (2011), there are several benefit to use H-band magnitude instead of K-band magnitude, which was the representative way before (e.g., Borys et al. 2005, Michałowski et al. 2010). Although the rest-frame K-band are

also insensitive to dust obscuration, the H-band is the better choice to limit the effect of thermally pulsating asymptotic giant branch (TP-AGB) stars (Henriques et al. 2011). The absolute H-band magnitude (M_H) is derived from the best-fit SEDs. We adopt the MOIRCS H band filter to calculate M_H in HYPERZ code for all ALMA sources. The estimated M_H are summarized in Table 4.8 – 4.9.

The stellar mass is calculated assuming a mass to luminosity ratio (M_*/L_H) derived in Hainline et al. (2011), which is based on the large number of SMG counterparts with spectroscopic redshifts and expected to be the most reliable. They utilized BC03 templates with Chabrier IMF as well as us and obtain $M_*/L_H = 0.17\ M_\odot L_\odot^{-1}$ and $M_*/L_H = 0.13\ M_\odot L_\odot^{-1}$ for constant and single burst star formation history, respectively. The two represent extreme star formation history and here we adopt the averaged value, $M_*/L_H = 0.15\ M_\odot L_\odot^{-1}$ for all ALMA sources in the SSA22. Hence stellar mass is calculated as:

$$M_* = 10^{-0.4(M_H - 4.71)} \times 0.15(M_\odot) \tag{4.2}$$

where 4.71 is the absolute H-band magnitude of the Sun. This estimate are for Chabrier IMF and would be higher by a factor of 1.8 (Hainline et al. 2011) if we assume Salpeter IMF (Salpeter 1955).

4.2.3 Results

Results are shown in Table 4.8 – 4.9 and Figure 4.6. The median absolute magnitude of 54 ALMA sources with ≥ 3 band detections is $M_H = -24.35^{+0.16}_{-0.33}$. Stellar mass corresponding this magnitude is $M_* = 6.3 \times 10^{10}$ $M_\odot$ and $M_* = 1.1 \times 10^{11}$ $M_\odot$ for Chabrier IMF and Salpeter IMF, respectively.

We, however, must note that to estimate stellar mass of SMGs is not easy and the above result contain large uncertainties. Our survey mostly relies on photometric redshifts and therefore the redshift information itself should contain significant uncertainty. SMGs tend to optically faint, which results in hampering to restrict star formation history. Simpson et al. 2014b found that the mass to light ratio have large diversities ($> 3\times$ for $\sim 40\%$ of the ALESS sources) between the constant/burst star formation history, though it is difficult to distinguish them through SED fitting. Furethremore IMF is crucial. In the following sections, we utilize the derived individual stellar mass estimate while being careful.

4.2.4 Comparison with other surveys

As shown in Figure 4.6, ALMA survey in the SSA22 and ALESS survey represent similar median absolute magnitudes. The ALESS survey and radio-identified survey in Chapman

et al. (2005) have the median value of $M_H = -24.56^{+0.22}_{-0.34}$ and $M_H = -24.45 \pm -0.20$, which is consistent with our estimates. Whilst ALMA sources in our survey tend to lie at higher redshift compared to the two survey as discussed previous sections, we cannot find significant deference in the representative value of stellar mass. Therefore this result might stand for the similarity in stellar components in 870μm selected SMGs and 1.1mm selected SMGs.

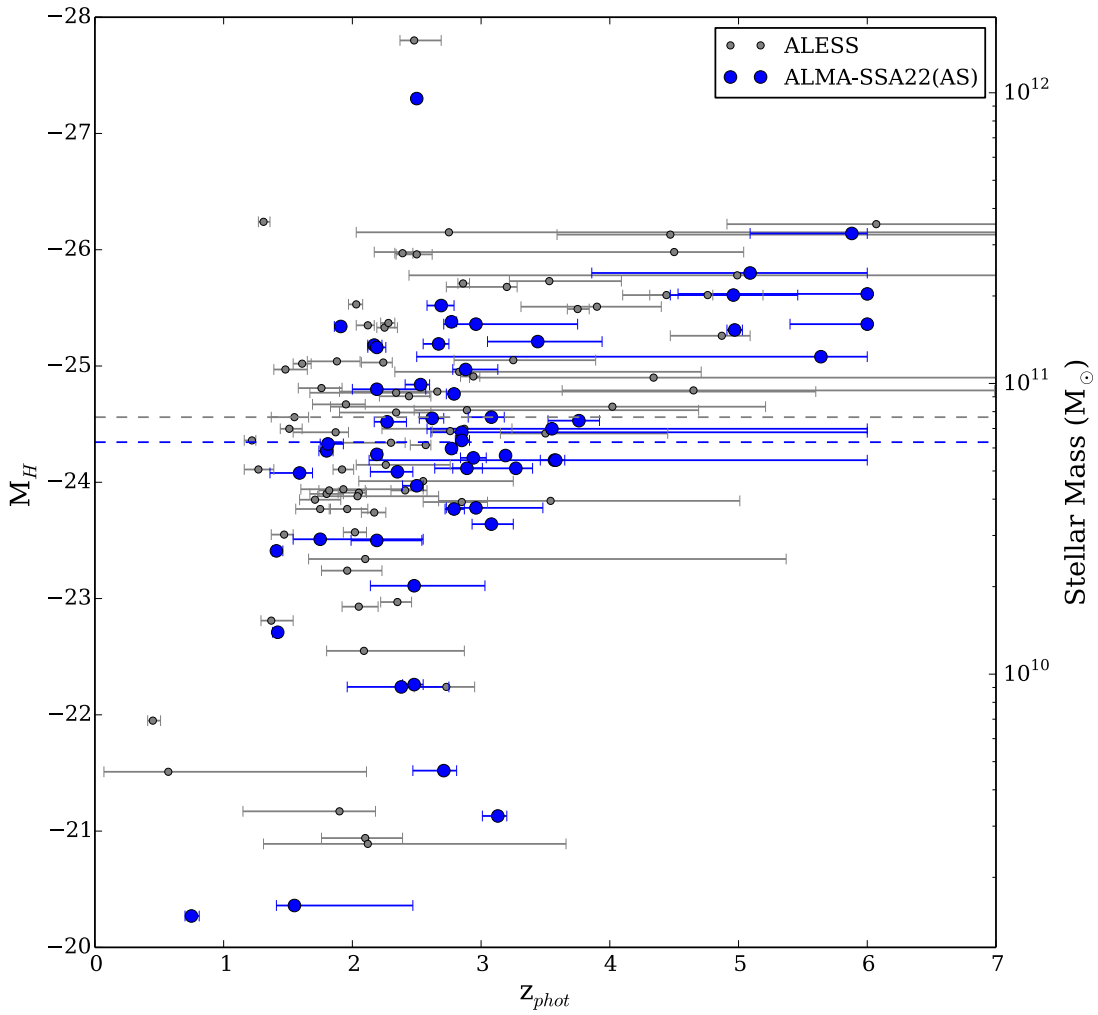

Fig. 4.6 The rest-frame H-band absolute magnitudes of ALMA sources in the SSA22 against photometric redshifts. Here 54 ALMA sources with ≥ 3 band detections are considered. For comparison, we also show the results of ALESS survey (Simpson et al. 2014b). The dashed lines show the median absolute magnitudes.

Chapter 5

AGNs and SMBHs in SMGs

5.1 Chandra X-ray Observations

5.1.1 X-ray Source Catalog

An ultra-deep X-ray survey taken with the ACIS-I (Advanced CCD Imaging Spectrometer) camera (Garmire et al. 2003) onboard *Chandra* was conducted in the central 330 arcmin^2 field of the SSA22 (P.I.: D.M. Alexander). The details of the observations and data analysis were reported in Lehmer et al. (2009b) and here we just describe them briefly. The observations were carried out from October to December 2007. The *Chandra* survey comprises of four individual exposures of 70-120 ks and totally at most 392 ks exposure time was achieved. Though the variation in the exposure time across the map is large, a point-source sensitivity limit of 4.8×10^{-17} erg s^{-1} cm^{-2} and 2.7×10^{-16} erg s^{-1} cm^{-2} are achieved in the soft band (0.5–2.0 keV) and the hard band (2.0–8.0 keV), respectively. Totally 297 X-ray point sources[1] has been discovered over the entire field.

5.1.2 Catalog Matching

As shown in Figure 5.1, 29/45 ALMA fields are within the area observed by *Chandra*. We compare the coordinates of the ALMA sources with those of Chandra sources to find that three ALMA SMGs, ASA 1.1, ASA1.2, and ASA14.1, have X-ray counterparts with a angular offset of smaller than $0''.5$, not considering the positional error in each catalog. We cannot find any additional combination even if we relax the criteria to the acceptable offset of $< 1.5''$. In addition, there are three 870 μm-detected SMGs, which have been originally selected as *Chandra* sources, SA-AGN1.1, SA-AGN5.1, and SA-AGN7.1. Among them,

[1]The catalog is available at http://astro.dur.ac.uk/ dma/SSA22/

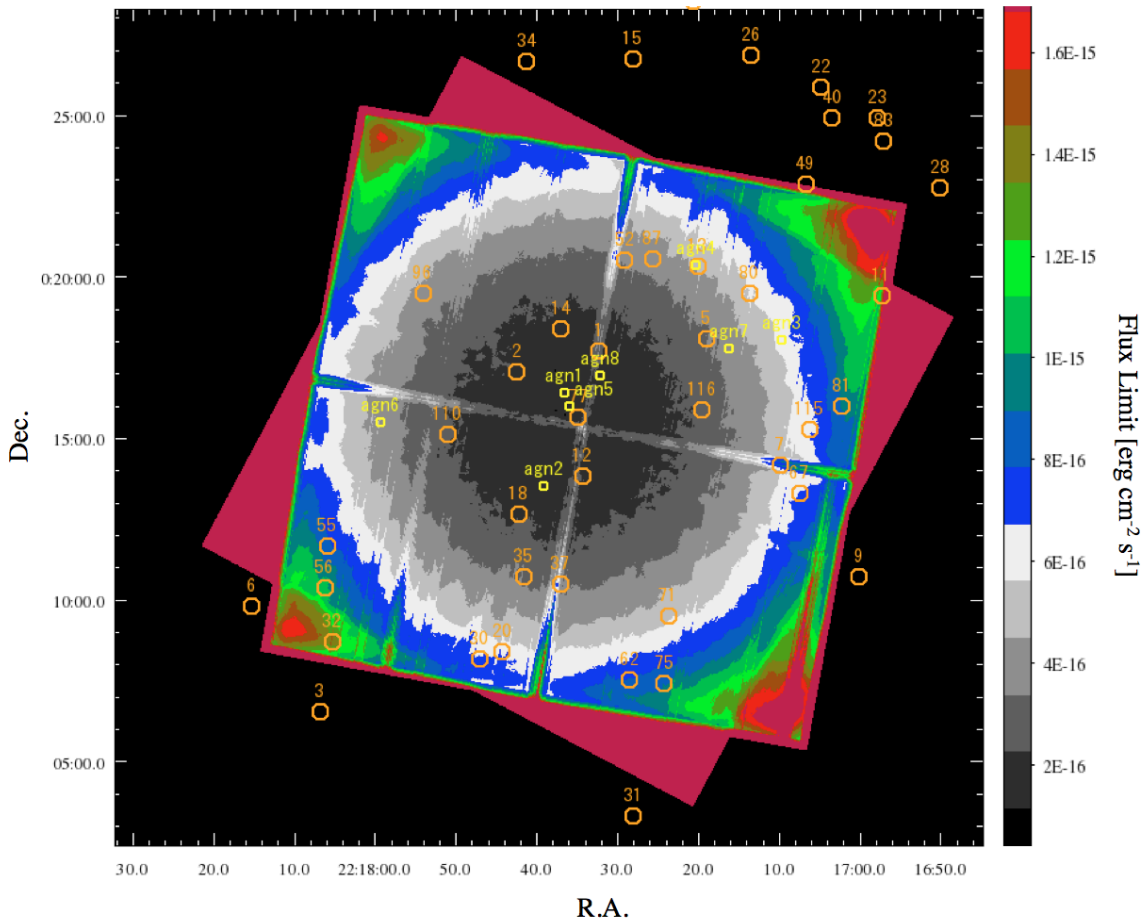

Fig. 5.1 Full-band (0.5–8.0 keV) X-ray sensitivity map for the SSA22 field (Lehmer et al. 2009b). The back ground color scale shows the area with each flux limit, representing in the right color bar. Orange circles with a diameter of 30″ stand for our ALMA 1.1 mm survey area and each number corresponds to the AzTEC ID. We also plot the observed position in the ALMA 870 μm survey (cycle0, Alexander et al.) using yellow circles.

we note that SA-AGN7.1 is detected in the ALMA image 1.5″ away from X-ray position and 3.1″ away from LAE position as shown in Figure 5.2. In addition we can recognize a K-band source at the exact X-ray source position. Due to heavy source blending in IRAC bands, it is impossible to derive secure photometric redshifts for the three sources individually (, though we have spectroscopic redshift for the LAE). Therefore in principal we exclude SA-AGN7.1 in the following discussion because it is not clear whether SA-AGN7.1 really corresponds to the *Chandra* source.

We summarized the matching result in Table 5.1. Totally there are five X-ray detected SMGs. We show the X-ray images at 0.5–2.0 keV and 2.0–8.0 keV in Figure 5.3 and Figure 5.4 as well as the pseudo two-color images of both bands. It is interesting that all five SMGs with X-ray counterparts are considered to be at $z = 3.1$. ASA 1.1 has $z_{\rm phot}$ of $2.96^{+0.79}_{-0.25}$ as derived in section 4.1.3 and Tamura et al. (2010) estimated mid-infrared to radio photometric redshift of $3.19^{+0.26}_{-0.35}$. Furthermore the marginal detections of ^{12}CO(3-2) molecular line was obtained with NRO45m and LMT30m observations (Umehata et al. in prep, Figure B.3). ASA 1.2 is estimated as $z_{\rm phot} = 3.08^{+0.17}_{-0.15}$ as shown in Table 4.8. ASA 14.1 has a counterpart of a $z = 3.1$ Lymanα absorber (LAA), which is the Lyα line-absorbing object that lacks a NB497 flux relative to the adjacent BV band, indicating a galaxy rich in Lyα absorbing material at $z = 3.1$. The derived $z_{\rm phot}$ of $2.19^{+0.04}_{-0.02}$ isn't reliable due to source blending as mentioned in section 4.1.1. The two 870 μm selected SMGs have $z_{\rm spec}$ of 3.084 (ASA1.1) and 3.089 (ASA5.1). Therefore we conclude all five are $z = 3.1$ sources.

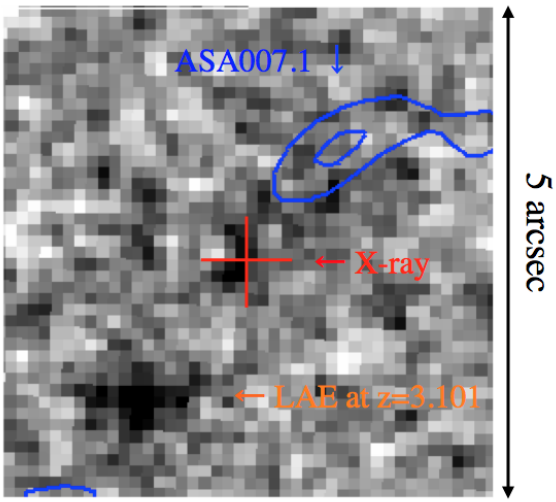

Fig. 5.2 The enlarged MOIRCS Ks-band image around AGN007.1. The position of X-ray source in Lehmer et al. (2009b) is shown using a red cross, of which size stands for 1σ positional uncertainties. The $z_{\rm spec} = 3.101$ LAE position are also printed. The contours represent 870 μm emission (SA-AGN007.1).

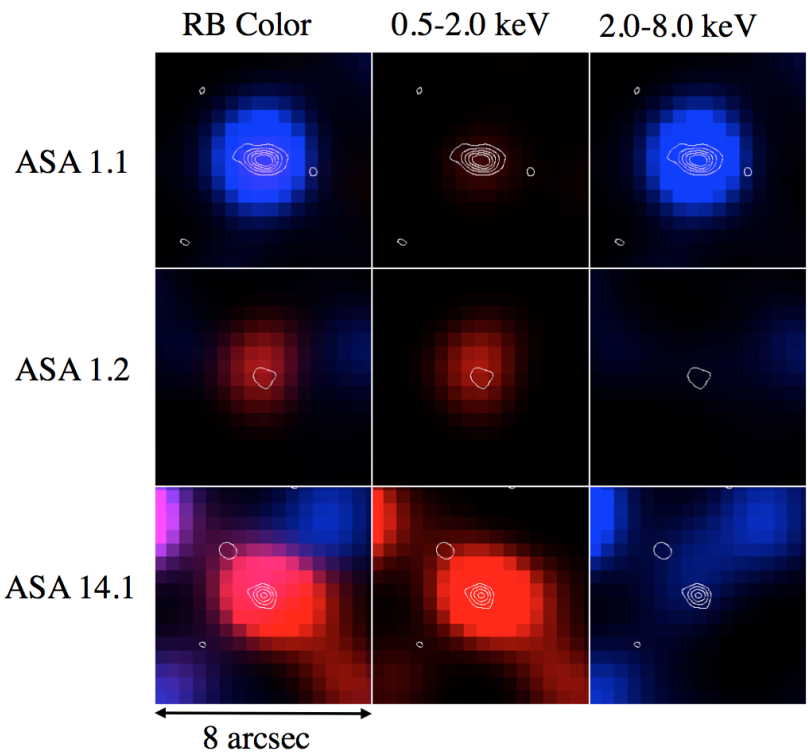

Fig. 5.3 X-ray images of the SMGs with X-ray counterparts in the ALMA 1.1 mm survey. Each left panel shows a pseudo two color map (red: soft band (0.5–2.0 keV), blue: hard band (2.0–8.0 keV)) and the middle and right panel represents soft and hard band images. All panels are centered at ALMA positions. We also superpose ALMA emission at 1.1 mm on each panel using white contours in steps of 3.0σ ($1\sigma \sim 0.16$ mJy beam^{-1}). Each ALMA source ID is shown on the left side of panels.

5.2 SMGs as AGN-host galaxies

5.2.1 X-ray Properties

The detailed properties of each X-ray counterpart are summarized in Table 5.2. The fundamental quantities such as net counts, count rate, band ratio, and effective photon index ($\Gamma_{\rm eff}$) are from Lehmer's catalog (Lehmer et al. 2009b). Additionally we estimate flux, luminosity, and hydrogen column density, modeling the X-ray spectrum with Portable, Interactive Multi-Mission Simulator (PIMMS) v.4.7b [2] as well as Tamura et al. (2010). The Galactic column density for SSA22 is 4.1×10^{20}cm^{-2} (Kalberla et al. 2005). All five sources are

[2]the PIMMS package is available from http://heasarc.gsfc.nasa.gov/docs/software/tools/pimms.html

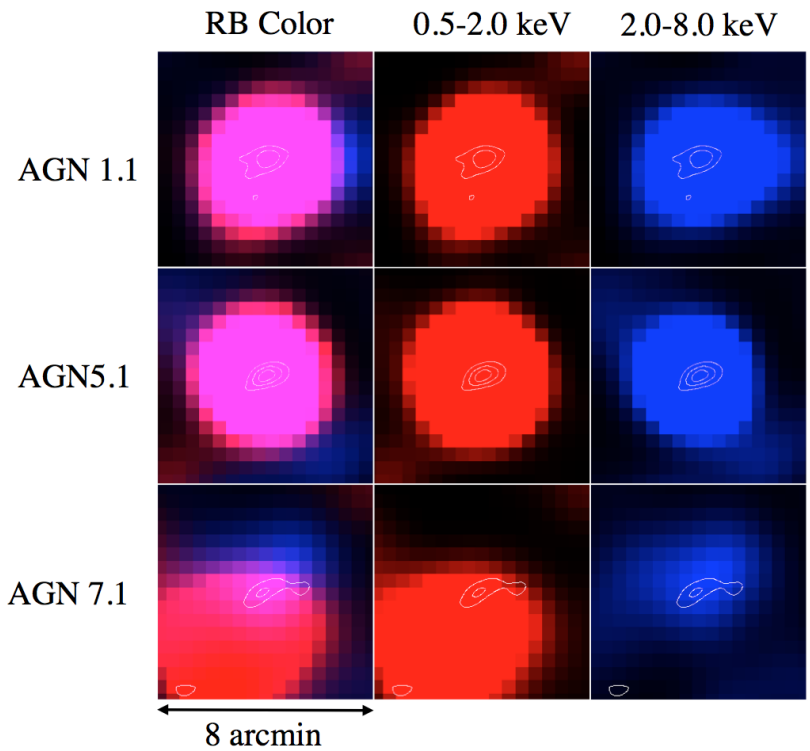

Fig. 5.4 X-ray images of the 870 μm-selected SMGs in a similar way of Figure 5.3. The $3\sigma, 6\sigma$, and 9σ contours are shown (1σ= 0.21-0.27 mJy beam^{-1}) .

considered to be at $z = 3.09$ here[3]. The X-ray counterparts have merely full band net counts of 5–65 so that complicated analysis using XSPEC is difficult. That is why we only consider a single power low intrinsic spectra in the modeling. We adopt a photon index of $\Gamma_{\rm int} = 1.8$ since it is a typical value for nearby AGNs (e.g., Tozzi et al. 2006). The column density is derived based on the 2.0–8.0 keV (hard) band to 0.5–2.0 keV (soft) band count rate ratio (band ratio) as illustrated in Figure 5.5. We derive the apparent (i.e., no–absorption correction) flux and intrinsic (i.e, absorption corrected) flux from count rates using PIMMS. The rest-frame 0.5–8.0 keV luminosity is calculated as

$$L_{0.5-8\rm keV} = 4\pi d_{\rm L}^2 f_{0.5-8.0\rm keV}(1+z)^{\Gamma-2} \tag{5.1}$$

where $d_{\rm L} = 26.4$ Gpc is the luminosity distance, $f_{0.5-8.0\rm keV}$ is flux density at observed frame 0.5–8.0 keV, and Γ is photon index. In calculating the apparent luminosity, we set $\Gamma_{\rm eff} = 1.4$ for ASA1.2 and ASA14.1, which is representative for faint sources that should give reason-

[3]Though the three 1.1 mm-selected SMGs don't have spectroscopic redshift yet, their photometric redshifts and the existence of the Lyman-alpha absorber suggest that the three lie within the $z = 3.09$ large-scale structure.

able fluxes (e.g., Lehmer et al. 2009b). Though ASA 1.2 and ASA 14.1 weren't detected in the hard band, the five X-ray SMGs is likely to be heavily obscured ($N_{\rm H}$=10^{23-24}) and generally have intrinsically large X-ray luminosity ($L_{0.5-8{\rm keV,corr}} \sim 10^{44}$ erg s^{-1}).

We should note that our estimates rely on a simple model and can be affected by several factors not considered here. For instance, it is predicted that not only an absorbed power low component but also refection and scattering components can contribute to shape the X-ray spectrum if a X-ray source have high ($> 5 \times 10^{23}$ cm^{-2}) column density (e.g., Tamura et al. 2010). And the faint X-ray sources such as ASA 1.2 and ASA 14.1 can suffer the Eddington bias and can have intrinsically fainter flux. Here, however, the low counts prevent us from the more complicated analysis and we adopt the values above.

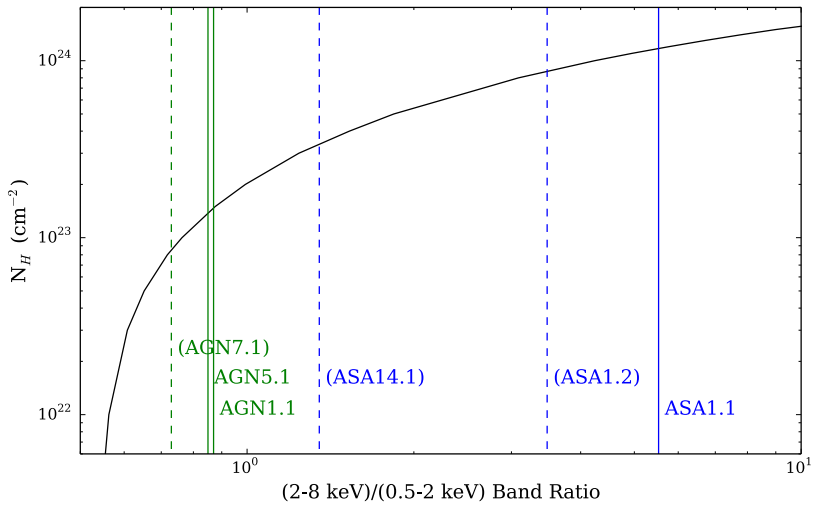

Fig. 5.5 The simulated intrinsic hydrogen column density against the band ratio between the 2.0–8.0 keV (hard) band and 0.5–2.0 keV (soft) band with PIMMS v4.7b. The solid vertical lines show the obtained band ratio and the dashed line shows the upper limit. The 1.1 mm selected SMGs and the 870 μm selected SMGs are represented with blue and green lines.

ALMA ID [a]	$S_{\mathrm{BEST,pbcorr}}$ [b] (mJy)	X-ray ID [c]	X-ray Position [d] R.A. , DEC. (J2000)	Offset [e] ($''$)	z
ASA 001.1	6.40 ± 0.27	L120	22 17 32.42 +00 17 43.9	0.08	$2.96^{+0.79}_{-0.25}$
ASA 001.2	1.44 ± 0.20	L116	22 17 32.19 +00 17 36.0	0.41	$3.08^{+0.17}_{-0.15}$
ASA 014.1	2.24 ± 0.13	L142	22 17 36.97 +00 18 20.8	0.15	$2.19^{+0.04}_{-0.02}$ (3.1?) [f]
AS-AGN 001.1	2.52 ± 0.18	L140	22 17 36.54 +00 16 22.6	0.15	3.084
AS-AGN 005.1	3.08 ± 0.15	L139	22 17 35.84 +00 15 59.1	0.15	3.094
(AS-AGN 007.1	2.38 ± 0.28	L043	22 17 16.16 +00 17 45.8	1.48	3.101[g])

Table 5.1 The catalog of X-ray detected SMGs.
[a]: ID in this work.
[b]: 1.1 mm (sources named as ASA) or 870 μm (sources named as AS-AGN) flux density measured by ALMA.
[c]: Source ID in the catalog of Lehmer et al. (2009b).
[d]: Coordinate in the catalog of Lehmer et al. (2009b).
[e]: The angular offset between ALMA position and *Chandra* position calculated from our catalog and Lehmer et al. (2009b) catalog.
[f]: The derived photometric redshift is not very reliable due to heavy source blending in some bands. This sources is likely to be a $z = 3.1$ Lyman alpha absorber (LAA).
[g]: The ALMA source position is $\sim 1''$ away from the $z = 3.101$ LAE.

ALMA ID [a]	FB [b] Counts	Band [c] Ratio	$\Gamma_{\rm eff}$ [d]	$L_{0.5-8\rm keV}$ [e] (log ergs s^{-1})	$\Gamma_{\rm int}$ [f]	$N_{\rm H}$ [g] (10^{23} cm^{-2})	$L_{0.5-8\rm keV,corr}$ [h] (log ergs s^{-1})	$L_{1.4\rm GHz}$ [i] (W Hz^{-1})
ASA 001.1	$19.74^{+6.22}_{-4.90}$	$5.53^{+8.46}_{-3.24}$	$-0.34^{+0.57}_{-0.61}$	42.8	(1.80)	11.6	44.5	24.65
ASA 001.2	$5.58^{+4.20}_{-2.77}$	<3.48	(1.40)	43.2	(1.80)	<8.8	<43.8	< 24.48
ASA 014.1	$14.46^{+5.76}_{-4.44}$	<1.35	(1.40)	43.3	(1.80)	<3.4	<43.8	< 24.40
AS-AGN 001.1	$51.81^{+9.10}_{-7.85}$	$0.87^{+0.33}_{-0.26}$	$1.09^{+0.29}_{-0.29}$	43.6	(1.80)	1.5	44.2	< 24.44
AS-AGN 005.1	$65.80^{+10.07}_{-8.82}$	$0.85^{+0.28}_{-0.23}$	$1.11^{+0.26}_{-0.25}$	43.7	(1.80)	1.4	44.3	< 24.44

Table 5.2 X-ray Properties of ALMA SMGs. All six SMGs are considered to be at $z = 3.09$.
[a]: ID in this work.
[b]: Full band counts (Lehmer et al. (2009b)).
[c]: Observed counts ratio between hard (2.0–8.0 keV) and soft (0.5–2.0 keV) bands (Lehmer et al. (2009b)).
[d]: Effective photon index (Lehmer et al. (2009b)). For ASA001.2, ASA014.1, and AS-AGN007.1, we set 1.4 because of low counts.
[e]: Rest-frame 0.5–8.0 keV apparent luminosity.
[f]: Intrinsic photon index. We set 1.8 for all sources because of low counts.
[g]: Intrinsic column density derived from PIMMS.
[h]: Rest-frame 0.5–8.0 keV absoroption-corrected luminosity.
[i]: Rest-frame 1.4 GHz luminosity (or 4σ upper limits).

5.2.2 AGN Diagnostics

Our focus is to identify AGNs hosted in SMGs. For this purpose, we need to assess the origin of the X-ray emission (i.e., AGNs or star-fomation). Here we applied four classification methods suggested in previous works (e.g., Alexander et al. 2005, Xue et al. 2011, Lehmer et al. 2008, Bauer et al. 2004, Wang et al. 2013b) for the five X-ray detected SMGs.

Effective Photon Index

The effective X-ray slope (or photon index, $\Gamma_{\rm eff}$) can provide us with a useful tool for this classification if the SMGs present hard ($\Gamma_{\rm eff} < 1.0$) signature (e.g., Alexander et al. 2005). For most cases, star-forming galaxies without recognizable AGNs and unobscured AGNs have similar steep X-ray spectra ($\Gamma_{\rm eff} \sim 2$) (e.g., Kim et al. 1992b, Kim et al. 1992a, Nandra & Pounds 1994, Ptak et al. 1999, Lehmer et al. 2010). Compared with them, obscured AGNs present a flat ($\Gamma_{\rm eff} < 1.0$) spectra because softer X-ray emission suffered photoelectric absorption more effectively (e.g., Maiolino et al. 1998, Risaliti et al. 1999). Hence we regard a SMG of which a X-ray counterpart has effective photon index of $\Gamma_{\rm eff} < 0.5$ as an AGN-host SMGs as well as Alexander et al. (2005). (While Wang et al. (2013b) adopted a criteria of $\Gamma_{\rm eff} < 1.0$, Alexander et al. (2005) pointed that high-mass X-ray binary (HMXB) in star-forming galaxies can produce comparatively flat X-ray spectra ($\Gamma_{\rm eff} \sim 0.5 - 1$). Here we adopt a strict criteria following Alexander et al. (2005).) In Figure 5.6, we stand for effective photon index against X-ray luminosity for our data as well as ECDF-S(Wang et al. 2013b) and CDF-N (Alexander et al. 2005). In the following discussion, we exclude ALESS66.1. It is listed as a AGN-host SMGs in Wang et al. (2013b) but a recent paper from ALESS team contradicted that based on their newly followup spectroscopy. Consequently ASA1.1 is classified as an AGN shown in Figure 5.6.

Absorption-corrected X-ray Luminosity

Second, we focus on the absorption-corrected (i.e., intrinsic) X-ray (0.5–8.0 keV) luminosity. Previous works suggest that all local star-forming galaxies have X-ray luminosities of less than 3×10^{42} erg s^{-1} (e.g., Zezas et al. 2001, Ranalli et al. 2003), which enable us to consider a X-ray source with X-ray luminosity of more than 3×10^{42} erg s^{-1} as an AGN. We adopt the luminosity as one of the classification methods like Bauer et al. (2004), Lehmer et al. (2008), Xue et al. (2011), and Wang et al. (2013b). All five SMGs in the SSA22 satisfy the criteria and we consider them as AGNs, though ASA2.1 and ASA14.1 have just upper limit due to the non-detection in the 2–8 keV band.

X-ray Luminosity vs Radio Luminosity

Next, we directly compare the apparent X-ray luminosity with the expected X-ray luminosity from star-formation activity. We follow the methods described in Wang et al. (2013b) and derived expected amount of X-ray luminosity assuming that the observed 1.4 GHz emission is arisen by star-formation. First we calculate the rest-frame 1.4 GHz monochromatic luminosity of $L_{1.4\mathrm{GHz}}$ following Alexander et al. (2003) as

$$L_{1.4\mathrm{GHz}} = 4\pi d_{\mathrm{L}}^2 f_{1.4\mathrm{GHz}} 10^{-36} (1+z)^{\alpha-1} \mathrm{WHz}^{-1} \tag{5.2}$$

where d_L is the luminosity distance in the unit of cm, $f_{1.4\mathrm{GHz}}$ is the 1.4 GHz observed flux density (μJy), and α is the radio spectral index. We assume $\alpha = 0.8$, which is the average spectral index for star-forming galaxies (e.g., Yun et al. 2001), as well as Alexander et al. 2005. Then we derive the expected X-ray luminosity for star-forming galaxies as

$$\mathrm{SFR} = L_{1.4\mathrm{GHz}}/8.93 \times 10^{20} \tag{5.3}$$

$$\log(L_{\mathrm{X,SF}}/1.21) = 39.49 + 0.74\log(\mathrm{SFR}/1.8) \tag{5.4}$$

Equation (6.3) and (6.4) are originally from Persic & Rephaeli (2007) and Lehmer et al. (2010), respectively. The factor 1.8 stand for conversion factor from Kroupa IMF (Kroupa 2001) to Salpeter IMF introduced in Wang et al. (2013b).

Figure 5.7 shows the rest-frame 1.4 GHz luminosity and the rest-frame apparent 0.5–8.0 keV luminosity. Each value is summarized in Table 5.2. Following Wang et al. (2013b), we adopted the criteria of $L_{0.5-8.0\mathrm{keV}} > 5 \times L_{\mathrm{X,SF}}$ to consider the SMGs as AGNs. All SSA22 SMGs but ASA1.1 are considered as AGNs here.

The origin of X-ray detected in SMGs

Summarizing the above, three diagnostics methods support that all five X-ray counterparts are obscured-AGNs. This result might be not worth being surprised since the sensitivity achieved in the SSA22 is not enough to detect X-ray emission from pure star forming galaxies or moderately luminous AGNs at $z = 3.1$ (see the second clarification methods), though this field has one of the deepest X-ray survey. In the following discussion, we consider all five SMGs as AGN-hosts.

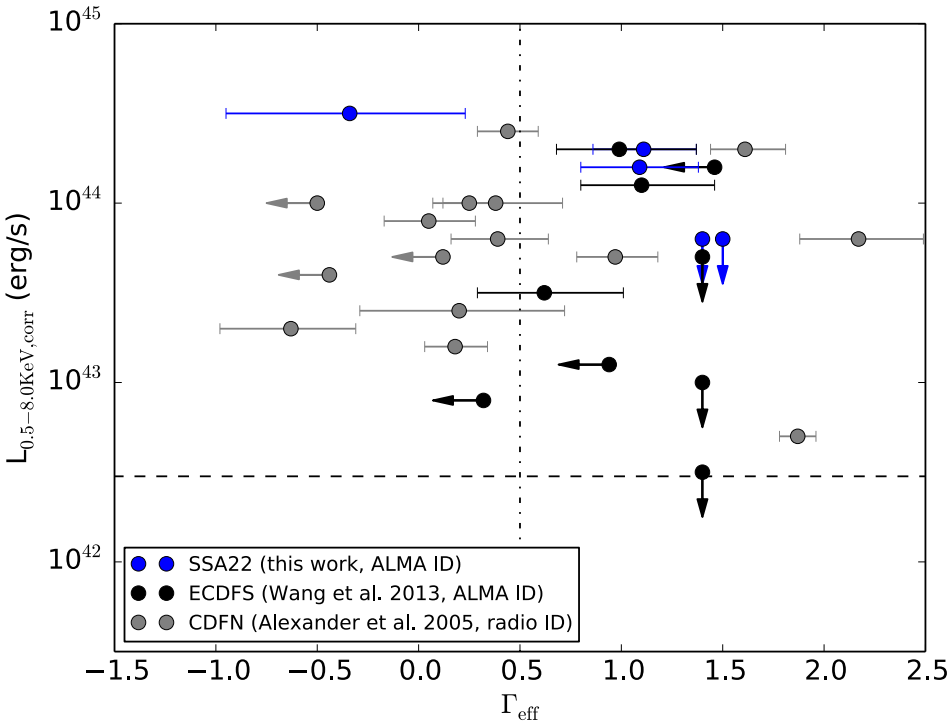

Fig. 5.6 The relation between the effective photon index (Γ_{eff}) and the absorption corrected X-ray luminosity. The five X-ray detected SMGs in the SSA22 are shown using blue circles. AGN1.1 and AGN5.1 have similar value in both axis and therefore we artificially shift a plot for a clear view. For comparison, the properties in ECDF-S (Wang et al. 2013b) and CDF-N (Alexander et al. 2005) are also shown. Please note the sample in CDF-N is not identified by submm/mm interferometers, just identified by radio data. The filled circles stand for sources classified as AGNs in the previous works and the empty circles are sources classified as sources which might be starbursts. The vertical dot-dashed line represents the criteria from the view point of Γ_{eff}. The horizontal dashed line shows the standard line in terms of absorption-corrected X-ray luminosity.

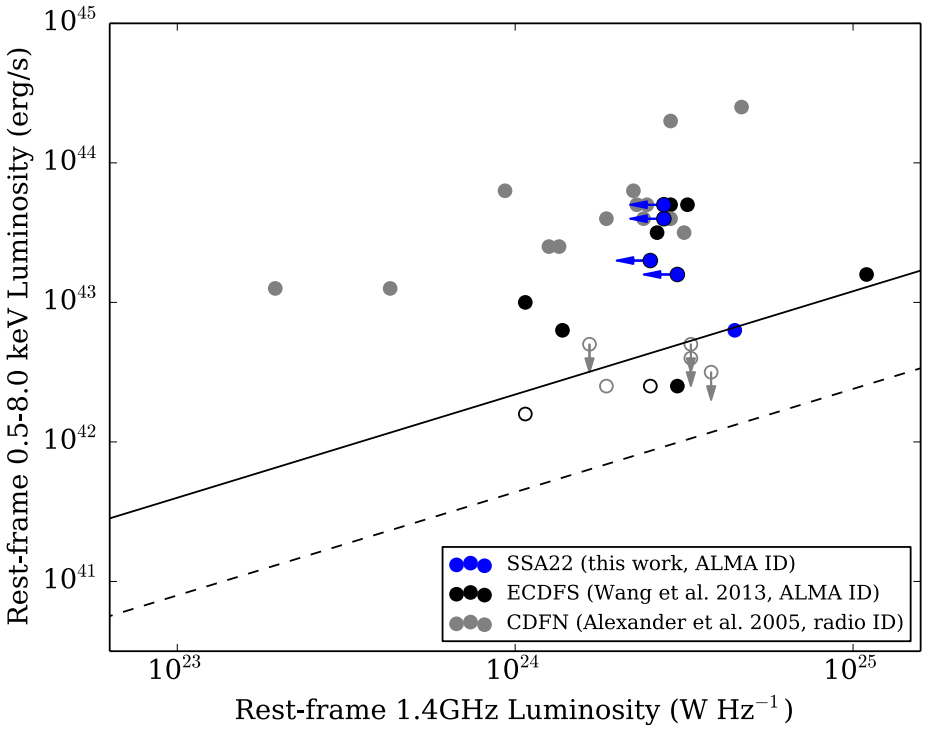

Fig. 5.7 The relation between rest-frame 1.4 GHz luminosity and the apparent rest-frame 0.5–8.0 keV luminosity. The dashed and solid lines stand for $L_{0.5-8.0\mathrm{keV}} = L_{\mathrm{X,SF}}$ and $L_{0.5-8.0\mathrm{keV}} = 5 \times L_{\mathrm{X,SF}}$, respectively. $L_{\mathrm{X,SF}}$ is the expected X-ray luminosity for star-forming galaxies. We also plot the results of previous works similar with Figure 5.6.

5.3 AGN Fraction

In this section, we derive the fraction of SMGs which harbor AGNs (or simply AGN fraction, $f_{\rm AGN}$). Here we only consider AGNs which are detected and identified by *Chandra* X-ray observations in the previous section.

5.3.1 Methodology

The X-ray deep surveys ubiquitously suffer the influence of the inhomogeneous sensitivity limit as shown in Figure 5.1, which can be a critical issue in calculating the AGN fraction. To conquer this difficulty, we calculate the flux-dependent cumulative fraction as well as previous works (Lehmer et al. 2007, Silverman et al. 2008, and Wang et al. 2013a). The AGN fraction ($f_{\rm AGN}$) is calculated as follows:

$$f_{\rm AGN}(f_X \geq f_{X,\rm lim}) = \sum_{i=1}^{N} \frac{1}{N_{\rm SMG},i} \tag{5.5}$$

where $f_{X,\rm lim}$ is the threshold X-ray flux at observed-frame 0.5–8.0 keV, $f_{\rm AGN}(f_X \geq f_{X,\rm lim})$ represents the fraction of SMGs that host X-ray AGNs with X-ray flux of $\geq f_{X,lim}$, $N_{\rm SMG,i}$ is the number of SMGs which have enough X-ray sensitivity to detect the AGNs with X-ray flux of equal or greater than $f_{X,lim}$. In other words, we count the number of SMGs corresponding to each flux of AGN-SMGs (i.e., five points are calculated.) The error is estimated by adding in quadrature the error derived from (3.2) and (3.3).

5.3.2 The AGN fractions

The derived AGN fractions are shown in Figure 5.8 and Table 5.3. To exclude the uncertainty in converting apparent or intrinsic X-ray luminosity, we computed the AGN fraction against the observed-frame X-ray flux and compared it with the result of ALESS survey. Wang et al. 2013a reported that eight ALESS SMGs host AGNs, but the followup spectroscopic observation reveals that ALESS 66.1 hasn't X-ray counterpart and the identified X-ray source is the foreground QSO (Danielson et al, in prep). Hence we except the source and recalculate the AGN fraction of the ALESS survey based on the remaining seven SMGs. The faintest AGN in our survey has flux of $f_{0.5-8.0\rm keV}$=5.0$\times10^{-16}$ erg cm^{-2} s^{-1} and therefore we compare the total AGN fraction based on this flux limit.

As shown in Figure 5.8, the AGN fraction of SSA22 ($16.8^{+1.6}_{-1.2}$ %) is around twice larger than that of ECDF-S ($\sim$ 9%). The AGN fraction in SSA22 would increase to ($32.1^{+2.9}_{-2.0}$ %) if we only consider the SMGs with $2.7 < z < 3.4$ (We discuss this criteria in the next chapter

in detail). Only one of seven ALESS AGN-host SMGs lie at this redshift range ($z = 2.94$) and therefore the difference between the two regions is obvious. We will focus on this issue in the next chapter in more detail.

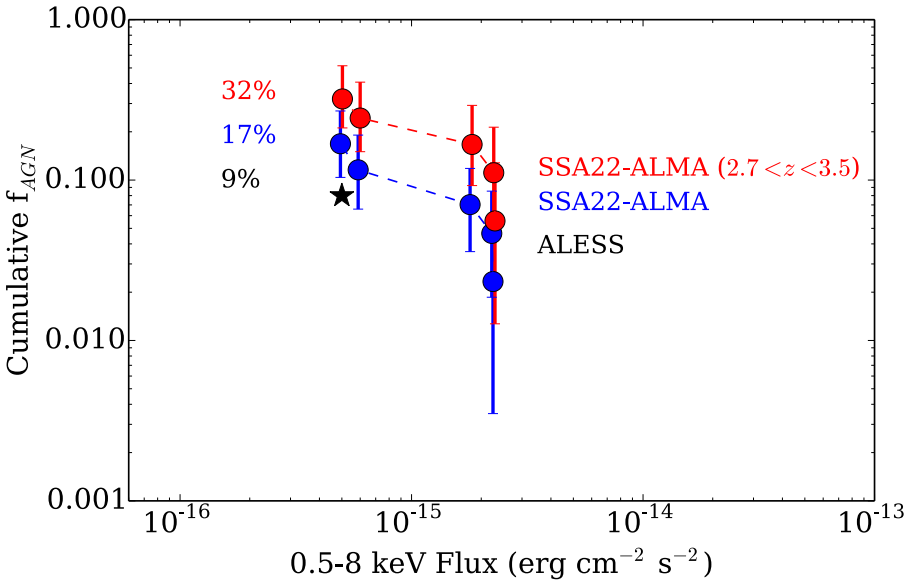

Fig. 5.8 The derived AGN fraction considering the spatial inhomogeneity of the X-ray sensitivity limit. While the blue plots show the AGN fraction of all SMGs in SSA22, the red points represent the fraction of $2.7 < z < 3.5$ SMGs in the SSA22. The inserted percentages are the AGN fraction at the sensitivity limit of 5×10^{-16} erg cm^{-2} s^{-1} for the two SSA22 samples as well as the ALESS survey.

ALMA ID [a]	$S_{\mathrm{BEST,pbcorr}}$ [b] (mJy)	$f_{0.5-8.0\mathrm{keV}}$ [c] (10^{-15} erg cm^{-2} s^{-1})	f_{AGN} [d] %	$f_{\mathrm{AGN,z\sim3}}$ [e] %
AS-AGN 005.1	3.08 ± 0.15	2.25	$2.3^{+0.4}_{-0.4}$	$5.6^{+1.7}_{-1.3}$
ASA 001.1	6.40 ± 0.27	2.22	$4.7^{+0.6}_{-0.5}$	$11.1^{+2.4}_{-1.8}$
AS-AGN 001.1	2.52 ± 0.18	1.79	$7.0^{+0.7}_{-0.6}$	$16.7^{+2.9}_{-2.2}$
ASA 001.2	1.44 ± 0.20	0.59	$11.6^{+1.4}_{-1.1}$	$24.3^{+4.1}_{-3.0}$
ASA 014.1	2.24 ± 0.13	0.49	$16.8^{+2.1}_{-1.6}$	$32.1^{+5.0}_{-3.6}$

Table 5.3 The catalog of X-ray detected SMGs.
[a]: ID in this work.
[b]: 1.1 mm (sources named as ASA) or 870 μm (sources named as AS-AGN) flux density measured by ALMA.
[c]: The observed-frame apparent 0.5–8.0 keV flux.
[d]: Cumulative AGN faction at each threshold considering all SMGs.
[e]: Cumulative AGN faction at each threshold considering only SMGs with $2.7 < z < 3.5$.

Chapter 6

Dusty Starburst Formation and SMBH Growth in the z=3.1 Proto-cluster

6.1 Dusty Starburst Formation at a z=3 Biased Environment

The SSA22 field is known for having a remarkable large-scale structure at $z = 3.1$, traced by more than 1000 narrow-band (NB) selected LAEs across over 1 deg^2 (Steidel et al. 2000, Hayashino et al. 2004, Matsuda et al. 2005, Yamada et al. 2012). Yamada et al. (2012) found that the SSA22 field has an extremely high dense region in $\sim$30 Mpc scale (co-moving), where number density of LAEs corresponds to 8–10 times the standard deviation derived from general fields. Yamada et al. (2012) also estimated the underlying mass fluctuation assuming the standard ΛCDM model. Consequently they derived that the $\sim$20 Mpc scale over density region represents 19 times larger mass fluctuation than that of the averaged value. Thus this field is one of the most massive environment in the era and expected to be a unique laboratory to investigate the influence of density environment on galaxy formation.

The AzTEC/ASTE 1.1 mm survey swept over 900 arcmin^2 sky area, which covers the central part of the SSA22 large-scale structure and contain the densest region, which is suggested by previous studies (e.g., Hayashino et al. 2004, Kubo et al. 2013), completely (Tamura et al. 2009 and Umehata et al. 2014), and provided us with a complete flux-limited SMG catalog from the single-dish survey with a coarse angular resolution. Subsequent ALMA 1.1 mm survey allowed us to know the accurate position and flux for the majority of such dusty starbursts. Therefore now that we can shed the light on a number of unexplored spheres related to the environmental dependence such as the amount of obscured star formation activity, the location of dusty starbursts, characteristics of such obscured starbursts, and

a trigger of violent starbursts, as well as the contribution to the whole cosmic star formation and galaxy formation history.

6.1.1 Excess of SMGs in the SSA22 field

As a first step, we compare the number density of SMGs in SSA22 with that in a general field as a whole. In the followings, we address the selection of a general field, how to define environment, and the results.

The ECDF-S as a control field

The Extended Chandra Deep Field South (ECDF-S), a $30' \times 30'$ field with rich deep multi-wavelength data sets from the radio to the X-ray (e.g., Giacconi et al. 2001, Giavalisco et al. 2004, Lehmer et al. 2005), is adopted for comparison in this work. The reasons are as follows. First the ECDF-S field doesn't have known remarkable overdensities of galaxies and hence it can be used as a good control field. The second is from the viewpoint of SMG surveys. The ALESS survey can provide us with the largest sample of SMGs observed by ALMA at the moment, which were found with LABOCA on the 12-m APEX telescope (Weiß et al. 2009) and were subsequently observed at higher angular resolution with ALMA (Karim et al. 2013, Hodge et al. 2013). Therefore their SMG sample is of the same quality of ours. At last, we can address the environment around SMGs in ECDF-S as well as in SSA22. Gronwall et al. (2007) conducted a panoramic $z = 3.1$ LAE search for almost same area observed by LABOCA and ALMA, which enable us to define the underlying density environment as we describe in details in the next section.

LAEs as a tracer of environment

For our purpose, it is essential to describe the environment each SMG inhabit for both of a biased (SSA22) and a general (ECDF-S) field in an unified way. It is natural to use the number density of known galaxy populations to illustrate the baryonic density distributions and speculate the structure of underlying dark matter halos. To measure spectroscopic redshifts for various galaxies completely is impossible, though it is ideal. Alternatively, NB emitters are anticipated to be a good building block because we can construct flux-limited samples with well-restricted redshifts.

Here we utilize the LAE surface number density as a tool to describe the density environment in the $z = 3.1$ universe. Table 6.1 shows the characteristics of LAE surveys in both fields. Since the two surveys were executed with different telescopes, cameras, and filters, we need to compensate such artificial influence to make the fair comparison. We compare

the two after we unify the threshold of NB sensitivity in AB magnitude ($\mathrm{mag}_{AB} \geq 25.4$) and observed-frame equivalent-width ($\geq$190 Å) and correct a 1.5 times volume difference in a unit area, arising from the bandwidth of NBs which were used in the SSA22 and ECDF-S surveys (77 and 50 Å, respectively; see Table 6.1), in a same way in Yamada et al. (2012). Some of the detected line-emitting objects might not be $z = 3.1$ LAEs, but we consider all candidates in the following discussion, assuming that the fraction of contaminants is negligible in both fields [1].

Up to this point, we succeed to build homogeneous LAE catalogs for both fields. What do these catalogs and the number density of LAEs mean? Shimizu et al. (2011) reported that $z = 3.1$ LAEs are typically hosted by dark matter halos with $\sim 10^{11}$ $\mathrm{M}_{\odot}$ through the comparison between their cosmological hydrodynamical simulation and observations (Ouchi et al. 2008, Gawiser et al. 2006, Hayashino et al. 2004). This predicts that we are approximately seeing the distribution of dark matter halos with relatively small masses via the LAE map. Additionally, as we touched in the beginning of this chapter, Yamada et al. (2012) showed that the density excess seen in SSA22 corresponds to an extraordinary (or unique) mass fluctuation peak. On the other side, Kubo et al. (2013) reveled that the number density of DRGs and K-selected galaxies in SSA22 is also higher than that in a general field and the density peak of these populations is consistent with that of LAEs. This supports that LAE density trace not only young galaxy populations but general density gradient containing massive galaxies. Hereafter we utilize this surface number density of LAEs at z=3.1 as a tracer of galaxy density environment.

In the following discussions, we compare the two fields, SSA22-sb1 and ECDF-S, shown in Figure 6.1 and 6.2, considering both of the LAE survey coverages and the AzTEC or LABOCA and ALMA survey area. These areas correspond $\sim$50–60 Mpc (co-moving) scale on a side at $z = 3.1$. In the case of ECDF-S, there are 109 LAEs satisfying the unified criteria in the 992 arcmin^2 region. Hence the total surface density is 0.16 arcmin^{-2} after the volume density correction, which is consistent with the earlier estimate for that of ECDF-S in Yamada et al. (2012). The surface density of SSA22-sb1[2] is 0.34 arcmin^{-2} (Yamada et al. 2012). Consequently it is found that SSA22 field is more than twice as dense as ECDF-S field in terms of LAE surface number density in $\sim$30 arcmin scale.

[1] Matsuda et al. (2005) and Gawiser et al. (2007) support this assumption. Matsuda et al. (2005) observed 84 LAE candidates with the Faint Object Camera and Spectrograph (FOCAS; Kashikawa et al. 2002) and detected 56 single emission lines. They found no evidence of contaminants. Gawiser et al. (2007) conducted follow-up spectroscopy with Magellan-Baade+IMACS for 92 LAE candidates to confirmed 61 $z = 3.1$ LAEs and find only one contaminant ($z = 1.60$ AGN).

[2] Hereafter, we refer to the SSA22-sb1 as a 23.5$\times$27.5 arcmin^2 region toward SSA22, which is shown in Figure 6.1

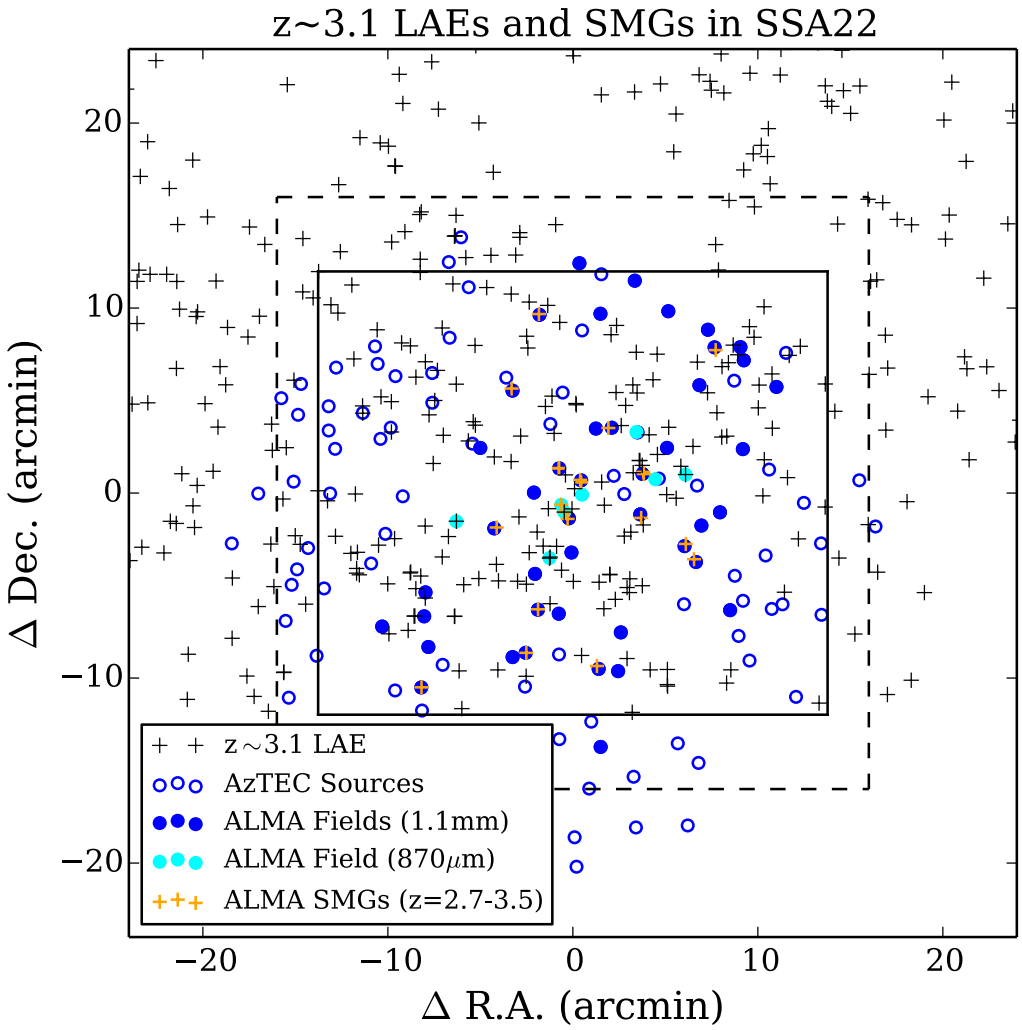

Fig. 6.1 The spatial distributions of original and ALMA-observed AzTEC sources as well as 870 μm ALMA fields, which is targeted to X-ray sources, in the SSA22 field are displayed. The black cross points represent the $z = 3.1$ LAEs satisfying the unified criteria. The orange cross points stand for the $2.7 < z < 3.5$ ALMA SMGs. The solid rectangle shows the area named SSA22-sb1 in Hayashino et al. (2004) and Yamada et al. (2012). The dashed square stands for the area correspond to the LAE survey at ECDF-S for comparison.

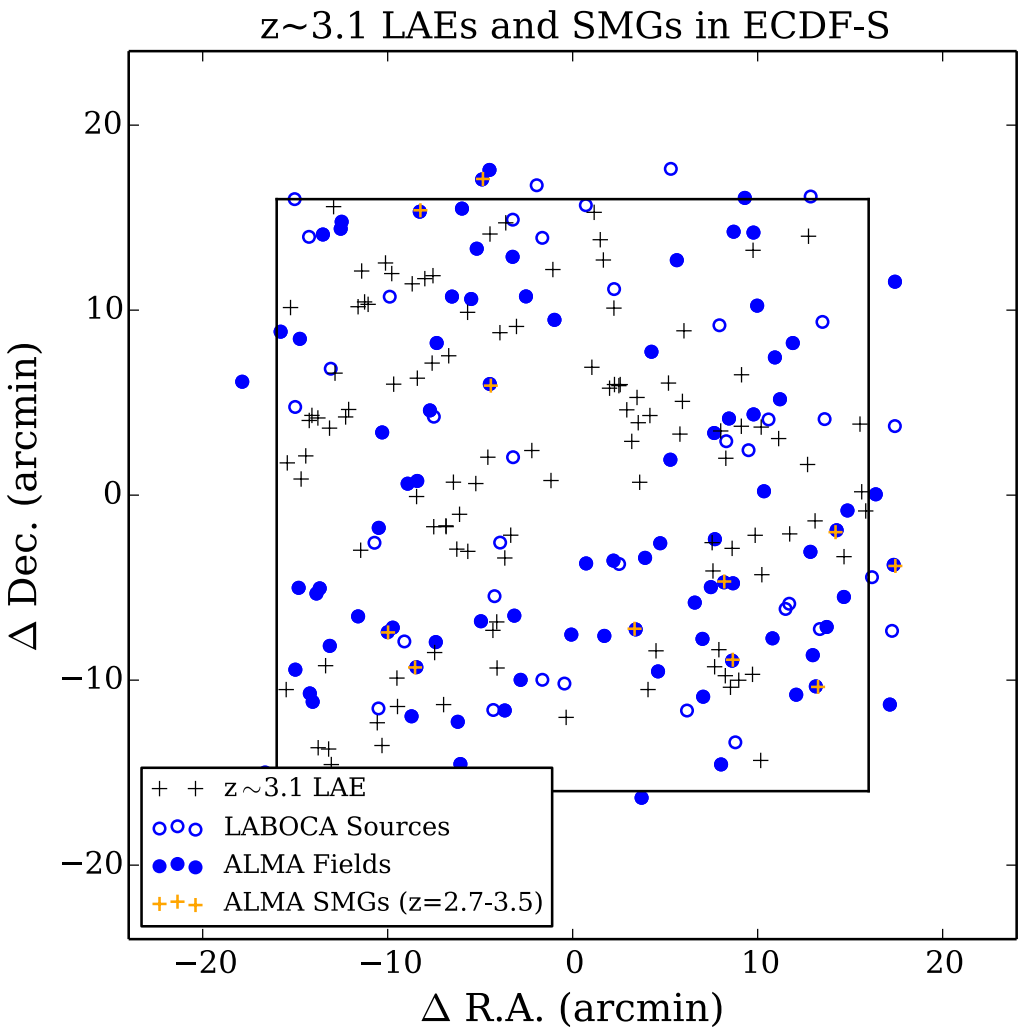

Fig. 6.2 The spatial distribution of LABOCA SMGs and z=3.1 LAEs in the ECDF-S field. Each point is similar with Figure 6.1.

Field	SSA22 (sb1)	ECDF-S
FoV (arcmin^2)	647	992
Sensitivity limit (erg cm^{-2} s^{-1})	1.8×10^{-17}	1.5×10^{-17}
NB magnitude limit (AB)	26.3	25.4
Central wavelength of NB filter (Å)	4977	5000
Width of NB filter (Å)	77	50
Redshift range of LAEs	$3.06\lesssim z\lesssim3.12$	$3.09\lesssim z\lesssim3.13$
Number of LAE candidates	281	162
Observed EW threshold (Å)	190	80

Table 6.1 Properties of LAE surveys in SSA22 and ECDF-S from Yamada et al. (2012) and Gronwall et al. (2007). Yamada et al. (2012) reported totally seven field (sb1–sb7) just in the SSA22 field, but here we just utilize sb1, which contains our ALMA survey area.

SMGs in SSA22 and ECDF-S

The spatial distributions of SMGs discovered by single-dish surveys taken with AzTEC/ASTE (SSA22) or APEX/LABOCA (ECDF-S) are shown in Figure 6.1 and 6.2 as well as those of $z = 3.1$ LAEs in SSA22 and ECDF-S. As shown in the figures, the large part of the AzTEC and LABOCA sources are observed with ALMA (For SSA22, we restrict the area more in section 7.1.2). The properties of SMG surveys in both fields are summarized in Table 6.2. The ALMA detection limit in ECDF-S is $S_{870\mu\mathrm{m}}$ = 1.3 mJy and hence we extract only ALMA sources with $S_{1.1\mathrm{mm}}$ = 0.65 mJy in the SSA22 field to unify the sensitivity limit, considering the difference of observed wavelength in a similar way in section 3.1.1. In addition, two 870 μm selected ALMA SMGs are also considered in the SSA22 field. Hereafter SMGs mean ALMA-identified SMGs.

Excess of SMGs at $z\sim$3.1 SMGs in the SSA22 field

We found possible excess at the cumulative and differential number counts of the SSA22 field as discussed in section 3.1.1, which may indicate that relatively large number of SMGs are formed in the biased environment. Though such source counts are the most fundamental quantities to speculate the variance in various fields, redshift information is essential to improve our understanding.

Although spectroscopic redshifts are strongly required to pick up SMGs at z=3.1 (and exclude SMGs at different redshifts) undoubtedly, a small number of ALMA sources in both of SSA22 and ECDF-S have z_{spec}. Hence we largely rely on optical to near-infrared photometric redshifts (in this work and Simpson et al. 2014b) in the following discussion. We extract $2.7 < z_{\mathrm{best}} < 3.5$ ALMA sources for both fields as $z = 3.1$ candidates SMGs (or

Field	SSA22	ECDF-S	Ref
Area (arcmin^2)	954	1260	1,2
Wavelength of a single-dish survey (μm)	1100	870	1,2
Angular resolution of a single-dish survey ($''$)	30	19	1,2
1σ noise revel of a single-dish survey (mJy beam^{-1})	$\sim$0.7–1.3	$\sim$1.2	1,2
Number of SMGs in a single-dish survey	125	126	1,2
Wavelength of an ALMA survey (μm)	1140	870	3,4
Number of observed Area	45	88 [a]	3,4
Angular resolution of an ALMA survey ($''$)	$\sim 0.6 \times 0.6$	$\sim 1.6 \times 1.2$	3,4
1σ noise revel of an ALMA survey (mJy beam^{-1})	$\sim$0.07–0.16	$\sim$0.4(0.2)	3,4
Detection limit (mJy)	0.3	1.3 (0.7)	3,4

Table 6.2 Properties of SMG surveys in SSA22 and ECDF-S. We express the converted noise revel and detection limit from 870 μm to 1140 μm assuming a 35K gray body radiation at $z = 2.5$ in parentheses.
[a]: The ALESS survey obtained 88 good quality fields out of 122 field observed by ALMA(Hodge et al. 2013).
1) Umehata et al. (2014), 2) Weiß et al. (2009), 3) this work, 4) Hodge et al. (2013)

$z \sim 3.1$ SMGs). Here the most reliable redshifts, $z_{\rm best}$, are defined as follows.

First spectroscopic redshifts are considered to be $z_{\rm best}$ if a SMG have the redshift. Second we extract $2.7 < z_{\rm phot,best} < 3.5$ ALMA sources (here $z_{\rm phot,best}$ represents the most authentic photometric redshift). This threshold is determined from the comparison between $z_{\rm spec}$ and $z_{\rm phot}$ for $z_{\rm spec} > 2$ SMGs. As shown in Figure 4.2, 7/7 ALMA sources (100 %) in the SSA22 field satisfy $|z_{\rm spec} - z_{\rm phot,best}/(1+z_{\rm spec})| < 0.1$. In the case of ALESS survey, 16 out of 19 (84 %) of ALMA sources satisfy this criteria (Simpson et al. 2014b, Figure 3). Thrid we also include a SMG that have a counterpart of a $z = 3.1$ NB emitter or absorber and consider $z_{\rm best}$ of them as 3.1. Principally these sources should have photometric redshifts in the second criteria, ASA 14.1 is selected based on only this criteria. As described in section 6.1.2, to derive the photometric redshifts of ASA14.1 is difficult due to heavy source blending.

If a SMG has $2.7 < z_{\rm spec} < 3.5$ but the redshift does't agree with $z = 3.1$, we in principal add the source for fair comparison. We ignore the SMGs without reliable $z_{\rm phot}$ for both fields. Though some of these SMGs can be $z = 3.1$ (for instance, they might be very optically faint due to extremely heavy dust-extinction or small stellar mass), it is impossible to assess such possibility for individual sources.

As a result, 11 SMGs are selected in the ECDF-S field and 9 out of them lie within the LAE survey area (Figure 6.1). In the SSA22 field, 21 SMGs are listed up in SSA22-sb1. Consequently it is found that the SSA22-sb1 and ECDF-S show the surface number density of 0.032 arcmin^{-2} and 0.011 arcmin^{-2}, respectively. If we only consider the part

of the SSA22-sb1 which are also observed by IRAC (see next section), the density rises to 0.050 arcmin^{-2}. These results directly mean that the surface number densities of SMGs at $z = 3.1 \pm 0.4$ in SSA22 are about five times higher than ECDF-S, which strongly supports that the $z = 3.1$ large-scale structure in SSA22 host a large number of SMGs. We examine this scenario more closely in the next section.

We should note the issue caused by incompleteness here. First our ALMA survey and ALESS survey don't cover all SMGs. We observed 45 out of 56 AzTEC sources in the above-mentioned area and 80 out of 119 LABOCA sources were observed by ALMA. If we apply linear interpolation for both filed, the density would be 0.062 and 0.016 arcmin^{-2}. Hence this incompleteness is supposed not to be a matter. Second as ALMA reveals that a lot of AzTEC or LABOCA sources comprise multiple SMGs, both of our and ALESS survey which are based on pre-sampling by single-dish surveys are, as a matter of fact, not flux-limited surveys and we might miss some SMGs which have comparable mm/submm flux of detected ALMA sources. But such uncertainties are anticipated to be applicable for both field and it is expected not to be affected the relative relation seriously. Therefore we argue again that the very large density excess of SMGs in the SSA22 field is robust.

6.1.2 Where are SMGs Located within a Large-scale Structure?

Methodlogies

We have shown an enhancement in the number density of SMGs in SSA22 in the previous section. Now, the question becomes in what environment SMGs reside *within* the z = 3.1 large-scale structure. The area, SSA22-sb1, corresponds to the central part of the over 1 deg^2 filamentary structure and we can recognize the filaments and nod in the area. The goal of this section is to clarify the spatial relationship between SMGs and such underlying structures. For this purpose, we utilize the surface number density of the $z = 3.1$ LAEs, smoothed with a Gaussian kernel with a FWHM of 5 arcmin to define and describe the environment at the position of each SMG. This way is also utilized in some previous works (e.g., Tamura et al. 2009, Smail et al. 2014) and take advantages to describe the global environment compared to the Nth nearest neighbor methods (e.g., Tran et al. 2010), which tends to address more local environment and suffers the influence of contaminants seriously. (Smail et al. 2014).

The created smoothed density map of SSA22 field and ECDF-S is shown in Figure 6.3 and 6.4. The positions of $z = 3.1$ candidate SMGs are also shown in the figures. We measure the $z = 3.1$ LAE surface density at each SMG position on the smoothed maps. Figure 6.5 and 6.7 show the relation between the density environment and the 1.1 mm flux density. Since

our objective here is to examine the dependence of SMG formation on density environment, we calculate the number density of SMGs in each density bin as shown in Figure 6.6 and 6.8 using gray plots. In order to reduce the effect of incompleteness, we here only consider the area that is also observed with the IRAC 3.6 μm band (not including the wide and shallow survey. see section 4.1.1 and Figure 6.3) in SSA22. This area occupies central 419 arcmin^2 out of 647 arcmin^2 SSA22-sb1 field. Errors are estimated as 1σ Poisson confidence limits as well as section 3.1.1.

Results

In SSA22, we can recognize that the number density of SMGs (dN(SMG)) peaks at high density end (dN(SMG)=0.08 arcmin^{-2} at a bin with LAE surface density of 0.4-0.5 arcmin^{-2}) and declines steeply in the middle range density bin (dN(SMG)=0.01 arcmin^{-2} at LAE surface density of 0.2-0.3 arcmin^{-2}). While the number density of SMGs in the two lowest density bins (0.0-0.2 arcmin^{-2}) is likely to be higher than that at middle range bin, the small number of sample and the deficit of area make it controversial. In ECDF-S, the majority of the area has the LAE density of 0.0-0.2 arcmin^{-2}, which indicates this density range can be interpreted as general environment. To supply a shortage of the less dense area in SSA22, finally we combine the number density of SMGs in both fields (Figure 6.9). The number density of SMGs increases as the LAE density becomes large.

The effect of uncertainties in photo-z

In the previous section, we have defined the criteria focusing on not missing the possible sources. The comparison between $z_{\rm spec}$ and $z_{\rm phot}$ indicates that all SMGs at $z = 3.1$ in SSA22 should be contained in the selected $2.7 < z_{\rm best} < 3.5$ samples, except for the source which are so faint at optical to near-infrared wavelengths that the photo-z measurements are not realistic. Though such wide $z_{\rm phot}$ range leads the good completeness, the percentage of contaminants of non-protocluster members is, however, also anticipated to be large. To find a point of compromise between completeness and a fraction of contaminants, we created the strict sample, which are $2.8 < z_{\rm best} < 3.4$ SMGs. In addition, we exclude sources with $z_{\rm spec}$, which is not in the range of the NB coverage. This strict sample is anticipated to have less contaminants and therefore the trend against density environment is expected to be sophisticated. The results are also displayed using blue plots for both fields. In SSA22, the degree of elevation at 0.0-0.2 arcmin^{-2} bins becomes small and hence this signature seen in Figure 6.6 are possibly caused by the SMGs at different redshift. As shown in Figure 6.9, the whole trend doesn't change dramatically for the strict sample.

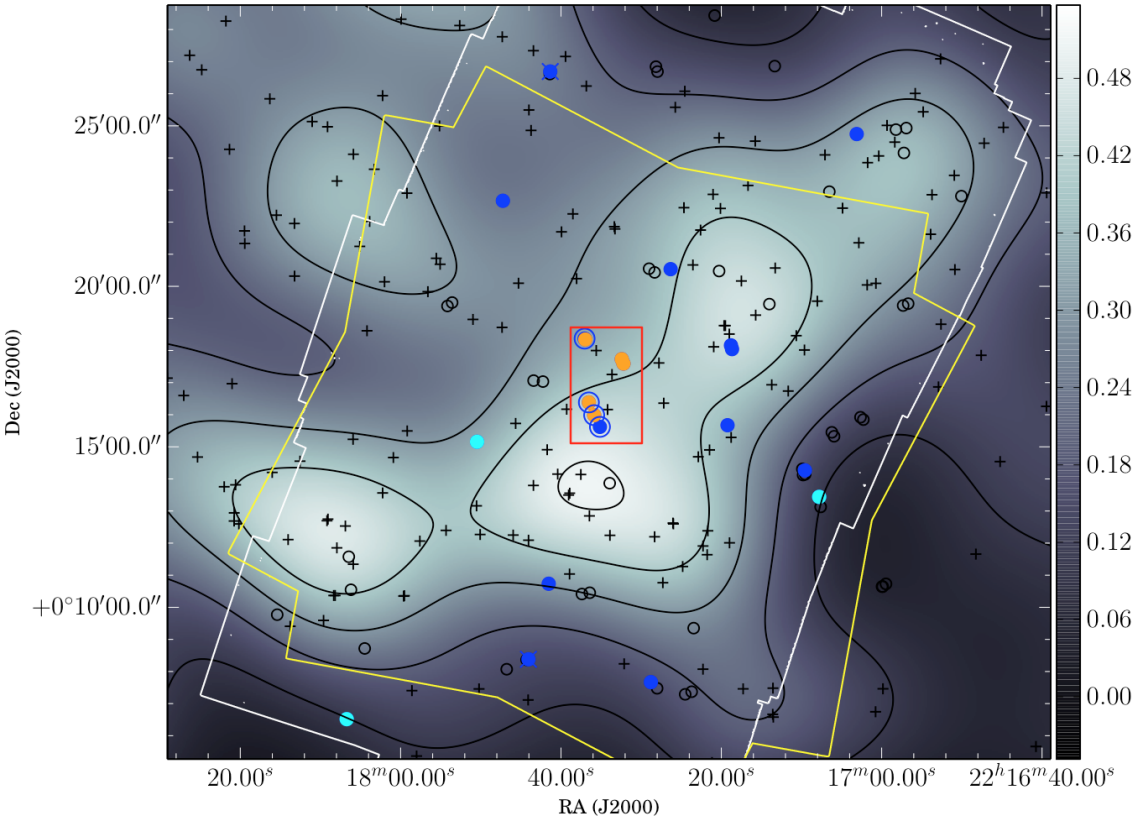

Fig. 6.3 Two-demential spatial distribution of $z = 3.1$ candidate SMGs in the area, SSA22-sb1. Blue and yellow filled circles without overlaid blue circles represent $2.8 < z_{\rm phot} < 3.4$ SMGs and cyan filled circles show $2.7 < z_{\rm phot} < 2.8$ SMGs. Yellow filled circles stand for AGN-host SMGs. The overlaid blue open circles mean that the source have $z_{\rm spec} = 3.1$. Small black empty circles shows the remaining ALMA source positions. On the contrary, the overlaid 'x' makers indicate that the source has spec-z, which is inconsistent with $z = 3.1$. The background map shows the $z = 3.1$ LAE density surface density (Yamada et al. 2012) and black contours represent 0.1, 0.2, 0.3, 0.4, and 0.5 arcmin^{-2}. The color bar also corresponds to the LAE density. Each cross shows the positions of individual LAEs. White contours represent the area of the deep IRAC 3.6 μm image, which is utilized to calculate the source counts for each density bin. The yellow lines show the observed area of *Chandra*/ACIS-I. The red rectangle shows the ADF22 area.

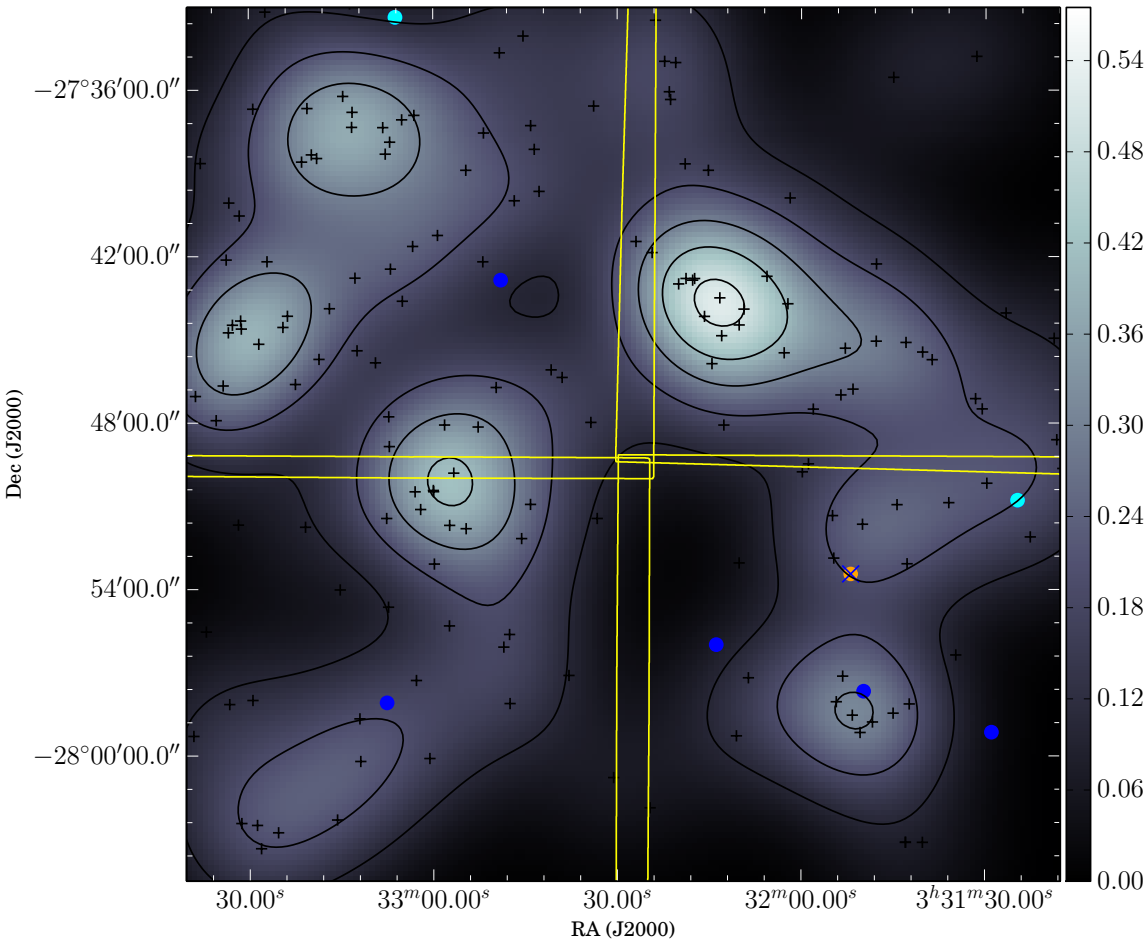

Fig. 6.4 Two-demential spatial distribution of $z = 3.1$ candidate SMGs in the area, ECDFS. Each marks are similar with Figure 6.3.

The site of SMG formation

As shown in Figure 6.6 and 6.8, there are little area which have LAE density of >0.3 arcmin^{-2} in ECDF-S. In other words, such overdense fields correspond to the large-scale structure in SSA22. Our results indicates that the number density of SMGs in such dense environment are much larger than that in less dense environment. For instance, dN(SMGs) at 0.4-0.5 arcmin^{-2} bin is about 8 times larger than dN(SMGs) at 0.0-0.3 arcmin^{-2} bins for strict sample. We also focus on the relation between the increments of dN(SMGs) and the LAE density. In considering the LAE surface number density as an ideal tracer of general galaxy number density, this relation can provide us with the trend on the fraction of SMGs among the all galaxies. If there are linear relation between the two, it means that the fraction of SMGs would be constant at all density environments and the number density of SMGs would be proportional to that of whole galaxy populations. As shown in Figure 6.9, the number density of SMGs increases more steeply than such linear relation. Whilst dN(SMGs) is almost constant at the bins of 0.0–0.3 arcmin^{-2}, it become about 7 and 8 times larger at 0.3–0.4 and 0.4–0.5 arcmin^{-2} bins, respectively. Furthermore there is no SMG with $z_{\rm spec} = 3.1$ at $0.0-0.3$ arcmin^{-2} bins whilst 4 SMGs with $z_{\rm spec} = 3.1$ lie at $0.3-0.5$ bins. These results strongly support that SMGs are preferentially formed in overdense environment.

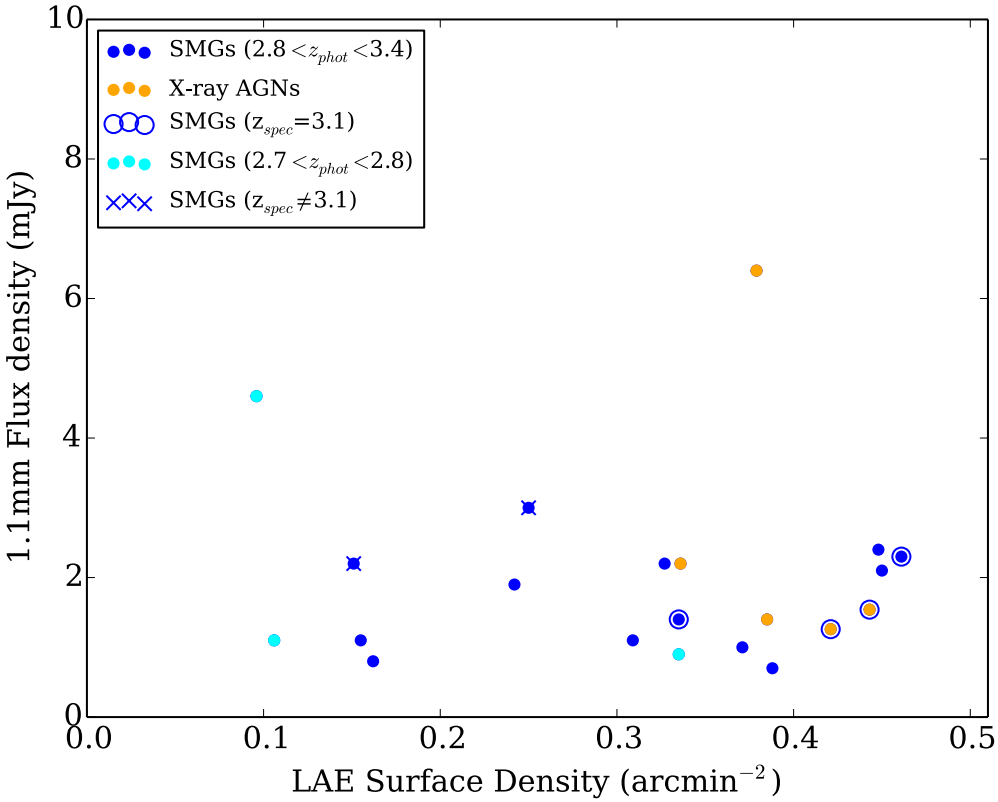

Fig. 6.5 Observed 1.1mm flux densities of $z = 3.1$ candidate SMGs as a function of LAE surface density in the SSA22. Each point are reflected the redshift and AGN classification described in the left corner of the diagram. For two 870μm detected SMGs, we converted to 1.1 mm flux density as described above.

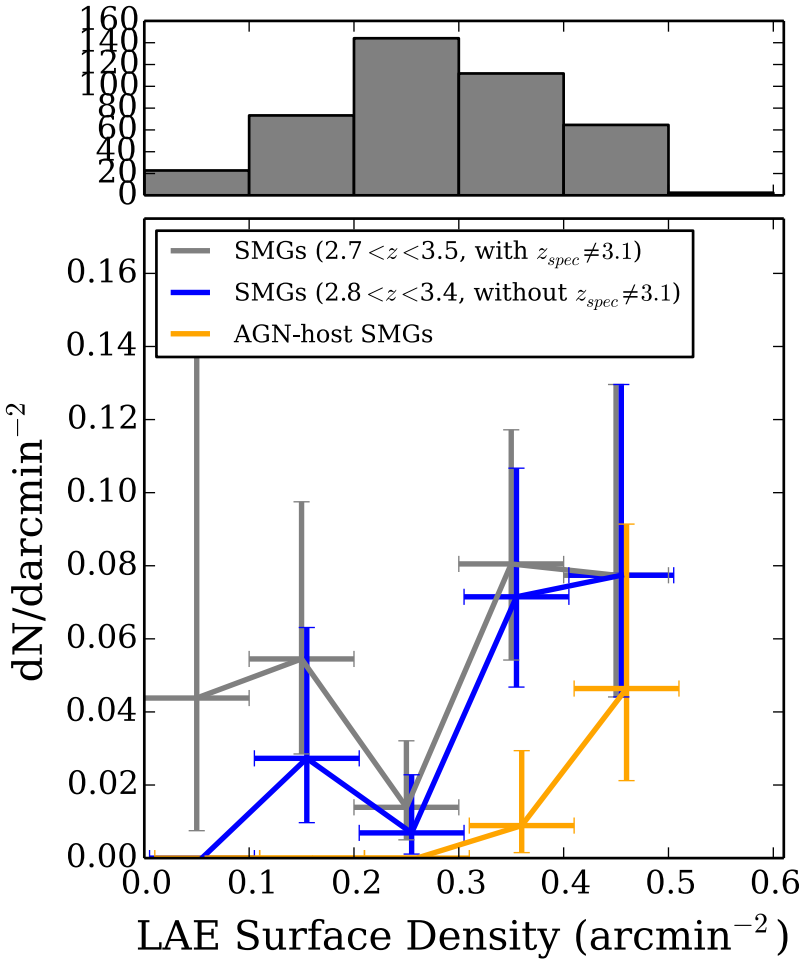

Fig. 6.6 The number of SMGs per unit area as a function of $z = 3.1$ LAE surface number density in SSA22. In principal, we plot all SMGs with $2.7 < z_{\rm best} < 3.5$ (gray). In addition, we also show 'strict' candidate SMGs with $2.8 < z_{\rm best} < 3.4$ except for $z_{\rm spec} \neq$3.06–3.12 (blue). In the yellow plots, SMGs which harbor X-ray luminous AGNs are considered.

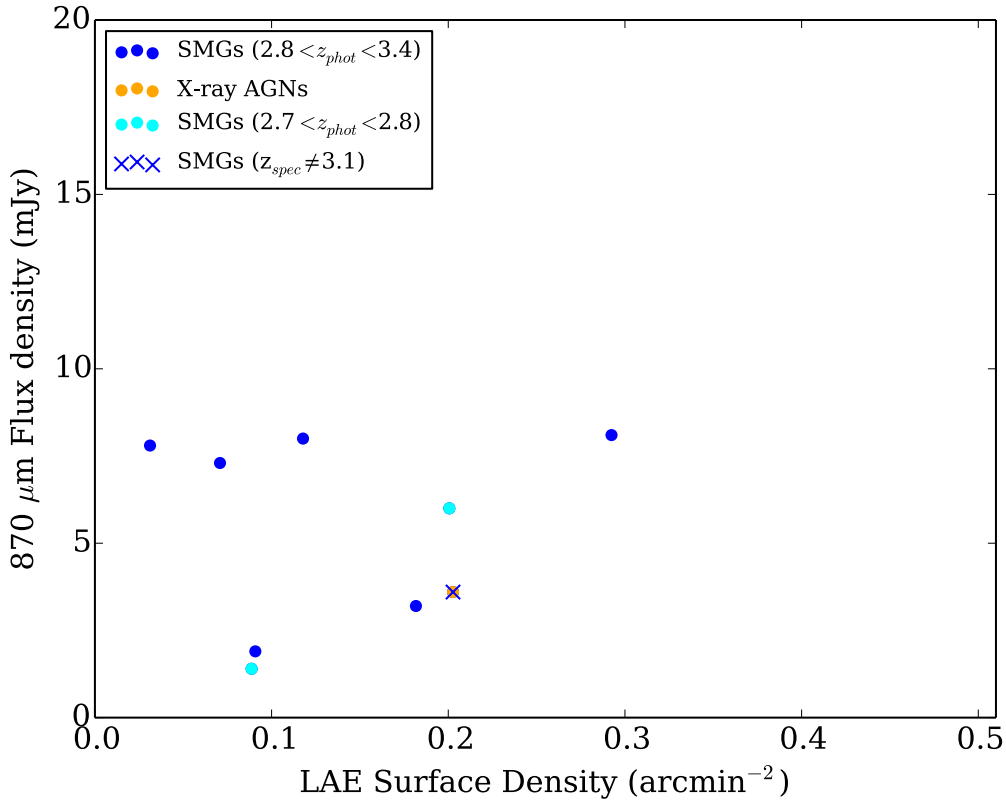

Fig. 6.7 Observed 870 μm flux densities as a function of LAE surface density in ECDFS as well as Figure 6.5.

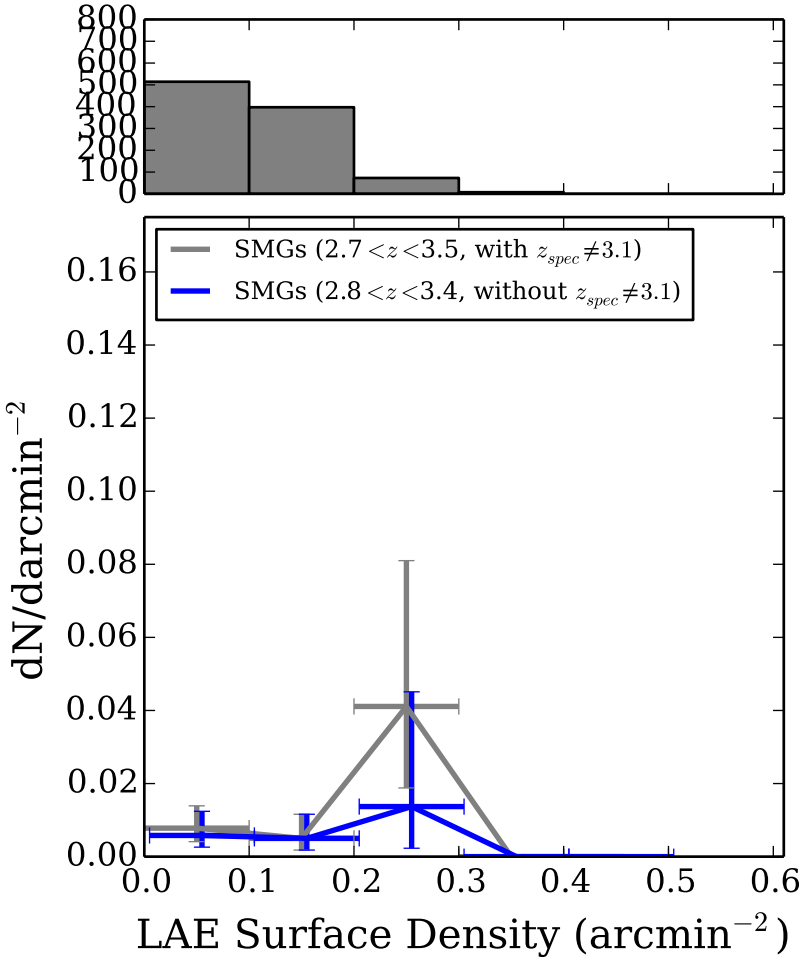

Fig. 6.8 The number of SMGs per unit area as a function of $z = 3.1$ LAE surface number density in ECDFS as well as Figure 6.6.

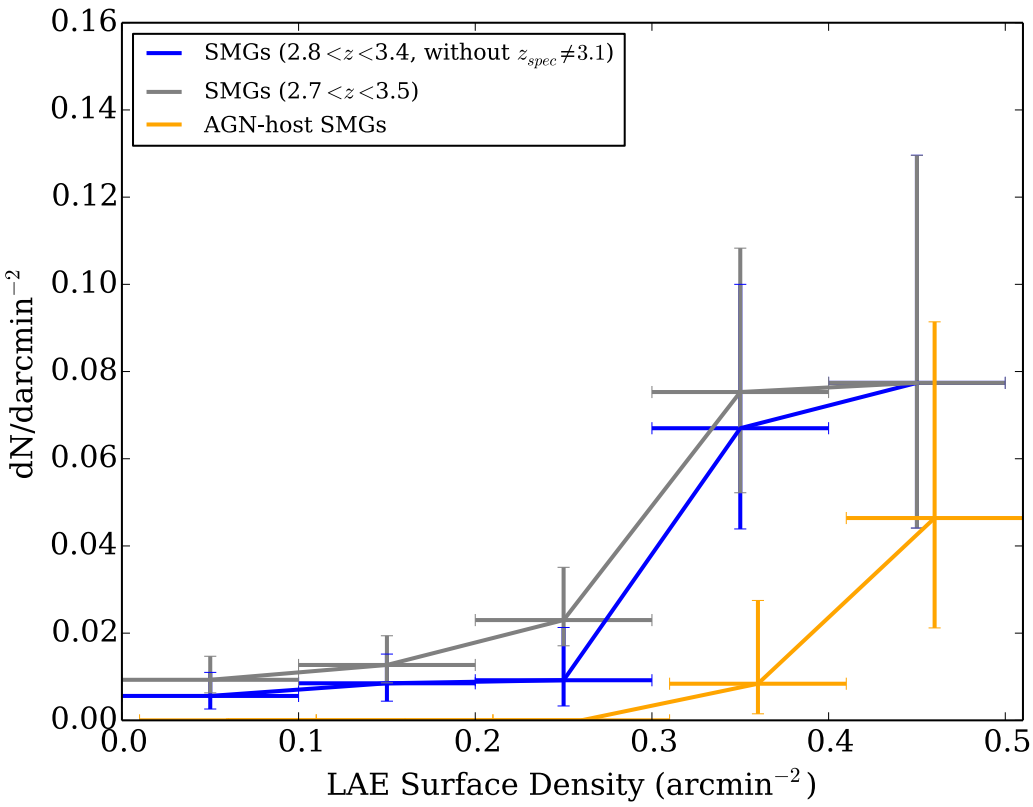

Fig. 6.9 The number of SMGs per unit area as a function of $z = 3.1$ LAE surface number density combining both of SSA22 and ECDFS. Source classification is similar with Figure 6.6.

6.1.3 Individual Properties of SMGs for General and Biased fields

We have revealed that the SSA22 field have about five times larger number of SMGs per unit area compared to the ECDF-S as a whole in section 6.1.1. Moreover in section 6.2.2 it is found that the majority of SMGs in SSA22 reside at relatively dense environment and the SMG number density at around the LAE density peak reach around 8 times of that at general density environment. In this section, we take a step forward to investigate the individual properties, SFR, stellar mass, and specific SFR (sSFR) for SMGs in various density environment at $z = 3.1$. In the following calculation and discussion, we adopt $z_{\rm best}$ if we need to utilize redshifts.

SFR

Here SFR, star-formation rate, is calculated based on total infrared luminosity ($L_{\rm IR}$) derived from 1.1 mm or 870 μm flux densities. Since we don't have dust temperature ($T_{\rm d}$) information, we assume a single component graybody with dust temperature of $T_{\rm d}$= 35^{+12}_{-9} K, which has been measured for bright lensed ALMA sources at $z_{\rm spec}$=2.7–3.5 (Weiß et al. 2013), for all SMGs [3]. The equation to calculate $L_{\rm IR}$ is:

$$L_{\rm IR} = 4\pi\Gamma(\beta+4)\zeta(\beta+4)D_{\rm L}^2\left(\frac{h\nu_{\rm rest}}{k_{\rm B}T_{\rm d}}\right)^{-(\beta+4)}\left[\exp\left(\frac{h\nu_{\rm rest}}{k_{\rm B}T_{\rm d}}\right)-1\right]S_{\rm obs}\nu_{\rm obs} \tag{6.1}$$

where Γ and ζ are the Gamma function and the Riemann zeta function, β is emissivity index of 1.5, $\nu_{\rm rest}$ and $\nu_{\rm obs}$ are rest-frame and observed frequency, and $S_{\rm obs}$ is observed flux density (h and $k_{\rm B}$ are the Planck constant and the Boltzmann constant, respectively.). Then we estate SFR based on a Chabrier IMF as follows:

$$\mathrm{SFR}[M_\odot \mathrm{yr}^{-1}] = 10^{-10} \times L_{\rm IR}[L_\odot] \tag{6.2}$$

(Kennicutt 1998). Figure 6.10 shows SFR of each SMG as a function of the LAE number density, which we have derived in section 6.2.1.

[3] Though $T_{\rm d}$ is critical to derive $L_{\rm IR}$ and SFR, it is not easy to derive it for our sample. We have *Herschel*/SPIRE photometries at 250, 350, and 500 μm for all ALMA fields (PI. Y. Matsuda), but the crude angular resolution (FWHM of 18, 25, 36 $''$, respectively) causes heavy source blending and sensitivity limit regulated by confusion limit. In addition, we focus on $z = 3$ SMGs, which are generally too faint to detect by SPIRE even if we conduct some deblending procedures (e.g., Swinbank et al. (2014)). Hence we assume the temperature range measured for bright sources at same redshift.

Stellar Mass

As the thorough procedures have been described in section 4.2, we have calculated stellar mass for SMGs in SSA22 utilizing the absolute H band magnitude derived from HYPERZ [4]. Though Simpson et al. (2014b) suggested a mass to light ratio for each ALESS SMG, here we recalculate stellar mass for SMGs in ECDF-S using a same light to mass ratio (L_H/M = 6.85±1.05 $L_\odot M_\odot^{-1}$) following Hainline et al. (2011) for fair comparison. Figure 6.11 presents the results.

sSFR

Specific star formation rate (sSFR), which is defined as SFR/M_*, is known to be an indicator of star-formation mode. In other words, this parameter tells us the activity or burstiness of star-formation. We calculate sSFR for each SMG and plot in Figure 6.12.

Results

As shown in Figure 6.12, SMGs have SFR of ∼100–800 $M_\odot$ yr^{-1}, which seems to be independent of the underlying density environment at z=3.1. The median value is constant for both of the low (<0.25 $arcmin^{-2}$ LAE density) and high density bin (≥0.25 $arcmin^{-2}$ LAE density) within errors. This trend doesn't differ even if we only consider strict samples. We contain three AGN-host SMGs which are so heavily obscured that the measurement of stellar mass is possible. Though the statistics is so poor, we cannot recognize any dependence of SFR on density environment. One extremely high SFR source in SSA22 is ASA1.1. This source is the brightest source in SSA22 and ECDF-S and locates in relatively dense field. Therefore the dense environment might be attributed to ignite the extraordinary starbursts. But, as a whole, there seems to be no trend.

Most of SMGs are massive ($M_* \sim 10^{10.5} - 10^{11}$ $M_\odot$) at any environment as shown in Figure 6.11. Similarly there is no recognizable trend between low and high density bin for both of the whole and strict samples. (There are two less massive SMGs in the lower environment in the SSA22. We need to be careful to interpret the low stellar mass of the two, ASA7.4 and ASA67.1[5].)

[4]There is one additional estimate. ASA14.1 is heavily blended source and we consider it as one of the $z = 3.1$ members because a z = 3.1 LAA is associated to it. Thus the $z_{\rm phot}$ of 2.1 and the stellar mass derived from this redshift, displayed in Table 4.8, shouldn't be utilized here. Here we assume the same stellar mass as ASA 14.2 because both show quite similar photometry in IRAC four bands (Table 4.5) and both are considered to be $z = 3.1$ candidates.

[5]ASA7.4 is detected significantly (5.1σ), but the photometry is likely to be seriously affected by the nearby bright sources for all bands. It is not sure whether ASA7.4 and this nearby galaxy is physically associated or not. Hence the derived photometric redshift and stellar mass are less reliable. ASA67.1 is detected with

Throughout all environment in SSA22 and ECDF-S, sSFR seems to be between 1 and 10 Gyr^{-1}, which is also independent of the density environment. Combining the result of three parameters, we do conclude that the nature of individual SMGs is independent from the underlying environment. This result provides us with a persuasive scenario for SMG formation. It is suggested that if the conditions to ignite the violent starburst are satisfied and galaxies reach the stage that we can observe them as SMGs, the galaxies are expected to show similar properties such as high SFR, large stellar mass, and relatively high activity.

ALMA securely (7.8σ) and is well isolated in all multi-wavelength images. The best-fit photometric redshift is $z_{\mathrm{phot}} = 2.71$, but the $\chi^2_{\mathrm{reduced}}$ distribution indicates that there is a secondary likelihood peak at a lower redshift ($z = 1.99$), which would decrease the stellar mass if this is the case.

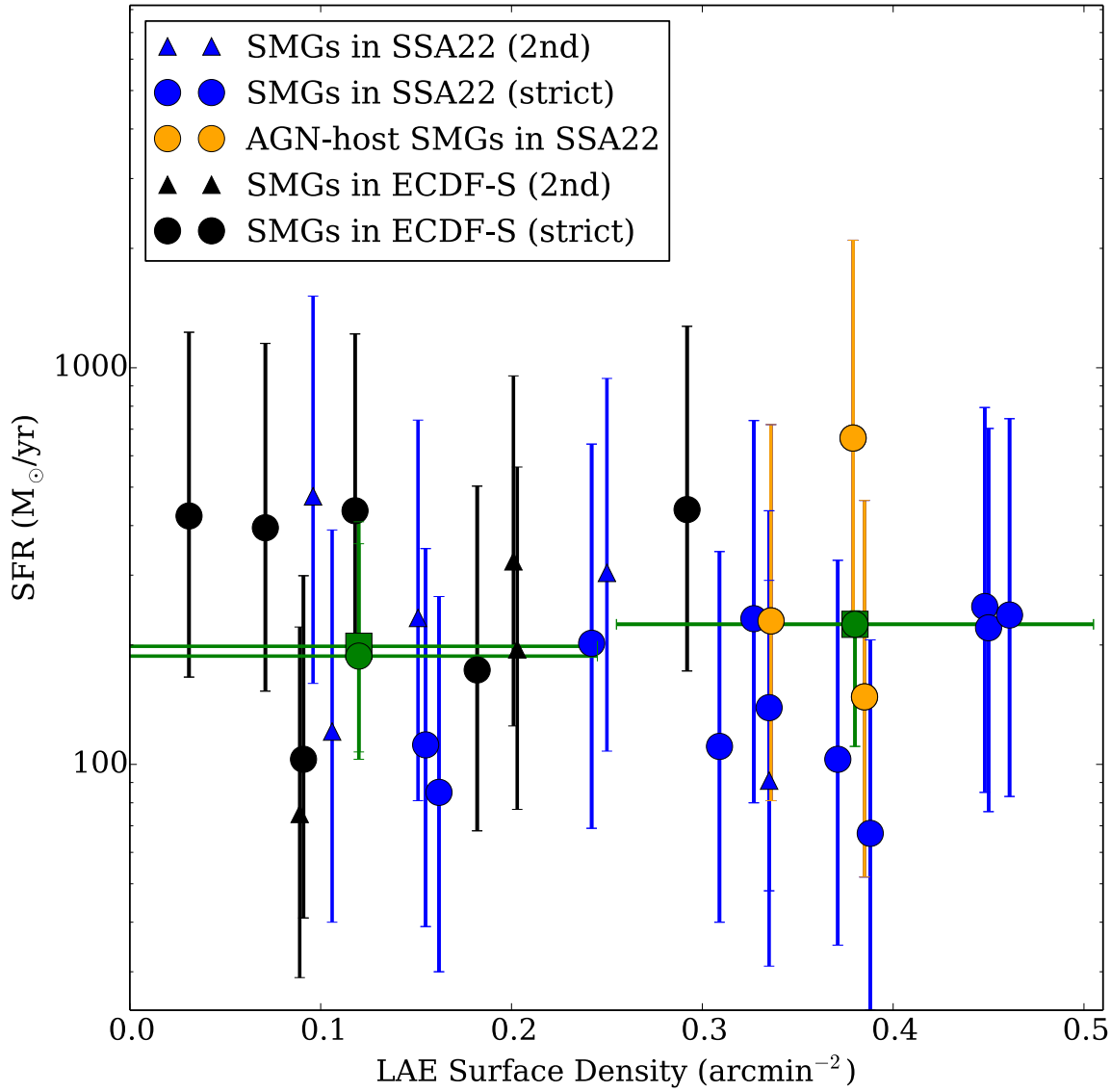

Fig. 6.10 SFR of SMGs in SSA22 (blue symbols) and ECDF-S (black symbols) as a function of $z = 3.1$ LAE surface density. Strict samples are shown using circles. The remaining SMGs, which have $2.7 < z_{\rm best} < 3.5$ but doesn't satisfy the strict criteria, are illustrated with triangles (Hereafter we call them '2nd' samples). Green plots represent the median value of SFR for low and high density environment (LAE number density of $<$0.25 arcmin^{-2} and $\geq$0.25 arcmin^{-2}, respectively) with 1σ error. While green circles stand for the strict samples, green squares represent whole $z = 3.1$ candidate SMGs.

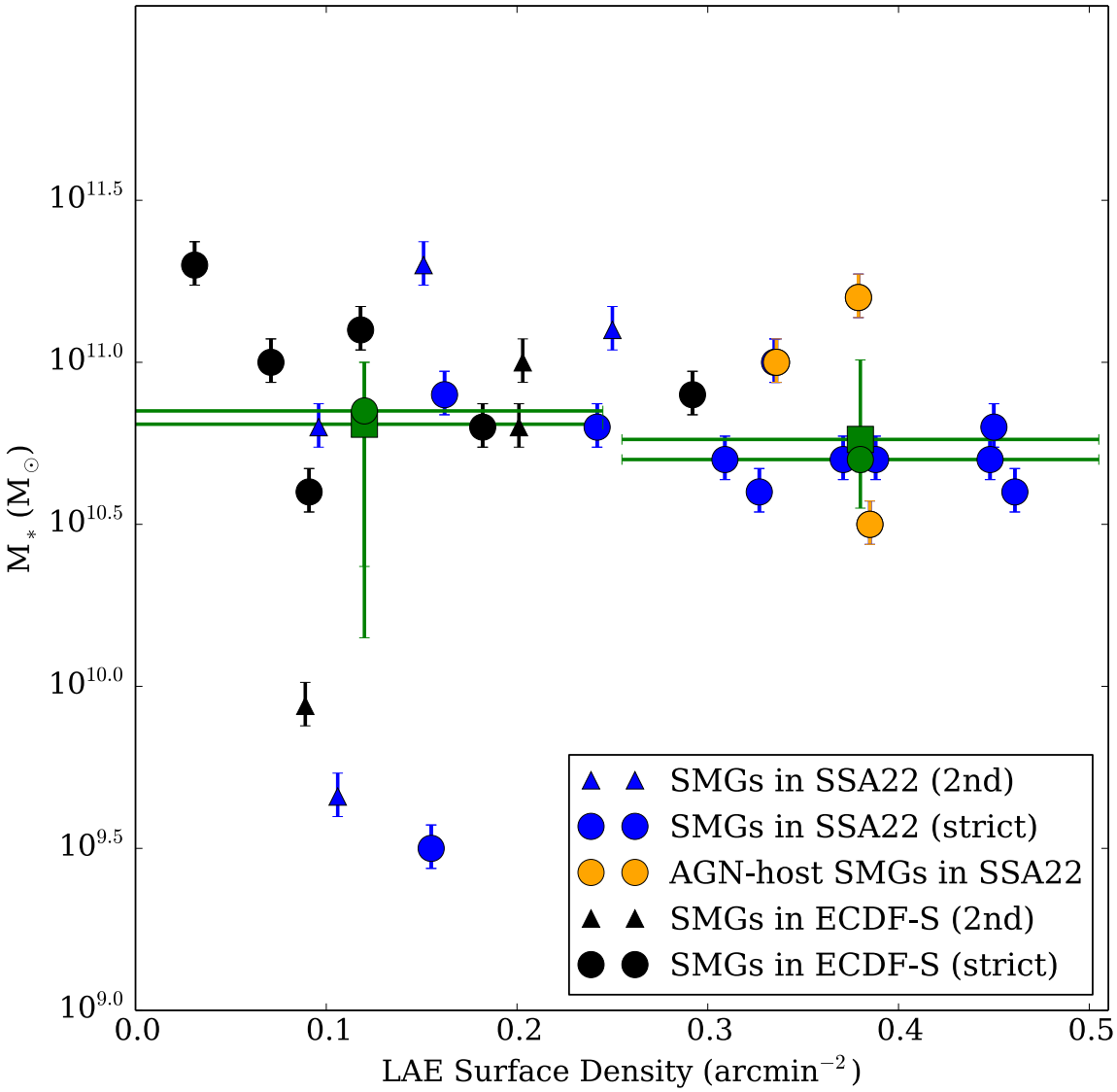

Fig. 6.11 Stellar masses of SMGs in SSA22 and ECDF-S as a function of $z = 3.1$ LAE surface density. Each symbol are same as described in Figure 6.10.

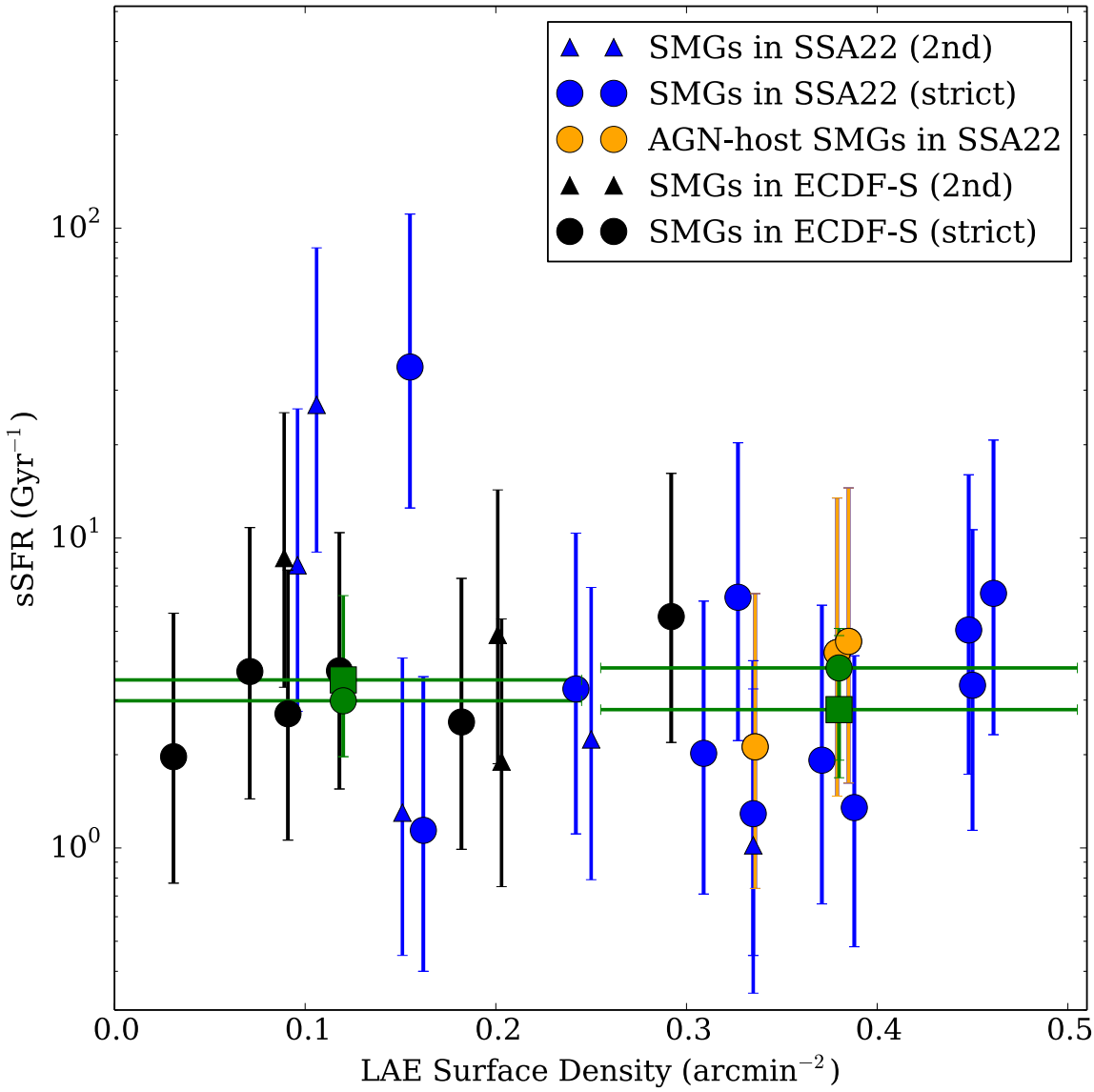

Fig. 6.12 Specific star-formation rate of SMGs in SSA22 and ECDF-S as a function of $z = 3.1$ LAE surface density. Each symbol are same as described in Figure 6.10.

6.1.4 Mergers as the Most Plausible Trigger

Previous works

Until today various studies, such as molecular line profiles (Engel et al. 2010), kinematics derived from integral field unit (IFU) observations of Hα emission (Swinbank et al. 2006, Alaghband-Zadeh et al. 2012), and Sersic index (Kartaltepe et al. 2012), have indicated that the violent active starbursts seen in SMGs would be caused by mergers. In addition, recently two additional strong observational evidences have been proposed.

The first one is the compactness of submm/mm images of ALMA SMGs reported by Simpson et al. (2014a) and Ikarashi et al. (2014). They found the sizes of SMGs are totally very small. Simpson et al. (2014a) found that the median value of FWHM is 0.30$\pm$0.04$''$ and the median physical half-light diameter is 2.4$\pm$0.2 kpc. Ikarashi et al. (2014) also found that their $z \gtrsim 3$ SMGs have the median FWHM of 0.22$''$. Such compact starbursts are similar with local ULIRGs which are in a late stage merger (e.g., Iono et al. 2007, Sakamoto et al. 2008) and recent numerical simulation also indicated that at high redshift mergers would generate compact starbursts (Hopkins et al. 2013). The second one is from the distributions of stellar components, which is a collision less tracer of the morphologies. Chen et al. (2014) conducted deep H-band imaging with HST/WFC3 for 48 ALMA-identified SMGs to find that the rest-optical counterparts of these ALESS SMGs are usually (more than 80 % of the detected SMGs) show disturbed morphologies (i.e., irregulars and/or interactions).

We examine whether this merger scenario is applicable to SMGs in SSA22 from the view points of these (i) ALMA source sizes and (ii) near-infrared morphologies.

Source size measurements

Since high signal to noise ratios are preferable to measure the source size of SMGs, we focus on six SMGs at $z \simeq 3.1$ with $>$10 σ detections as well as Simpson et al. (2014a) and Ikarashi et al. (2014).

First we utilize final cleaned images to conduct gaussian fitting with the IMFIT routine. This fitting reveals that 4 out of 6 sources are not resolved in $\sim$0.6–0.7 $''$ scale (Table 6.3). The results of beam deconvolution suggest that the image component size may be as large as $\sim 0.3'' \times 0.2''$. On the contrary the brightest one, ASA 1.1 is clearly resolved in our image. To examine the profile of ASA 1.1 in more detail, we created a higher angular resolution image with 'uniform' weighting (Figure 6.14). The beam size got small to $\simeq 0.58'' \times 0.45''$. The high-resolution imaging reveals disturbed morphologies of the SMGs in SSA22, which can be an evidence for multiple mergers. The remaining one, ASA 77.1, also might be resolved in the ALMA image. Second we performed the model fit on the (u, v) plane (see

Appendix C.1 for more detail). As a result, it is indicated that a median intrinsic angular size of FWHM = $0.25''$. This corresponds to a physical half-light diameter of 1.9 kpc at $z = 3.1$. Our results are consistent with previous works (or slightly smaller than Simpson's results).

Near-infrared morphologies

Next we check the near-infrared (WFC3/F160W or MOIRCS/Ks bands) images of these SMGs as shown in Figure 6.13. The WFC3/F160W band images have typical angular resolution of $0''.2$, which is vary helpful for us to examine morphologies of stellar components, though the band correspond to the rest-frame 3900 Åat $z = 3.1$, which is smaller than the 4000 Åbreak. The MOIRCS/Ks band images have slightly larger angular resolution ($\sim 0''.4$), but we can observe at the rest-frame 5200 Å, which is a relatively good tracer of the stellar mass distribution.

We detect counterparts for 4 out of 6 and two SMGs have two components[6]. Though generally the signal to noise ratios are low and it is rather difficult to measure the morphologies of such counterparts, it is found that there is clear positional difference between the ALMA source and the near-infrared source in the remaining two SMGs. This is similar with some local ULIRGs in the merger stage and also supports the interaction[7].

Summary and Future Plans

Combining the results, all six SMGs at $z \simeq 3.1$ are anticipated to be an interaction stage. This result would supports that the major-driven scenario can also be applicable for SMGs in SSA22 and in the following discussions we assume this scenario.

The more secure observational evidence is, however, required for the undoubted conclusion. For instance, IFU observations of [OIII] λ5007 emission line with VLT/SINFONI, KMOS or high resolution CO ([CII]) spectroscopy with ALMA, PdBI can investigate the kinematics directly. Or much deeper Ks-band observations will reveal the distribution of stellar mass, which is a collision-less tracer. Such observations are achievable using Subaru/IRCS with AO.

[6] ASA14.1 has no counterpart. The bright source seen in Figure 6.13 is a foreground galaxy (our VLT/VIMOS observations, Kubo2014)

[7] As discussed in Chen et al. (2014), If the ALMA positions are intrinsically consistent with the stellar distribution and obscured by dust, the fraction of consistency should increase as redshift decrease since the rest-frame wavelength move to longer side and the effect of dust extinction become weak.

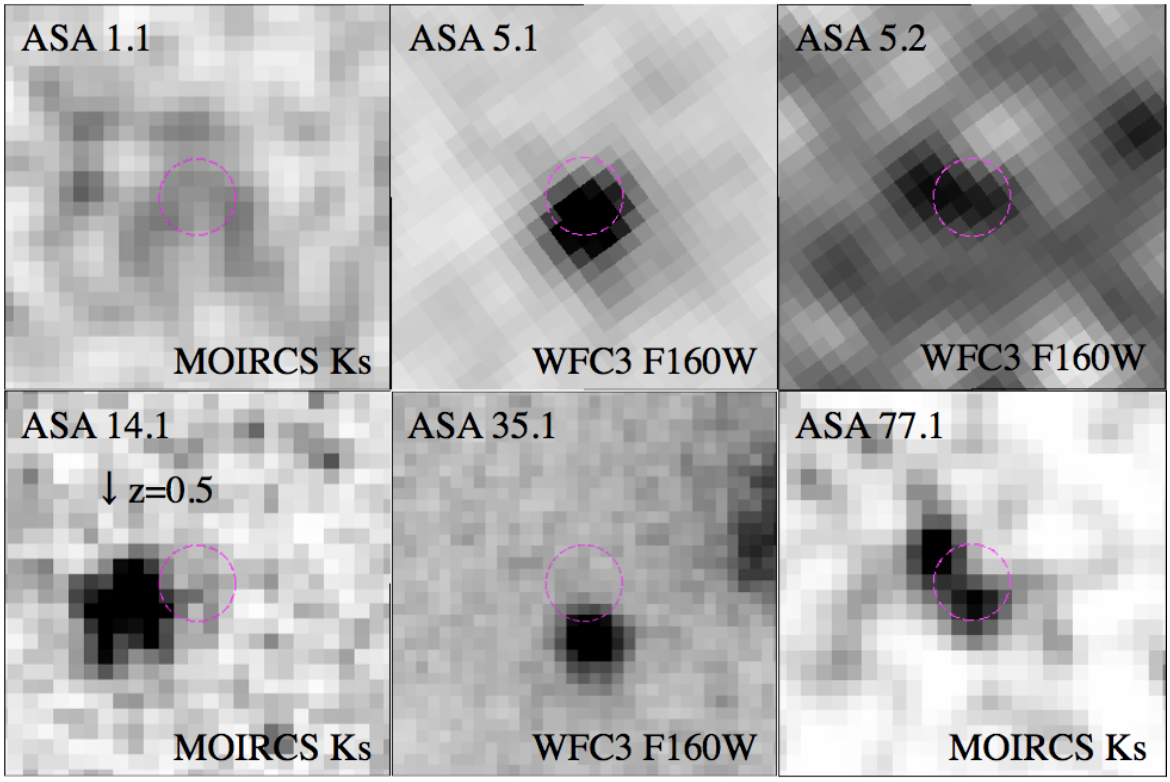

Fig. 6.13 Near-infrared (HST/WFC3+F160W or Subaru/MOIRCS+Ks) inverse color images of 6 $z = 3.1$ candidate SMGs detected with S/N>10. Magenta dashed circles represent the ALMA beam ($0''.6$). Each panel is $3'' \times 3''$. The bright source in the ASA14.1 field is a nearby galaxy.

ID [a]	$S_{\rm pk}$/N [b]	Image Size [c] (IMFIT, $''$)	Image Size [g] (UVAMP, $''$)	ALMA [d] View	NIR [e] view	Inter- [f] raction
ASA 1.1	19.5	$1.07'' \times 0.68''$	$\sim 0.55''$	Resolved, Disturbed	Non-detection	Y
ASA 5.1	11.2	$0.71'' \times 0.63''$	$\sim 0.35''$	Non-resolved	Offset	Y
ASA 5.2	10.4	$0.69'' \times 0.53''$	$\sim 0.20''$	Non-resolved (p)	Two Components	Y
ASA 14.1	13.7	$0.69'' \times 0.53''$	$\sim 0.25''$	Non-resolved (p)	Non-detection	Y
ASA 35.1	11.0	$0.69'' \times 0.53''$	$\sim 0.20''$	Non-resolved (p)	Offset	Y
ASA 77.1	22.9	$0.80'' \times 0.58''$	$\sim 0.30''$	Resolved?	Two Components	Y

Table 6.3 Merger Classification of SSA22 ALMA SMGs with S/N >10.0.
[a]: ALMA Source ID in this work
[b]: S/N defined as the ratio between peak flux and r.m.s. noise.
[c]: 1.1 mm source size convolved with the synthesized beam, measured with CASA/IMFIT. We use 'natural' weighting maps, which have the synthesized beam size of $0.69'' \times 0.55''$ (for ASA 1.1, ASA 5.1, ASA 5.2, and ASA 14.1), $0.68'' \times 0.57''$ (for ASA 35.1), $0.64'' \times 0.54''$ (for ASA 77.1).
[d]: Characteristics of ALMA sources. 'Non-resolved' means the measured source size is equal or smaller than the synthesized beam. If IMFIT failed to deconvolve from beam or found to be fitted well as a point source, we additionally mark '(p)'. The size of ASA 77.1 is slightly larger than the beam and therefore might be resolved. ASA 1.1 is clearly resolved and show the signature of interaction as shown in Figure 6.14.
[e]: Visual speculation of near-infrared counterparts (images are shown in Figure 6.13). We utilized WFC3 F160W and MOIRCS Ks band images, of which FWHM is $\sim 0.2''$ and $\sim 0.4''$, respectively.
[f]: Interaction classification. The detail conditions are in section 7.1.4.
[g]: 1.1 mm source size estimated by MIRIAD/UVAMP.

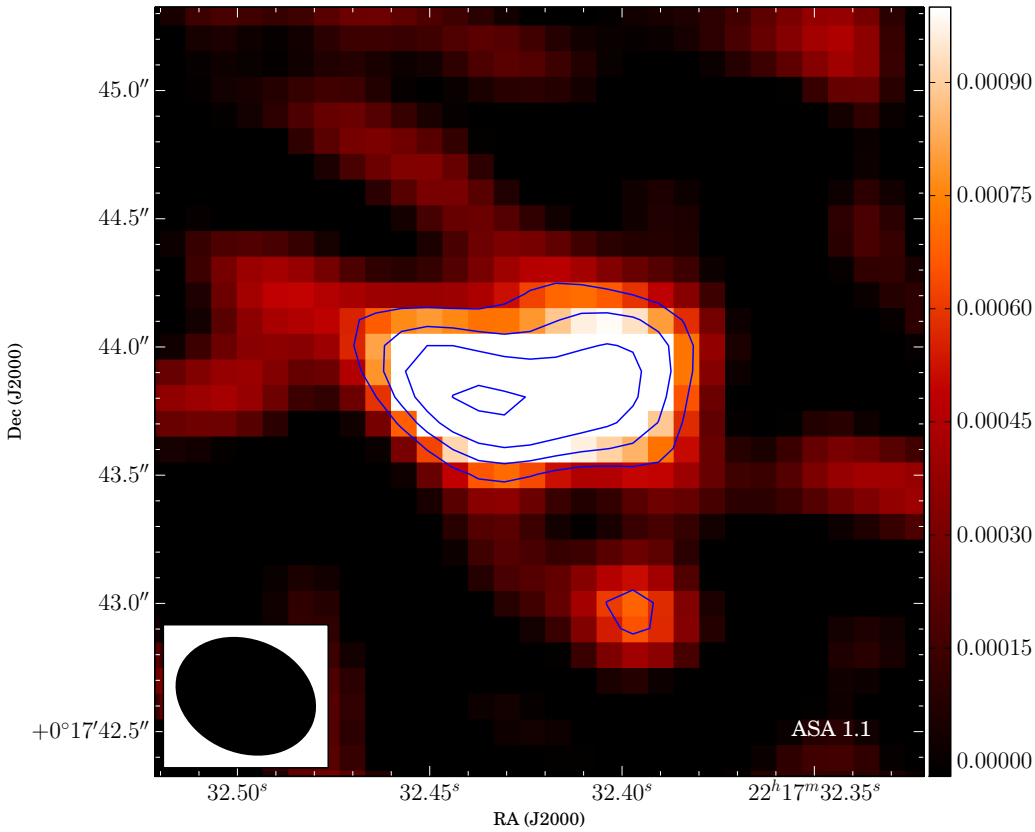

Fig. 6.14 The high resolution 1.1 mm image of ASA 1.1. The size is $3'' \times 3''$. We conducted CLEAN imaging with 'uniform' weighting, which achieved $0.58'' \times 0.45''$ beam shown in the figure. Contours stand for 0.6. 0.9, 1.2, 1.6 mJy beam^{-1}. ASA 1.1 show disturbed morphology and is likely to be in a major-merger phase.

6.1.5 The Role of Environment in SMG Formation

The Enhanced Frequency of SMGs in the $z = 3.1$ Proto-cluster

Until today, the relationship between SMGs and the large-scale structure in the early universe has been discussed indirectly. For instance, in the field of models and simulations, the association of SMGs to the underlying large-scale structure has been suggested. Chapman & Baugh (2004) and Suwa et al. (2010) conducted cosmological simulations to illustrate the positional relation between SMGs and the mass structures present in large volumes ($\sim$150 Mpc). While they found a number of sources with SMG-class $L_{\rm IR}$ ($\sim 10^{12} L_{\odot}$) in the mass overdensity regions, it is also indicated that significant portion of such sources would also appear in less dense environment and the spatial relation was not established strongly.

In addition, clustering analysis is one way to explore the relation to the large-scale structure. Blain et al. (2004) reported that SMGs at z=2–3 show strong clustering. They found that SMGs are likely to be reside in relatively massive dark matter halos compared to the $z \sim 2$ QSOs and $z \sim 3$ LBGs and suggested that SMGs trace the densest large-scale structure. Hickox et al. (2012) conducted clustering analysis for z=1-3 LABOCA-selected SMGs in ECDF-S to also derive a large dark matter halo mass of $10^{12.8} h^{-1} M_{\odot}$ and imply the association to the large-scale structure. Though such statistically measurements are useful to describe the global nature of a galaxy population, they are ineffectual for the insight for individual fields at a redshift.

In this work we have illustrated how SMGs are related to large-scale structures at $z = 3.1$ in the unprecedentedly direct way. In section 7.1.2 we have unveiled the strong environmental dependence on the underlying environment: the number of SMGs rapidly increase as the environment gets dense and on the contrary SMGs are very sparse in the less dense environment. This is the first insight for the environmental dependence on SMG formation in terms of $z \sim 3$ universe, large-scale structure ($\sim$ 50 Mpc), and a large number of SMGs identified by subm/mm interferometers such as ALMA. As described in section 7.1.4, the majority of SMGs in the proto-cluster are considered to be mergers as well as other field SMGs and hence it is inferred that the high merger rate and the high interaction efficiency as well as large gas reservoir lead the high frequency of SMG formation around the density peak in the SSA22 proto-cluster.

The individual nature as starbursts

In section 6.1.3 we found that the individual characteristics of star-formation including SFR, Stellar mass, and sSFR, do not depend on the large-scale environment. What does this result mean?

As discussed in section 6.1.4, violent starbursts seen in SMGs are considered to be triggered by mergers or interactions. It is thought that mergers can effectively remove angular momentum from gas and consequently the gas fall into the center parts to induce nuclear starbursts (e.g., Hopkins et al. 2008, Hopkins et al. 2013). In such scenarios only the exact small scale events are considered. Our results indicate there seems to be no more critical parameters shaping the nature of starbursts arising from large-scale structures. That is, individual properties of starbursts which lie in the overdensity region is suppose to be similar with that of field SMGs. In the first place we selected flux / SFR limited samples of starbursts as SMGs. And each galaxies should have randomly distributed starburst ages within the short lifetime, gas reservoirs, masses, and so on. Considering these, the independence of individual properties on the large-scale density environment should be reasonable.

It is suggested that SMGs would appear at any field once the conditions to cause starbursts, which is represented by interactions, are satisfied. The formation site is expected to be the relatively dense environment locally, but it not usually reflect the $\sim$50 Mpc scale larger structures.

6.1.6 Extended Star-formation Activity–Density Relation

Our survey focuses on the $z \sim$3 universe. It is also crucial to trace the evolution for various era in terms of the relation between SMGs and the underlying structure. Smail et al. (2014) investigated the dusty starbursts including one ALMA-identified SMG at a $z = 1.6$ cluster field and found that the SMGs do not reside in the densest regions of the structure and lie in the moderately dense or low dense regions. Their results make an remarkable contrast with our survey. Chapman et al. (2009) also discovered similar trend in the $z = 2$ universe. They discover a spike of SMGs at $z = 1.99$, which comprise six SMGs discovered by SCUBA. This fielddoes not host a significant overdensity of BX/BM galaxies and they concluded that SMGs reside in less overdense environments. We should note that their SMGs have not been confirmed by interferometers and can be derived false counterparts and redshifts. Indeed, Bothwell et al. (2013) reported non-detection for two of them whilst they detected CO emission from three candidates. In any case, their conclusion, which the location of SMGs doesn't exactly match the density peak of normal star forming galaxies at $z \sim 2$, is consistent with the result of Smail et al. (2014).

It is also reported by Smail et al. (2014) that the densest regions in the $z = 1.6$ cluster host passive and massive galaxies while these galaxies are rare in the lower dense regions. This trend is in line with the appearance of red-sequence galaxies in a protocluster at $2 < z < 3$ presented by Kodama et al. (2007). They also found a trend that such red-sequence galaxies tend to lie near a protocluster center at $z = 2.2$. Recent deep and high resolution near-

infrared imaging observations utilizing HST have discovered that the most massive galaxies ($M_* > 10^{11} M_\odot$) at $z \sim 2$ are old compact quiescent systems (e.g., Toft et al. 2007, van Dokkum et al. 2008) and their evolved, dense stellar populations suggest formation through intense, compact starbursts 1–2 Gyr earlier (at $3 \leq z < 6$) (e.g.Toft et al. 2014).

These results listed above may be interpreted in one unified evolutionary trend. SMGs are the violent starburst population and therefore they tell us the site of the most active star-formation in the (proto-)cluster at the era. Hence the observations indicate that the 'hot' site moves from inner regions to the outer side regions as redshift decreases. Inversely the fraction of passive galaxies in the dense environment should increase. This trend should connect reasonably to the local well-established morphology-density relation (Dressler 1980).

It is also suggested that SMGs are key to establish the relation between the star-formation activity and environment in the early universe. Until today, some co-existence system that contain SMGs at $z \geq 4-5$ and several normal star forming galaxies (e.g., Carilli et al. 2010,Capak et al. 2011). Such smaller-scale galaxy groups might be the primitive proto-cluster, which corresponds to the ancestors of the passive galaxies seen the core of the $z = 3.1$ SSA22 proto-cluster (Kubo et al (2015)).

6.2 The SMBH Growth within the $z = 3.1$ Large-scale Structure

In section 6.1, we have investigated the nature of SMGs and their environmental dependence from the view point of starbursts. In this section, we focus on the SMGs as galaxy population at a growth phase of SMBHs and explore the role of the large-scale structure.

6.2.1 AGNs within SMGs in SSA22

Enhanced AGN fraction in SSA22

As described in section 5.3.2, the AGN fraction in SSA22 is significantly higher than that in ECDF-S. If we focus on only the $z = 3.1$ candidate SMGs, $f_{\rm AGN}$ reaches 32% in SSA22. In contrast there is no AGN-host SMGs at $z = 3.1$ in ECDF-S. This indicates that the AGN fraction is very sensitive to density environment and the AGN fraction in biased field would be much higher than that in the general field. Interestingly, it has been reported that LBGs and LAEs in SSA22 show somewhat larger AGN fraction compared to the general field

(CDF-N, ECDF-S) (Lehmer et al. 2009a)[8]. Therefore AGN fraction might be largely enhanced in biased fields at $z \sim 3$.

Where do AGN-host SMGs reside?

The dependence of AGN fraction on the underlying structure is illustrated more clearly in Figure 6.9. It is suggested that AGN-host SMGs appear in only the area around the density peak and the number of AGN-host SMGs increase more steeply in the dense field compared to all $z = 3.1$ SMGs. This result indicates that the appearance of AGNs within SMGs is really sensitive to the underlying density environment.

As show in Figure 6.3, the five AGN-host SMGs concentrated into the central $2' \times 3'$ field named ADF22[9]. In this field another heavily obscured X-ray AGN, J221737.3+001823.2, has been discovered (Tamura et al. 2010) and confirmed as the protocluster member spectroscopically ($z_{\rm spec,[OIII]} = 3.09$) (Kubo et al 2015), though we cannot detect significant 1.1 mm emission by our ALMA survey. Therefore totally six X-ray luminous AGNs lie this small area[10]. Even though we cannot completely rule out the possibility of "shot noise"-like clustering, this "AGN cluster" represents the extreme excess in volume density. While the averaged volume density above the SSA22 detection limit at $z = 3.1$ derived from the latest X-ray luminosity function (Ueda et al. 2014) is $\sim 3 \times 10^{-5}$ Mpc^{-3}, the volume density in ADF22 reaches $\sim 4 \times 10^{-3}$ Mpc^{-3}. [11] Hence it is suggested that AGN-host SMGs are formed in crowds.

It is worth noting that the position of $z = 3.09$AGN group in ADF22 completely coincidences with the node of the LAE filaments three-dimensionally (Figure 6.15). We might be seeing the accelerated SMBH growth in the deepest potential well.

[8]They simply defined the AGN fraction of LBGs/LAEs as the fraction of X-ray sources in each bin. And the elevation in the AGN fraction of SSA22 were found in all bin for both of LBGs and LAEs.

[9]We have conducted deep 1.1 mm mosaic continuum survey in this field using ALMA (PI. Umehata, #2013.1.00162.S). We named this field ADF22, which means "ALMA Deep Field in SSA22".

[10]Three sources have been confirmed spectroscopically. The remaining three are also supported various indications as discussed in chapter 5.

[11] We consider the redshift range of $z = 3.06 - 3.12$ here. The luminosity function is for rest-flame 2.0–10.0 keV intrinsic luminosity and therefore we converted the 0.5–8.0 keV luminosity into the luminosity multiplying 0.62 assuming $\Gamma = 1.80$.

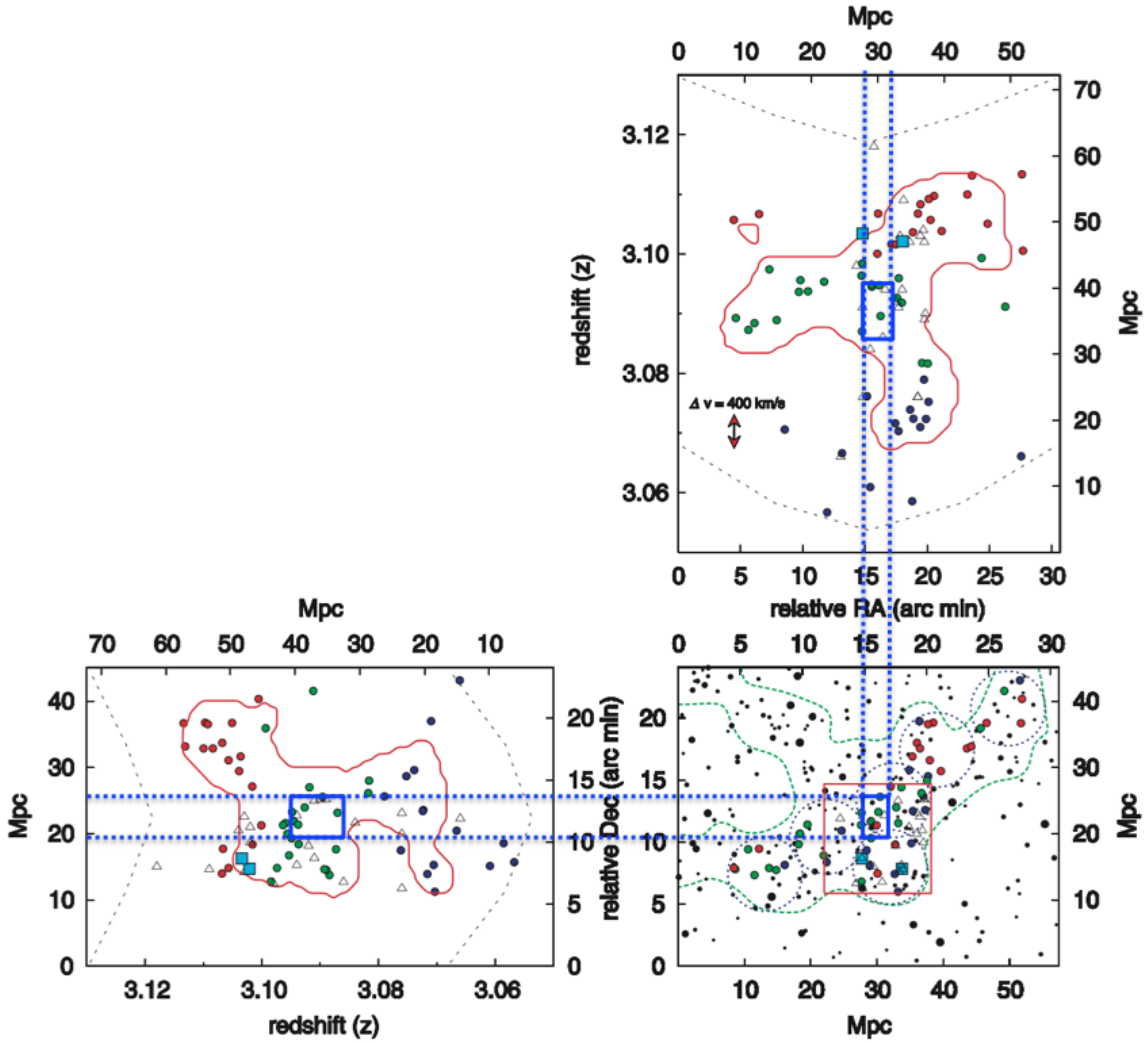

Fig. 6.15 The position of ADF22. Back ground figures represent the large-scale filamentary structure traced by $z = 3.09$ LAEs from Matsuda et al. (2005)

6.2.2 The Nature of AGN-host SMGs

Characterization of the AGN-host SMGs in ADF22 is the next issue. In terms of the large number of ALMA sources and deep X-ray observations, the ALESS survey is the best for comparison as well as previous discussions. In addition, the combination of a SCUBA and *Chandra* survey in CDF-N assisted by VLA identification (Alexander et al. 2005 and Alexander et al. 2008) are helpful to increase the number of X-ray SMGs, though we should note that some of CDF-N samples are not confirmed as indeed X-ray bright SMGs (i.e., there is no evidence but radio identification).

Luminosity Ratio

First we compare the intrinsic X-ray luminosity with the FIR luminosity ($L_{40-120\mu\mathrm{m}}$, or L_{FIR}) to investigate the contribution of AGNs to FIR luminosity as well as Alexander et al. (2005) and Wang et al. (2013a). The calculated FIR luminosity are listed in Table 6.4 and the results are shown in Figure 6.16. The median slope of five AGN-host SMGs in SSA22 is 0.0125, which implies that the bolometric luminosity of the host galaxies is dominated by star-formation like other SMGs. On the other side, these SMGs are likely to have (i) large X-ray luminosity and (ii) large slope compared to the remaining two fields. The first trend might be not a surprising result. While the majority of other X-ray SMGs are at $z \sim 2$, our target redshift is beyond 3 and hence we can only detect the bright X-ray sources. For the second trend, we investigate in detail in the next.

ID [a]	ALMA ID [b]	L_{FIR} [c] $10^{12}L_{\odot}$
1	ASA 001.1	6.4
2	ASA 001.2	1.5
3	ASA 014.1	2.3
4	AS-AGN001.1	1.3
5	AS-AGN005.1	1.6

Table 6.4 The catalog of FIR luminosity (rest-flame 40-120 μm).
[a]: a clipped ID displayed in Figure 6.16.
[b]: an ALMA source ID.
[c]: rest-frame 40–120 μm luminosity. We converted the total IR luminosity to the $40-120$ μm FIR luminosity by multiplying 0.8 This factor is evaluated from Wang et al. (2013a).

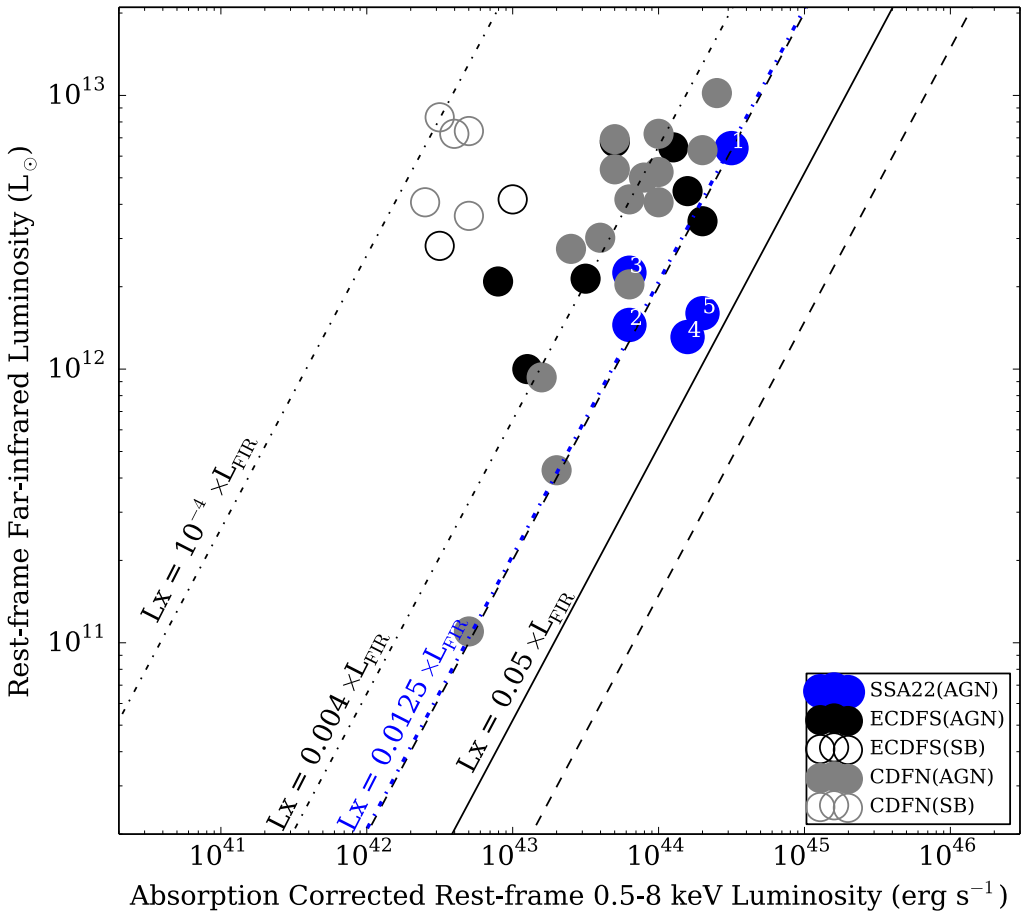

Fig. 6.16 Rest-frame FIR luminosity ($L_{\rm FIR}$) against rest-frame 0.5–8.0 keV absorption-corrected luminosity for SMGs in the SSA22 field (this work) as well as in the ECDF-S (Wang et al. 2013a) and in the CDF-N (Alexander et al. 2005). Filled circles shows the distributions of SMGs classified as AGNs. The overlaid number corresponds to the ID in Table 6.4 The SMGs of which X-ray counterpart is classified as starburst candidates (i.e., not AGNs) are represented using empty circles. The solid black line shows the median ratio between the two-type luminosity for the quasars (Elvis et al. 1994). The area between the dashed black lines stands for the standard deviation. The black dot-dashed line is the median ratio of the SMGs in CDFN, classified as AGNs(Alexander et al. 2005). The dot-dashed blue line shows the median ratio of SSA22 AGN-SMGs.

Relative SMBH and Galaxy Growth Rates

We estimate the mean SMBH growth rates $\dot{M}_{\rm BH}$ via some assumptions. As well as Lehmer et al. 2013, here we calculate it as follows:

$$\dot{M}_{\rm BH} = (1-\varepsilon)L_{\rm bol}^{\rm AGN}/\varepsilon c^2 \tag{6.3}$$

where ε is the efficiency when accreting mass convert into radiative energy, $L_{\rm bol}^{\rm AGN}$ is AGN bolometric luminosity, and c is the speed of light. We assume $\varepsilon = 0.1$ (Marconi et al. 2004) and that the 0.5 to 8 keV X-ray luminosity from the AGN is equivalent to 6 per cent of its total bolometric luminosity (Elvis et al. 1994). Combining this estimate with SFR derived from ALMA observations, we can infer the mean growth ratio of SMBH and stellar components as suggested by a number of previous works (e.g., Lehmer et al. 2013, Willott et al. 2013).

Figure 6.17 represents the growth ratio for SMGs in ADF22 (SSA22) and ECDF-S. The ratio of SSA22 SMGs is significantly larger than that of SMGs in ECDF-S. This result suggests that the accelerated SMBH growth in the node of the cosmic web.

6.2.3 The Role of Large-scale Density Environment in the SMBH Growth

In contrast to the nature of starbursts, it is suggested that the AGN fraction of SMGs is really sensitive to the large-scale structure. This fact suggests the importance of density environment in the growth of SMBHs. The triggering mechanism to induce the SMBH growth is also considered to be mergers, which cause the inflow of gas into the inner regions (e.g., Menci et al. 2008, Hopkins et al. 2008, Lamastra et al. 2010). This significant environmental dependence is also addressed in the merger paradigm. In the case of SMGs that lie around the density peak in SSA22, these sources are considered to be hosted in the most massive haloes, in which the merger rate, the interaction efficiency, and the amount of destabilized gas are relatively large compared to the general field. Consequently the accretion activity should be increased. It is also indicated that AGN-host SMGs in SSA22 tend to have more luminous X-ray counterparts, which principally represents larger SMBH masses, compared to CDF-N / ECDF-S as shown in Figure 6.16. Although the X-ray sensitivity limit in SSA22 is shallower than that in CDF-N / CDF-S and therefore it can be affected by the selection bias, it might support rapid growth of SMBHs in the most dense environment.

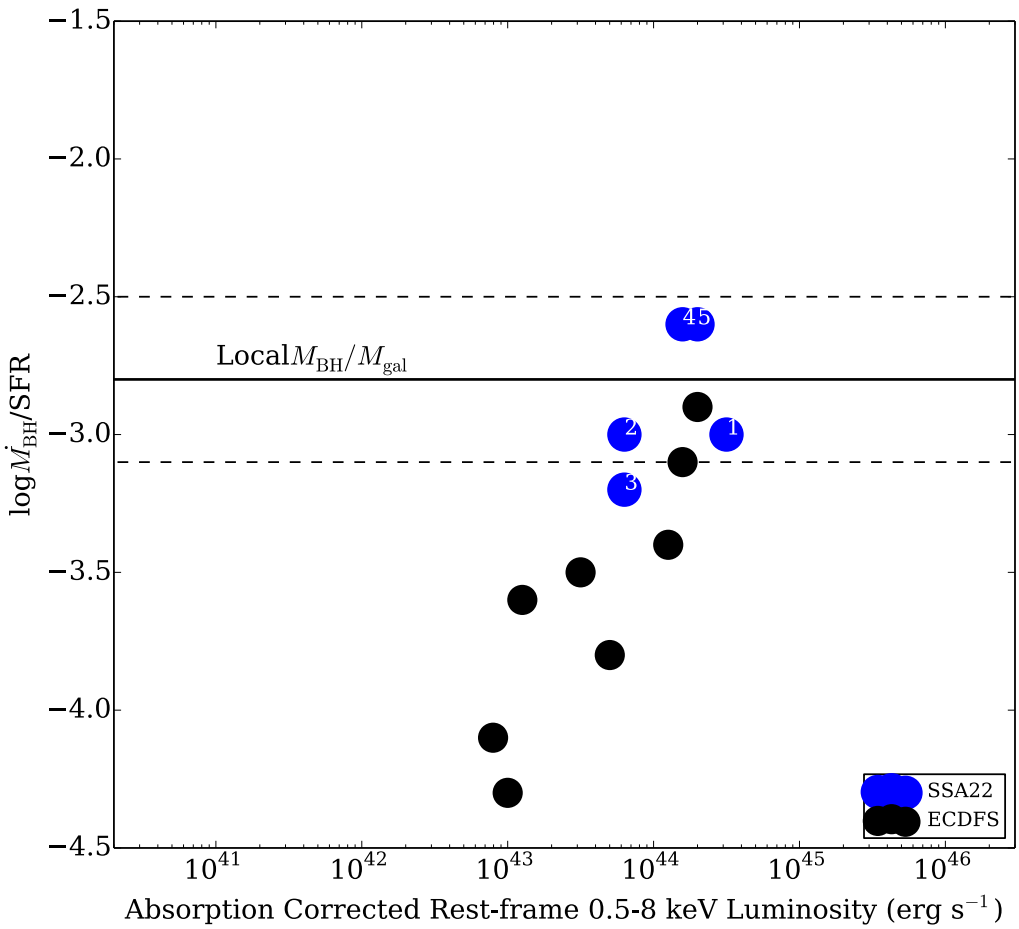

Fig. 6.17 The averaged growth ratio, $\log\dot{M}_{\rm BH}$/SFR, as a function of intrinsic X-ray luminosity. The area between the dashed line represents the local $M_{\rm BH}/M_{\rm gal}$ relation (Häring & Rix 2004). Symbols and IDs same as Figure 6.16.

Chapter 7

Summary

We conducted two large SMG surveys at 1.1 mm by AzTEC/ASTE and ALMA toward the SSA22 proto-cluster field. Subsequently inspected the characteristics of ALMA-detected SMGs utilizing a rich multi-wavelength data set including X-ray, optical, near- to mid-infrared, and radio. Finally we unveiled the strong environmental dependence on such SMG formation compared our survey to the other ALMA survey in a general field.

Here we summarize as follows:

1. We conducted to 1.1 mm continuum mapping survey with the AzTEC bolometer camera onboard the ASTE 10m telescope. We observed 954 arcmin^2 area of the SSA22 field down to 1σ noise of 0.7 mJy beam^{-1}. We achieved the angular resolution of $\sim$30$''$. Totally 125 dusty sources with deboosted flux density of 1.9–11.3 mJy were discovered with S/N$\geq$3.5. Our simulations suggested about 6 % of the detected sources can be spurious sources.

2. Based on the results of the AzTEC/ASTE survey, we performed the 1.1 mm continuum imaging observations with ALMA for 45 AzTEC sources (PI. Umehata). The targets were divided into three scheduling blocks. The 1 $^{\sigma}$ noise revel of $\sim$160, $\sim$100, $\sim$70 μJy beam^{-1} were achieved for each scheduling blocks. The achieved angular resolution reached $0.7'' \times 0.6''$. Hence there were great jumps in sensitivity ($\times$4-10 times) and in angular resolution ($\times$50). Consequently ALMA revealed that 45 AzTEC sources are divided into 64 individual SMGs.

3. We calculated number counts of 1.1 mm sources from our ALMA survey. This survey is the largest survey in ALMA band 6 as well as the largest survey in a biased field. While the derived number counts are well consistent with the previous 870 μm large survey at the 1.1 mm flux density of 3–4 mJy, we also discovered the inconsistency in

the bright and faint end. In the bright end the previous works from the ALESS 870 μ survey argued that the number counts decrease rapidly but we find a significantly bright source (ASA1.1, 1.1 mm flux density of 6.40 mJy). This result weakened their argument. In the faint end we found possible excess in the SSA22 counts compared those in ECDF-S. This might be reflected that the large number of SMGs would reside in the $z = 3.1$ proto-cluster.

4. We checked the predictions from the 1.4 GHz radio data, MIPS 24μm data, and IRAC 3.6–8.0μm data in counterpart identification. We found the high accuracy of the radio data (79%), moderate reliability of the IRAC data (52%), and the really poor answer rate of the MIPS data (33%). These results strongly support the necessity of ALMA identification for single-dish selected duty starburst galaxies.

5. The multi-wavelength photometries of the ALMA sources in the optical to near-infrared wavelengths show that most of the ALMA detected SMGs (27/64) are so faint that we cannot detect even at K (Ks) band (>22.7 $\mathrm{mag_{AB}}$). On the contrary, the detection rate rapidly increase to 90% (55/61) at 3.6 μ. These result supports the usefulness of IRAC data in identifying and/or investigating the nature of SMGs. It is also suggested that the radio-selected sample in Chapman et al. (2005) are highly biasd sample. The median AB magnitude of our survey is 1.6 mag fainter than their survey.

6. We performed SED fitting using the HYPERZ code to derive photometric redshifts. We utilized uniformly smoothed images at $B, V, R, i', z', J, H, K(Ks)$ bands. The derived photometric redshifts represent the excellent consistency with the spectroscopic redshift for five sources ($z_{\mathrm{phot}} = z_{\mathrm{spec}} \pm 0.15(1 + z_{\mathrm{spec}})$). The obtained redshift distributions show different profiles compared to the ALESS survey. It is still controversial, but this might be affected by the $z = 3.1$ large-scale structure.

7. Although it is not easy to derive stellar mass for SMGs, we calculated it from the absolute H band magnitude derived from SED fitting and compared the mass distribution of SSA22 with that of ECDF-S. There seems to be no significant difference in both 1.1 mm and 870 mm selected populations and therefore both may have similar stellar mass as a whole.

8. Utilizing the existing deep *Chandra* X-ray data, we searched for the SMGs which harbor obscured but X-ray luminous AGNs. We identified five SMGs have X-ray counterparts, all of which are considered to be at $z = 3.1$. Subsequent classification procedures supported that all of these five sources host AGNs. The X-ray luminosity

– FIR luminosity ratio and the derived growth ratio of SMBH and stellar components suggest the accelerated SMBH growth in the node of the cosmic web. Local environment can be a key factor in SMBH Growth and high interaction rate and large gas reservoir at the core should lead the high X-ray detection rate.

9. We address the density environment at the position of SMGs using the number surface density of $z = 3.1$ LAEs for both fields and inspect the influence of environment on the nature of SMGs. Consequently three remarkable trends are discovered. First, the number of SMGs per unit area increases as the environment becomes dense. Second, there is no recognizable environmental dependence on individual properties such as star formation rate, stellar mass, specific star formation rate. Third, the AGN fraction of SMGs steeply increases at the densest regions. The merger is considered to be the most plausible trigger and indeed we found the signature of mergers in many cases. It is expected that in the densest environment the high interaction rate and efficiency, and large amount of destabilized gas can cause the starbursts as well as the rapid growth of central SMBHs.

Appendix A

Muti-wavelength Data Set of ALMA SMGs

A.1 Photometries and SEDs

In Figure A.1 – A.6, we present the photometries and best fit spectral energy distributions (SEDs), as well as the reduced χ^2 distributions as a function of redshift, for ALMA sources which have at least one detection. (If a source have no photometric point (i.e., just upper limits), HYPERZ doesn't work.)

A.2 Postage Stamps

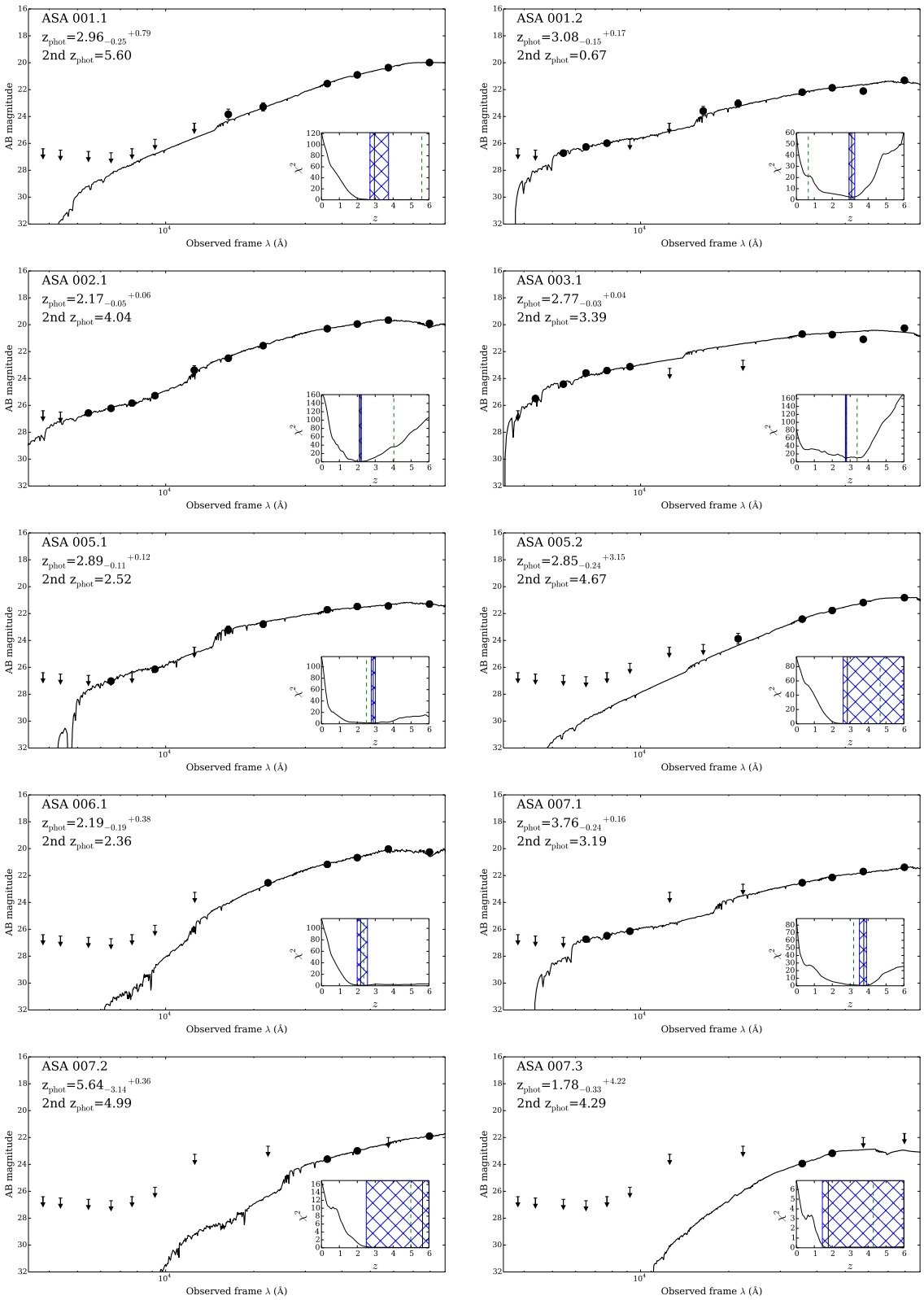

Fig. A.1 SEDs (1/6)

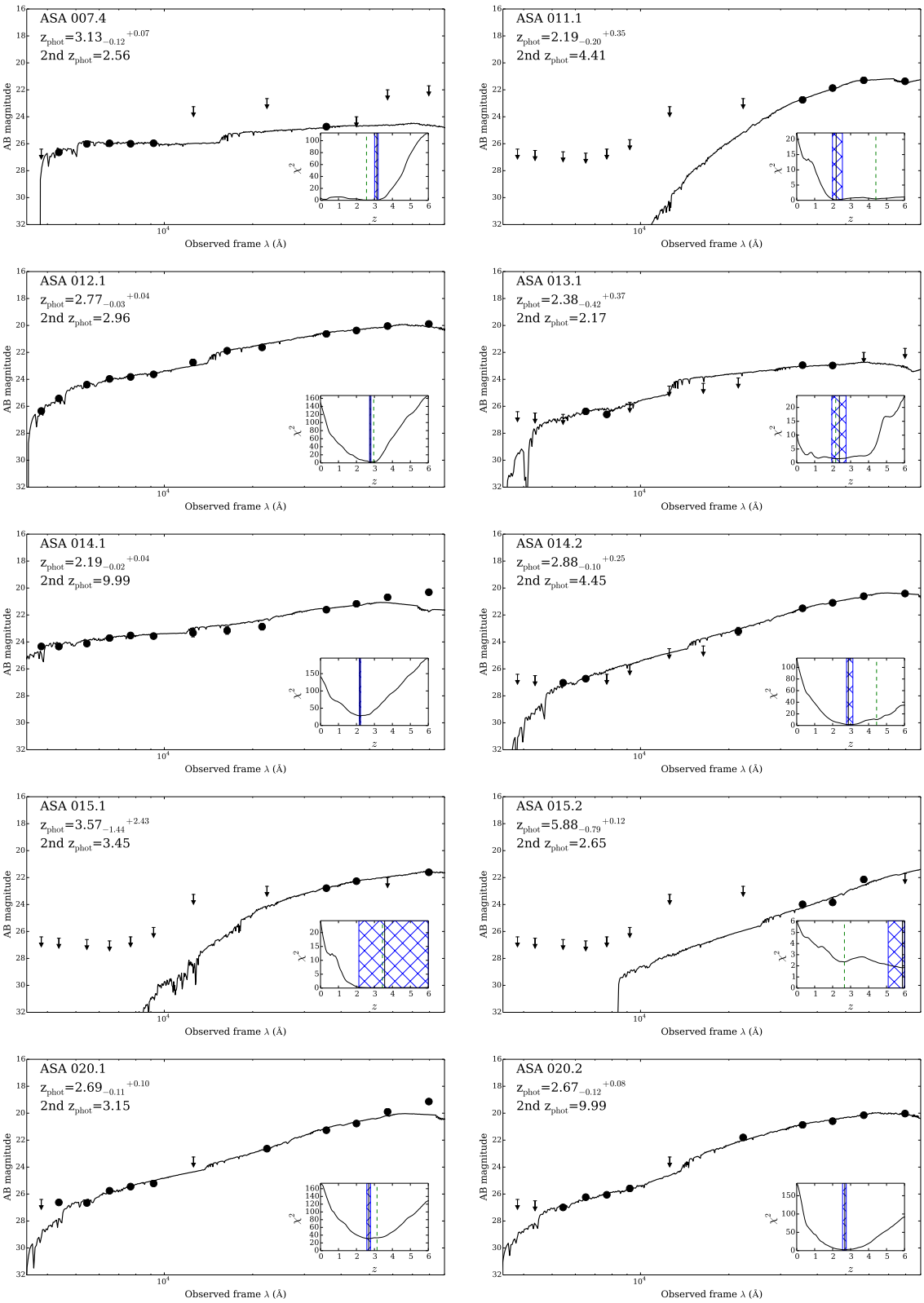

Fig. A.2 SEDs (2/6)

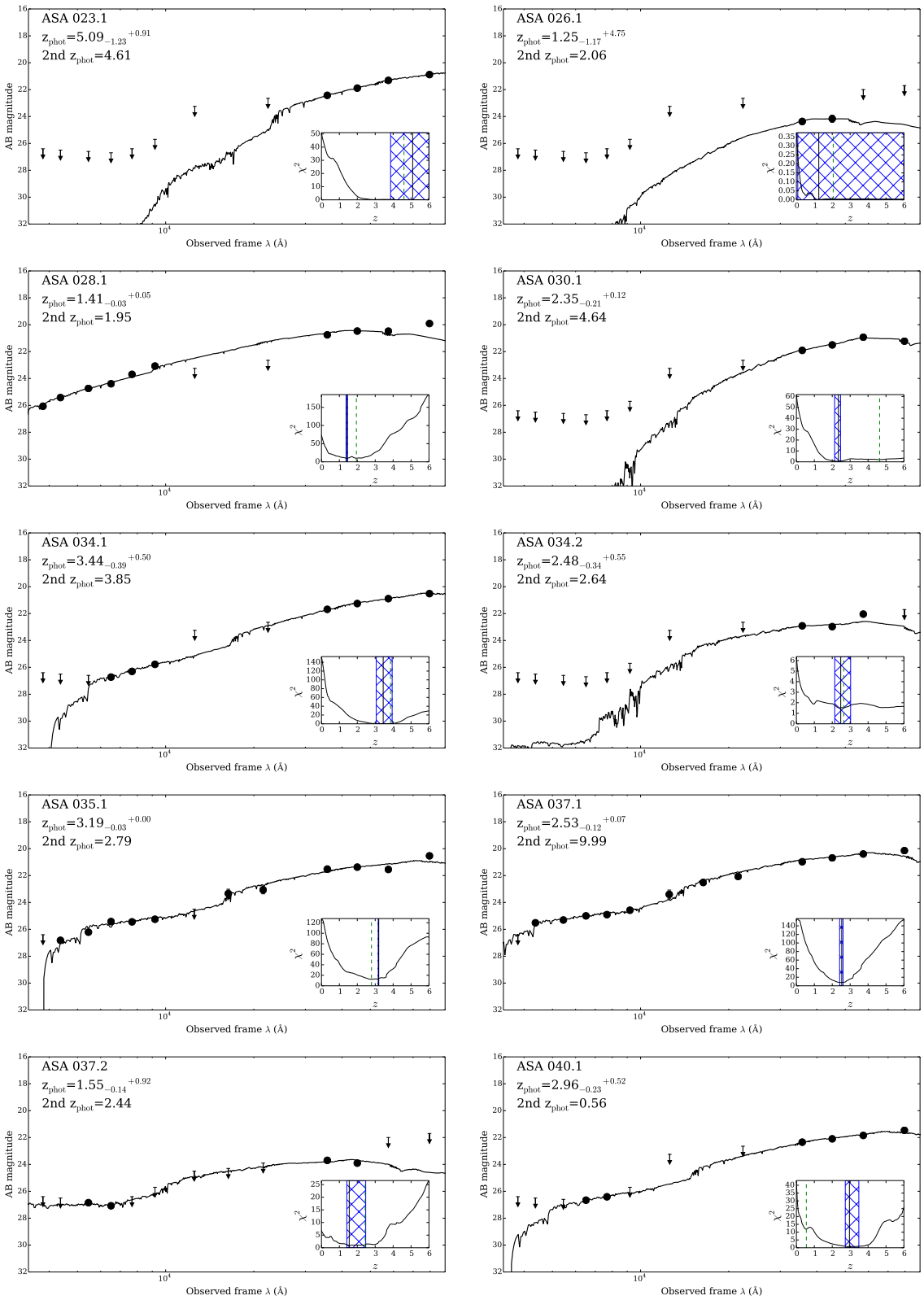

Fig. A.3 SEDs (3/6)

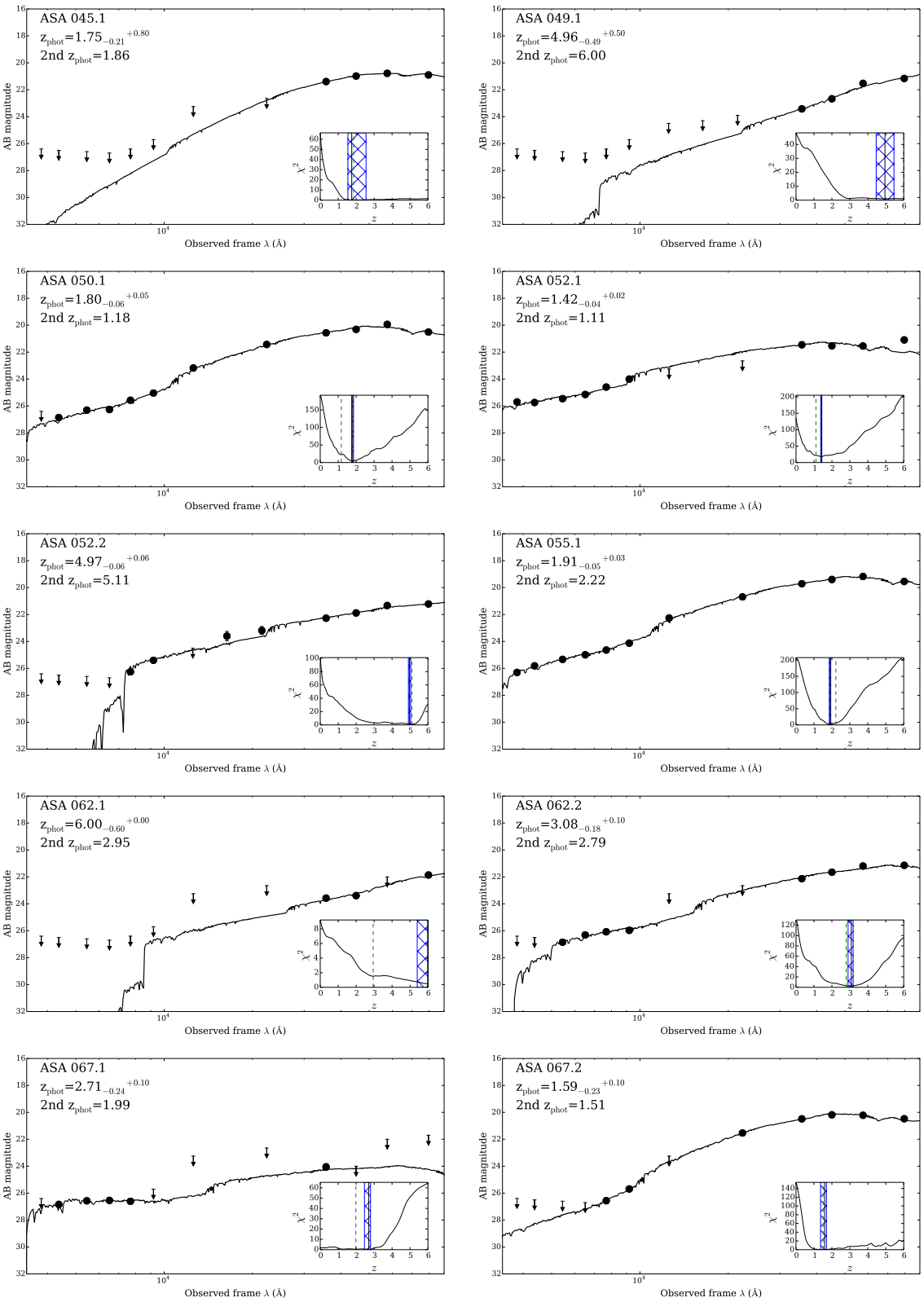

Fig. A.4 SEDs (4/6)

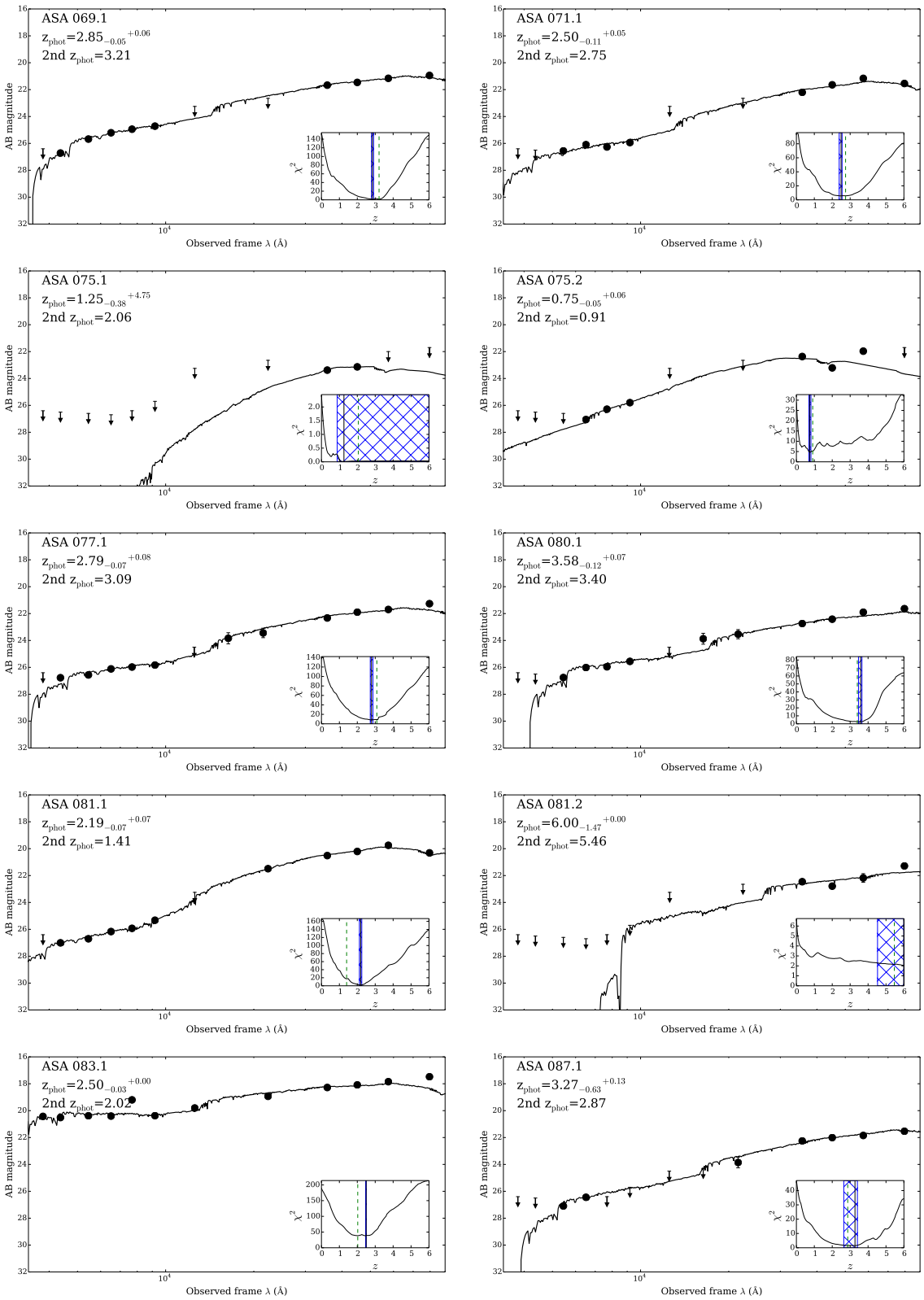

Fig. A.5 SEDs (5/6)

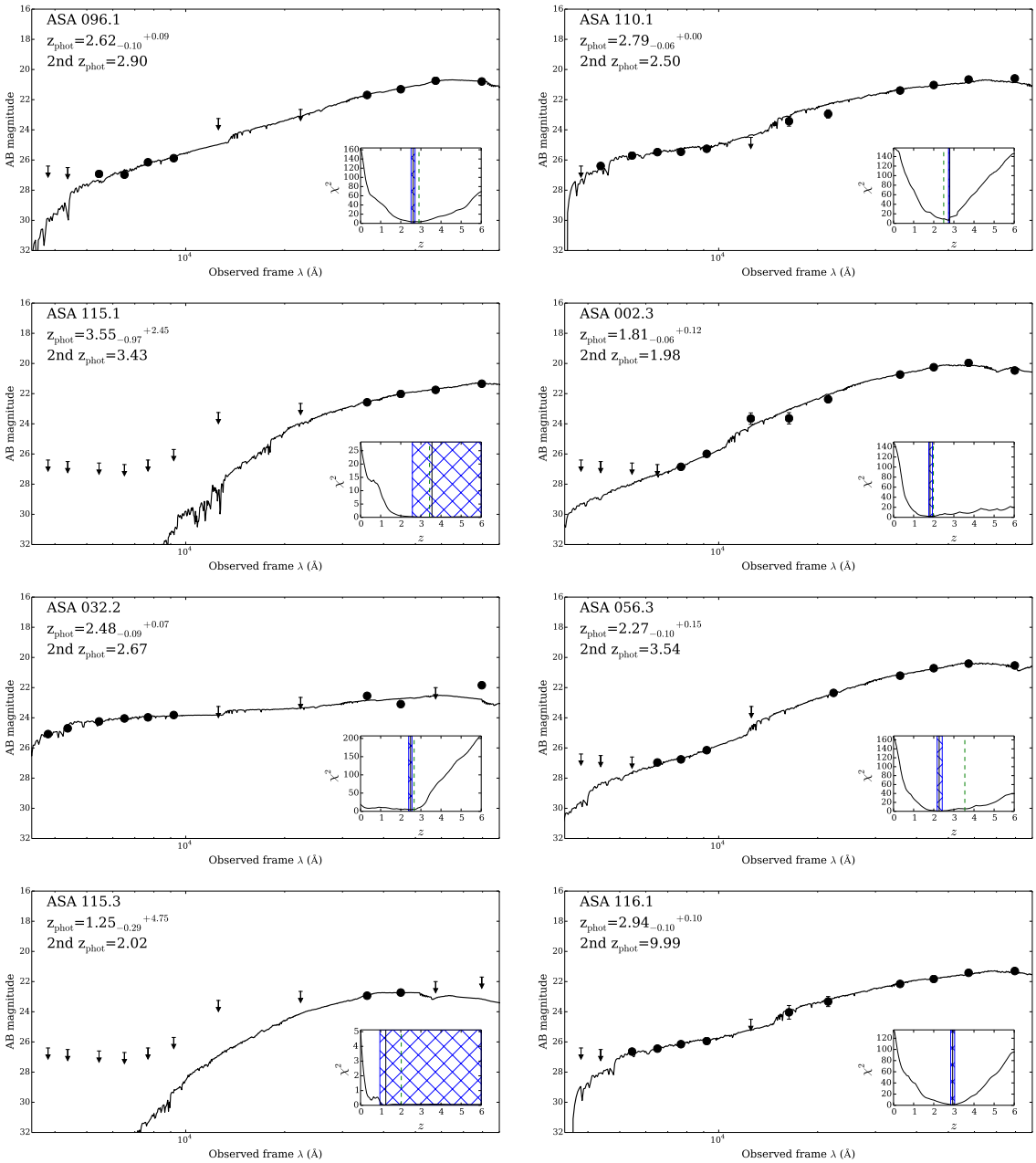

Fig. A.6 SEDs (6/6)

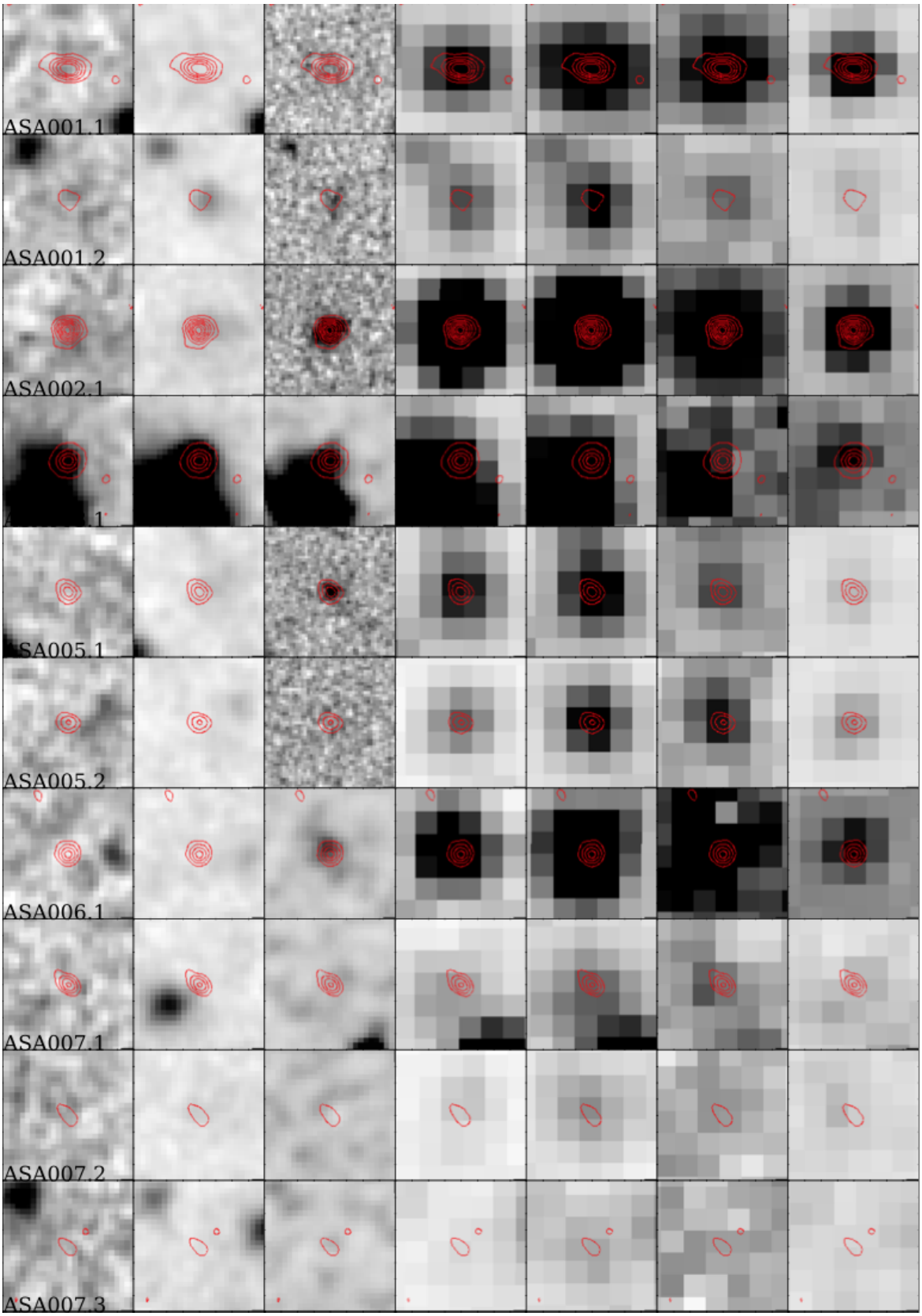

Fig. A.7 Postage Stamp (1/7)

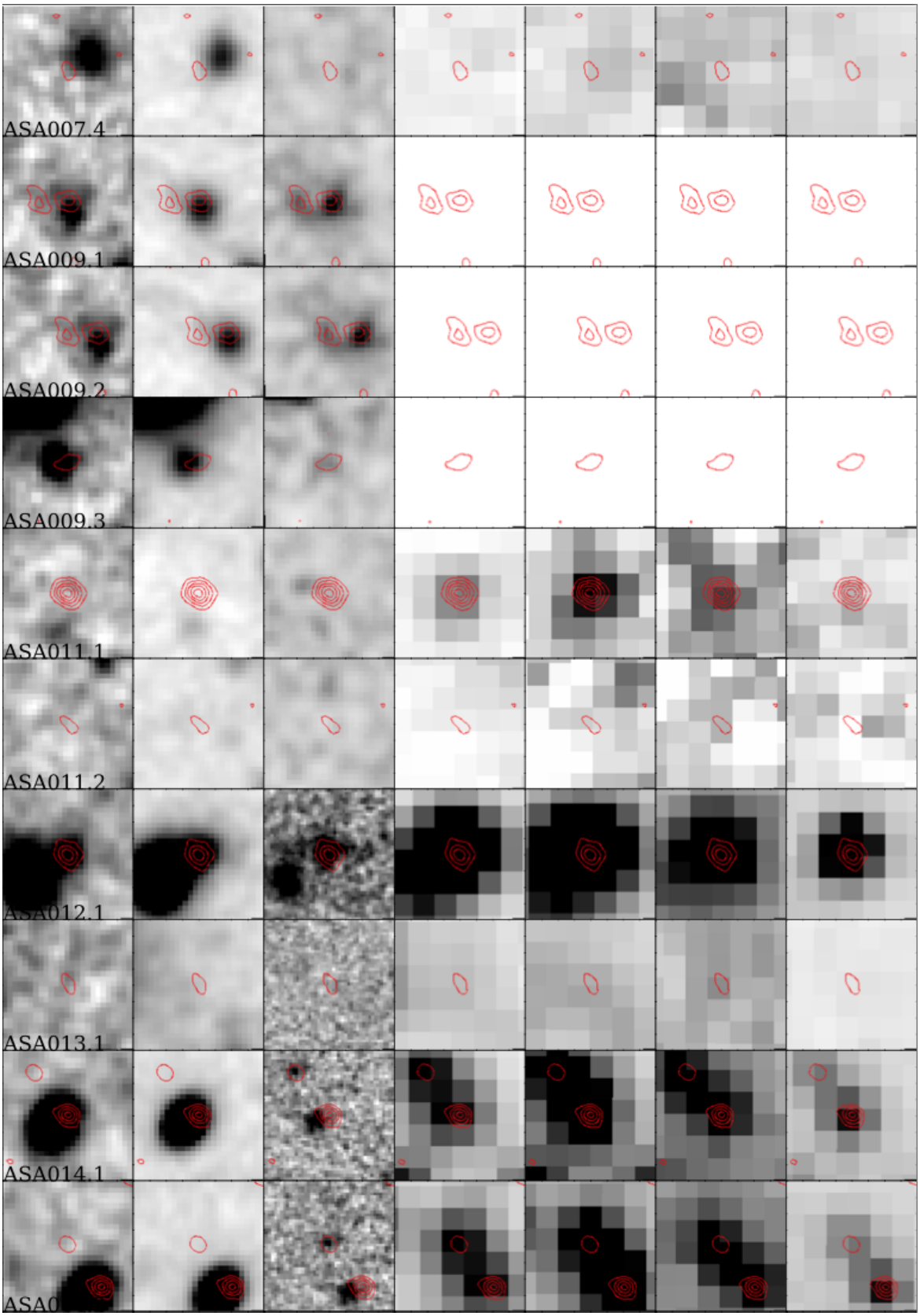

Fig. A.8 Postage Stamp (2/7)

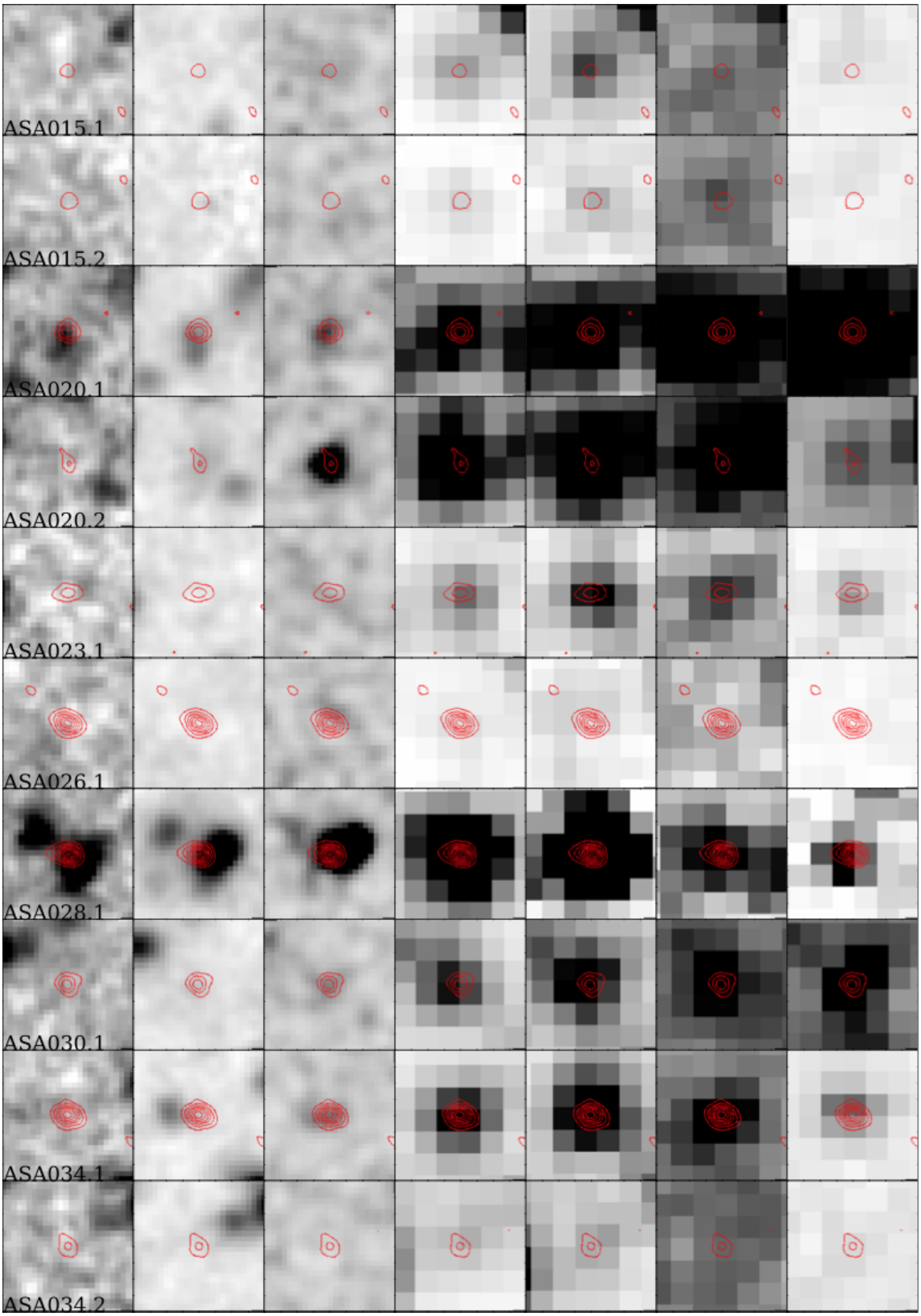

Fig. A.9 Postage Stamp (3/7)

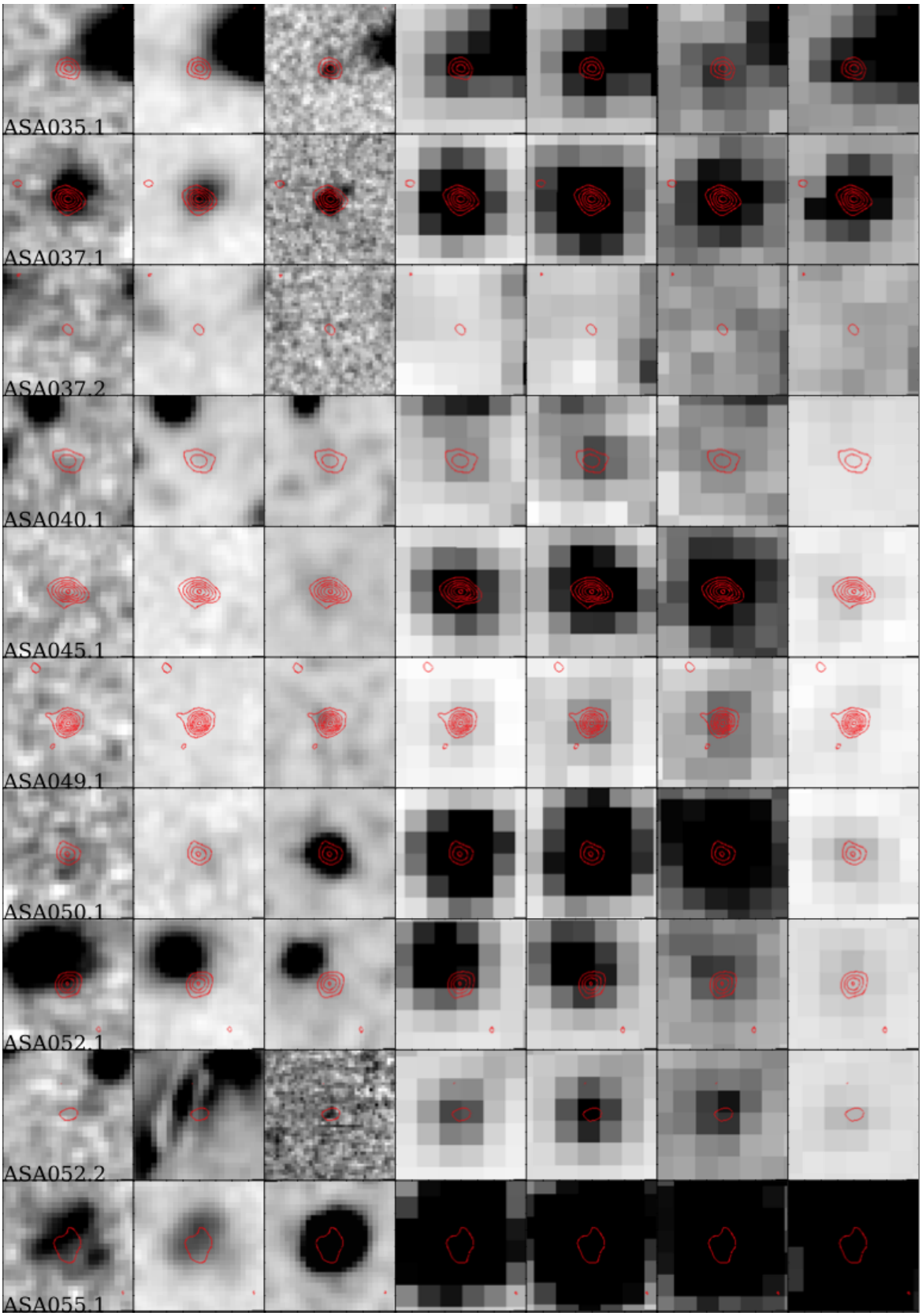

Fig. A.10 Postage Stamp (4/7)

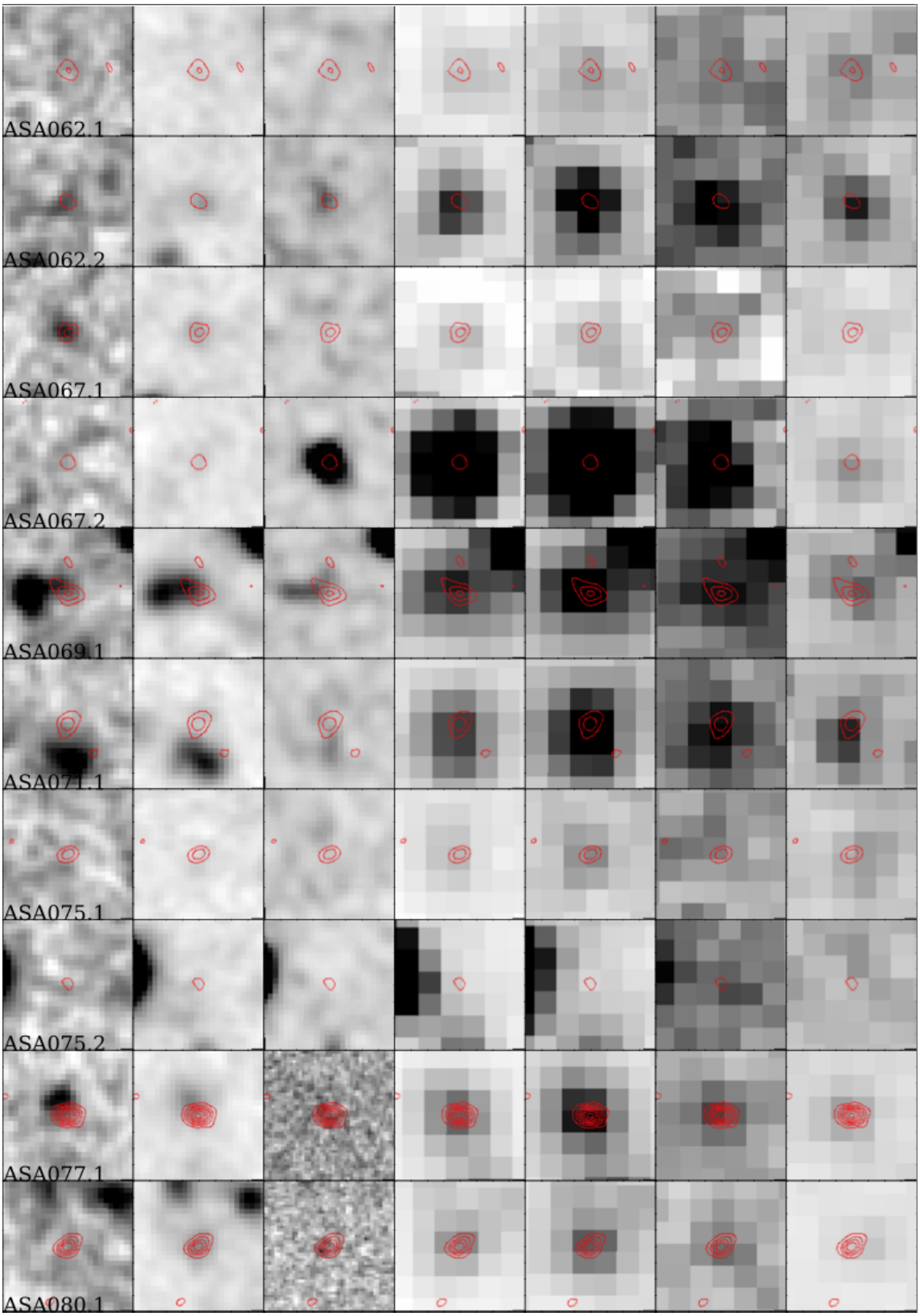

Fig. A.11 Postage Stamp (5/7)

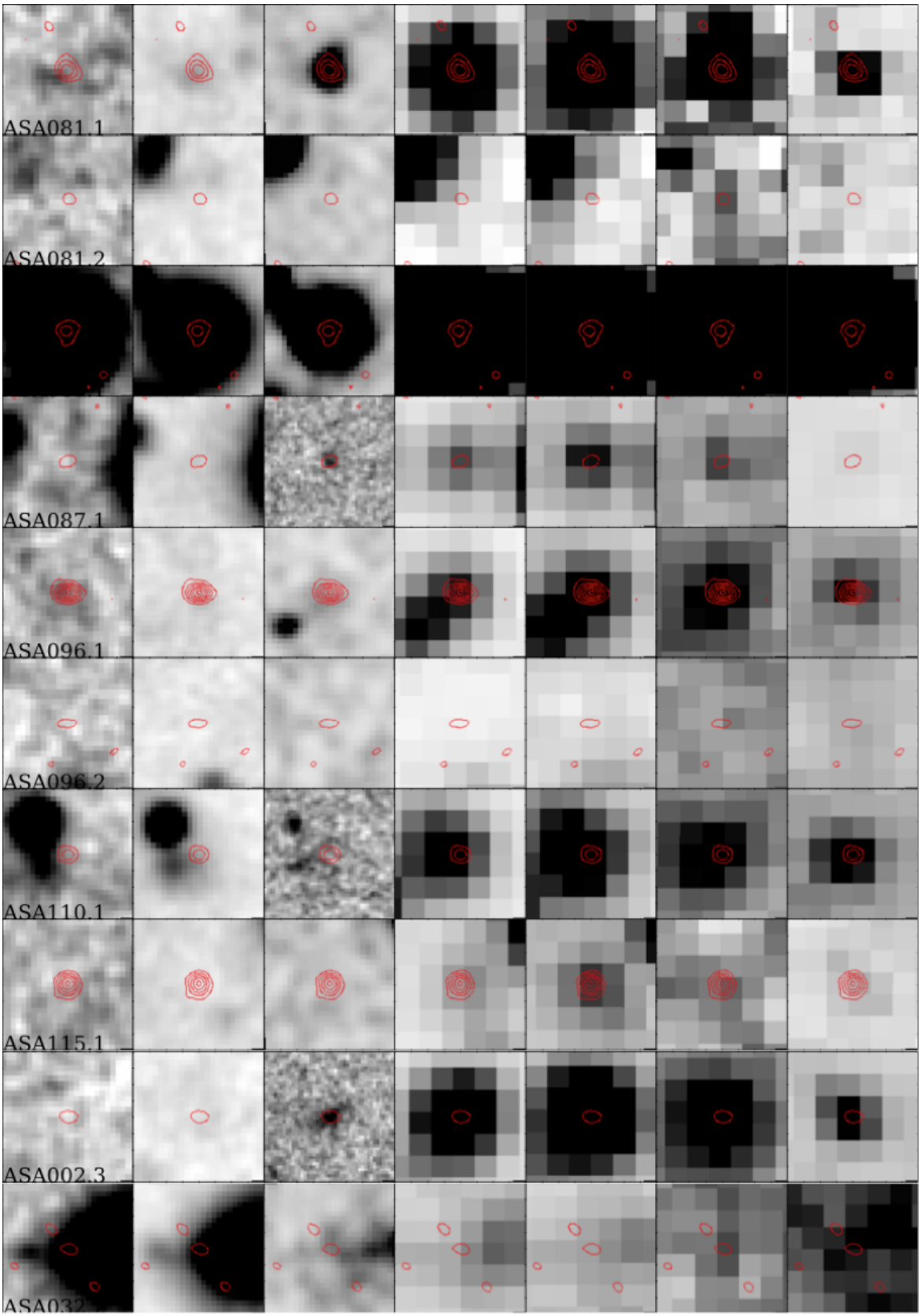

Fig. A.12 Postage Stamp (6/7)

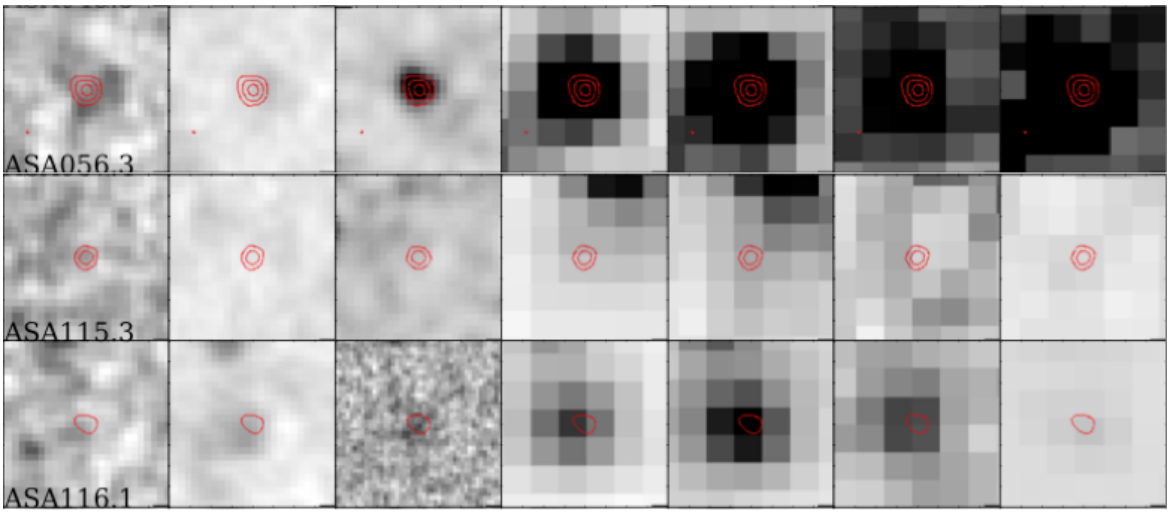

Fig. A.13 The gallery of ALMA sources listed in the main catalog. Each panel shows the images at B, R, $K(Ks)$, 3.6μm, 4.5μm,5.8μm, and 8.0μm bands. If the source have MOIRCS images, we show them at the three column. The area of 5 arcsec on four sides are shown for each panel. The red contour shows the $3, 6, 9, ...\sigma$ 1.1 mm emission. (In the case of ASA 003.1, the $3, 9, ..\sigma$ contours are shown for a clear view.) ALMA ID is represented in the left bottom of each row.

Appendix B

Spectra of ALMA SMGs

B.1 Optical Spectroscopy with VLT/VIMOS

We performed a optical spectroscopic observation with VLT/VIMOS (PI. Umehata, ID. #089.A-0740). Observations were taken with the LR-Blue grism (R = $\lambda/\Delta\lambda \simeq 180$, dispersion of 5.3 Å/pix). The slit width was set to $1''.0$. The wavelength coverage is around 4000–7000 Å.

Here we just present individual spectra at rest-frame. The green lines show the originally obtained spectra. The blue lines represent the 4-pix binning spectra. We newly obtained $z_{\rm spec}$ for two ALMA SMGs, ASA20.1 and ASA34.1.

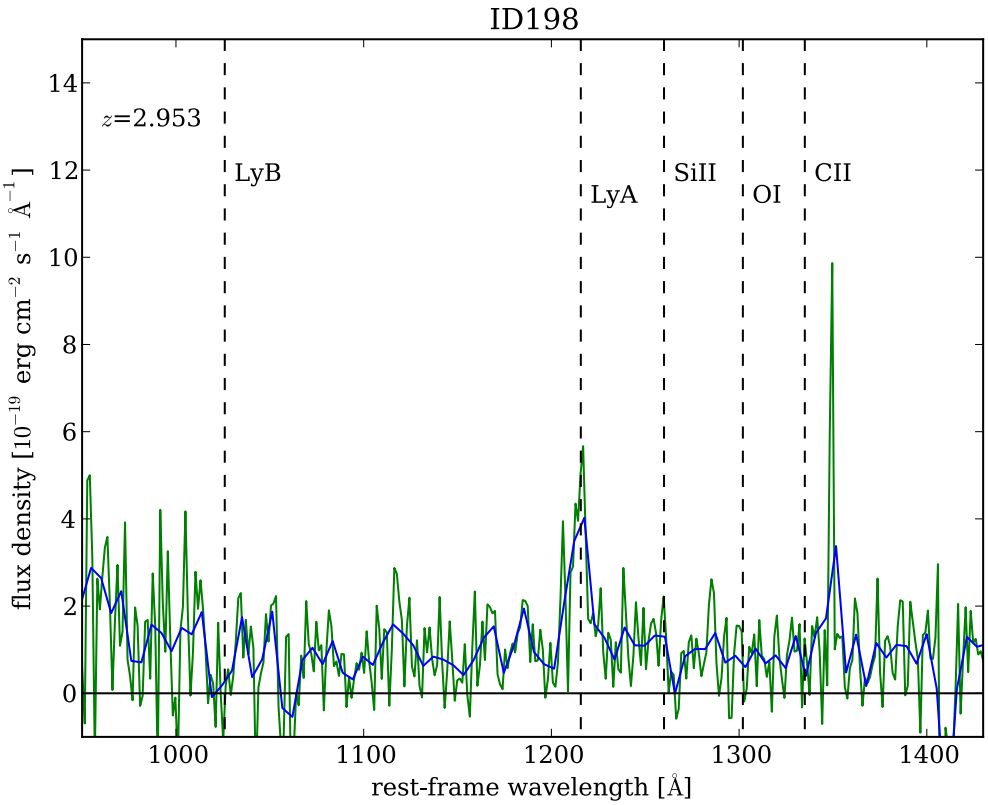

Fig. B.1 Rest-frame Optical Spectra of ASA 20.1

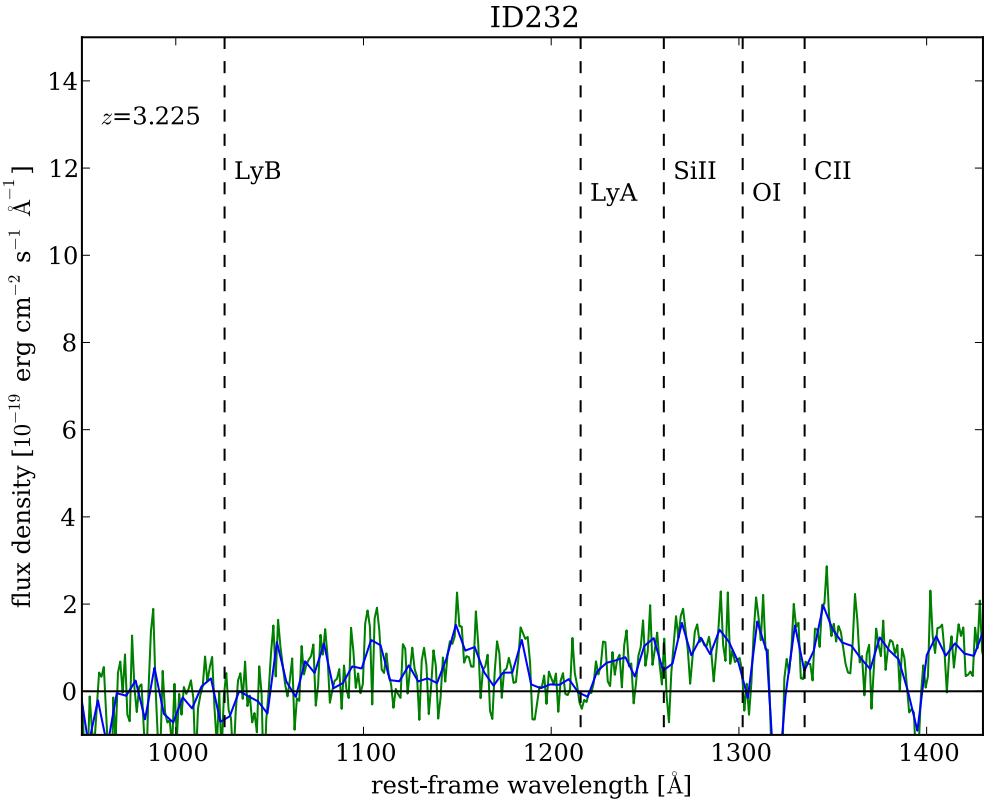

Fig. B.2 Rest-frame UV Spectra of ASA 34.1

B.2 CO Spectra Obtained with NRO45m

The spectra of SSA22-AzTEC1 taken with Nobeyama 45 m dish. There is an excess ($\sim 2\sigma$) in the region where two spectrometer coverages overlap. The excess is at 84.67 GHz and it can be the ^{12}CO(3-2) emission. If so, its redshift would be $z = 3.083$. The solid black line shows the spectra of "low" side spectrometer and the dashed green line represents that of "high" side one. The best-fitting single Gaussian profiles of the spectra of "low" side one is overlaid.

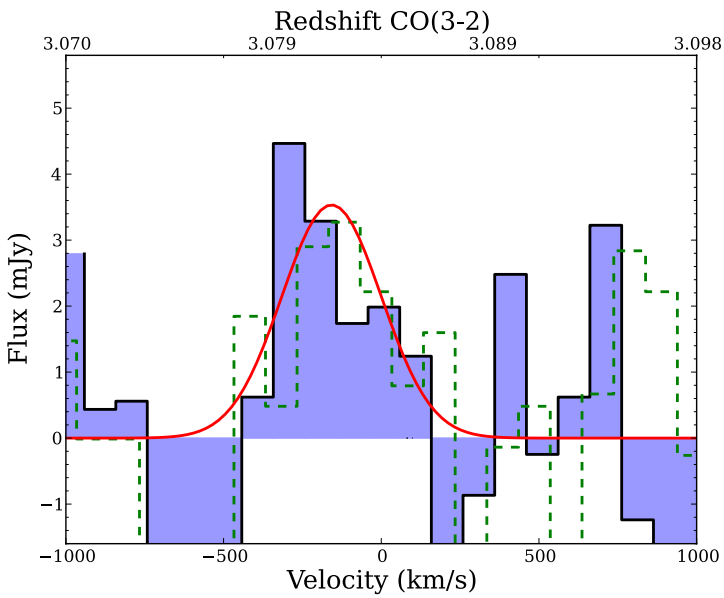

Fig. B.3 Possible CO(3-2) Spectra of ASA 1.1

Appendix C

Additional Remarks

C.1 Source Size Measurement in u-v Plane

To measure source size exhaustively, we perform the model fit in the (u,v) plane as well as previous works (e.g., Younger et al. 2008, Tamura et al. 2010, Simpson et al. 2014a, Ikarashi et al. 2014). We assume a single circularly symmetric component of Gaussian as follows (Purcell 1973),

$$f(r) = \frac{1}{\sqrt{\pi/4\ln 2a}}\exp\left(\frac{-4\ln 2 r^2}{a^2}\right) \tag{C.1}$$

$$F(\rho) = \exp\left(\frac{-(\pi a\rho)^2}{4\ln 2}\right) \tag{C.2}$$

where $f(r)$ is a model brightness distribution in the sky plane and $F(\rho)$ is the model visibility, computed by Fourier transformation. The arguments, r and ρ are $r = \sqrt{l^2+m^2}$ and $\rho = \sqrt{u^2+v^2}$, respectively. The units of u and v is the wavenumber. The term a represents the FWHM of the model Gaussian (rad).

As shown in Figure C.1, u,v distribute between $\sim -400\mathrm{k}\lambda$ and $\sim 400\mathrm{k}\lambda$. The longest baseline is 558.2m, which corresponds to 489 kλ at 263 GHz.

The annular averaged amplitude is calculated in each bin, which has 50–100 kλ using the MIRIAD task, uvamp. In Figure C.2 and C.3, we plot the result for the bin with S/N>2. The median value of five 10σ sources but ASA 1.1 is 0.25 arcsec, which correspond to 2 kpc at $z = 3.1$.

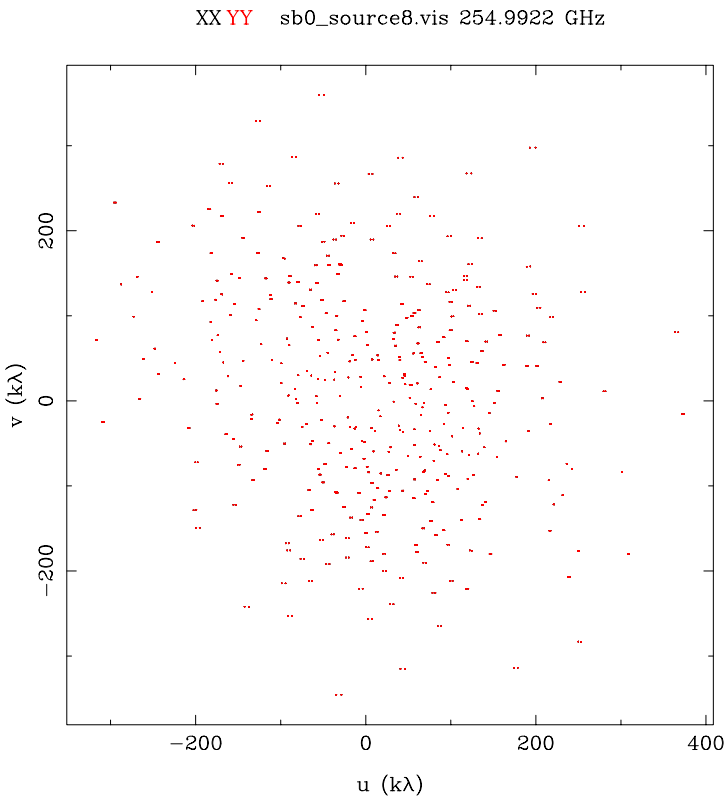

Fig. C.1 u, v plot of ASA 1.1

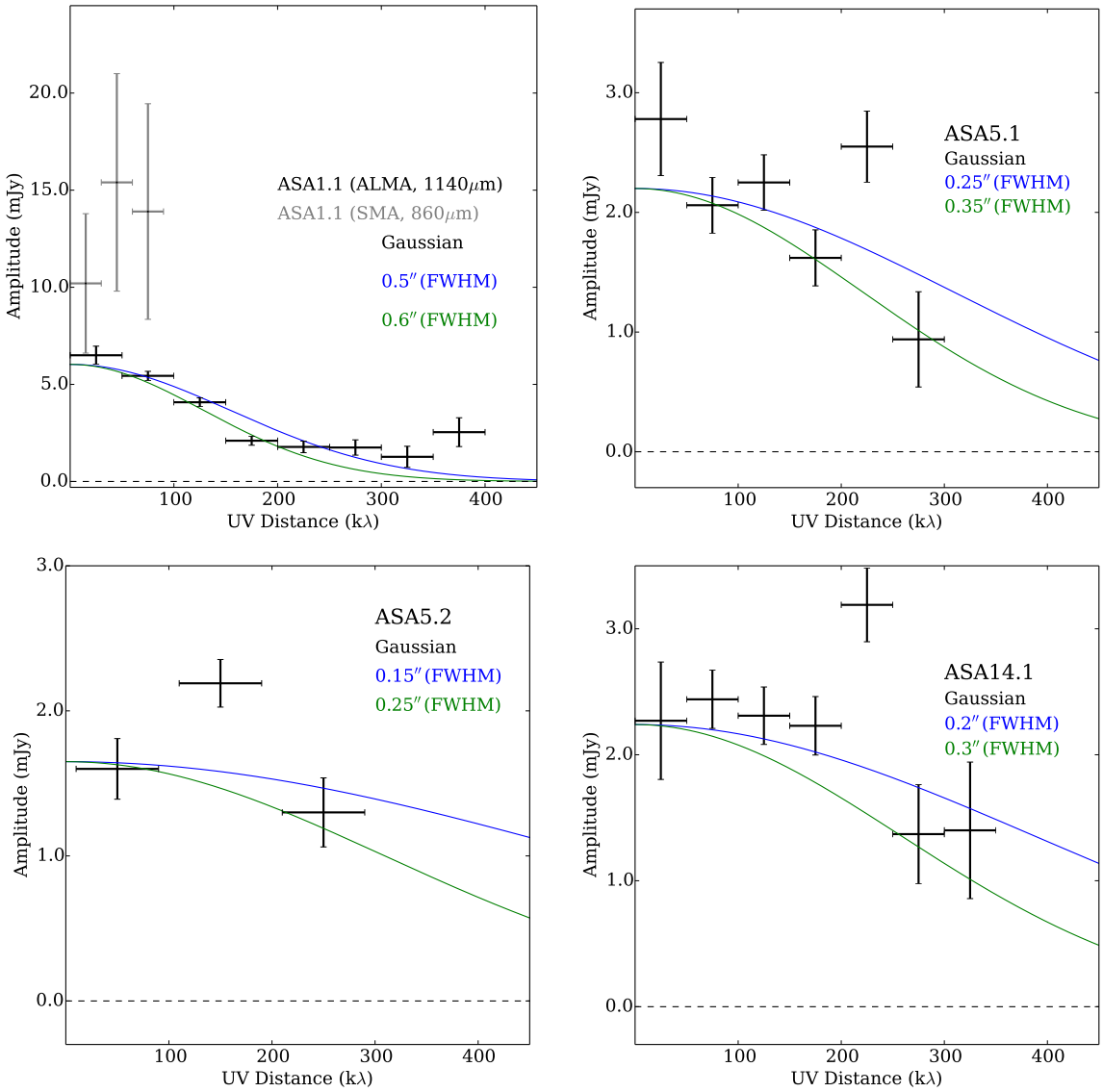

Fig. C.2 The results of u, v model fit

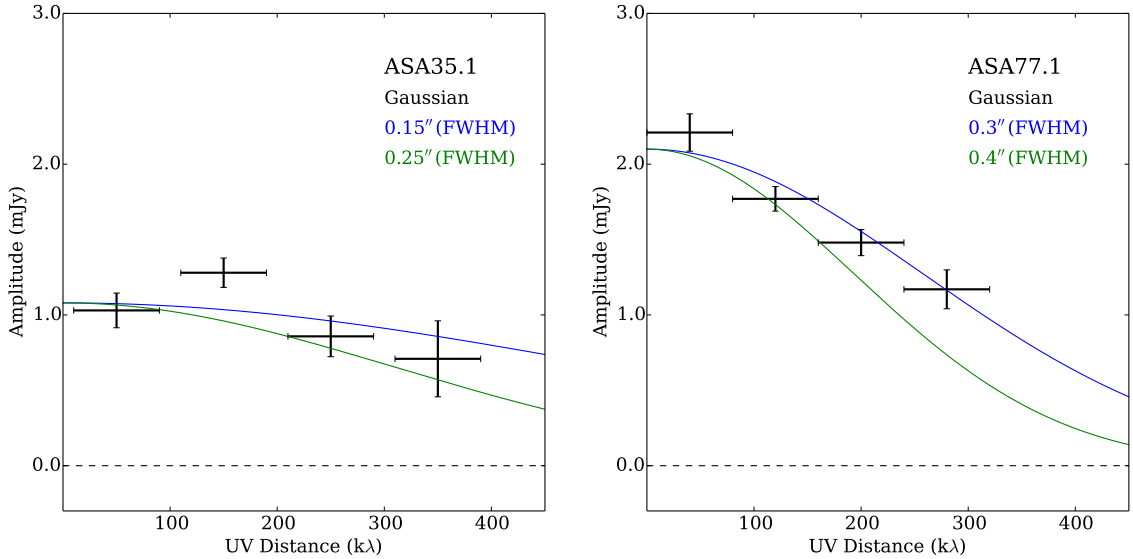

Fig. C.3 The results of u, v model fit

C.2 K-S test

In comparing the photometric redshift distribution and LAE surface number density in SSA22 and other fields, we implement the Kolmogorov-Smirnov (K-S) two-sample test to determine if two samples have the same distribution statistically.

The results are summarized in Table. C.1. The K-S test shows the redshift distribution of SSA22 is consistent with that of ALESS with a confidence level of $<0.1\%$.

Sample1	Sample2	p %
SSA22	ECDF-S	0.80
SSA22	Chapman 2005	0.02
SSA22	SPT-ALMA	0.97
SSA22	COSMOS-AzTEC	40.14
SSA22(radio)	Chapman 2005	17.47

Table C.1 KS-test: Photo-z Distribution.

C.3 Picture of the Kohno Laboratory Members

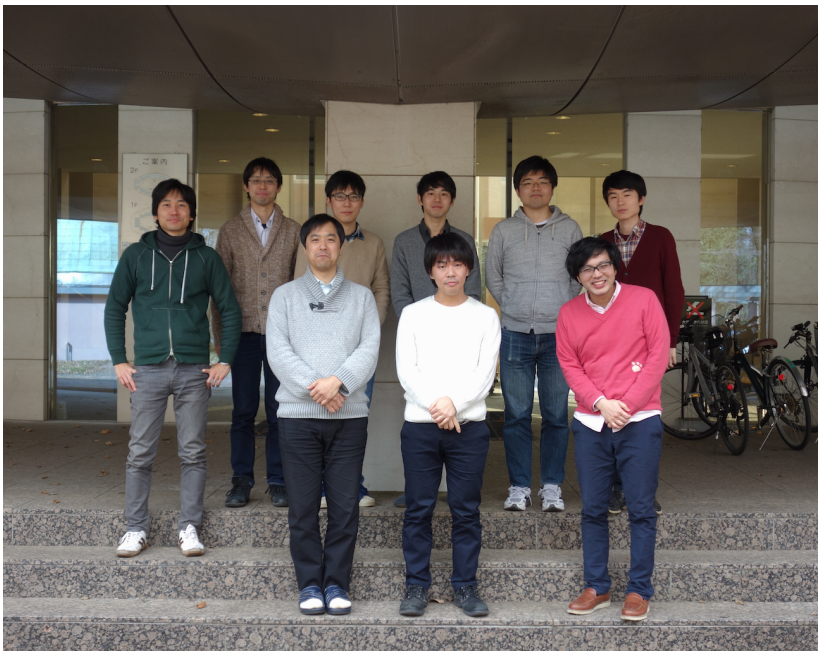

Fig. C.4 Picture of the Kohno Laboratory members.
(*The front row, from left to right*) Kotaro Kohno, Hideki Umehata, Ryu Makiya.
(*The back row, from left to right*) Yoichi Tamura, Shun Ishii, Takuma Izumi, Akio Taniguchi, Yuki Yamaguchi, Ryo Ando.

References

Alaghband-Zadeh, S., Chapman, S. C., Swinbank, A. M., et al. 2012, MNRAS, 424, 2232

Alexander, D. M., Bauer, F. E., Chapman, S. C., et al. 2005, ApJ, 632, 736

Alexander, D. M., & Hickox, R. C. 2012, New A Rev., 56, 93

Alexander, D. M., Bauer, F. E., Brandt, W. N., et al. 2003, AJ, 125, 383

Alexander, D. M., Brandt, W. N., Smail, I., et al. 2008, AJ, 135, 1968

Arias, E. F., Charlot, P., Feissel, M., & Lestrade, J.-F. 1995, A&A, 303, 604

Austermann, J. E., Dunlop, J. S., Perera, T. A., et al. 2010, MNRAS, 401, 160

Barger, A. J., Cowie, L. L., Sanders, D. B., et al. 1998, Nature, 394, 248

Barger, A. J., Wang, W.-H., Cowie, L. L., et al. 2012, ApJ, 761, 89

Bauer, F. E., Alexander, D. M., Brandt, W. N., et al. 2004, AJ, 128, 2048

Bedregal, A. G., Scarlata, C., Henry, A. L., et al. 2013, ApJ, 778, 126

Bell, E. F., McIntosh, D. H., Katz, N., & Weinberg, M. D. 2003, ApJS, 149, 289

Bertin, E., & Arnouts, S. 1996, A&AS, 117, 393

Bertoldi, F., Carilli, C., Aravena, M., et al. 2007, ApJS, 172, 132

Biggs, A. D., Ivison, R. J., Ibar, E., et al. 2011, MNRAS, 413, 2314

Blain, A. W., Chapman, S. C., Smail, I., & Ivison, R. 2004, ApJ, 611, 725

Bolzonella, M., Miralles, J.-M., & Pelló, R. 2000, A&A, 363, 476

Borys, C., Smail, I., Chapman, S. C., et al. 2005, ApJ, 635, 853

Bothwell, M. S., Smail, I., Chapman, S. C., et al. 2013, MNRAS, 429, 3047

Bower, R. G., Lucey, J. R., & Ellis, R. S. 1992, MNRAS, 254, 601

Bruzual, G., & Charlot, S. 2003, MNRAS, 344, 1000

Calzetti, D., Armus, L., Bohlin, R. C., et al. 2000, ApJ, 533, 682

Capak, P. L., Riechers, D., Scoville, N. Z., et al. 2011, Nature, 470, 233

Carilli, C. L., Daddi, E., Riechers, D., et al. 2010, ApJ, 714, 1407

Casey, C. M., Narayanan, D., & Cooray, A. 2014, Phys. Rep., 541, 45

Chabrier, G. 2003, PASP, 115, 763

Chapman, S. C., & Baugh, C. 2004, Clusters of Galaxies: Probes of Cosmological Structure and Galaxy Evolution, 7

Chapman, S. C., Blain, A., Ibata, R., et al. 2009, ApJ, 691, 560

Chapman, S. C., Blain, A. W., Smail, I., & Ivison, R. J. 2005, ApJ, 622, 772

Chapman, S. C., Scott, D., Windhorst, R. A., et al. 2004, ApJ, 606, 85

Chen et al., Ian Smail, A. M. S. J. M. S. C.-J. M. 2014, ApJ in press

Condon, J. J. 1974, ApJ, 188, 279

—. 1992, ARA&A, 30, 575

Coppin, K., Chapin, E. L., Mortier, A. M. J., et al. 2006, MNRAS, 372, 1621

Coppin, K., Halpern, M., Scott, D., et al. 2008, MNRAS, 384, 1597

Coppin, K. E. K., Smail, I., Alexander, D. M., et al. 2009, MNRAS, 395, 1905

Daddi, E., Dannerbauer, H., Stern, D., et al. 2009, ApJ, 694, 1517

Downes, T. P., Welch, D., Scott, K. S., et al. 2012, MNRAS, 423, 529

Dressler, A. 1980, ApJ, 236, 351

Eales, S., Lilly, S., Gear, W., et al. 1999, ApJ, 515, 518

Elvis, M., Wilkes, B. J., McDowell, J. C., et al. 1994, ApJS, 95, 1

Engel, H., Tacconi, L. J., Davies, R. I., et al. 2010, ApJ, 724, 233

Evans, I. N., Primini, F. A., Glotfelty, K. J., et al. 2010, ApJS, 189, 37

Ezawa, H., Kawabe, R., Kohno, K., & Yamamoto, S. 2004, in Society of Photo-Optical Instrumentation Engineers (SPIE) Conference Series, Vol. 5489, Ground-based Telescopes, ed. J. M. Oschmann, Jr., 763–772

Ezawa, H., Kohno, K., Kawabe, R., et al. 2008, in Society of Photo-Optical Instrumentation Engineers (SPIE) Conference Series, Vol. 7012, Society of Photo-Optical Instrumentation Engineers (SPIE) Conference Series

Fazio, G. G., Hora, J. L., Allen, L. E., et al. 2004, ApJS, 154, 10

Garmire, G. P., Bautz, M. W., Ford, P. G., Nousek, J. A., & Ricker, Jr., G. R. 2003, in Society of Photo-Optical Instrumentation Engineers (SPIE) Conference Series, Vol. 4851, X-Ray and Gamma-Ray Telescopes and Instruments for Astronomy., ed. J. E. Truemper & H. D. Tananbaum, 28–44

Gawiser, E., van Dokkum, P. G., Gronwall, C., et al. 2006, ApJ, 642, L13

Gawiser, E., Francke, H., Lai, K., et al. 2007, ApJ, 671, 278

Gehrels, N. 1986, ApJ, 303, 336

Giacconi, R., Rosati, P., Tozzi, P., et al. 2001, ApJ, 551, 624

Giavalisco, M., Ferguson, H. C., Koekemoer, A. M., et al. 2004, ApJ, 600, L93

Greve, T. R., Ivison, R. J., Bertoldi, F., et al. 2004, MNRAS, 354, 779

Greve, T. R., Bertoldi, F., Smail, I., et al. 2005, MNRAS, 359, 1165

Gronwall, C., Ciardullo, R., Hickey, T., et al. 2007, ApJ, 667, 79

Hainline, L. J., Blain, A. W., Smail, I., et al. 2011, ApJ, 740, 96

—. 2009, ApJ, 699, 1610

Häring, N., & Rix, H.-W. 2004, ApJ, 604, L89

Hatsukade, B., Ohta, K., Seko, A., Yabe, K., & Akiyama, M. 2013, ApJ, 769, L27

Hatsukade, B., Kohno, K., Aretxaga, I., et al. 2011, MNRAS, 411, 102

Hayashino, T., Matsuda, Y., Tamura, H., et al. 2004, AJ, 128, 2073

Hayward, C. C., Narayanan, D., Kereš, D., et al. 2013, MNRAS, 428, 2529

Henriques, B., Maraston, C., Monaco, P., et al. 2011, MNRAS, 415, 3571

Hickox, R. C., Wardlow, J. L., Smail, I., et al. 2012, MNRAS, 421, 284

Hodge, J. A., Karim, A., Smail, I., et al. 2013, ApJ, 768, 91

Holland, W. S., Robson, E. I., Gear, W. K., et al. 1999, MNRAS, 303, 659

Hopkins, P. F., Cox, T. J., Hernquist, L., et al. 2013, MNRAS, 430, 1901

Hopkins, P. F., Hernquist, L., Cox, T. J., et al. 2006, ApJS, 163, 1

Hopkins, P. F., Hernquist, L., Cox, T. J., & Kereš, D. 2008, ApJS, 175, 356

Hughes, D. H., Serjeant, S., Dunlop, J., et al. 1998, Nature, 394, 241

Ikarashi, S., Ivison, R. J., Caputi, K. I., et al. 2014, submitted to ApJL

Ilbert, O., Capak, P., Salvato, M., et al. 2009, ApJ, 690, 1236

Iono, D., Wilson, C. D., Takakuwa, S., et al. 2007, ApJ, 659, 283

Ivison, R. J., Greve, T. R., Smail, I., et al. 2002, MNRAS, 337, 1

Ivison, R. J., Greve, T. R., Dunlop, J. S., et al. 2007, MNRAS, 380, 199

Kalberla, P. M. W., Burton, W. B., Hartmann, D., et al. 2005, A&A, 440, 775

Karim, A., Swinbank, A. M., Hodge, J. A., et al. 2013, MNRAS, 432, 2

Kartaltepe, J. S., Dickinson, M., Alexander, D. M., et al. 2012, ApJ, 757, 23

Kashikawa, N., Aoki, K., Asai, R., et al. 2002, PASJ, 54, 819

Kauffmann, G., Heckman, T. M., White, S. D. M., et al. 2003, MNRAS, 341, 33

Kennicutt, Jr., R. C. 1998, ApJ, 498, 541

Kim, D.-W., Fabbiano, G., & Trinchieri, G. 1992a, ApJS, 80, 645

—. 1992b, ApJ, 393, 134

Kodama, T., Tanaka, I., Kajisawa, M., et al. 2007, MNRAS, 377, 1717

Kroupa, P. 2001, MNRAS, 322, 231

Kubo, M., Uchimoto, Y. K., Yamada, T., et al. 2013, ApJ, 778, 170

Kubo et al, Toru Yamada, T. I. M. K. Y. M. I. T. 2015, ApJ submitted

Lamastra, A., Menci, N., Maiolino, R., Fiore, F., & Merloni, A. 2010, MNRAS, 405, 29

Lawrence, A., Warren, S. J., Almaini, O., et al. 2007, MNRAS, 379, 1599

Lehmer, B. D., Alexander, D. M., Bauer, F. E., et al. 2010, ApJ, 724, 559

Lehmer, B. D., Brandt, W. N., Alexander, D. M., et al. 2005, ApJS, 161, 21

—. 2007, ApJ, 657, 681

—. 2008, ApJ, 681, 1163

Lehmer, B. D., Alexander, D. M., Geach, J. E., et al. 2009a, ApJ, 691, 687

Lehmer, B. D., Alexander, D. M., Chapman, S. C., et al. 2009b, MNRAS, 400, 299

Lehmer, B. D., Lucy, A. B., Alexander, D. M., et al. 2013, ApJ, 765, 87

Madau, P., & Dickinson, M. 2014, ARA&A, 52, 415

Maiolino, R., Salvati, M., Bassani, L., et al. 1998, A&A, 338, 781

Makovoz, D., & Marleau, F. R. 2005, PASP, 117, 1113

Marconi, A., Risaliti, G., Gilli, R., et al. 2004, MNRAS, 351, 169

Matsuda, Y., Yamada, T., Hayashino, T., et al. 2005, ApJ, 634, L125

Menci, N., Fiore, F., Puccetti, S., & Cavaliere, A. 2008, ApJ, 686, 219

Michałowski, M., Hjorth, J., & Watson, D. 2010, A&A, 514, A67

Michałowski, M. J., Dunlop, J. S., Ivison, R. J., et al. 2012, MNRAS, 426, 1845

Miyazaki, S., Komiyama, Y., Sekiguchi, M., et al. 2002, PASJ, 54, 833

Nandra, K., & Pounds, K. A. 1994, MNRAS, 268, 405

Ono, Y., Ouchi, M., Kurono, Y., & Momose, R. 2014, ApJ, 795, 5

Ouchi, M., Shimasaku, K., Akiyama, M., et al. 2008, ApJS, 176, 301

Persic, M., & Rephaeli, Y. 2007, A&A, 463, 481

Pope, A., Borys, C., Scott, D., et al. 2005, MNRAS, 358, 149

Postman, M., Franx, M., Cross, N. J. G., et al. 2005, ApJ, 623, 721

Ptak, A., Serlemitsos, P., Yaqoob, T., & Mushotzky, R. 1999, ApJS, 120, 179

Purcell, G. H. 1973, PhD thesis, California Institute of Technology

Ranalli, P., Comastri, A., & Setti, G. 2003, A&A, 399, 39

Rieke, G. H., Young, E. T., Engelbracht, C. W., et al. 2004, ApJS, 154, 25

Risaliti, G., Maiolino, R., & Salvati, M. 1999, ApJ, 522, 157

Sakamoto, K., Wang, J., Wiedner, M. C., et al. 2008, ApJ, 684, 957

Salpeter, E. E. 1955, ApJ, 121, 161

Sanders, D. B., Soifer, B. T., Elias, J. H., et al. 1988, ApJ, 325, 74

Scott, K. S., Austermann, J. E., Perera, T. A., et al. 2008, MNRAS, 385, 2225

Scott, K. S., Yun, M. S., Wilson, G. W., et al. 2010, MNRAS, 405, 2260

Scott, K. S., Wilson, G. W., Aretxaga, I., et al. 2012, MNRAS, 423, 575

Scott, S. E., Dunlop, J. S., & Serjeant, S. 2006, MNRAS, 370, 1057

Shimizu, I., Yoshida, N., & Okamoto, T. 2011, MNRAS, 418, 2273

—. 2012, MNRAS, 427, 2866

Silverman, J. D., Mainieri, V., Lehmer, B. D., et al. 2008, ApJ, 675, 1025

Simpson, J. M., Smail, I., Swinbank, A. M., et al. 2014a, ApJ in press

Simpson, J. M., Swinbank, A. M., Smail, I., et al. 2014b, ApJ, 788, 125

Smail, I., Ivison, R. J., & Blain, A. W. 1997, ApJ, 490, L5

Smail, I., Geach, J. E., Swinbank, A. M., et al. 2014, ApJ, 782, 19

Smolčić, V., Aravena, M., Navarrete, F., et al. 2012, A&A, 548, A4

Springel, V., White, S. D. M., Jenkins, A., et al. 2005, Nature, 435, 629

Steidel, C. C., Adelberger, K. L., Dickinson, M., et al. 1998, ApJ, 492, 428

Steidel, C. C., Adelberger, K. L., Shapley, A. E., et al. 2000, ApJ, 532, 170

Surace. 2005

Suwa, T., Hirashita, H., & Tamura, Y. 2010, Ap&SS, 330, 219

Suzuki, R., Tokoku, C., Ichikawa, T., et al. 2008, PASJ, 60, 1347

Swinbank, A. M., Chapman, S. C., Smail, I., et al. 2006, MNRAS, 371, 465

Swinbank, A. M., Simpson, J. M., Smail, I., et al. 2014, MNRAS, 438, 1267

Tamura, Y., Kohno, K., Nakanishi, K., et al. 2009, Nature, 459, 61

Tamura, Y., Iono, D., Wilner, D. J., et al. 2010, ApJ, 724, 1270

Tamura, Y., Matsuda, Y., Ikarashi, S., et al. 2013, MNRAS, 430, 2768

Tody, D. 1986, in Society of Photo-Optical Instrumentation Engineers (SPIE) Conference Series, Vol. 627, Instrumentation in astronomy VI, ed. D. L. Crawford, 733

Toft, S., van Dokkum, P., Franx, M., et al. 2007, ApJ, 671, 285

Toft, S., Smolčić, V., Magnelli, B., et al. 2014, ApJ, 782, 68

Tozzi, P., Gilli, R., Mainieri, V., et al. 2006, A&A, 451, 457

Tran, K.-V. H., Papovich, C., Saintonge, A., et al. 2010, ApJ, 719, L126

Uchimoto, Y. K., Suzuki, R., Tokoku, C., et al. 2008, PASJ, 60, 683

Uchimoto, Y. K., Yamada, T., Kajisawa, M., et al. 2012, ApJ, 750, 116

Ueda, Y., Akiyama, M., Hasinger, G., Miyaji, T., & Watson, M. G. 2014, ApJ, 786, 104

Umehata, H., Tamura, Y., Kohno, K., et al. 2014, MNRAS, 440, 3462

van Dokkum, P. G., Franx, M., Förster Schreiber, N. M., et al. 2004, ApJ, 611, 703

van Dokkum, P. G., Franx, M., Kriek, M., et al. 2008, ApJ, 677, L5

Vieira, J. D., Crawford, T. M., Switzer, E. R., et al. 2010, ApJ, 719, 763

Vieira, J. D., Marrone, D. P., Chapman, S. C., et al. 2013, Nature, 495, 344

Wang, R., Wagg, J., Carilli, C. L., et al. 2013a, ApJ, 773, 44

Wang, S. X., Brandt, W. N., Luo, B., et al. 2013b, ApJ, 778, 179

Wardlow, J. L., Smail, I., Coppin, K. E. K., et al. 2011, MNRAS, 415, 1479

Webb, T. M. A., Yamada, T., Huang, J.-S., et al. 2009, ApJ, 692, 1561

Weiß, A., Kovács, A., Coppin, K., et al. 2009, ApJ, 707, 1201

Weiß, A., De Breuck, C., Marrone, D. P., et al. 2013, ApJ, 767, 88

Whitaker, K. E., van Dokkum, P. G., Brammer, G., et al. 2013, ApJ, 770, L39

Willott, C. J., Omont, A., & Bergeron, J. 2013, ApJ, 770, 13

Wilson, G. W., Austermann, J. E., Perera, T. A., et al. 2008, MNRAS, 386, 807

Xue, Y. Q., Luo, B., Brandt, W. N., et al. 2011, ApJS, 195, 10

Yamada, T., Nakamura, Y., Matsuda, Y., et al. 2012, AJ, 143, 79

Younger, J. D., Fazio, G. G., Wilner, D. J., et al. 2008, ApJ, 688, 59

Yun, M. S., Reddy, N. A., & Condon, J. J. 2001, ApJ, 554, 803

Yun, M. S., Aretxaga, I., Ashby, M. L. N., et al. 2008, MNRAS, 389, 333

Yun, M. S., Scott, K. S., Guo, Y., et al. 2012, MNRAS, 420, 957

Zezas, A., Fabbiano, G., Prestwich, A., Murray, S., & Ward, M. 2001, in Astronomical Society of the Pacific Conference Series, Vol. 249, The Central Kiloparsec of Starbursts and AGN: The La Palma Connection, ed. J. H. Knapen, J. E. Beckman, I. Shlosman, & T. J. Mahoney, 425